

ASPECTS OF THE ELECTROSLAG WELDING PROCESS

by

WILLIAM GORDON BACON

B.A.Sc., University of British Columbia, 1967

A THESIS SUBMITTED IN PARTIAL FULFILLMENT OF
THE REQUIREMENTS FOR THE DEGREE OF
DOCTOR OF PHILOSOPHY

in

THE FACULTY OF GRADUATE STUDIES
Department of Metallurgical Engineering

We accept this thesis as conforming
to the required standard

THE UNIVERSITY OF BRITISH COLUMBIA

February, 1979.

© William Gordon Bacon

In presenting this thesis in partial fulfilment of the requirements for an advanced degree at the University of British Columbia, I agree that the Library shall make it freely available for reference and study.

I further agree that permission for extensive copying of this thesis for scholarly purposes may be granted by the Head of my Department or by his representatives. It is understood that copying or publication of this thesis for financial gain shall not be allowed without my written permission.

Department of METALLURGY

The University of British Columbia
2075 Wesbrook Place
Vancouver, Canada
V6T 1W5

Date MARCH 15, 1979

ABSTRACT

The electroslog welding (ESW) process has been investigated utilizing consumable guide welding procedures. Electroslog welding employing large square cross-section electrodes was also studied.

The study of the process parameters is of importance in understanding the role which they play in determining the grain size attained in the heat affected zone of the resultant weld. The large grain size adversely effects the impact strength: the grain size is a direct consequence of the thermal history.

The thermal history of the base metal was determined during welding for various physical configurations and welding schedules. The welding parameters having the major effect on the thermal history are: mode of welding, electrode immersion depth, slag depth, welding velocity and specific power input. The penetration of the parent metal and size of the heat-affected zone as well as the grain size have been shown to be a consequence of the thermal history. The quazi-steady state electrical and temperature distributions in the slag are seen to determine the temperature distribution in the metal.

The preferred modes of welding are alternating current (AC) and direct current reverse polarity (DCRP) with direct current straight polarity (DCSP) being unacceptable due to the high inclusion content of the weld when DCSP is employed.

The electrode immersion depth, or interelectrode gap, has been found to determine the volume of the effective heat source

and thus the temperature and electrical distributions. The slag depth and electrode velocity are the principal factors which determine the interelectrode gap when the slag chemistry and physical configuration are constant. There exist ranges of slag depth and electrode velocity values outside of which welding is not achieved.

An analytical model has been employed which adequately describes thick plate welding practice, but which only applies to thin plate welds in a qualitative manner. In this model, an empirical equation has been used to calculate electrode immersion values which compare favourably with the measured values. In addition, the Bastein method of grain size calculation has been applied to the thermal histories obtained experimentally and has been found to be applicable.

In welds where impact strength is an important design criteria the weld/HAZ grain size is an important variable. We conclude that no combination of ESW process parameters will lead to an acceptable HAZ grain size giving HAZ impact values comparable with the parent plate. In such cases full heat treatment of the HAZ would be mandatory.

TABLE OF CONTENTS

<u>Chapter</u>		<u>Page</u>
1	INTRODUCTION	1
1.1	Introduction	1
1.2	Nature of the Process	2
1.2.1	Current Type and Polarity	3
1.2.2	ESW slags	4
1.3	Properties of Electroslag Welding	7
1.4	Nature of the Problem	9
1.5	Previous Work	9
1.5.1	Temperature Measurements	10
1.5.2	Calculation of Penetration	12
1.5.3	Solutions to Low HAZ Toughness	12
1.5.4	Process Parameter Investigations	14
1.5.5	The Present Research Program	20
2	MODELS AND CALCULATIONS	21
2.1	Introduction	21
2.2	An Analytical Model	23
2.2.1	Assumptions	23
2.2.2	Calculation of the Interelectrode Gap	24
2.3	Application of the Analytical Model	25
2.3.1	Data Generated by the Model	25

<u>Chapter</u>		<u>Page</u>
	2.3.2 Manipulation of the Data	25
2.4	Summary	27
3	EXPERIMENTAL PROGRAM	28
3.1	ESW Devices at U.B.C.	28
3.1.1	Wire or Consumable Guide Welders	28
3.1.2	Bar or Plate Electrodes	29
3.2	Initial Experimental Procedures	29
3.2.1	Stage One.. .. .	29
3.2.2	Stage Two, Consumable Guide to ESW	31
3.2.3	Slag Temperature	33
3.2.4	Electrode Immersion	33
3.2.5	Other Experimental Procedures	34
3.3	Butt Welds using Consumable Guide ESW	34
3.3.1	The Welding Jig	35
3.3.2	The Water Cooled Copper Shoes	36
3.3.3	The Consumable Guide Fixed Head	38
3.3.4	Run-In Sump and Run-out Blocks	39
3.3.5	Thermocouple Positions	39
3.3.6	Slag Additions and Other Procedures	40

<u>Chapter</u>		<u>Page</u>
	3.3.7 Electrical Current Distribution Measurements	40
3.4	Butt Welds using Bar Electrodes	41
	3.4.1 The Fixed Head	42
3.5	Evaluation of Weld Properties	42
	3.5.1 Hardness Values	42
	3.5.2 Toughness Values	43
	3.5.3 Inclusion Distributions	43
3.6	Experimental Records	43
4	RESULTS	45
	4.1 Power Supply Characteristics	45
	4.1.1 Published Power Characteristics	45
	4.1.2 Measured Power Characteristics	45
	4.2 Industrial Experiments	46
	4.2.1 Experimental Conditions	46
	4.2.2 Experimental Results	46
	4.3 Initial Large Electrode Experiments	46
	4.3.1 Temperature Time Cycles	46
	4.3.2 Power Characteristics and Apparent Resistance of the Slag	49
	4.3.3 Deposition Rate or Welding Velocity	49
	4.3.4 Penetration and Inclusion Distribution	50
	4.3.5 Hardness Traverses	50
	4.3.6 Oxygen Analyses	50

<u>Chapter</u>		<u>Page</u>
4.4	Consumable Guide ESW in Cylinders	50
4.4.1	Introduction	50
4.4.2	Slag Temperature Measurements	50
4.4.3	Slag Depth, Immersion and Inter-electrode Gap Measurements	52
4.4.4	Velocity Measurements	52
4.4.5	Temperature Time Cycles.. .. .	52
4.4.6	Penetration	55
4.4.7	Oxygen Analysis	55
4.4.8	Use of a 304 S.S. Consumable Guide	55
4.5	Consumable Guide ESW with A-36 Plates	55
4.5.1	Introduction	55
4.5.2	Temperature Time Cycles	57
4.5.3	Penetration and HAZ Values	57
4.5.4	Hardness Traverses	57
4.5.5	Inclusions	57
4.5.6	Grain Size Analysis	61
4.5.7	Charpy Traverses and Fracture Surfaces	61
4.6	ESW Utilizing Bar Electrodes	61
4.6.1	Introduction	61
4.6.2	Temperature Time Cycles	61
4.6.3	Penetration	64
4.6.4	Hardness Traverses	64
4.6.5	Charpy Traverses	64
4.7	Electrical Distribution	64
4.8	General Observations	66

<u>Chapter</u>		<u>Page</u>
5	DISCUSSION OF RESULTS	67
5.1	Discussion of POver Supplies	67
5.2	Industrial Experiments at Cannon	68
5.2.1	The Apparent Resistance of the Slag Pool	68
5.2.2	Energy Requirements.	69
5.3	Relating PUBLISHED Experimental and Production Welding Energy Requirements	69
5.4	Initial Large Electrode Experiments	74
5.4.1	Comparison of the Temperature Time Cycles ..	74
5.4.2	Apparent Resistance of the Slag	75
5.4.3	Energy Requirements	75
5.4.4	Use of Inclusion Distribution Measurements.. .. .	76
5.4.5	Measuring Penetration and the Heat Affected Zone using Hardness Traverses	76
5.4.6	Oxygen Analysis and the Interpretation of the Results	77
5.5	Consumable Guide ESW in Cylinders	77
5.1.1	An Overview of the Experimental Operating Conditions	77
5.2.2	Interpretation of the Slag Temperature Distribution.. .. .	77

<u>Chapter</u>		<u>Page</u>
5.5.3	The Effects of Slag Depth, Polarity and the Resultant Immersion and Interelectrode Gap	78
5.5.4	Velocity Measurements and Reliability.. .. .	79
5.5.5	Explanation of the Temperature Time Cycles	79
5.5.6	Penetration and Temperature Time Cycles ..	80
5.5.7	Hardness Traverses	80
5.5.8	Oxygen Analysis Results	81
5.5.9	Stainless Steel Consumable Guide and Mixing in the Liquid Steel Pool	81
5.6	Consumable Guide ESW with A-36 Plates	82
5.6.1	An Overview of the Experimental Operating Conditions	82
5.6.2	Explanation of the Temperature Time Cycles	82
5.6.3	Penetration and the Heat Affected Zone as a Function of the Thermal Profile	83
5.6.4	Hardness Traverses	84
5.6.5	Measured Grain Size and Austenite Grain Size	84
5.6.6	Inclusion Analysis	85
5.6.7	Charpy Impact Values	86
5.7	Electrical Distribution in Consumable Guide ESW	86
5.7.1	Possible Interpretation of the Current Distribution	87
5.7.2	Correlation with the Slag Temperature Distribution	87

LIST OF TABLES

<u>Table</u>		<u>Page</u>
1	Common Electroslag Welding Fluxes	6
2	Welding Conditions for Thermal Cycles in Figure 5 (from Patton, Ref. 1)	10
3	Relation Between Welding Schedule and Weld Shape	15
4	Canron Limited Welding Conditions	47
5	Canron Limited Welding Analysis	48
6	Experimental Conditions for Consumable Guide Electroslag Welding (CGESW) in Cylinders	51
7	Slag Depth, Immersion and Interelectrode Gap Measurements	53
8	Welding Velocity Measurements	54
9	Experimental Conditions for Consumable Guide Electroslag Welding (CGESW) with A 36 Plates	56
10	Penetration and Heat Affected Zone (HAZ) Values for the Experiments in Table 9	58
11	Grain Sizes in ASTM Numbers at Various Positions	59
12	Inclusion Distributions in CGESW of A 36 Plates	60
13	Charpy Values at Various Positions in Welded A 36 Plate	62
14	Experimental Conditions for ESW Utilizing Bar Electrodes	63
15	Charpy Values at Various Positions in ESW Welded T-1 Equivalent Plate	65
16	Experiment and Industrial Welding Conditions from the Literature	70

LIST OF SYMBOLS

Symbols

T	temperature, °K or °C
t	time, seconds
T ₀	preheat temperature, °C
q	heat source, cal. sec ⁻¹ cm ⁻¹
v	weld velocity, cm. sec ⁻¹
x	distance, cm.
y	distance, cm.
α	coefficient of thermal diffusivity cm ² sec. ⁻¹
b	coefficient of heat transfer sec. ⁻¹
k	thermal conductivity, cal. cm ⁻¹ sec ⁻¹ °C ⁻¹
c	specific heat, cal. gm. ⁻¹ °C ⁻¹
ρ	density, gm. cm ⁻³
δ	thickness of plates being welded, cm.
V	voltage, volts
I	amperage, amps.
η	efficiency, unitless.
R	resistance, ohms.
ρ	specific resistance, ohm-cm.
L	immersion, cm.
r	radius of electrode, cm.

ACKNOWLEDGEMENTS

The author sincerely appreciates the advice and direction provided by his research director, Dr. Alec Mitchell, throughout the course of this project.

The author is indebted to Mr. Jim Brezden and Mr. Rick Palylyk for their assistance throughout the program. The author also wishes to thank the entire technical staff for their helpful suggestions.

He thanks the departmental faculty members and fellow graduate students for their friendship and endless encouraging discussion.

Financial assistance in the form of the National Research Council of Canada Postgraduate Scholarship (1969-1972) and a Stelco Graduate Research Fellowship (1972-1974) is greatly appreciated.

A special thanks is given to Dr. Ed Teghtsoonian, Dr. Neil Riseborough and Dr. K. C. Donaldson for their moral support and understanding.

CHAPTER 1

INTRODUCTION

1.1 Introduction

Since the end of World War II there has been a marked increase in the size of fabricated equipment which in turn has caused a marked increase in the demand for efficient methods of joining or welding of large component parts. The increase in demand for welding heavier sections has led to the development of lower cost, faster methods, one of which is electroslag welding (ESW). ESW was developed by Prof. B.E. Paton at the E.O. Paton Electric Welding Institute of the Academy of Sciences of the U.S.S.R. and his book (1) is the only authoritative book available on ESW.

There has been a steadily increasing demand for the use of ESW, especially in the following areas:

1. Long, heavy section, vertical or near-vertical butt and T-type welds.
2. Large, heavy section circumferential welds.
3. Joining of large ingots for subsequent forging.
4. Surfacing of both flat and cylindrical surfaces.
5. As a replacement for automatic submerged arc.
6. Joining of large castings.

1.2 Nature of the Process

ESW is a welding process utilizing the heat produced by an electric current passing through a molten slag to produce a finished weld in a single pass. The parent metal components are placed in a vertical position and secured with a gap between them (Fig. 1). The bottom of the weld is started in a constructed sump and the top of the weld ended in a set of run-out blocks. A set of water cooled copper shoes (or molds) are affixed against the side of the parent metal, overlapping the gap completely. The shoes may be either the continuous length of the weld or moved up as welding proceeds. The electrode is lowered into the sump until arcing starts at which time the granulated slag is added slowly to extinguish the arc and thus provide the slag pool. Enough slag is added to prevent arcing, and keep the process stable. The electrode is lowered at a constant rate, with slag being added continuously until the weld has progressed into the run-out blocks and the electrode is stopped.

There are various types of ESW that have been patented and are in use:

1. Standard ESW employing from 1 to 15 bare electrode wires from 2 to 5 mm. in diameter. This is basically the process developed by Prof. B.E. Paton.
2. Consumable Guide ESW. The guide may be flux coated or bare and consists of a non-moving nozzle throughout the length of the weld. It is essentially a stationary electrode with a moving electrode in its centre. Both the wire and the guide are thus filler metals (1,2,3,4,5). The consumable guide is usually coated with a slag with a composition the same as the working slag, and the guide performs the function of insulating the wire and providing make-up

slag. This method is the most common when welding with wires and weld lengths that are less than 3 m. (Figure 1).

3. Plate Electrode ESW employs an electrode or electrodes that have the shape of the gap between the parent metal components. There may be one or more plates some of which may simply be filler metal (i.e. electrically neutral)(6,7,8,9,10).
4. Use of an additional filler metal, granulated in texture, to act as a filler or as an alloying agent is practical with any of the above three standard processes.

Various other ESW procedures have been tried but few are in common use and are not dealt with herein.

1.2.1 Current Type and Polarity

There are two electrodes, the filler metal and the parent metal, as in all welding processes. The welding can be accomplished by one of three methods:

1. Direct current, straight polarity (i.e. electrode or filler metal is negative) which is designated D.C.S.P. (This method is not commonly used in ESW).
2. Direct current, reverse polarity (i.e. electrode or filler metal is positive) which is designated D.C.R.P.
3. Alternating current designated A.C.

There are distinct differences between these methods with respect to the welding conditions and resultant physical properties. D.C.S.P. is virtually unused because of deleterious inclusion contents when the slag/metal pool interface is positive. D.C.R.P. and A.C. are common and both are used, but A.C. is more common. When employing ESW (and other

welding processes), it is advantageous to have a flat welding characteristic (Fig. 2) or, as it is sometimes called, a constant voltage source. ESW does not lend itself to a constant-current-type power supply. The constant-voltage-type source allows variation of the current without varying the voltage significantly.

Variation of the welding current in ESW is accomplished by varying the electrode feed rate which in turn controls the welding rate. This explains why A.C. is used more than D.C.R.P.; it is almost impossible to construct economically a D.C. welder with a completely constant voltage characteristic and consequently most welding of this type has a drooping characteristic (with increasing current, voltage drops). With A.C. it is possible to vary the current over a very wide range without a change in voltage. This feature is very important because it allows for a more stable process if voltage and current can be varied almost independently.

The mode of welding also distributes the current differently, thus distributing the heat differently. Thus, in actual practice, different welding schedules are necessary for D.C.R.P. and A.C. in order to achieve the same end results.

1.2.2 ESW slags

Slags or fluxes used for the ESW process must have the following features:

1. The flux must allow the process to be started easily and maintained over a range of slag depths, welding voltages and amperages.
2. The slag must wet the melting parent metal surfaces in order to attain complete fusion and controllable penetration.

3. The slag should not become too conductive at high temperatures or efficiency will suffer accordingly.
4. The solidified slag should be readily removable.
5. Chemical compatibility with the system to be welded.

The electrical conductivity and the viscosity of the slag are its two most important properties. Highly conductive slags facilitate the starting of the process and the stability of the process. The electrical conductivity also governs the amount of heat generated by the current passage and thus the welding rate attainable. The viscosity of the slag is also important in the process from both a practical and operating point of view. If the viscosity is too low (i.e. a "long" slag), the slag will leak between the shoes and the plates; if the viscosity is too high, the shoes commonly acquire very large 'buildups' and weld undercutting can occur. Also, the viscosity partially governs the motion of the slag which greatly affects thermal distribution in the slag and consequently the ability to weld.

Table 1 indicates the major slags and their compositions used in the U.S.S.R. (the most common quoted in the literature). ESW slags are low in SiO_2 and high in MnO because both allow far better stability. Calcium fluoride is added to increase the electrical conductivity and lower the viscosity. The chemical activity of the slag is also very important because it is necessary to wet the oxidized surfaces. Thus, a slag is required that can reduce the oxide films which form on the weld edges when the surface preparation consists of flame cutting only. This results in one of the advantages of ESW

TABLE 1

Common electroslag welding fluxes

Designation	Chemical composition in weight percentages						
	SiO ₂	Al ₂ O ₃	MnO	CaO	MgO	CaF ₂	Others
AN-8	33-36	11-15	21-26	4-7	5-7	13-19	
AN-8M	35-38	5.5 max.	28-32	4-8	1.0 max.	12-16	
AN-22	18-21.5	19-23	7-9	12-15	11.5-15	20-24	
FTs-7	46-48	3 max.	24-26	3 max.	16-18	5-6	
AN-25	6-9	-	-	12-15	2-4	33-40	30-40 TiO ₂
ANF-1	5 max.	-	-	-	-	92 min.	
ANF-7	-	-	-	20	-	80	
ANF-6	-	35	-	-	-	65	

1.3 Properties of Electroslag Welding

The most outstanding features of the process are the high deposition rate and the slow welding rate, hence its many advantages and its few disadvantages. The so called "soft" thermal cycle (Fig. 3) leads to the uniqueness of ESW compared to other processes. Any point in the parent metal will reach a particular temperature more slowly and also cool more slowly. This is due to the low welding velocity and comparatively high heat input of ESW. The slow cooling rate allows for the welding of steels that are susceptible to undesirable decomposition products at high cooling rates. Also preheating is eliminated because the initial heating is accomplished by radiation from the slag surface and conduction from the slag. However, the longer time at higher temperatures causes excessive grain growth in the heat affected zone.

The advantages of the process are:

- i. Increased efficiency compared to manual or submerged arc; once a weld has commenced, the operator efficiency is 100% for ESW compared to 40-60% for manual or submerged arc welding. A greater current efficiency also results, 20 g. per amp-hr for ESW versus 15 g. per amp-hr (6) for submerged arc; also 1.5 kWh/kg for ESW versus 2.5 kWh/kg for submerged arc (13) (Figure 4).
- ii. Virtually no edge preparation is necessary for ESW except where the faces are in contact with the cooling shoes.
- iii. There is a decrease in the possibility of porosity due to the slow moving solidification front and the continuous molten slag cover.
- iv. There is less distortion in ESW because the weld is made in a single pass (12). The single pass feature also decreases weld inspection costs.

- v. The process is very efficient thermally, with Paton quoting 1.2% of the energy input being lost to radiation and 7.8% to the cooling water (1); the percentage of total heat lost to the shoes decreases substantially with thickness (12).
- vi. There is usually no need to undertake any finishing procedures other than the removal of the single slag layer from both sides.

The disadvantages in ESW are two fold in nature, i.e. operating and metallurgical. The operating disadvantages are:

- i. Set up and initial capital outlay is expensive for shoes and electrode feeders.
- ii. A power failure results in a large defect that must be manually repaired.
- iii. Multiwire feeding machines are complicated and require strict maintenance.

As stated earlier the ESW process is characterized by the slow heating and cooling rates which lead to the metallurgical problems associated with ESW welds. The HAZ is above 1100°C for a long period of time, thus causing the austenite grains to grow excessively large and the cooling rate is so slow that the austenite decomposition to its products is slowed. The final structure on cooling is usually coarse grained ferritic/pearlitic or ferritic/bainitic, with some retained austenite or martensite (14) in the HAZ immediately adjacent to the fusion boundary. The superheating of this region can also have other effects if the steel is micro-alloyed; the carbo-nitrides will dissolve in this zone and, again, grain growth will occur (this is also true of the AlN precipitates.).

The problem with ESW properties is essentially a problem of toughness. In the HAZ it can be alleviated by adding aluminum and nitrogen (CaCN_2), normalizing, or quenching and tempering. However, in most cases, these solutions are uneconomical or impractical and the toughness problem in the HAZ of structural steel welds and in the high hardenability steels remains unsolved. This is true even when AlN is used to stabilize the small grain size at very high temperature. This is due to the long time at high temperature.

1.4 Nature of the Problem

The problem of large grain size in the HAZ can only be approached by altering the thermal cycle of the process. This can only be achieved by understanding how the heat is distributed during the process and what variables can be used to change the thermal generation and distribution.

1.5 Previous Work

The thermal distribution during ESW has been measured many times. References 1, 13 and 15 through 20 are typical. Some investigators (16-19) have attempted to predict the thermal cycle with good success (but have not tried to alter the cycle). Eregin has attempted to use these thermal cycles to predict penetration (21). However these investigators have not varied the welding conditions deliberately to determine if the thermal cycle and consequent penetration could be deliberately controlled and (i.e. the welding conditions) to minimize the penetration while attaining complete fusion.

The approach that has been taken is one of firstly producing a sound welding technique and then studying the resultant macrostructures, micro-

TABLE 2

Welding Conditions for Thermal Cycles
In Figure 5 (from Patton, Ref. 1)

Operating Conditions	ESW	ESW	ESW	Multi-Pass Submerged Arc	
	One 3 mm Electrode	Two 3 mm Electrodes	12 mm x 110 mm Plate	1	2
Mode	DC	AC	AC		
Welding Velocity (cm/sec)	.019	.028	.022	1.111	1.111
Voltage (Volts)	38-40	44-46	30-32	32-34	32-34
Current (Amps)	450	450	950	500	500
Slag Depth (mm)	40	55	25-30	-	-

structures and physical properties (22-38), and then developing a heat treatment schedule or alloying treatment to alleviate any problems caused by the welding technique. Many investigators have tried varying the welding parameters to vary the weldment and/or HAZ (28, 39-58) structures with varying degrees of success and disagreement.

Dilawari et al (76) have developed a model of the ESR process which indicates how the metal flows during the process. The model is useful in describing the observed metal flow in ESW.

1.5.1 Thermal Temperature Measurements

Paton (1) reports the thermal cycle (Fig. 5) for various welding conditions (Table 2) and makes comments on the slow thermal cycle for ESW versus submerged arc but does not comment on the difference between wire electrodes and plate electrodes. Lefevre (12) measures the thermal cycle and plots a contour map of isotherms around the electrode position but makes no comment on the extremely high temperatures attained and how this affected the HAZ (note: the welding conditions for the graphs were not provided). Mel'bard (15) plots a type of thermal cycle for the HAZ, the plot (Fig. 6) showing that there is very significant "preheating" of the parent metal above the slag surface. He also reports the mean temperature of the slag pool (about 1700^o C) and the temperature profile from the slag pool surface to the molten metal pool bottom (Fig. 7). These data are used to postulate that the current passes in the form of a cone from the electrode tip to the slag/molten metal pool interface, but no measurement of the current distribution was undertaken. Voloshkevich (39) states that "nearly all the heat is transferred to the parent metal through the weld puddle surface".

Pugin and Pertsovskii (16) have developed a model for the heat distribution by assuming a series of three moving linear heat sources and found

very good agreement with their measured thermal cycle. However they used an actual efficiency of 58%, 32.5% being lost to the cooling water and 9.5% by radiation; these are unrealistically high figures (1,12,17,18). The only reported heat balance calculations are those of Paton (1) and they are not referenced in his book.

1.5.2 Calculation of Penetration

One model, by Eregin (21), has been derived to calculate penetration and was reported to be in good agreement with the actual penetration. However most of the welding parameters were not presented and thus the model could not be evaluated correctly. No other references have attempted to calculate penetration as a function of changing welding parameters.

1.5.3 Solutions to Low HAZ Toughness

Rote (23) has investigated the ESW of various grade steels from A 285 to a high carbon, air hardening steel (Lukens D6AC). Only the A 212B and HY-80 were tested in the as welded condition, all other weldments were tested after various complicated heat treatments. Typical of many investigations, the results were inconclusive; in some welds the weldment had better ductility and impact strength than the parent metal and in other welds vice versa. Sometimes the HAZ had better impact strength than either the weldment or parent metal.

Zeke (24,32,56,57,59) has done exhaustive studies of ESW and written a review paper (59) for its use in the production of steel pressure vessels. He has determined that notch ductility is too low in the HAZ and has undertaken various heat treatment procedures on welds and specimens of parent metal to determine if the physical properties could be improved. It was determined that where the steel was subjected to a very complicated heat-

treatment (740°C/15 hr./air + 650°C/15 hr./air), the properties of the parent metal could be achieved. Makara (34) studied the effect of heat treatments between the AC₁ and AC₃ temperatures for ESW welded 1010 and 1015 and found essentially the same results can be achieved by 5 hr. at 780°C followed by furnace cooling. Makara (35) has also shown that 1015 can be heat treated successfully by tempering at 650°C for 2 hrs., furnace cooled to 300°C and then air cooled. Eichhorn (37) studied annealing between AC₁ and AC₃ for carbonitride former microalloyed steels to achieve improved impact strengths without normalizing (5 hours at 730°C, air cooled plus 4 hours at 630°C, air cooled) and achieved very good Izod impact values. Zeke and others (28) studied the weldmetal itself by electroslog remelting the welding wire and testing the as cast metal and the metal after various heat treatments. These studies commonly indicated that there is some suitable heat treatment schedule which will give the weldment good physical properties, but it is felt that this is an unreasonable way to study the HAZ problem. Woodley (25) ESW welded Lloyds grade B and Lloyds E and conducted wide plate fracture analysis and Charpy V-notch tests and concluded that both tests showed that the weldment and parent metal were at least as good as when submerged arc welded. The plates usually failed in the HAZ and the impact values in the HAZ were lower than either the parent metal or weldment. Woodley (27) also ESW welded JTA 101 (a normalized, silicon killed, carbon-manganese steel of boiler quality) and performed full plate slow bend tests and charpy V-notch impact tests (Fig. 8). Malinovska, and Hrivnak (28) studied various heat treatments between the A₁ and A₃ to eliminate the large HAZ grains in mild steel and found annealing between A₁ and A₃ could replace normalizing. Bentley (31) welded mild steel (Nb added) and performed Charpy V-notch tests in the HAZ for the welded, normalized and

double normalized conditions. He found that the HAZ was severely embrittled and the embrittlement could be eliminated by single or double normalizing, but double normalizing could lower the toughness of the parent metal.

Tempering of an ESW welded complex chromium-manganese steel (0.05% Ti, 0.5% Mo, 0.25% C) embrittles the HAZ according to Braun (33), normalizing will improve the toughness sufficiently. Novikov (36) has shown that plates can be locally normalized or tempered using industrial frequency current for plates up to 200 mm thick. This procedure gave very acceptable impact values and eliminated the requirements for very large furnaces, but does not appear to have been accepted commercially for plates over 50 mm.

The use of carbonitride formers to prevent the grain growth in high energy input welding has been investigated very extensively by Ikino et al (38). They found that only TiN could maintain the grain size at temperatures approaching 1400°C and, if enough TiN particles of less than 0.1 μ diameter were present, then the grain size in the HAZ could be kept at less than 100 μ . This is an advance in steel making technology and does not solve the general problem of ESW welding of structural and pressure vessel steels in existing specifications.

1.5.4 Process Parameter Investigations

Paton (1) has made a summary (Table 3) of the general effect of most of the process variables in ESW and devotes part of chapter 2 of his book (pp. 20-54) to this subject.

Gotal'skii (40) first (1954) proposed that the chemistry of ESW slags should be different from submerged arc slags based on the electrolytic reactions that take place during the process. Gotal'skii (41) showed that the basicity of the slag plays a major role in the reduction of silicon and increase in manganese, and that the electrical conductivity increases with basicity.

TABLE 3

Relation Between Welding Schedule and Weld
Shape (from Patton, Ref. 1)

Welding Conditions in Direction of
Increasing Values

Weld Characteristic	From 400 Amp or Higher	Welding Voltage	Slag Depth
Pool Depth	Increases	Slight Increase	Slight Decrease
Weld Width (Penetration)	Decreases	Increases	Decreases

However, these slags contained no fluorspar and as such are not used extensively. Gotal'skii (42) then investigated the effects of silica and fluorspar in ESW slags. He concluded that low silica fluxes would make the process more stable. He based his conclusion on the determination of the depth of the slag pool when arcing would initiate; when low silica slags were used he found arcing would commence only when the pool became very shallow. He also suggested that fluorspar would increase the conductivity of the slag and thus improve the stability of the process. He made no conclusions on the effect of the slag depth on the welds produced or on the thermal changes that must have occurred when the slag pool depth increased.

Zaitsev (44) has determined that fluorspar based slags have a stronger desulphurizing action than silicate based slags and that lowering the current and increasing the voltage helps desulphurizing. This data was produced on a small electroslag refining unit.

Shcherbina et al (60) have investigated slag compositions with regard to controlling the temperature of the molten pool. They conclude that the cause of the extremely high temperatures in the slag pool (1800-2000°C (15)) is the result of the high melting and boiling points of the slag components (SiO_2 , CaF_2 , Al_2O_3 , CaO and MnO etc.). They blame this excessive temperature for the high temperatures in the HAZ and were unable with standard fluxes to keep the slag pool cooler and still keep the process stable. They proposed that the slag chemistry could be altered so that the temperature of the stable process could be lowered and thus the penetration would be achieved by wetting and not by excessive heat. They used a flux with a fluoride-chloride-boride base and stabilized the process with borax which has a low boiling point (1575°C). This slag was used to ESW clad an 18-8 type stainless steel on a mild steel backing. A completely continuous bond was produced with no

penetration of the mild steel. They were also able to clad steel with brass by lowering the slag temperature even further by adding alkaline metal carbonates. They concluded that welding in this manner would decrease grain growth in the HAZ, allow higher welding rates and decrease power consumption.

Ostrovskaya (43) investigated the welding of SAE 1010 to 1045 grade steels using AN8 flux (22% SiO_2 , 20% Al_2O_3 , 21% CaF_2 , 32% MnO , 5% CaO) and varying the voltage, current (i.e. electrode feed rate) and the thickness of weld per wire to determine the causes of solidification cracking. It was found that, if the columnar grains growing into the weld centerline met nearly head on, centerline cracks would develop. Otherwise all the cracks observed were between adjoining dendrite arms. The shape factor (weld width divided by weld depth, ψ) was shown to be the critical parameter; the lower the shape factor the more likely solidification cracking will occur. It was found that increasing carbon content was more critical than any other element (e.g. S, Si, P and Mn) and that welding of SAE 1040 or above would likely result in crystallization cracks. Increasing the current (i.e. the electrode feed rate) decreases the penetration and decreases the shape factor, thus causing solidification cracking. It was also found that increasing the voltage has the opposite effect, because the penetration increases.

Poznyak (46) welded 100 mm spheroidal (magnesium treated) cast iron using plate electrodes of the same material and determined that, at a fairly high heat input ($160 \text{ kcal. cm}^{-1}$), the slow thermal cycle in the HAZ actually does not destroy the spheroidization structure as arc welding would using standard practice.

Kozulin (47) and Dubovestkif (4) have investigated the ESW process using 5 mm diameter wire instead of the normal 3 mm diameter wire in order to increase

the output of the process. They found that the welding rate could be increased but subsequent heat treatment was necessary before the HAZ impact strength could be realized, thus little if any gain was achieved.

Ivochkin (49) researched the addition of fine iron powder into the slag pool to lower the slag pool temperature, increase the electrical efficiency and to demonstrate the capability of alloying in the same manner. This method doubled the wire-only welding velocity, decreased penetration and increased the HAZ Charpy impact values. The process should work more efficiently the finer the powder as the superheating of the melted granules should not be excessive as it is for large droplets.

Makara (51) showed that the use of ANF-6 fluoride slag (60-70% CaF_2 and 30-40% Al_2O_3) permitted lower voltages and shallower slag depths due to the higher conductivity of ANF versus the common AN-8.

Ando et al (52) have undertaken an extensive program to study the major parameters in ESW that affect the resultant weld. They postulated that the convection currents in the slag are primarily caused by the electrical distribution. The electrical distribution was measured using an electrically insulated layer in the weld (i.e. a section of metal in the horizontal plane). The electrical distribution was subsequently measured and it was concluded that 21% of the total current was concentrated below the electrode tip to the slag/molten metal interface. Close examination of the measuring technique allows criticism as the insulated layers can be shown to affect greatly the thermal distribution if the insulated layers are placed on both sides of the plate. Also the current that was measured from below and for the layer was not calculated into current densities to give a true flux. This current distribution can be used to predict the convection pattern they assume and the penetration profile they observed. Other current distributions could also

produce other convection currents resulting in the same penetration profile. They found that in the standard reverse polarity (electrode positive) the electrode melted more quickly and was deeper in the slag than for straight polarity (electrode negative) for the same welding conditions. In straight polarity the current distribution was 62% to the metal below the insulated layer and the electrode more deeply immersed (Fig. 9).

Ando et al (53) in their second report investigated the voltage and current effects on penetration using direct current reverse polarity. They related the penetration to current for three voltages (Fig. 10) and two slag depths (Fig. 11). It should be noted here that Ando et al in ref. 52 and 53 used a submerged arc flux (38 SiO₂, 26 MnO, 10 CaO, 17 Al₂O₃) and not an ESW slag. In their third report (54) they studied slag composition conductivity at high temperature (Fig. 12). They found that, with a flux that has high conductivity at low temperature, the penetration was less than for a flux that has low conductivity at high temperature. This is not surprising in view of the Russian literature that has shown that penetration can be decreased using lower melting point slags (60).

Feldmann et al (55) investigated the use of manual arc welding, electron beam welding and electroslag welding in the construction of a large 316 L bubble chamber. They were able to utilize ESW only where the excessive grain growth in the HAZ did not cause a significant decrease in the impact strength or where impact strength was not important.

Lanyie and Zeke researched the effect of current, polarity and atmosphere on the weld metal during electroslag welding. As with most studies of this type, there was no actual welding, simply electroslag remelting of the welding wire into a small water cooled copper crucible. All the ingots were heat treated after the remelting and impact values found to be satisfactory. He

determined the relative impact strengths in increasing order were electrode negative, alternating current, electrode positive. The differences were attributed to electro-chemistry. He also concluded that nitrogen and argon are superior atmospheres to air, argon plus oxygen or nitrogen plus oxygen.

Shaheeb (58) has studied the influence of process parameters on the properties of ESW welds to determine if furnace normalizing could be eliminated. He also determined that alternating current and reverse polarity were much superior to straight polarity. He concluded that a heat treatment producing complete or partial transformation of the structure was necessary to achieve the desired impact strengths.

Sharapov (59) has investigated the grain growth of austenite in ESW of Cr-Mo-V steels and, by simulating the thermal cycle, has been able to show the effect of the thermal cycle. He reports the time above A_{C_3} to be critical to austenite grain growth and the initial part of the cooling cycle to be critical to the partial decomposition of austenite.

Vinokuruv (75) has predicted the transient stress and deformations around an ESW weld caused by structure changes and cooling rates.

1.5.5 The Present Research Program

The purpose of the present work is to determine the effect of certain process variables on the thermal cycle, and thus be able to minimize the inherent problems associated with ESW welding. An analytical model (63,64) will be compared with experimental data to determine if the model can be used to write welding schedules. In order to do this the process parameters will have to be varied and understood before the model can be used.

Since well defined ESW structures are to be produced, a useful side approach is to determine if chemical differences between the modes of welding lead to different inclusion compositions and thus affecting weldment Charpy values.

CHAPTER 2

MODELS AND CALCULATIONS

2.1 Introduction

Rosenthal (61,62) and Rykalin (63) developed all the basics for the development of analytical models in the field of heat flow in welding. Rosenthal first introduced the "quasi-stationary" state theory of heat flow as applied to a moving heat source in 1935 (64). Rykalin's book (63) titled "Calculation of Heat Flow in Welding" greatly expands Rosenthal's work and applies the equations to most welding applications of the late 1940s.

The study of the thermal properties of welding requires a definition of heating and cooling cycles of the metal, the heat source(s) and sink(s). The object of the welding exercise is to provide a heat source by an economic means such that the parent metal components are joined by a fused boundary. The quasi-steady state theory has been applied by Rosenthal (61) and Rykalin (63) to predict the temperature distribution around a single moving heat source in the following applications:

1. rate of fusion of the welding electrode in arc welding
2. arc welding of thin plates
3. flame cutting
4. submerged arc or manual arc welding
5. TIG and MIG welding
6. predicting the cooling rates after welding

Most recently Goldack et al (65,66) have applied the theory in Electron Beam Welding to predict the thermal distribution (65) and the microstructures (66) of EB welded eutectoid steels with good agreement.

The theory has also been applied to FSW by Pugin (16), Sharapov (17,18), and Trepov (19) with some success but not applying realistic thermal efficiencies from actual heat balances or using realistic distributions of heat sources.

2.3 An Analytical Model

2.3.1 Assumptions

Equation [2.1] is the equation developed (63,64) for the prediction of the thermal cycle for a single moving heat source. However we wish to incorporate the concepts of preheat and multiple heat sources. The equation by simple addition becomes:

$$T = T_0 + \sum_{i=1}^3 \frac{q_i}{2\pi k} e^{-\frac{v^2 t_i}{2\alpha}} K_0 \left[(v^2 t_i^2 + y^2) \sqrt{\frac{v^2}{4\alpha^2} + \frac{b}{\alpha}} \right] \quad [2.1]$$

where q_i is the power of the i th moving linear heat source and t_i incorporates the position of the i th source, T_0 is the initial preheat temperature. The use of equation [2.1] requires a knowledge of the position of the three heat sources. If we assume the literature is correct and that the highest heat evolution is between the electrode and slag/molten metal pool interface, then we can assume a configuration as shown in Fig. 13. The important decisions to be made are with regard to application of the three heat sources, their relative strengths and positions. Pugin (16) has assumed that q_1 is the at the slag surface, q_2 is intermediate between the electrode and the molten pool and q_3 is positioned at half the depth of the molten pool. Using this assumption the position of q_1 is always known, q_2 can be measured (but not predicted) and q_3 is assumed for a particular welding schedule as measured after sectioning. The relative values of heat input are assumed to be 25%/50%/25% for q_1 , q_2 and q_3 as is the efficiency η ($\eta = \sum_{i=1}^3 q_i / Q$, where Q is the total available energy) by Pugin.

The present research will try to show that the position of the heat sources can be assigned so that for a given set of welding conditions the

predicted welding thermal cycle is comparable to the actual welding thermal cycle.

2.2.2 Calculation of the Interelectrode Gap

The position of q_2 is in the center of the interelectrode gap and consequently if it could be calculated then the position of q_2 could be predicted.

Pertsovskii (67) has researched the passage of the current through the pool in ESW using a two dimensional model consisting of copper cut-outs to represent the metal components and potassium permanganate soaked paper to represent the slag. The power source was a 12V battery supply. The model did confirm the observations made when ESW is in operation:

1. the current density is highest around the electrode tip
2. more current leaves the end of the electrode than the sides, when the interelectrode gap is small

He then proposed an expression for the approximate calculation of the resistance of the slag to current flow. The expression is:

$$R = \frac{\rho}{4\pi L} \ln\left(\frac{2L}{r}\right) \quad [2.11]$$

where: R = total apparent resistance [ohms.]

ρ = specific resistance of the slag [ohm-cm]

L = depth of the immersed electrode [cm]

r = radius of the electrode [cm]

Thus if the total apparent resistance of the slag pool and the specific resistance is known, the depth of immersion of the electrode can be calculated, or if the immersion is known and the resistance drop calculated then the specific resistance can be calculated. Once the specific resistance is cal-

culated the immersion can be calculated for any total resistance (i.e. voltage and amperage reading).

2.3 Application of the Analytical Equation

2.3.1 Data Generated by the Equation

The application of the model is fairly simple and is accomplished using any digital computer. Using the computer the temperature can be calculated for a series of points in the parent metal as a function of the position of the weld itself (i.e. the bottom of the electrode) and the thermal cycle for each point calculated. This digital data can be then fed into a plotting device and a plot of the thermal cycle can be arrived at for any selected point. The data can also be contoured to give a mapping of the temperature field at any desired isothermal contour interval.

The thermal cycle plots can be used to predict microstructural changes at each point with the help of Continuous Cooling Transformation (C.C.T.) curves if an appropriate C.C.T. curve is available. The contours of isotherms allow the penetration to be read directly from the map.

2.3.2 Manipulation of the Data

Bastien et al (68) have characterised the entire mechanical properties of the HAZ of welds using three independent variables:

1. The austenitising parameter
2. The rate of cooling
3. The tempering parameter

The cooling rates can be calculated using Rykalin's (69) or Adam's (70) formulae both of which are derived from Rosenthal's equation. Adam's Equation, which is

$$V_c = 2\pi k \rho C \left(\frac{\delta}{q} \right)^2 (T - T_0)^3 \quad [2.12]$$

calculates the cooling rate from temperature T, for two dimensional heat flow and is usually applied to thin plates. However, due to the nature of ESW already described, it can be applied to the thermal cycle in ESW. This rate can also be arrived at by taking the slope at the appropriate point from the thermal cycle plotted from the analytical model generated data.

The austentising and tempering parameters allow the direct use of the temperature versus time curves and diffusion principles and are represented by a parameter P:

$$P = \frac{1}{T} - 2.3 \frac{R}{\Delta H} \log \frac{t}{t_0} \quad [2.13]$$

where: T = temperature in °K

ΔH = activation heat for the particular phenomenon

t = time

t₀ = time unit

and is expressed as an equivalent temperature for a thermal cycle for which the holding temperature equals the time unit t₀. The time, t, at holding is calculated by integrating the area under the curve above a certain temperature, T_E (850°C for austentising) and converting this to a rectangular thermal cycle of the same area and maximum temperature, T_M. Now

$$T_M - T_E = R \frac{T_M^2}{\Delta H} \quad [2.14]$$

$$\text{or } t_M = \frac{RT_M^2}{V_c \Delta H} \quad [2.15]$$

The activation enthalpy has been found (71) to be 110 kcal/mole for austenitisation and 92.5 kcal/mole for tempering over a wide range of steels. We can now calculate P in degrees Kelvin and using Figure 14 determine the average austenitic grain size.

2.4 Summary

An analytical equation has been presented which will be used to predict temperature-time cycles. The parameters that can be varied have been identified and incorporated into the equation. The formulae for the calculation of the interelectrode gap and austenite grain size have been presented. However, other than for the analytical model there is no published data relating these theories to actual field or experimental results. This has been undertaken in this experimental program. The procedures used are developed in Chapter 3, the results obtained in Chapter 4 and the comparisons with the equation and calculations in Chapter 6.

CHAPTER 3

EXPERIMENTAL PROGRAM

3.1 ESW Devices at U.B.C.

3.1.1 Wire or Consumable Guide Welders

When welding in the D.C. mode, power was supplied by a Hobart RC 750 welder with 750 amperes and operating voltage of 10-50 volts. The welder was partially controlled by a rheostat which varies the degree of saturation of its reactor. The rectification was not perfect and resulted in approximately 10% RMS of the total D.C. current. When this power supply was used for wire or consumable guide electrodes, it was used in conjunction with an Arcos Vertomatic GSp wire feeder and welding controller. This controller was a prototype and, as such, was never marketed in the form employed at U.B.C. The controller was wired into the Hobart RC 750 in such a way that the saturation of the reactor was varied at the controller. The only controls used in the experiments conducted at U.B.C. were the voltage and wire feeding controls. The voltage control essentially replaced the Hobart rheostat and the wire feeding control adjusted the amperage. The voltage and amperage can be read directly at the control panel.

A Hobart Model T-500 AC power supply was used in conjunction with the Arcos vertomatic wire feeder when welding in the AC mode. In this case both the voltage and current were measured externally, not at the controller. The voltage was adjusted using various tap connections with a fine control

varying the primary voltage to the step down transformers (tap changes can be made on-load).

3.1.2 Bar or Plate Electrodes

The U.B.C. electroslag remelting furnace was used for large cross-section electrodes. It is designed to undertake a range of research projects and has been described in detail by Etienne (72). It was used in the preliminary and final stages of the present research.

3.2 Initial Experimental Procedures

3.2.1 Stage One

To determine if there were significant differences in the three available modes of operating, and to see at the outset if ESW welds could be made using the U.B.C. remelting furnace, three welds were made, each using a different mode (D.C.R.P., D.C.S.P. and AC). These welds were made utilizing a colorlith plate (3/4" thick) between the base plate and a steel plate. The material to be welded was 5 1/4" x 5 1/4" x 12" in height (from Western Canada Steel continuous cast strand) AISI 1020 steel. The electrode was a 1 3/8" diameter AISI 1018 rod. Thus, for remelting, the water cooled copper mould was replaced with a solid billet of square cross section. The slag was 75 weight percent calcium fluoride (courtesy of Eldorado Nuclear Co.) and 25 weight percent alumina (Norton Abrasive Ltd.). Twenty four chromel/alumel thermocouples were placed in a grid. This grid consisted of four different distances from the vertical axis at six different heights. The thermocouple wires were sheathed in 1/8", double bore, alumina tubing and the end beaded by welding. Holes 3/16" in diameter were drilled into the blocks to four depths and the thermocouples inserted with pressure. The end of the holes were 1/4", 1/2",

3/4" and 1" from the surface of the axial hole in the horizontal plane (Fig. 15). It required a positive force to insert the sheathed thermocouples due to the non-round sheathing and, once the thermocouple was in contact with the base metal, it did not move. A multimeter, placed on resistance, was used to ensure the thermocouple bead made contact with the base metal.

This unconventional configuration was chosen for the following reasons:

1. There was very little preparation required to determine if the equipment set up was applicable to welding as well as remelting.
2. The blocks completely removed the problems associated with water cooled copper shoes or moulds.
3. There was no slag loss, because there were no shoes, and consequently no slag had to be added during the operation.
4. The slag had been used successfully by others to remelt steels with relative ease (72,73).
5. It should show the main differences between the temperature time distributions for the three modes of welding.
6. The set-up would allow testing of the thermocouple placement technique.

The weld was started cold using a compact consisting of metal turnings of AISI 1018 and calcium fluoride. The compacts were approximately 40 mm in height and contained 100 gms of calcium fluoride. The electrode is forced down onto the compact and the granulated, pre-fluxed slag is poured around the electrode and compact. The compact melts, due to its resistance, when the power is turned on and the process commences with a molten slag.

The voltage and amperage were measured and recorded using Sargent Model SR 10 Millivolt recorders (voltage required a 100:1 divider and amperage a calibrated shunt) when the operating mode was direct current. In order to

operate in the A.C. mode, it was necessary to start using D.C. and then change power supplies once the process was stabilized. The voltage was measured using an RMS AC Voltmeter (model Eico 250) and recorded manually. The amperage was measured using an AC to DC convertor and recorded using a Sargent Model SR Millivolt recorder. The thermocouple output emf. was recorded using a Texas Instrument Multi-point Recorder set on its fastest speed (one reading per sec.). The other process parameters recorded were:

1. The total electrode travel from start
2. The time from a fixed point
3. The electrode drive motor speed setting

3.2.2 Stage Two, Consumable Guide ESW

Stage two of the experimental setup was designed to research the ESW parameters for the Consumable Guide process. The single wire non-consumable guide technique was not studied because of the complexity of travelling cooling shoes on the relatively short welds produced in our laboratory. Instead it was decided to study the process without the problems associated with the complicated heat sink created by a slag skin and water cooling.

The welds were produced in 5½" diameter, 24" long AISI 1020 and 4340 steel cylinders with a 1¼" diameter axially bored hole. The electrode wire was AISI 1010 and 1040 (2.4 mm and 2.5 mm diameter respectively). The slags were Arcos BV8 (an electros slag flux: 42 CaF₂, 26 Al₂O₃, 24 CaO, 8 SiO₂) and Hobart PF 201 (an electros slag flux: 10 Al₂O₃, 5 MgO, 35 CaO + CaF₂, 15 MnO, 30 SiO₂). The wire was fed through a nominal 1/8" mild steel pipe which was used as the consumable electrode. Two methods were used to insulate this consumable guide from the sides of the hole and to keep the electrode central in the hole:

1. Silica tubes approximately 3/4" long were flared to give approximately 180° included angle. A wire was wrapped around the pipe and fixed by 3 very small tack welds. The silica tube was then slipped over the pipe and the flared flange lay on the wire. A 1/16" thick flat, six-pointed mild steel disk was then placed on top of the flare. The silica acted as an insulator and the disk as a positioner (Fig. 16).
2. The silica insulators were replaced by an insulated guide for the top 8" of the pipe (Fig. 17). This was found to be superior to the silica guides which tended to break. This guide also allowed the use of the vertical travel of the wire feeder itself. Thus, in the event of the wire fusing with the pipe, the consumable guide was lowered and became the active electrode until the wire once again started feeding.

The thermal cycles were monitored using 14 internal thermocouples at seven different depths at 1/4" intervals starting 1/8" from the hole surface. Six thermocouples were placed on the surface of the cylinders by spot welding at positions between the internal thermocouples. This thermocouple set-up is shown in Figure 18, and was used for the first 10 experiments. The remainder of the runs were monitored using 24 internal thermocouples as shown in Figure 19.

The weld was started by adjusting the power rheostat at the highest possible reading to provide the highest voltage. The wire advance rate was kept very low and as soon as the wire started to arc some slag was added to extinguish the arc. This procedure was continued until the wire advanced without arcing any further, at this point the power was reduced until the required voltage was just exceeded. The wire rate was then increased until

the desired current was attained. During this period the desired amount of slag was added. The entire start-up procedure was completed before the molten metal was above the top of the run-in sump. During the remainder of the weld, the voltage and amperage were kept as close as possible to the desired values. The weld was stopped once the molten slag surface was even with the top of the cylinder.

3.2.3 Slag Temperature Measurements

The slag temperatures were measured during the run using a W3Re/W25Re thermocouple with a boron nitride sheathing (Fig. 20). The thermocouple was held in two eye-loops and, to prevent thermal shock, the molten slag was allowed to approach the sheathed end at the welding velocity. Once the slag was touched the thermocouple was lowered at 10 mm intervals until the sheathing was destroyed and the thermocouple ceased working. The thermocouple emf. was recorded on a Sargent Model SR4 Millivolt recorder.

3.2.4 Electrode Immersion

The immersion of the electrode was measured using a rather simple mechanical means and was only possible when the fixed head (with insulated holes) was in use. Two straight tungsten wires, each with a circular loop at right angles (Fig. 21) were placed over the nozzle and moved to the top of the cylinder and held by the top fixing head. When the slag surface approached the level of the lowest thermocouple position, the lower loop was lowered down the nozzle and over the extending wire with a small lateral force. As soon as the loop moved sideways, it was immediately withdrawn and held at the fixed head by bending it over.

The second loop was lowered after the uppermost thermocouple position had been passed by the slag metal pool interface. The same procedure was

used for the second loop as for the first. The electrode immersion was assumed to be the same as the length of wetted (slag coated) tungsten wire.

3.2.5 Other Experimental Procedures

The welding velocity was calculated by recording the time for the entire length of the final weld. However, because the exact point of the welding start was never actually known, it was decided to add tungsten powder before the slag/air interface reached the bottom thermocouples and after the molten metal/metal interface passed the last thermocouple. The times of addition were recorded and the position determined after sectioning of the deposited metal.

In some instances 304 S.S. 1/8" pipe consumable nozzles were used instead of the mild steel pipe commonly used. These experiments were sectioned and 4% nital etchs were used to determine if the stainless components were evenly distributed during the welding process.

3.3 Butt Welds using Consumable Guide ESW

Once the parameters and procedures involving the cylinders were fairly well understood, it was decided to produce full scale production type welds using the Arcos Vertomatic GSP wire feeder, Hobart A.C. and D.C. welders and water cooled copper shoes. This decision led to many changes in the equipment and procedures. It necessitated the design of a welding jig, water cooled copper shoes, a fixed head for the consumable guide, run-in and run-out sumps and some method for adding slag. The essential differences between the cylinders and 1½" plates are:

1. There is heat lost to the moulding shoes and this must be measured and accounted for in the power input.
2. There is a continual loss of slag to the faces of the cooling shoes and this slag must be replenished at frequent equal intervals or at a constant rate.

3.3.1 The Welding Jig

The welding jig was designed to perform the following functions:

1. The jig would hold the plates vertical so that there was no play or movement perpendicular to the plates and at the same time allow a slight movement parallel to the plates.
2. The jig must have the fixed head attached to it so that, by aligning the head and jig once, the consumable guide would remain in the center of the gap.
3. The jig would hold the water cooled copper moulding shoes as tightly against the plates as feasible without distorting the shoes.

The jig was designed and constructed out of mild steel as shown in Figure 22. The twelve screws in the vertical members were rounded on the contact ends to provide movement of the plates in the plane of the plates. The bottom of each plate was shimmed to provide a vertical gap. The top of the vertical members were drilled and threaded to hold the fixed head. The jig was elevated with two I-beams to accommodate the run-in sump. Two sets of horizontal clamps were used to hold the copper shoes in alignment throughout the weld. Steel bars were sometimes used to back up the copper shoes when the plates were not flat; this allowed the clamping screws to be torqued very high and forced the shoes to conform to any bend in the plates. This jig, with no changes, was used for the remainder of the experiments.

3.3.2 The Water Cooled Copper Shoes

There are three types of water cooled copper shoes commercially used:

1. The moving shoe which is approximately 8-12" long and 3" wide with water channels through a solid block. These shoes move up both sides of the plate at the welding velocity and retain the molten metal and slag.
2. The walking shoe is any length from 8" to 36". The walking shoe can be designed in a number of ways to accommodate the water flow but is usually formed from a solid block of copper with milled out water channels and a facing plate. The water enters the bottom and exits from the top of the shoe. The walking shoe method requires four shoes, two for each side. The procedure involves placing two shoes at the start of the weld and welding until the slag/air face is a few minutes from the top of the shoe. The second set of shoes is then attached above the first set and, when the weld is in the second set, the first set is removed and placed above the second set, thus the so-called walking shoe method.
3. Full length shoes are also used in circumstances which warrant a large capital investment. They are usually used when the weld is not vertical, not straight or has section changes throughout its length. It can also be used when many welds of exactly the same configuration are being made.

The full length shoe (24") was used for the following reasons:

1. The problems associated with the moving shoe and wire feeder were immediately eliminated.
2. The procedure of walking shoes is time consuming, requires more materials and cooling connections than the single shoe.

3. The length of the welds in the present program was constant (22 in.) and short enough to use one set of shoes. (The set of shoes could be considered the first set of shoes in the walking shoe method).

The shoes were designed as shown in Figure 23. A solid $\frac{1}{2}$ " thick, $1\frac{3}{4}$ " wide and 22" long was milled $\frac{3}{8}$ " deep making a channel $1\frac{1}{4}$ " wide, $21\frac{1}{2}$ " long. A water inlet hole was drilled at the bottom and an outlet hole at the top and $\frac{1}{4}$ " nipples welded onto the back of the shoe. The channel was then closed by heliarc welding a $\frac{1}{8}$ " thick plate to the channel and the shoe pressure tested. The $\frac{1}{8}$ " thick plate is the cooling surface and had to be milled to contain the frozen slag. Therefore the milled channel was $\frac{1}{16}$ " (1.6 mm) deep, $1\frac{3}{8}$ " wide and $21\frac{3}{4}$ " long. This allowed for a slag skin $\frac{1}{16}$ " thick and $\frac{1}{16}$ " wider than the $1\frac{1}{4}$ " wide root gap and ensured the weld deposit would be at least as thick and wide as the parent metal. It also allowed for $\frac{3}{16}$ " contact width with the plates on each side of the weld. It would have been preferable to have the $\frac{1}{2}$ "- $\frac{5}{8}$ " contact width that is used commercially but this would have interfered with the placement of the thermocouples. It should be noted that the shoes did wear out and had to be replaced with a second set. This set was made using $1\frac{3}{4}$ " x $\frac{1}{2}$ " structural grade channel instead of a copper channel. The facing plate was the same as before because the thermal conductivity of copper is essential for the required heat transfer. The new set was used for the remainder of the experiments and performed as well as the entirely copper shoes.

The shoes were cooled using a mixture of hot and cold water to provide 25°C water, which would not condense water vapour from the air. The flow of this water was controlled using a rotameter and the temperature measured using thermistors on the inlet and outlet water flows.

3.3.3 The Consumable Guide Fixed Head

The fixed head and jig were really one solid component, once the head was attached to the jig. It performed the following functions:

1. It held the guide so that there was virtually no movement of the guide, and electrically insulated the guide from the parent metal as shown in Fig. 24.
2. It contained other guides for slag temperature measurement and electrode immersion measurements.
3. It held the tube for the addition of tungsten powder and make-up slag.
4. It also allowed for the vertical movement of the consumable guide if the welding wire became fused to the guide.

The head was electrically insulated from the jig and parent metal by a 1/2" plate of colorlith, colorlith sleeves for the bolt holes, and rubber washers under the steel washers. The four vertical posts were machined with two steps to hold the horizontal guide plates. The bottom guide plate had four holes with exactly the same diameter of the middle section of the vertical posts. This provided the pivot point for the aligning of the consumable guide with the rectangular section to be welded. The top guide plate had four holes 1/16" larger in diameter than the diameter of the top section of the vertical posts. This play allowed movement of the top guide plate parallel and perpendicular to the plates and thus the ability to center the electrode and guide with respect to the bottom of the plates. This, in conjunction with the jig screws, provided for alignment of the guide along the centerline of the entire gap between the shoes and plates.

3.3.4 Run-in Sump and Run-out Blocks

The run-in sump was constructed out of 1 1/4" square bars providing a sump 2" deep. The sump was constructed this way to ensure the penetration of the parent metal before the slag metal interface reached the actual blocks. The 1 1/4" thickness was used because it had adequate strength to hold the plates and yet was thin enough to provide a poor heat sink and allow overheating. The overheating ensured penetration of the base metal in the sump and at the start of the weld. The sump was fabricated by partial penetration, manual arc welding; it was ground off so the shoe faces would fit the sump faces and prevent slag run-outs.

The run-out blocks were 1 1/4" square and simply tack welded to the top of the plates to provide a sump to contain the slag after welding was complete. They were only 2" high to ensure the weld ended in the plate and to permit observation of the metal/slag interface after welding. In actual practice they are 3-4" high to ensure the weld is complete above the plates.

3.3.5 Thermocouple Positions

Chromel/alumel thermocouples were inserted into the plates as shown in Figure 25. There were two groups of thermocouples used, with 20 thermocouples in each group (sometimes only one block). Each group consisted of five rows of thermocouples at four depths. The four depths were 1/4", 1/2", 3/4" and 1" from the original surface of the plate and 5/8" deep into the plate. Five thermocouples at each depth were used to establish if the welding was in steady state (i.e. if all five reached the same millivolt readings, then steady state was achieved). The millivolt output was recorded on a printing HP Model 2070 A Datalogger with a visual digital display. This device allowed quick, accurate collection of data. The

lowest, closest thermocouple in the group was recorded continuously (using a Sargent Model SR 4) as a reference for all the other thermocouples. The second block of thermocouples was used for two applications during the test-work. Firstly, if the first set of thermocouples was found to be in steady state throughout the range, the second group could be used to see how "steady" the process really was over a long period of time. Secondly, the second set could be used for a second experiment if the first group was in steady state. Therefore, the welding parameters could be changed between thermocouple groups and a second weld achieved from the same set-up. This second method was used as often as possible to provide the most data possible from one experiment. It should be noted that the change in the groups meant that the cooling cycle was not completely recorded for many of the uppermost thermocouples, and this necessitated using the cooling cycle for the first one, two or three thermocouples at each depth to obtain the entire thermal cycle. Also, the first thermocouple was sometimes found to be not in the steady state condition when the other four were (the first always read low if this happened) and then the readings from this first thermocouple were disregarded.

3.3.6 Slag Additions and Other Procedures

Appropriate slag additions were made in 5 gm amounts at intervals depending upon the welding rate. Tungsten powder additions were made at the start and finish of the thermocouple readings for each block. Both additions were made using the slag addition tube on the fixed head.

3.3.7 Electrical Current Distribution Measurements

Electrical current measurements were made by placing plates in the parent metal and electrically insulating these plates from each other and the shoes by the use of asbestos sheets. These plates were 1/4" thick,

1 1/8" wide and 2 inches longer than the parent metal plates (see Figure 26). A shunt was bolted to the end of each plate and the other end of the shunt to the same side of the welder as the parent metal. The precise location of each shunt was recorded with respect to a thermocouple in the block opposite the shunt. The millivolt drop across each shunt was continuously monitored using Sargent Model SR 4 and 10 recorders as the weld passed the shunt. Thus the current distribution was recorded as the weld passed the shunt. This procedure was only possible while welding in the D.C. mode. When welding in the A.C. mode, only one plate was used with one shunt and the A.C. millivolt drop was converted to D.C. using a HP Model 8807 A A.C. to D.C. converter-amplifier. Only one plate was used because only one converter was available. However, the moving current distribution was measured and the relative position of the shunt and interfaces calculated.

3.4 Butt Welds Using Bar Electrodes

Once consumable guide electrode welding was completed, it was decided to study the large or plate electrode method of ESW. This necessitated few changes from the consumable guide process and, with the exception of the electrode feed mechanism, fixed electrode guide and slag addition method, no changes were made. The electrodes for the majority of the welds were 3/4" square leaving a gap of 1/4" on all four sides of the electrode for misalignment or deviation during electrode travel. The electrodes were fabricated by cutting 3/4" slabs off the parent metal sections and cutting the slabs to 3/4" x 3/4" x 18". The ends of these bars were bored and tapped to receive a 1/2" N.C. bolt and joined together. Three and one-half 18" electrodes were joined using 1/2" bolts to provide the electrode for one weld. The welds were started using calcium fluoride Armco iron compacts that had been

shaped to fit the 1 1/4" square gap. The electrode feed mechanism was the mechanism of the electroslag refining unit described by Etienne (72). The slag was continuously added using the electroslag refining slag feeder described by Joshi (74) and recalibrated for the appropriate electroslag slag.

3.4.1 The Fixed Head

The most extensive change required to weld using large electrodes was the welding head. Both horizontal plates had to be modified to accommodate the larger electrode. The head was rebuilt so that the upper plate became the pivot point and the electrode drive the guide point. Alignment was most important during large electrode welding because the gap was very narrow between the electrode and parent metal. The actual guides were made out of colorlith to allow for the electrodes not being perfectly square and not the same size for each section of the electrode. Essentially the fixed guide serves the same purpose as in consumable guide ESW.

3.5 Evaluation of Weld Properties

3.5.1 Hardness Values

Hardness traverses were performed using a Vickers Pyramid Hardness Testing Machine. Transverse sections were cut and surface ground so that the transverse sides were parallel. One side was polished to a 1 μ finish and lightly etched using 2% nital to distinguish the fusion boundary and HAZ. The hardness readings were taken at 1/8" intervals from the centerline of the weld into the parent metal. The majority of the traverses were performed using a 10 kilogram load and a 2/3 objective lens.

3.5.2 Toughness Values

A limited series of Charpy Impact tests were performed on plate welded cast T-1 equivalent steel, (ASTM 487 (Q7)) provided by Esco Ltd. These tests were made using Warnock Hersey Internationals Charpy testing machine and in accordance with ASTM-370 at 40°F. The specimens were taken so that the 2 mm V-notch was located at 1/4" intervals from the weld centerline into the parent metal. Only AC and DCRP were toughness tested.

3.5.3 Inclusion Distributions

Transverse samples were taken across the weld in 1/4" cubes for oxygen analysis using a digital readout Leco oxygen analyser. Polished sections were taken adjacent to the samples for oxygen analysis and the inclusion distribution determined using the Quantimet with the microscope attachment. This procedure was used on two welds for each mode of welding.

3.6 Experimental Records

The following parameters were recorded for each run when applicable:

1. Welding mode; AC, DCRP, DCSP
2. Weld type; block, cylinder, plate
3. Electrode type; consumable guide, plate
4. Materials; slag, electrode, parent metal
5. Voltage, recorder
6. Amperage, recorder
7. Power setting
8. Slag addition rates
9. Temperatures, slag and parent metal

10. Time, recorder
11. Tungsten addition times
12. Immersion times and depths
13. Time slag temperatures taken
14. Cooling water flow rate and temperature change
15. Slag skin thickness
16. Final Slag depth
17. Length of weld
18. Operational problems

CHAPTER 4

RESULTS

4.1 Power Characteristics

4.1.1 Published Power Characteristics

Figures 27 and 28 respectively show the published voltage amperage characteristics for D.C. and A.C. welders used in this research. Figure 29 shows the variable resistance device constructed to measure the voltage amperage characteristics of the welders; these appear as the lines through the dots on Figure 27 and the lower voltage curves on Figure 28.

4.1.2 Measured Power Characteristics

The voltage amperage characteristics indicate the working range within which the welders would have to be operated to attain the required input energy essential for a sound weld. In both cases, A.C. and D.C., the welders required much higher settings than the published data by the manufacturer indicated.

4.2 Industrial Experiments

4.2.1 Experimental Conditions

A series of welds were made at Cannon Limited using the voltage amperage settings shown in Table 4. The other following conditions used were:

- i) D.C.R.P.
- ii) 3.18 cm root gap
- iii) A 441 Grade C hot rolled plate (see Table 5)
- iv) Hobart PF 201 flux (3.81 cm operating depth)
- v) HB 25P wire (see Table 5)
- vi) 1.27 cm diameter consumable guide

4.2.2 Experimental Results

The weld regions were examined for the inclusion distribution (Fig. 30), oxygen distribution and penetration (Figs. 31 and 32), and HAZ (Figure 33). The results were used to predict the actual weld velocity required to produce an acceptable weld in the laboratory, using different weld crosssectional areas (Figure 34). These data were used in later wire welding techniques but were also used to determine the melt rate-energy requirements for the large electrode experiments.

4.3 Initial Large Electrode Experiments

4.3.1 Heat Balance and Thermal Profiles

The thermal profile (verus position) for the three modes of operation are shown in Figures 35-37.

TABLE 4

Canron Limited Welding Conditions

Thickness of Plate in.	Root Opening (in.)	Electrode		Arc Voltage	Oscillation Distance in/min		Wire Feed Speed Inch per min	Approx. Amperage
		Type	Dia (in.)					
3/4	1 1/4	E70S3	3/32	38-39	-	-	100	400
1	1 1/4	E70S3	3/32	38-39	-	-	110	450
1 1/4	1 1/4	E70S3	3/32	38-39	-	-	120	500
1 1/2	1 1/4	E70S3	3/32	39-41	-	-	130	500
1 3/4	1 1/4	E70S3	3/32	39-41	1 1/2	35	140	525
2	1 1/4	E70S3	3/32	39-41	1 1/2	35	150	550
2 1/4	1 1/4	E70S3	3/32	41-44	1 1/2	35	160	600
2 3/8	1 1/4	E70S3	3/32	41-44	1 1/2	35	165	650
2 1/2	1 1/4	E70S3	3/32	41-44	1 1/2	35	170	700
2 3/4	1 1/4	E70S3	3/32	41-44	1 1/2	35	180	700
3	1 1/4	E70S3	3/32	41-44	1 1/2	35	190	750

TABLE 5

Canron Limited Welding Analysis

BASE METAL SPECIFICATION AND COMPOSITION A441 to A441							
Base Metal	Carbon	Manganese	Silicon	Cu	V	P.	S.
A441	0.20	1.10	0.023	0.26	0.06	0.011	0.019

FILLER METAL COMPOSITION E70S-3 (Hobart HB-25P) Typical					
Type	Carbon	Manganese	Silicon	P.Max.	S.Max.
HB-25P	0.11	1.20	.50	0.020	0.019

DEPOSITED METAL ANALYSIS Hobart PF201 Flux							
Type	Carbon	Manganese	Silicon	Cu	V	P.	S.
HB-25P	0.14	1.11	0.45	0.20	0.03	.008	.019

Figure 38 compares the thermal profiles for DCRP, DCSP and AC for a thermocouple positioned 1/4 inch from the original surface of the weld.

4.3.2 Power Characteristics and Apparent Resistance of the Slag

The apparent resistance of the slag was found to be:

Mode	Volts	Amps	R(Ω)
DCRP	23 \pm .4	1135 \pm 152	.0229
DCSP	23 \pm .9	1107 \pm 100	.0169
AC	26.5 \pm .1	1387 \pm 45	.0285

It should be noted that the A.C. experiments using the U.B.C. Electroslag Remelting furnace must be started using D.C.S.P. until the slag is entirely molten and thus the apparent resistance for the A.C. experiment could be affected by the electrolytic reactions during the D.C. portion of the experiment. The specific slag resistance can not be calculated because of the relatively large electrode diameter, low current density and a conical shaped melting electrode.

4.3.3 Deposition Rate or Welding Velocity

The deposition rates and welding velocities were:

	melt rate (g.s. ⁻¹)	welding velocity (cm.sec ⁻¹)
DCRP	4.28	.018
DCSP	4.51	.019
AC	7.13	.030

with corresponding power inputs in terms of Kcal.gm⁻¹ of:

DCRP	1.49 Kcal gm ⁻¹
DCSP	1.24 Kcal gm ⁻¹
AC	0.81 Kcal gm ⁻¹

and Kcal.cm⁻¹ of weld: 353 Kcal cm⁻¹ respectively
 293 Kcal cm⁻¹
 193 Kcal cm⁻¹

4.3.4 Penetration and Inclusion Distribution

The penetrations, measured as the maximum plus the minimum divided by two, minus the original hole diameter were found to be:

mode	penetration (cm)
DCRP	4.53 cm
DCSP	1.06 cm
AC	0.91 cm

Figures 39-41 show the inclusion distribution for crosssections of the above three welds.

4.3.5 Hardness Traverses

Figure 42 presents the hardness traverses through the same sections from which the oxygen and inclusion analyses were obtained. The measured penetration is also shown. (R.G. is the original root gap.)

4.3.6 Oxygen Analyses

Figure 43 represents the oxygen gradient along the same traverses used for the hardness surveys.

4.4 Consumable Guide ESW in Cylinders

4.4.1 Introduction

A total of thirteen successful experiments were performed using the consumable guide method described in Chapter 3. Table 6 presents the data obtained or calculated for the experimental conditions.

4.4.2 Slag Temperature Measurements

The slag temperature was measured twice for each D.C. mode and once for the A.C. mode. The temperatures are plotted with the corresponding weld profile, electrode immersion and interelectrode gap in Figures 44-49.

TABLE 6

Experimental Conditions for Consumable Guide Electroslag
Welding (CGESW) in Cylinders

Experiment Number	Operating Mode	Volts	Amps	Penetration cm	Weld Velocity cm sec ⁻¹	Slag Depth cm	Immersion cm	Apparent Resistance ohms	Specific Power kcal/cm
1	DCRP	40	370	.159	.0351	3.18	1.74	.108	100
2	DCRP	41	510	.079	.0361	8.26	2.63	.080	140
5	DCRP	40	460	.318	.0303	5.84	2.35	.087	147
10	DCRP	52	435	.079	.0330	6.60	1.49	.120	165
11	DCRP	40	460	.300	.0301	3.81	2.35	.087	150
12	DCRP	38	400	.406	.0357	4.45	2.08	.095	115
3	DCSP	41	460	.318	.0328	5.08	2.01	.089	140
4	DCSP	40	390	.000	.0305	5.08	1.64	.103	125
6	DCSP	41	440	.238	.0252	6.35	1.89	.093	170
7	DCSP	40	540	.040	.0254	6.10	2.59	.074	205
8	DCSP	38	600	.000	.0339	6.60	3.20	.063	160
9	DCSP	40	500	.000	.0328	7.10	2.33	.080	145
14	AC	36	843	.238	.0357	7.00	4.89	.043	205

4.4.3 Slag Depth, Immersion and Interelectrode Gap Measurements

Table 7 shows the slag depth and immersion as measured physically during and after the experiment (above and below the thermocouple region) using the tungsten wire method. The same table gives the measured electrode immersion and calculated interelectrode gap distance.

4.4.4 Velocity Measurements

The welding velocity was measured using three different methods:

- i) the total length of the weld in cm divided by the total time of welding in sec.
- ii) the tungsten marker bed above and below the thermocouple region
- iii) the time between temperature maxima on thermocouples as recorded by the Hewlett Packard DVM output.

These results are presented in Table 8.

4.4.5 Temperature Time Cycles

The thermal profiles for each mode of operation are presented in Figures 50-52. The thermocouple arrangement allowed for averaging the profiles because four thermocouples were available for each position only in the later experiments. A new thermocouple set-up described in Chapter 3 measured four levels at six depths. Only the average thermal profile is plotted in Figures 50-52. There is no comparison of the actual profiles with any theoretical model because this experimentation was designed to determine the differences between the modes for actual welding during the later stages of the research program.

TABLE 7

Slag Depth, Immersion and Interelectrode Gap Measurements

Experiment Number	After Run	Slag Depth (cm)		Ave	Immersion (cm) Measured	Interelectrode (cm) Gap Calc.
		Below Thermocouple	Above			
1	3.00	3.30	3.05	3.18	1.80	1.77
2	8.10	8.40	8.15	8.28	2.80	5.42
5	5.70	5.90	5.75	5.84	2.50	3.34
10	-	6.65	6.55	6.60	1.65	4.95
11	3.40	3.80	3.82	3.81	2.55	1.26
12	4.20	4.60	4.30	4.45	2.20	2.25
3	4.80	5.15	5.00	5.08	2.50	2.58
4	4.85	5.15	5.00	5.08	1.85	3.23
6	6.15	6.45	6.25	6.35	2.05	4.30
7	5.95	6.30	5.90	6.10	2.65	3.45
8	6.20	6.70	6.50	6.60	3.35	3.25
9	6.90	7.20	7.00	7.10	2.50	4.60
14	6.65	7.20	6.80	7.00	5.00	2.00

TABLE 8
Welding Velocity Measurements

Experiment Number	Total Weld Length cm.sec ⁻¹	Tungsten Marker Bed cm.sec ⁻¹	Time Between Temp. Maxima cm.sec ⁻¹
1	.0351	-	-
2	.0361	-	-
5	.0303	-	.0295
10	.0330	.0330	.0330
11	.0301	-	.0288
12	.0357	.0355	.0308
3	.0328	-	-
4	.0305	-	.0300
6	.0303	-	.0298
7	.0254	-	.0256
8	.0339	.0340	.0335
9	.0328	-	.0314
14	.0357	.0355	.0355

4.4.6 Penetration

The penetration depth, or fusion boundary position, was determined optically by direct measurement after macroetching. The penetration was also determined using changes in VPN and microstructure. Figure 53 presents typical VPN traverses for each mode and difference between 4340 and mild steel. Figure 53 also presents the fusion boundary and HAZ positions.

4.4.7 Oxygen Analyses

Figure 54 presents the oxygen traverses from the weld centerline through the fusion boundary for the three modes of welding.

4.4.8 Use of a 304 S.S. Consumable Guide

Figure 55 shows the nital etched surface of an experiment where the consumable guide was a 304 S.S. 1/8" pipe instead of the standard mild steel 1/8" pipe.

4.5 Consumable Guide ESW with A 36 Plates

4.5.1 Introduction

A rotameter flowmeter was calibrated to give a consistent 15 liters of water per minute to each cooling shoe in order to produce a uniform slag thickness of approximately 1.0 mm. This was achieved in a preliminary set of experiments designed to confirm the general value of the welding set-up. Table 9 presents the actual and calculated experimental conditions for seventeen experiments. The slag feeder was also calibrated to deliver the necessary material to replace that lost to the slag skin, and thus maintain a constant slag depth throughout the experiment (see Figure 56).

TABLE 9

Experimental Conditions for Consumable Guide Electroslag
Welding (CGESW) with A 36 Plates

Experiment Number	Operating Mode	Volts	Amps	Penetration cm	Weld Velocity cm sec ⁻¹	Slag Depth cm	Immersion cm	Apparent Resistance ohms	Specific Power kcal.cm ⁻¹
P13	DCRP	32	685	.381	.0159	1.59	1.42	.047	340
P14	DCRP	36	760	.669	.0232	1.91	1.11	.047	215
P15	DCRP	35	690	.191	.0205	2.06	1.59	.051	280
P18	DCRP	38	750	.254	.0191	1.50	1.27	.051	360
P20	DCRP	39	570	.320	.0174	3.65	6.79	.068	310
P21	DCRP	39	565	.318	.0189	3.96	0.79	.069	280
P16	DCSP	36	735	.064	.0223	3.18	1.62	.049	270
P22	DCSP	40	590	.254	.0200	3.18	0.95	.068	285
P04	AC	35	450	.325	.0166	2.86	1.10	.078	230
P05	AC	42	490	.445	.0140	3.18	1.03	.086	350
P06	AC	40	520	.191	.0147	2.86	2.06	.077	340
P08	AC	35	500	1.207	.0131	3.49	0.95	.070	320
P09	AC	40	530	.254	.0217	1.91	1.11	.075	230
P10	AC	35	450	.699	.0228	1.91	0.95	.078	170
P11	AC	40	560	.445	.0194	1.27	0.64	.071	275
P12	AC	44	510	.445	.0202	3.49	0.95	.086	265
P23	AC	45	510	.508	.0227	4.13	0.79	.088	245

4.5.2 Temperature Time Cycles

Figures 57-60 present the raw data from one experiment showing the five thermal profiles for each of the four thermocouple positions. Figure 61 presents the same profiles when shifted by the welding velocity divided by the distance between the thermocouples and then averaged. All four thermocouple positions were then plotted on a single graph. The thermal profiles for the other experiments were plotted in the same manner and are presented in Figures 62-73.

4.5.3 Penetration and HAZ Values

The penetration was measured using a scale and correcting for any closure of the gap between the parent plates after welding. The HAZ was determined by microstructural and VPN analysis. The results are presented in Table 10.

4.5.4 Hardness Traverses

In Figure 74 three typical hardness traverses are shown for the widest range of penetrations in order to indicate the effect of grain size on VPN values.

4.5.5 Inclusions

i) Table 12 presents the cumulative percentage size distribution for six typical welds as determined using the Quantimet.

ii) Figure 75 presents the oxygen content traverse along the same section as the above inclusion counting was taken.

iii) Figures 76-77 are scanning electron micrographs of inclusions from the same specimens used for the sizing survey.

TABLE 10
Penetration and Heat Affected Zone (HAZ)
Values for the Experiments in Table 9

Experiment Number	Penetration cm.	Heat Affected zone cm.
P13	.381	1.32
P14	.699	2.05
P15	.191	1.46
P18	.254	1.555
P20	.320	0.92
P21S	.318	1.65
P16	.064	0.54
P22S	.254	1.40
P04	.325	2.23
P05	.445	2.02
P06	.191	1.86
P08	1.207	2.68
P09	.254	1.49
P10	.699	1.65
P11	.445	1.08
P12	.445	0.91
P23S	.508	-

P13 to P21S above are DCRP mode
P16 to P22S above are DCSP mode
P04 to P23S above are AC mode

TABLE 11

Grain Size in the Heat Affected Zone
of CGESW of A36 Plates

Experiment Number	Thermocouple Position*	ASTM Grain Size Number Measured	ASTM Grain Size Number Determined	Diameter of Average Grain** mm.
P13	1	1-2	1.0	.254
	2	6-7	7.0	.032
P14	1	7	7.75	.025
	2	10	10.75	.0094
P15	1	7	8.0	.0224
	2	11	12.0	.00561
P18	1	6.5	6.5	.038
P21S	1	6.0	6.5	.038
	2	11	11.25	.0070
P16	1	7	7.75	.025
P22S	1	9	10.00	.0112
P04	1	5	5.5	.0534
	2	9.5	10.75	.008
P05	1	6	6.5	.038
P08	2	8.5	9.0	.0159
P10	1	4	4.0	.0898
	2	7.5	8.0	.0224
P11	1	6	6.5	.038
P08	2	8.5	9.0	.0159
P10	1	4	4.0	.0898
	2	7.5	8.0	.0224
P11	1	6.5	6.75	.0350
	2	10	10.50	.0094
P23S	1	6.5	6.75	.0350

* Positions 1 and 2 are 6.34mm ($\frac{1}{4}$ ") and 12.70mm ($\frac{1}{2}$ ") from the original roof gap surface.

** Average diameter of grain is for calculated grain size number.

P13 to P21S above are DCRP mode

P16 to P22S above are DCSP mode

P04 to P23S above are AC mode

TABLE 12

Inclusion Distributions in CGESW of A 36 Plates

Experiment Number	DCRP 13		DCRP 14		DCRP 18		DCSP 16		AC P5		AC P10	
	Ind%	Cum%	Ind%	Cum%	Ind%	Cum%	Ind%	Cum%	Ind%	Cum%	Ind%	Cum%
Size μ												
0 - 0.52	34.1	100.0	34.2	100.0	33.8	100.0	33.9	100.0	34.4	100.0	32.3	100.0
0.52 - 1.04	28.1	65.9	28.8	65.7	27.1	66.2	29.6	66.1	30.4	65.6	27.6	67.7
1.04 - 1.82	22.0	37.8	23.9	37.0	22.5	39.1	22.8	36.5	2.3	35.2	23.1	40.1
1.82 - 2.60	10.1	15.8	9.1	13.1	12.2	16.6	8.7	13.7	8.5	13.9	12.4	17.0
2.60 - 3.90	14.2	5.7	2.6	4.0	3.1	4.4	2.6	5.0	2.7	5.4	3.4	4.6
> 3.90	1.5	1.5	1.4	1.4	1.3	1.3	2.4	2.4	2.7	2.7	1.2	1.2
Total Number	1783		1549		1186		967		840		1201	

4.5.6 Grain Size Analysis

Grain size analysis was studied optically and compared to a standard ASTM grain size chart to obtain an ASTM grain size number. Figures 78 and 79 show typical grain sizes obtained at various positions for both DCSP and DCRP. Table 11 presents the grain size for many experiments at the same positions. The grain size numbers were obtained by comparing a transparent ASTM overlay over the translucent viewing plate of a Unitron microscope at 100 X magnification.

4.5.7 Charpy Traverses and Fracture Surfaces

Standard Charpy V-notch Impact tests (30°) (ASTM E23) were performed with the center of the notch in the weld, adjacent to the F.B. in HAZ 0.5 to 3 mm from the fusion boundary and 5 mm into the HAZ. The tests were performed at room temperature and the results tabulated in Table 13 for all three modes of welding. SEM fractographs were taken of the fracture surfaces, Figures 80-86.

4.6 ESW Utilizing Bar Electrodes

4.6.1 Introduction

Eleven welds were made with bar electrodes and plates of the same material. Eight of the welds were made from ASTM A36 plate and bars and four of the welds were made using cast T-1 equivalent plate and bars. Table 14 presents the data obtained or calculated for the operating conditions.

4.6.2 Temperature Time Cycles

Figures 87-94 are the thermal profiles for the three modes of welding under the operating conditions presented in Table 14. Figure 95 compares

TABLE 13

Charpy Values at Various Positions in
Welded A 36 Plate

Experiment Number	Position of V-notch	Charpy Impact at Room Temp. ft.lbs.
DCRP P21	WELD CENTER	116
	0.5 mm into HAZ	27
	1 mm into HAZ	75
	2 mm into HAZ	Off Scale*
	3 mm into HAZ	Off Scale
DCSP P22	WELD CENTER	70
	0.5 mm into HAZ	37
	1 mm into HAZ	41
	spheroidized region (2 mm)	Off Scale
AC P23	WELD CENTER	95
	Half way into weld	55
	Adjacent to F.B. in parent metal	18
	0.5 mm into HAZ	29
	1.5 mm into HAZ	30

* Off scale denotes off scale above 220 ft. lbs. or the specimen did not completely break.

TABLE 14

Experimental Conditions for ESW Utilizing Bar Electrodes

Experiment Number	Operating Mode	Volts	Amps	Penetration cm	Weld Velocity cm sec ⁻¹	Slag Depth cm	Apparent Resistance ohms	Specific Power kcal cm ⁻¹
PP3	DCRP A 36	35	690	0.417	.0767	2.69	.051	75
PP4	DCRP A 36	24	610	1.270	.0111	3.81	.039	321
PP5	DCRP A 36	33	725	0.826	.0582	2.79	.046	99
PP6	DCRP A 36	36	640	0.635	.0609	2.22	.056	92
PP7	DCRP A 36	34	710	0.640	.0512	3.68	.048	113
E1	DCRP T-1	38	625	0.826	.0440	1.27	.061	128
E2	DCRP T-1	34	725	1.080	.0364	2.86	.047	160
E3	DCRP T-1	30	575	0.826	.0334	2.54	.052	124
PP1	DCSP A 36	40	775	1.27	.0685	0.953	.052	110
PP8	AC A 36	33	730	.950	.0544	4.06	.045	106
E4	AC T-1	28	750	.064	.0440	1.27	.037	115

one thermocouple position for the three most different specific power inputs in the D.C. mode of welding.

4.6.3 Penetration

Figure 96 indicates the measured and hardness determined penetration for both the A36 and T-1 equivalent welds. One penetration for each mode welding A36 and each penetration for all the T-1 equivalent weld specific power inputs is shown in Figure 97.

4.6.4 Hardness Traverses

Hardness traverses were only carried out on the T-1 equivalent plate. These traverses were carried out at 6.35 mm (.25 in.) intervals on horizontal sections along the center line of the section and parallel to the center-line near the surface of the plate (see Figure 98). The traverse along the plate edge was considered necessary because of the high hardness that can be achieved in T-1, even when only air quenched. The hardness traverse values were made using a Wilson Rockwell Hardness tester on the Rockwell C scale.

4.6.5 Charpy Traverses

Standard Charpy V-notch Impact tests (30°) (ASTM E32) were performed on the base metal, weld metal and in the HAZ adjacent to the fusion boundary at - 40°C. Table 15 presents the impacts values determined.

4.7 Electrical Distribution

Figures 99-101 indicate the quasi-steady state electrical distribution determined as described in Chapter 3. In addition, each figure shows the quasi-steady state physical and thermal characteristics of the weld.

Figures 102-104 show the experimental arrangement.

TABLE 15

Charpy Values at Various Positions in ESW
Welded T-1 Equivalent Plate

Experiment Number	Operating Mode	Charpy Impact Value and Position ft.lbs. at - 40°C
E1	DCRP	Base Metal 56 Weld Deposit 22.5 HAZ Adjacent to F.B. 8
E2	DCRP	Base Metal 52 Weld Deposit 21 HAZ Adjacent to F.B. 11.5
E3	DCRP	Base Metal 52.5 Weld Deposit 22.5 HAZ Adjacent to F.B. 10
E4	AC	Base Metal 56 Weld Deposit 23 HAZ Adjacent to F.B. 8 HAZ 6.4 mm from F.B. 13.5

4.8 General Observations

Figure 105 illustrates the shape of the penetration in vertical and horizontal positions during a typical AC weld (PP8).

Figure 106 illustrates the shape of the penetration when welding in the DCRP mode using bar electrodes.

Figures 107 and 108 show the resultant welds using Consumable Guide Electroslag welding for unstable and stable conditions respectively.

Figure 109 shows the surface obtained from a good weld. Figure 110 shows the surfaces of the welds used to determine the electrical distribution.

Figure 111 indicates the situation when the penetration becomes so great as to cause the slag and molten metal to run out around the shoe.

Figure 112 shows two welds in vertical and horizontal section plus the hardness test indentations.

Figure 113 is actually a casting and was obtained during Consumable Guide Electroslag welding when the slag depth was approximately 10 cm deep. The penetration was uniform on both sides but only about 4 cm below the slag/air interface; the molten filler metal and parent metal simply flowed downward and formed a casting.

CHAPTER 5

DISCUSSION OF RESULTS

5.1 Power Supply Characteristics

Both the Hobart welders used were constant voltage type welders in that the slope of the voltage amperage curve was 16.6° (see Fig. 27). It is probable that the published data were obtained by use of a variable resistance across the terminals with no lead wires, and readings were taken from the panel mounted gauges for voltage and amperage. The input voltage (published) was 230 volts to the welder and, in the experiments carried out in the present research, the input voltage was only 206 volts. This would account for some of the loss in power as would the resistance of the leads used in the experiments. The nature of the resistance of the slag pool is not really known at this time but it certainly involves the temperature dependence of the conductivity of the slag, and the polarity and the mode of welding.

For these reasons, each welding configuration and mode will be discussed later; the dead load curves shown in Figures 27 and 28 are probably not applicable to the resistance that the welding supply experiences during actual welding. There is one well established observation throughout this research - AC always presents a greater overall resistance than either DCRP or DCSP. This result is possibly explained by the fact that the

polarization field during AC is very much smaller than during DC, because of the change in polarity every 60 seconds. During DC the formation of highly conducting surface layers (77) may reduce the apparent resistance drop significantly as the polarization fields are much larger.

5.2 Industrial Experiments at Canron

5.2.1 The Resistance of the Slag Pool

The series of welds made at Canron were made using Hobart 750 welders and thus the weld results should have been useful in predicting and obtaining the voltage and amperage characteristics desired. Because the slag depth was constant, and the only desired property was full penetration of the welds, most of the other variables were eliminated.

Figure 114 presents the amperage-voltage characteristics and Figure 115 presents the amperage-apparent resistance characteristics. The voltage amperage characteristic is approximately what was expected; it would be expected to be a straight line through origin if the resistance was constant and not dependent on the slag temperature and weld configuration. The apparent slag resistance drops dramatically with increasing current due to the increase in temperature. Figures 116 and 117 show that the amperage is markedly increased when the wire feed rate is increased, and that the resistance drops markedly with increasing wire feed velocity. This can be explained by the probability that the faster wire rate allows for a greater immersion of the wire before it melts off, and thus the interelectrode gap is smaller and the current density higher, causing a higher temperature below the electrode tip. It is also possible that the higher current density is achieved when the wire setting is higher, and thus a higher temperature

is achieved in the slag pool and a lower apparent resistance.

5.2.2 Energy Requirements

Figure 118 presents the energy required to melt one gm of deposited metal as a function of the melt rate (or wire velocity). This may be explained by the lower resistance and increased amperage when the melt rate is high. This view is simplistic because it does not take into account the degree of melting of the parent metal, or the increasing loss of heat to the water cooled copper shoes as the wire velocity decreases. However, it would appear that if a higher melt rate is achieved, the energy and thus the power requirement is lower for the same weld.

5.3 Relating Published Experimental and Production Welding Parameters

Table 16 presents the operating conditions for experimental and production welding from the references cited.

Figure 119 indicates that the data from the literature must be interpreted carefully before any predictions can be made for the correct welding procedure. There should be some relation between voltage and amperage that is nearly a straight line, or curves as shown in Figure 114. Figure 119 can only mean that the welding conditions of the present program must differ appreciably from the welding conditions of the published work.

Figure 120 again shows the relationship between welding rate and amperage. In general an increase in amperage causes the welding rate to increase. However, for AC, this is not the case and cannot be accounted for by a change in voltage (see Table 16.).

TABLE 16

Experimental and Industrial Welding Conditions from the Literature

Reference	Mode	Volts	Amps	Thermal Energy kcal sec ⁻¹	Welding Rate cm sec ⁻¹	Resistance ohms	Energy kcal gm ⁻¹	Melt Rate gm sec ⁻¹
4	DCRP	33	405	3.2	.115	.081	1.67	1.92
	DCRP	36	415	3.6	.104	.086	1.75	2.06
	DCRP	39	415	3.9	.092	.094	1.75	2.23
	DCRP	39	425	4.0	.061	.092	2.00	2.00
	DCRP	39	475	4.4	.056	.082	2.25	1.96
	DCRP	40	500	4.8	.051	.080	2.50	1.92
	DCRP	40	525	5.0	.057	.076	3.08	1.62
	DCRP	40	550	5.3	.051	.073	3.08	1.72
	DCRP	40	550	5.3	.047	.073	3.08	1.72
	DCRP	40	550	5.3	.046	.073	3.08	1.72
	DCRP	42	575	5.8	.040	.073	3.42	1.70
	DCRP	46	575	6.3	.026	.080	3.42	1.84
	DCRP	34	450	6.3	.089	.076	3.78	1.67
	DCRP	40	600	5.8	.061	.067		
	DCRP	40	500	4.8	.042	.080	2.80	1.71
	DCRP	40	700	6.7	.042	.057		
	DCRP	40	450	4.3	.061	.089	2.21	1.95
	DCRP	40	450	4.3	.056	.089	2.35	1.83
	DCRP	40	600	5.8	.064	.067	1.88	3.09
	DCRP	40	550	5.3	.047	.073	2.36	2.25
	DCRP	42	450	4.5	.036	.093	2.29	1.97
	DCRP	40	470	4.5		.085		
	DCRP	40	450	4.3	.056	.089	2.32	1.85
	DCRP	40	470	4.5				

TABLE 16 (cont.)

Reference	Mode	Volts	Amps	Thermal Energy kcal sec ⁻¹	Welding Rate cm sec ⁻¹	Resistance ohms	Energy kcal gm ⁻¹	Melt Rate gm sec ⁻¹
23	AC	42	500	5.0	.029	.084	1.72	2.91
	AC	39	650	6.1	.025	.060	1.27	4.80
	AC	44	625	6.6	.020	.070	2.10	3.14
	AC	47	500	5.6	.035	.094	1.20	4.67
	AC	41	550	5.4	.032	.075	1.95	2.77
	AC	44	625	6.6	.028	.070	2.01	3.28
	AC	48	550	6.3	.029	.087	1.85	3.41
	AC	46	475	5.2	.037	.097	1.59	3.27
16	-	34	480	3.9	.0157	.071	2.73	1.43
	-	35.5	650	5.5	.0240	.055	2.51	2.19
	-	53	390	5.0	.0153	.136	2.98	1.68
	-	42	900	9.1	.0350	.047	1.78	5.62
52	DCRP	36	280	2.42	.0268	.129	1.65	1.47
	AC	36	280	2.42	.0225	.129	1.96	1.23
	DCRP	43	300	3.10	.0279	.143	2.03	1.53
	DCRP	41	250	2.46	.0252	.164	1.78	1.38
	DCRP	41	280	2.76	.0266	.146	1.90	1.46
	DCRP	41	300	2.95	.0273	.137	1.97	1.49
	DCRP	41	350	3.44	.0327	.117	1.92	1.79
	DCRP	41	380	3.74	.0343	.108	1.99	1.88

TABLE 16 (cont.)

Reference	Mode	Volts	Amps	Thermal Energy kcal sec ⁻¹	Welding Rate cm sec ⁻¹	Resistance ohms	Energy kcal gm ⁻¹	Melt Rate gm sec ⁻¹
52	DCRP	41	400	3.94	.0386	.013	1.86	2.11
	DCRP	41	440	4.33	.0429	.093	1.84	2.35
	DCSP	41	450	4.43	.0466	.091	1.74	2.55
	DCSP	41	250	2.46	.0193	.164	2.33	1.06
	DCSP	41	300	2.95	.0214	.137	2.52	1.17
	DCSP	41	345	3.39	.0252	.119	2.46	1.38
	DCSP	41	380	3.74	.0268	.108	2.55	1.47
	DCSP	41	420	4.13	.0322	.098	2.34	1.76
	DCSP	41	450	4.43	.0375	.091	2.16	2.05
17	DCRP	38	2600	23.7	.0097	.015	.86	
	DCRP	39	2500	23.4	.0083	.016	.99	
	DCRP	45	2000	21.6	.0090	.023	1.83	
	DCRP	54	1500	19.4	.033	.036	.84	
	DCRP	43	1600	16.5	.029	.027	.77	
47	-	54	1400	18.1	.056	.039	.95	
	-	48	825	9.5	.075	.058	.50	

TABLE 16 (cont.)

Reference	Mode	Volts	Amps	Thermal Energy kcal sec ⁻¹	Welding Rate cm sec ⁻¹	Resistance ohms	Energy kcal gm ⁻¹	Melt Rate gm sec ⁻¹
2	DC	27	575	3.7	.0635	.047	1.70	2.18
	DC	29	575	4.0	.0508	.050	1.71	2.35
	DC	33	575	4.6	.0339	.057	1.45	3.18
	DC	37	585	5.2	.0339	.063	0.84	6.21
	DC	49	585	6.9	.0169	.084	0.94	7.38
	AC	51	585	7.2	.0169	.087	0.65	11.00
	DC	42	585	5.9	.0203	.072	1.11	5.29
35	DCRP	42	700	7.1	.053	.060	1.31	5.42
	DCRP	43	900	9.3	.081	.048	1.12	8.28
	DCRP	43	750	7.7	.063	.057	1.20	6.44
	DCRP	43	925	9.5	.086	.046	2.01	4.72
	DCRP	43	925	9.5	.086	.046	2.01	4.72
	DCRP	33	925	7.3	.112	.036	1.22	5.97
	DCRP	33	925	7.3	.112	.036	1.22	5.97
34	AC	54	700	9.1	.017	.077	1.78	5.11
	DCRP	42	700	7.1	.050	.060	1.32	5.38

Figure 121 indicates that in general the apparent resistance decreases with an increase in welding rate. This effect can be attributed to higher current causing a higher temperature and, consequently, a higher conductivity of the slag or, alternatively, that the interelectrode gap at higher welding rates is smaller and the resistance path shorter. There is a problem with both of these interpretations because the higher temperature causes the electrode to melt more quickly and thus increases the interelectrode gap, which should increase the resistance causing the temperature to rise. This synergistic effect apparently gives rise to a quasi-steady state resistance, temperature distribution and interelectrode gap.

The energy required to deposit a gm of metal decreases rapidly to approximately 1 kcal per gm as the melt rate increases (See Figure 122).

5.4 Initial Large Electrode Experiments

5.4.1 Comparison of the Temperature Time Cycles

Figure 38 indicates the difference between the three modes of welding using large electrodes and a high conductivity slag (75% CaF_2 and 25% Al_2O_3). The resultant thermal profiles show that the softness of the thermal cycle in order of increasing softness is: DCRP, DCSP, AC. This suggests that the order of increasing penetration would be DCRP, DCSP and AC which, in turn, suggests that if maximum energy utilization at minimum penetration is desired, then the weld velocity should increase in the following order: DCRP, DCSP, AC. However, decreased penetration can also be achieved by decreasing the electrode immersion (i.e. the welding amperage or resistance of the slag). If the immersion is decreased, the heat source volume will be expanded to a larger area and the penetration decreased. The shape of the

thermal profiles seen in Figure 38 are of utmost importance as the objective is to achieve the least penetration possible while still obtaining complete fusion, and this is only possible with a soft thermal profile.

5.4.2 Resistance of the Slag

As stated in Chapter 4, the resistances are .017, .023 and .029 ohms for DCRP, DCSP and AC respectively. Under normal electrolytic reactions, where the interelectrode gap remains constant, it would be expected that the resistance for DCSP would be less than for the DCRP mode due to the higher production of FeO in the DCSP mode. In this case it must be assumed that the apparent resistance of the DCRP is due to a very pointed electrode tip which actually results in producing a small interelectrode gap and resultant small resistance path. This small electrode gap could only be due to the current distribution in the slag, and radiation plus convection of the slag. The AC resistance is always higher regardless of the type of electroslag welding or refining, and is believed to be due to the small polarization fields around the electrode and parent metals' surfaces - which leads to an essentially ohmic resistance. With the higher resistance the interelectrode gap becomes larger and, consequently, the heat source is expanded leading to a softer thermal regime. Unfortunately, in the AC experiment the slag was inadvertently deeper which also causes a higher resistance; however, the welding velocity was 1.6 times faster and this could rule out the deeper slag as a prime cause of the higher resistance.

5.4.3 Energy Requirements

The energy requirements per gram of deposited metal are 1.49, 1.24 and 0.81 kcal per cm of weld height for DCRP, DCSP and AC respectively. This would appear to mean that the most efficient energy utilization order would

be AC, DCRP and DCSP, but this does not account for the great differences in penetration for the three modes. When the cylinder of penetrated metal is taken into consideration, the energy for melting the metal per gram becomes 0.88, 1.06 and 0.71 kcal for DCRP, DCSP and AC respectively.

5.4.4 Use of Inclusion Distribution Measurements

Figures 39-41 show the inclusions to be uniformly small and very numerous. The inclusion distributions could be construed to mean that the impact values are adversely affected by the inclusions, but probably no more than in normal welding due to the small size (usually less 5 μ m). Except for the size, shape and frequency of the inclusions, the usefulness of these data is minimal without other data (i.e. oxygen and silicon analysis).

5.4.5 Measuring Penetration and the Heat Affected Zone using Hardness

Traverses

The Vickers Pyramid Number (VPN) traverse is considered to be a useful technique for determining the fusion boundary (FB) and heat affected zone (HAZ). If the steel can be sectioned, polished and viewed microstructurally, this is the best method. However, in many cases this is not possible and the use of the hardness traverse is very easy in comparison. The hardness values drop significantly at the fusion boundary and slowly rise again in the grainrefined/spheroidized region. This is considered to be due mainly to a Hall-Petch type relationship. Figure 42 shows the microstructural FB and HAZ and the VPN determined FB and HAZ; the agreement is very good and, thus, hardness traverses have been used throughout this research to confirm macroetched and microetched surfaces. (R.G. denotes the original preweld root gap position.)

5.4.6 Oxygen Analysis and the Interpretation of Results

Figure 43 represents the oxygen analysis across the three modes of welding. It is obvious that the DCSP is high in oxygen, approximately six times DCRP or AC. This is due to production of oxygen at the anode (metal pool surface). The oxygen analyses make the inclusion distribution values more meaningful in that there are many more silica inclusions in DCSP than DCRP or AC. Since they are more harmful to impact values, these latter are also lower for DCSP.

5.5 Consumable Guide ESW in Cylinders

5.5.1 An Overview of the Experimental Operating Conditions

This series of experiments (see Table 5) was undertaken to determine the variables of the process not mentioned in the literature. There were no reliable measurements of slag temperature distributions for electrosag welding. There were no values of current distribution when electrosag welding with an electrosag slag. There were no values for electrode immersion during welding. The present experiments were designed to determine these values and to attempt to explain the observed thermal profiles and penetration mechanism. Figure 123 represents the electrode immersion for both DC modes of operating as a function of the slag resistance. It seems reasonable that the electrode immersion should increase with decreasing resistance, because the joule heating decreases.

5.5.2 Interpretation of the Slag Temperature Distribution

The slag temperature measurements are only indicative of the real temperature because the power had to be turned off and the boron nitride

sheathing dissolved quickly. In addition, the millivolt readings were only over a range of 20 mv to approximately 30 mv during a very brief time interval. Plus or minus 0.5 cm or 0.5 mv was observed and is considered to be the error in the Figures 44, 46 and 48. All three modes have the highest temperature region at the bottom of the electrode or just below this point. However, DCRP has the steepest temperature gradient and AC the lowest temperature gradient. The electrode immersion would appear to have the greatest effect on the temperature gradients but this is ambiguous as the slag resistance will drop with increasing temperature causing more current to flow through the hot region and thus also regulate the immersion.

5.5.3 The Effect of Slag Depth, Polarity and the Resultant Immersion and Electrode Gap on Penetration

Figure 124 indicates that there is a maximum in the immersion versus energy per cm of weld produced. This curvature is interpreted as the interplay between the velocity of the electrode forcing it further into the slag and increasing energy available to melt the electrode. This effect appears to be independent of slag depth and therefore it should be possible to select a slag depth which will utilize the immersion data to produce the desired interelectrode gap. This allows for an estimate to be made to attain the desired penetration. The higher energy for the same immersion for DCSP is considered to be due to the lower resistance in the DCSP mode.

Figure 125 indicates there is a definite relationship between penetration and energy input per cm of weld. The penetration shows a maximum for both DC modes, with DCSP requiring more energy than DCRP. With a constant slag depth this can be explained by assuming the heat is generated mostly in the interelectrode gap and, therefore, the maximum in the penetration curve is caused by the same effect as the maximum in the

immersion curve. Once again the higher conductivity of the slag in the DCSP mode shifts the penetration maximum to higher energy requirements.

Figure 126 indicates the penetration for both slag depth and inter-electrode gap values. The points to the right of the vertical line are due to the slag depth and interelectrode gap values being too high and presumably the current path is to the sides and not to the molten steel pool.

5.5.4 Velocity Measurements and Their Reliability

Three methods were used and the results are compiled in Table 8. There is a great deal of discrepancy between the methods, particularly when one divides the total length of the weld by the time taken to produce the weld. The tungsten marker bed gives good results if the tungsten can be cut through and is not too thick. The measurement of the time differential between the maxima on the thermal profiles for thermocouples, the same distance from the fusion boundary, gave consistently good results.

The problem with calculating the velocity using the total length is that the sump does not necessarily fill up; slag is often left behind with some metal and this amount of metal varies with each experiment. Because of this problem the marker bed method, or more often the distance between peak maxima, has been used for the remainder of the interpretations.

5.5.5 Explanation of the Thermal Profiles

Three thermal profiles are shown at positions .318 or .636 intervals from the original position of the root gap. These three thermal profiles correspond with three sets of slag temperature measurements in Figure 44, 46, 68. Experiment number 10 shows a fairly shallow rise but large high temperature region adjacent to the molten slag. Experiment number 8 shows a slow rise to a small high temperature region and a subsequent drop in

temperature. Experiment number 14 shows a much slower rise in temperature and small region that is fairly hot. The respective weld velocities were .0330, .0339, .0557 cm sec⁻¹ and, therefore, the compressed nature of the profiles cannot be caused by large changes in velocity. They all have approximately the same slag depth (6.60-7.00 cm) and, therefore, the slag depth has not caused the change in profiles. This suggests that the only cause for the compression is the observed slag temperatures which are probably caused by the immersion variation with polarity; DCRP 1.49 cm, DCSP 3.20 and AC 4.89. The time above 900°C for DCRP, DCSP and AC for the thermocouple .318 cm from the original root gap was 100 sec, 0 sec, 25 sec respectively. This is consistent with the penetration observed when the electrode immersion is taken into account. It will be shown later that this is due in part to the current distribution.

5.5.6 Penetration and Thermal Profiles

When a cross sectioned view is taken (see Figure 127) of the thermal profiles, it becomes significant that the steeper the gradient the larger the penetration. When this is integrated with the time above 900°C, the order of penetration becomes rational.

5.5.7 Hardness Traverses

Care has to be taken when analysing the hardness data as some welds were made with AISI 1020 wire into A 36 cylinders, some with AISI 1042 into A 36 cylinders and some with AISI 1042 into AISI 4340 and A 36 cylinders. Welds made with AISI 1042 wire into A 36 cylinders (i.e. experiment 10 and experiment 8) show a dramatic decrease in hardness at the fusion boundary due to lower carbon content and increased grain size. Those with AISI 1020 into A 36 show a small decrease in hardness due to increased grain size.

The welds with AISI 1042 into AISI 4340 show an increase in hardness due to the alloying constituents of the AISI 4340 producing a bainitic structure on cooling. All welds show a slight increase in hardness at the HAZ due to grain refinement and spheroidization of the carbide banding. Figure 53 indicates typical hardness traverses; the microstructurally determined fusion boundary (FB) and the heat affected zone (HAZ) are also shown. There is good agreement between the microstructure and hardness changes.

5.5.8 Oxygen Analysis Results

The oxygen analysis indicates that DCRP and AC have advantages over DCSP. The weld region for DCRP and AC has an oxygen content very close to the base metal analysis but the DCSP is up to 100 ppm (or four times the base metal analysis). This would lead to higher susceptibility of DCSP welds to brittle fracture in the weld zone (see Figure 54).

5.5.9 Stainless Steel Consumable Guide and Mixing in the Liquid Steel Pool

Figure 55 shows the distribution of the 304 S.S. nozzle as it has solidified after melting the nozzle. When the consumable guide melts during welding, it does not do so steadily but melts at regular intervals. This leads to the banding seen in most welds and, in the case where the nozzle is stainless steel, a simple nital etch reveals the pattern of the solidification front. In this case it is seen that the 304 S.S. does not mix with the AISI 1042 to any appreciable extent. A trace across one of the bands using the electron microprobe revealed very low concentration of nickel in the areas between the 304 S.S. bands. This is true for both the transverse and longitudinal sections.

5.6 Consumable Guide ESW with A 36 Plates

5.6.1 An Overview of the Experimental Operating Conditions

This series of experiments (see Table 9) was undertaken to provide information pertinent to production welding as the procedures used were as close to those used in industry as it is possible to achieve in the laboratory. Again the thermal profiles were measured with time but emphasis was given to DCRP and AC because of their low oxygen content and wide industrial use. A series of three experiments, one for each mode, was undertaken to provide data for determination of the electrical distribution.

Figure 128 shows the electrode immersion as a function of the apparent resistance. The electrode immersion increases with decreasing apparent resistance because there is less heating of the molten slag even though the amperage is increasing. The apparent systematic difference between the AC and DCRP modes may be due to an error in measuring the RMS voltage and current, or a phase shift when welding in the AC mode. Figure 129 indicates that the amperage decreases rapidly with increasing resistance and therefore the heating of the molten slag should be higher and the immersion shallower.

5.6.2 Explanation of the Temperature Time Cycles

The thermal profiles are presented in Figures 61 to 73. The same figures also indicate the time position of the slag/air interface, the electrode immersion and slag/molten steel interface. The profiles are for thermocouples at 6.35 mm (1/4 inch) spacing with number one 6.35 mm from the original parent metal root gap edge. The profile for the number one thermal couple 6.35 mm from this surface simply means that a thermal profile

for a thermocouple at the surface would be shifted to the left on figures 61 to 73 and would indicate a much higher temperature.

All the thermal profiles show that significant heating of the parent metal takes place long before the slag/air interface is reached.

When the slag is medium depth and the electrode immersion fairly shallow as in experiments P04, P05, P08, P22S, P23S (Figures 62-64, 72, 73) the thermal profiles are much shallower. The heat generated is distributed over a much longer parent metal/slag surface for a greater period of time.

In all cases a large amount of heat is liberated from the molten steel pool as can be seen from the profiles; however this would appear to be less than the slag heat. The heat from the molten steel pool is both superheat and latent heat of fusion.

The comparison between AC and DCRP profiles will be discussed later in section 5.7.

5.6.3. Penetration and the Heat Affected Zone as a Function of the Thermal Profiles

The measured penetration and heat affected zone for these experimental welds are presented in Table 10. Experiments P13 through P21 are DCRP, P16 and P22S are DCSP and P04 through P23S are AC. DCRP, as a generalization, has less penetration than AC. This is probably due to the deeper electrode immersion and shallower slag depth with the exception of P20S and P21S which -

were operated with a deeper slag depth for the electrical distribution measurements. In AC the penetration is deeper even with the shallow thermal profiles and deeper slag. If the slag as in P10 (Figure 65) is shallower and the profile steeper, the penetration is even deeper. P08 (Figure 64) seems to be anomalous but the innermost thermocouples were melted and thus the penetration is believed to be correct.

5.6.4 Hardness Traverses

Figure 74 presents the root gap (RG), fusion boundary (FB) and heat affected zone (HAZ) as determined microstructurally. It also presents the Vickers Pyramid Number (VPN) hardness traverses. There is a very good correlation between the two methods. The hardness change at the fusion boundary is due to the very large grain size and the increase at the end of the heat affected zone is due to the small grain size and spheroidization. An attempt has been made to apply the austenitizing parameter of Bastien et al (68) to predict the austenite grain size for regions that are in the austenite phase region for a significant length of time (i.e. greater than 10 seconds at temperatures over 850°C).

5.6.5 Measured Grain Size and Austenite Grain Size

Table 11 compares the measured grain size and the calculated grain size. The calculated grain size is obtained by a semi-empirical relationship which defines an austenitizing parameter P:

$$P = \left(\frac{1}{T_E} - \frac{R}{\Delta H} \log \frac{t}{t_0} \right)^{-1}$$

where T_E = the equivalent maximum temperature over a period t , °K

ΔH = the activation energy for austenite grain growth,
110,000 cal mol⁻¹.

t = time in the austenitizing phase region

t_o = time unit, 1 sec.

and
$$T_E = T_M - R \frac{T_M^2}{\Delta H}$$

where T_M = the maximum temperature attained

R = the universal gas constant, 1.98 cal mol⁻¹ °K⁻¹

A nomograph, Figure 14, is used to determine the grain size of the austenite grains prior to decomposition. As seen in Table 11, the decomposition grain size is (within error of the measuring technique) the same size as the austenite grain size calculated by this method. In the two phase field, alpha plus gamma, there is no formula that can be applied to calculate the ferrite and pearlite grain sizes. However, the large grain size observed and calculated suggests that the heat affected zone near the fusion boundary would cause a decrease in the impact strength of this region.

Figures 78 and 79 show the grain size for DCRP and DCSP respectively at various positions through the weld zone into the unaffected parent metal.

5.6.6 Inclusion Analysis

Table 12 presents the Quantimet inclusion analysis of six weld sections and Figure 75 the oxygen analysis from the corresponding sections. The same total area was observed in each case and thus, even though the oxygen analysis was as expected, the total area fraction of inclusions was found to be higher for DCRP than for DCSP at AC. This reverse order of area fraction with respect to DC modes can not be explained by the oxygen analysis as inclusion distributions.

The inclusions were examined at 3000 X magnification on the scanning electron microscope and analysed for qualitative chemistry. Figure 76 is a

photo of the DCRP mode and Figure 77 of the DCSP mode. The DCRP inclusions were found to be very high in MnS with some Si. The DCSP inclusions were found to be very high in Si and low in sulphur. This can be explained by the much deeper penetration in the DCRP mode than in the DCSP mode and thus much more sulphur has to be removed due to greater dilution.

5.6.7 Charpy Impact Values

The Charpy impact values using the ASTM V-notch technique are not meant to be accurate, only relative; they are presented in Table 12. The notch was oriented in the plane of the plate parallel to the welding direction. Table 13 is consistent with the fact that DCRP has greater penetration due to higher temperatures and thus the grain size effect causes a very large drop in the relative impact strength. This is also observed in DCSP and AC. The very low value of 18 ft. lbs. obtained for the AC weld is only due to the notch being almost at the fusion boundary but still in the heat affected zone. Figures 80 through 86 are fractographs of the Charpy fracture surfaces.

5.7 Electrical Distribution in Consumable Guide ESW

5.7.1 Possible Interpretation of Current Distribution

Figures 99 through 101 give the electrical distribution for DCRP, DCSP and AC for very similar operating conditions. Between the DC modes there is very little difference in the current distribution. This is confirmation of the thermal distribution shown in Figures 50 and 51. Also this is verified by the essentially same shapes of the thermal profiles for the DC modes. AC on the other hand appears to have an almost even current distribution and this is confirmed by the thermal distribution in the slag

(Figure 52) but only slightly in the thermal profiles.

It is very significant that the electrical distribution in the slag is assumed in the literature to be almost always from the electrode tip to the molten liquid steel and very little to the side walls. The present research would indicate that, within a 25% margin of error in the position of the slag with respect to the shunt positions, the current to the molten pool does not exceed 50% of the total current. It is very possible that the difference between the present research findings and published research findings is due to current being carried by the consumable guide which has very shallow immersion and thus would tend to pass current to the side walls and not the molten steel pool. The current distribution to molten pool would be much higher if the slag were shallower or the immersion much deeper. However, in the present experiments the slag depth was only slightly greater than in industrial practice. According to Dilawari et al (76) the slag flow is dominated by transport caused by the applied current over convective transport.

5.7.2 Correlation with Slag Temperature Distribution

The temperature in the slag is achieved at a quasi-steady state simply by the ability of the slag surroundings to remove heat from the slag and the source(s) of heat generation. The current distribution of all modes of operation shows the maximum current is just below the electrode tip (Figures 99 to 101) and the temperature distributions also show a maximum below the electrode tip for conditions of deep slag and shallow immersion (Figures 50 and 51). This would appear to be reasonable because the current is high, the slag will heat up due to resistance heating, and once it does its conductivity increases until steady state is achieved between the current, temperature and conductivity. However,

the induced flow that is obvious from the scooped out nature of the penetration shows that there is considerable flow due to electromagnetic forces and this flow is toward the side of weld away from the electrode.

Most of the publications that cite slag temperatures also show a maximum temperature in the slag above the slag/metal interface. The temperatures in the literature are not for the common electroslag weld fluxes and therefore the actual temperatures cannot be compared with those obtained in the present research. Temperatures have been cited as high as 2000°C (52) using a submerged arc welding flux for electroslag welding.

Dilawari and Szekely (76) have modelled the electroslag process for an unusual physical configuration, but have shown that the electromagnetic forces in small electrodes (i.e. wire) are predominant and the mass flow is as shown in Figure 130. Unfortunately the current distribution assumed is not reported but the flow is not unreasonable when referred to the current distribution reported in the present research.

5.8 ESW Utilizing Bar Electrodes

5.8.1 Overview of the Experimental Operating Conditions

The bar electrode welding conditions (see Table 14) were found to be much different from those of consumable guide welding. Voltage was consistently lower, amperage higher and the welding velocity extremely high. The specific power was lower than for wire welding except for PP4 where the low voltage apparently caused the excessive penetration and low velocity. All but three of the welds were made using DCRP. The slag depth varied significantly because the degree of melting of the starting compact in the sump was not uniform. The addition of slag was kept constant throughout the

experiment. Generally the electrode immersion was constant and never more than 5 mm average. The electrode always melted off with a small cone in the center and four sharp corners which in effect made the electrode surface flat (Figure 131).

Table 14 also indicates that, using bar electrodes, the deposition rate in g sec^{-1} is much higher.

While the electrical distribution was not measured in bar electrode ESW, it is apparent from Figure 106 that the current must be near the surface, as would be expected from the very shallow immersion. The figure is taken from the end of the experiment and therefore shows the effect of the runout blocks, but the transverse sections show that the weld is sound and it is a typical weld achieved when electroslag welding with bars. The penetration does start at upper surface of the slag area and not lower down, as in wire welding. Dilawari et al (76) have shown that, within the limits of the restrictions of their model, the flow is reversed with large electrodes (compared with wire electrodes) and this could explain the penetration starting at the top. In this case the buoyancy forces are assumed to be pre-dominant over the electromagnetic forces. Buoyancy forces are simply natural convection. Dilawari et al (76) have assumed for their model calculations a linear velocity in the slag pool of 0.40 m. sec^{-1} for wire and 0.02 m. sec^{-1} for bar electrodes. While velocities were never measured in the present research, there is no doubt from visual observation of the slag surface that the wire system has a much higher velocity than the bar system.

It is felt that the penetration morphology is due to the actual interelectrode gap occurring between the electrode and the parent metal and not between the electrode and the molten metal pool.

5.8.2 Explanation of the Temperature Time Cycles

The thermal profiles are steeper (see Figures 87-94) than for consumable guide welding, as might be expected for much higher welding velocities. However, in many cases the maximum temperature reached by the thermocouple closest to the weld is lower. This generalization applies to A 36 plates and bars welded in the DCRP mode.

Experiments E1 through E4 were made utilizing cast T-1 equivalent plate and with intentionally shallow slag depths. These experiments resulted in much steeper thermal gradients.

One explanation for steeper gradients in bar electrode welding could be the reverse direction of the slag flow and lower overall flow rate of the slag itself as predicted by Dilawari et al (76). The heat should then be more concentrated in the smaller slag volume (due to the higher fill ratio) and probably transferred in the upper regions where the current should pass, this being the smallest interelectrode gap. Figure 106 shows that the penetration does start at the top of the slag. The transverse section of the same figure also shows the uneven penetration due to misalignment of the electrode; the position of the thermocouples was at the side closest to the electrode, thus measuring the maximum temperatures obtained in the weld.

The values of penetration presented in Table 14 show that in the DC mode of operation the values of penetration are all high with respect to consumable guide electroslag welding. In the AC mode however, the penetration is comparable to consumable guide electroslag welding. If the same argument is applicable to penetration as to the thermal profiles, then, because the current and temperature are very concentrated, one would expect

a thermocouple near the fusion boundary to give a very high reading (i.e. the liquidus temperature of the base metal). However, if experiment PP4 is used as an example, then number 1 thermocouple which is 0.635 mm from the parent metal face should have recorded a millivolt reading equal to the liquidus as the penetration was 0.640 mm. This is true for many of the bar electrode experiments and was investigated after the first readings on PPI. The thermocouples were affixed as usual to a plate of the same thickness, placed in a furnace and heated to approximately 1000°C and cooled, readings being taken with exactly the same recording device used in the welding experiments. No logical explanation can be suggested for this discrepancy; the readings were reasonable in the furnace. Furthermore, the readings for E3 and E4 showed that the liquidus was reached; after that point the readings were erratic and unusable.

The problem with experiments PPI through PP7 was the inability to keep the electrode aligned exactly in the center. This resulted in the penetration being more to one side, the side the electrode approached more closely. This resulted in abnormally deep penetration on one side and shallow penetration on the other. If the thermocouples were situated on the shallow side, there would be intermittent slag inclusions or even a slight slag skin and, even though the profile was steep, the absolute values would be low. Therefore the profiles are not as informative as the total penetration. For experiments PP8 through E4 the guiding apparatus was improved and the profiles were more consistent with much higher temperatures recorded.

5.8.3 Hardness and Charpy Values

Figures 96-98 show the hardness values obtained for A 36 and T-1 equivalent. The values were as expected with the T-1 being very much harder except adjacent to the fusion boundary in the heat affected zone.

Figure 114 demonstrates that the effect of the surface cooling by the water cooled shoes is non-existent and the quenching by the parent metal is at least as effective.

The Charpy values, Table 15, indicate again that the weldment has sufficient notch toughness. However, the area adjacent to the fusion boundary in the heat affected zone was unacceptable for most applications if a post heat treatment procedure is not employed. This is completely consistent with the decreased Charpy values obtained for A 36 at room temperature, when welded using consumable guide electroslag.

5.9 Large Electrode Technology and Its Implication

5.9.1 Potential Advantages and Disadvantages

The utilization of large (i.e., plate) electrodes leads to several advantages:

- 1) simple mechanical feeding in comparison with multiwire feeding.
- 2) relatively cheap filler metal.
- 3) good chemical control in comparison with multiwire (1).
- 4) a short term power interruption does not result in a large defect, such as lack of penetration or slag inclusions.
- 5) the process is very stable during operation.

However, there are significant disadvantages:

- 1) Long set-up times are required.

- 2) A larger gap between the parent metal plates is required and thus more energy is required.

5.9.2 Potential Uses

The field of greatest potential use for large electrodes is in heavy section welding. The production of large ingots (100 ton) can be achieved in many ways. The most important choice in fabrication is the decision to weld to the finished size before or after forging and heat treatment. The choice is dictated by metallurgical reasons, since the HAZ developed in the weld is extremely large. For static applications, this may well be of no disadvantage and welding of two or more components may be acceptable. In the case where a heat treatment sequence is mandatory for the final properties, electroslog welding must be accomplished before such a heat treatment. In this latter case, there is no advantage in having a narrow gap, or small HAZ, and therefore electroslog welding with plates is desirable because of process reliability.

ESW utilizing plate electrodes is potentially very usefully when many heavy section items of the same geometry are to welded and subsequently heat treated.

CHAPTER 6

DISCUSSION OF MODELS

6.1 Introduction

There are essentially three equations to be evaluated for the ESW process in the present work. The first is the analytical solution (64,65) for the temperature field in the plates being joined. The second is the empirical model of Pertsovskii (67) for calculating the immersion of the electrode during welding. The third is the application of the austenising parameter of Bastien et al (68) to calculate grain size in the heat affected zone.

6.1.1 The Analytical Solution Equation

The analytical solution equation was solved for those experiments utilizing a consumable guide and a wire electrode. A comparison of the temperatures, calculated and measured, is made.

The analytical solution equation was solved for temperature-time distributions published in the literature (16,17,18,19). A comparison of the temperatures, calculated and measured, is made.

TABLE 17

Input Data Used for Solving the Analytical Solution for Consumable
Guide Electroslag Welding (CGESW) with A36 Plates

Parameter	Math Symbol	Computer Symbol	Units CGS	Experiment Number						
				P05	P06	P08	P09	P10	P11	P12
Preheat Temp	To	PREH	°C	25.	25.	25.	25.	25.	25.	25.
Voltage	V	VOLT	volt	42.	40.0	35.	40.	35.	40.	44.
Amperage	I	AMP	amp	490.	520.	500.	530.	450.	560.	510.
Weld Velocity	Vw	VEL	cm.sec-1	.0140	.0147	.0131	.0217	.0228	.0194	.0202
Conductivity	k	AK	cal.cm-lsec-1°C-1	0.1	0.1	0.1	0.1	0.1	0.1	0.1
Specific heat	Cp	CEPE	cal.gm-1°C-1	.163	.163	.163	.163	.163	.163	.163
Density	p	RHO	gm.cm-3	7.5	7.5	7.5	7.5	7.5	7.5	7.5
Time step	dt	ΔTIME	sec	20.	20.	20.	20.	20.	20.	20.
Thickness	δ	THICK	cm	3.18	3.18	3.18	3.18	3.18	3.18	3.18
Efficiency	%	EFF	%	58.	58.	58.	58.	58.	58.	58.
Slag Depth	-	SLDEP	cm	3.18	2.86	3.49	1.91	1.91	1.27	3.49
Immersion	-		cm	0.93	1.10	1.27	1.15	1.10	1.00	.93
Pool Depth	-	POOLDP	cm	1.60	1.40	1.75	.95	.95	.70	1.70
Percentage Top Heat Source	-	SORS1	%	25.	30.	30.	30.	30.	20.	20.
Percentage Middle Source	-	SORS2	%	50.	40.	40.	50.	40.	60.	60.
Percentage Bottom Source	-	SORS3	%	25.	30.	30.	20.	30.	20.	20.
Root Gap	Y _{rg}	RTGAP	cm	3.18	3.18	3.18	3.18	3.18	3.18	3.18
Surface Heat Transfer coeff.	α	SHTC	cal.cm-2sec-1°C-1	.0005	.0005	.0005	.0005	.0005	.0005	.0005

TABLE 17 (continued)

Parameter	Math. Symbol	Computer Symbol	Units CGS	Experiment Number			
				P13	P14	P18	P20
Preheat Temp.	To	PREH	°C	25.	25.	25.	25.
Voltage	V	VOLT	volt	32.	36.	38.	39.
Amperage	I	AMP	amp	685.	760.	750.	570.
Weld Velocity	Vw	VEL	cm.sec-1	.0159	.0232	.0191	.0174
Conductivity	k	AK	cal.cm-1sec-1°C-1	0.1	0.1	0.1	0.1
Specific Heat	Cp	CEPE	cal.gm-1°C-1	.163	.163	.163	.163
Density	p	RHO	gm.cm-3	7.5	7.5	7.5	7.5
Time step	dt	ΔTIME	sec	20.	20.	20.	20.
Thickness	δ	THICK	cm	3.18	3.18	3.18	3.18
Efficiency	%	EFF	%	58.	58.	58.	58.
Slag Depth	-	SLDEP	cm	1.59	1.91	1.50	3.65
Immersion	-	AIMMER	cm	1.42	1.42	1.27	.81
Pool Depth	-	POOLDP	cm	.80	.95	.75	1.80
Percentage Top Heat Source	-	SORS1	%	5.	25.	10.	15
Percentage middle Source	-	SORS2	%	80.	50.	50.	65.
Percentage Bottom Source	-	SORS3	%	15.	25.	40.	20.
Root Gap	Y _{rg}	RTGAP	cm	3.18	3.18	3.18	3.18
Surface Heat Transfer coeff.	α	SHTC	cal.cm-2sec-1°C	.0005	.0005	.0005	.0005

6.1.2 The Electrode Immersion Equation

The electrode immersion equation is solved and a comparison of the calculated and measured immersions is made.

6.1.3 Grain Size Determination

The method of Bestien et al (68) is applied to a number of experiments and a comparison of the predicted and observed grain size determinations is made. The results of the calculations (Appendix B) are presented in Table 20.

6.2 Application of the Analytical Model

6.2.1 Model Parameters

The value of the various terms in equation [2.1] were assigned the values shown in Table 17 or values calculated from data in Table 17. The values from Table 9 are incorporated in Table 17 and the model input data.

The thermophysical properties are obtained from the literature (16, 17, 18 and 19). These values vary significantly with temperature and thus should be varied during computation; but this is impossible when applying an analytical solution.

The efficiency of 58 percent is one that is used by other investigators (15,16) and is close to the value in this research. The low efficiency is due to the relatively thin plates (3.18 cm) and the consequent high heat loss to the cooling water.

6.2.2 Relative Position of the Heat Sources

The relative position of the three heat sources, q_1 , q_2 , and q_3 , is shown in Figure 13. q_1 is situated at the upper surface of the slag pool, q_2 is intermediate between the bottom of the electrode and the slag/liquid steel interface and q_3 is situated at the position equal to one half the depth of the liquid steel pool. This relative position is based upon the distribution assumed by Pugin (16). The percentage of the total heat available distributed to each position is determined by the relative strength of the sources and thus their relative positions.

6.3 Comparison of the Model Generated and Measured Thermal Profiles for CGESW

6.3.1 Computer Calculations, Digital Output and Graphical Output

A simple computer program was used to generate the temperature/time data required to plot the isothermal contours and temperature/time graphs displayed in figures 132-142. The computer input data is tabulated in Table 17. The temperature/time data obtained experimentally for this data are represented by a series of points for one thermocouple position on the same figures. The computer program and an example of the output are in Appendix C.

6.3.2 Analysis of Graphical Results

The predicted temperatures are always greater than the experimental temperatures. This difference is very large, with the experimental values sometimes only one half of the predicted value. The predicted temperatures are felt to be too high and the experimental temperature to be relatively accurate. The curves have the same shape, and heating and cooling rates are approximately the same. The major difference is caused by the maxima in the predicted temperatures. These values could be easily reduced by addition of a correction factor to the analytical solution but this would simply be an exercise in curve fitting and would have no basis in theory. It is evident here and in the next section, that when the predicted temperatures are not above the melting point, the experimental and predicted values do not differ greatly.

The experimental results are believed to be more accurate because there are experimental results for thermocouples which ceased functioning just prior to a run-out occurring and these thermocouples gave millivolt output readings consistent with the melting point with no discontinuities in the heating curve. In addition, the predicted temperatures would lead to the run-out condition if they were attained.

The actual lower temperatures realized may be a consequence of the consumable guide to some degree. The only data available for pure wire welding is shown in the next section where the correlation is better. The use of a consumable nozzle leads to the electrode alternating between a single wire electrode and a combination wire-nozzle electrode. The alternating between a high and low current density process may cause the temperature profiles to be less sharp and thus give lower maxima.

6.4 Comparison of the Model Generated and Measured Thermal Profiles for Published Results

6.4.1 Computer Calculations, Digital and Graphical Output

Another, essentially the same computer program was used to generate the predicted results for the temperature/time relationships. The plotted and digital output is compared to the values in the literature. The comparison data is from Pugin (16), Sharapov (17,18) and Trepov (19). The data used in the computer information input file is tabulated in Table 19 with those values which have been estimated or assigned noted by an asterisk. (these values were not given in the literature cited).

TABLE 18

Input Data Used for the Analytical Solution for Published Temperature-Time Relationships

Literature Reference	Thermocouple Placement from Plate edge cm.	Experiment Designation	Voltage Volts	Amperage amps.	Thickness cm.	Welding Velocity cm.sec-1	Thermal Efficiency %	Slag Depth cm.	Electrode Immersion cm.	Pool Depth cm.
Pugin (16)	1.8,3.0 4.3,5.0	1(a)	34.	480.	5.0	.0157	58	3.35	2.25*	1.40
Pugin (16)	1.5,2.7 3.0,5.5	1(b)	34.	480.	5.0	.0163	55	2.50	1.50*	1.50
Pugin (16)	2.2,3.4 4.5,5.0	2	35.5	650.	5.0	.0240	55	2.30	1.30*	2.00
Pugin (16)	1.0,2.0 3.0,4.0	3	53.	390.	6.0	.0153	60	3.60	2.50*	1.40
Sharpov(17)	1.0,2.5 3.5,4.0	1	38.	2600.	65.0	.0097	88	4.00	1.40	2.00
Sharpov(17)	0.5,1.5 2.5,5.0	1(b)	39.	2500.	65.0	.0083	83	4.00	1.40	2.00
Sharapov(17)	1.0,2.0 3.0,4.0	3	39.	2000.	30.0	.0090	88	4.50	3.30	3.00
Sharapov(17)	1.0,2.8 4.0,5.0	4	54.	1500.	16.0	.0330	87	7.50	1.37	7.50
Sharapas(17)	1.0,2.0 3.0,4.0	5	43.	1600.	17.0	.0290	83	4.50	2.50	3.40
Sharapov(18)	1.0,2.0 3.0,4.0	-	40.	3500.	65.0	.0180	85	3.00	2.50	2.50
Trepov (19)	1.0,1.5 2.0,5.0	1	40.	360.	1.8	.0517	52	2.50	1.50	1.50
Trepov (19)	1.0,1.5 2.0,5.0	2	38.	400.	7.0	.0150	61	2.00	1.75	1.00

TABLE 18 (continued)

N.B. 1) All other parameters are the same as those tabulated in Table 17.

2) The heat source allocations are q_1 - 25% (top)
 q_2 - 50% (middle)
 q_3 - 25% (bottom)

in all cases, these are assumed by the authors.

6.4.2 Analysis of the Predicted Temperature-Time Relationships

The predicted values and experimental values compare favourably. Once again, the experimental values are lower than the predicted value. The predicted temperature/time curves, see figures 143 to 153, have maxima in the region 1050-1150°C and as with the earlier lower temperature comparisons the correlation is better at these lower temperatures. The reason the predicted temperatures are much lower for these experiments are the specific power input is 30 to 40 kcal.cm⁻² for the literature cited and 50 to 110 kcal.cm⁻² for the present research. This difference in power required is usually attributed to the plate thickness being greater for the experiments in the literature and thus the relative loss of heat to the cooling water being much smaller. However, the thermal efficiencies used are not 100% higher as would be required (they are 35% higher). The analytical solution does predict the temperatures realized experimentally for these thicker plate experiments.

6.5 Application of the Analytical Solution to a Large Electroslag Weld

An attempt was made to apply the analytical solution predictions to a large electroslag weld. The weld in question was made with the following conditions:

Weld configuration

- parent metal 200 cm. cubic blocks
- root gap = 10 cm.
- slag depth ~ 7.5 cm.

- pool depth \sim 10 cm.
- plate electrodes.

Welding conditions

- power 800 kilowatts.
- voltage 40 volts.
- amperage 20,000 amps.
- welding velocity .00833 cm/sec.
- welding time \sim 7 hours.

The analytical solution program is applied to this weld the same way it is applied to the CGESW. This means the electrode immersion must be assigned a value. The value assigned was 2 cm.

The resultant contour map from the digital output was used to estimate the depth of penetration, this contour map is presented in figure 154. The penetration is estimated to be equal to the position in the parent metal that reaches 1450°C. The depth of the heat affected zone is assumed to be equal to the position in the parent metal that reaches 850°C.

The predicted penetration is 2.6 cm and the HAZ is 13 cm. These results seem reasonable for a weld of this size as a deep penetration is necessary and should be large to ensure a sound weld. The results are compatible (i.e., a ψ value of 1.5) with the results desired by the welding procedure design.

The model predicts results that are consistent with large electroslag welding technology and are reasonable.

TABLE 19

Electrode Immersion Values

CGESW Using PF 201 Slag and Plates

1) Alternating Current (AC)

Experiment	Immersion	Measured	Calculated
P04		1.10	1.10
P05		1.03	0.93
P06		2.06	1.10
P08		0.95	1.27
P09		1.11	1.15
P10		0.95	1.10
P11		0.64	1.00
P12		0.95	0.93
P13		0.79	0.89

2) Direct Current Reverse Polarity

Experiment	Immersion	Measured	Calculated
P13		1.42	1.42
P14		1.11	1.42
P15		1.59	1.27
P18		1.27	1.27
P20		0.79	0.81
P21		0.79	0.79

3) Direct Current Staright Polarity

Experiment	Immersion	Measured	Calculated
P16		1.62	1.62
P22		0.95	0.995

6.6 Application of the Electrode Immersion Equation

Equation (2.17) was proposed by Pertsovskii (67) to be applicable to ESW and was developed from a two dimensional analogue. The equation has been applied in the present research to both CGESW of plates and into cylinders. The results comparing the calculated and measured immersions are given in Table 19.

The calculation requires use of specific resistances from the literature (67) for slags of similar composition and in the same temperature range. However, it was found that an acceptable technique was to calculate the specific resistance from one immersion value known to be accurate. This specific resistance was then used to calculate the other electrode immersion values. This technique was used to obtain the values in Table 18. The measured and calculated values correlate reasonably considering the variation of the specific resistance with temperature. The calculation technique for electrode immersion is given in Appendix B.

TABLE 20

Grain Size Determined for CGESW A 36 Plate Experiments

Experiment Number	Thermocouple Position	Maximum Temperature Attained, T_M °K	Time above 850°C, t sec.	Equivalent Maximum Temperature, T_E °K	Austenizing Parameter (to = 1 sec)		ASTM Microgram Size Number
					°K	°C	
P13	1	1628	325	1580	1891	1618	1.0
	2	1323	205	1291	1473	1200	
P14	1	1308	120	1277	1260	1161	7.75
	2	1173	75	1148	1434	987	10.50
P15	1	1243	165	1215	1368	1095	8.0
	2	1123	20	1100	1169	896	12.0
P18	1	1353	220	1320	1514	1241	6.5
P21S	1	1353	225	1320	1515	1942	6.5
	2	1138	80	1114	1221	948	11.35
P16	1	1283	160	1268	1434	1161	7.75
P22S	1	1183	165	1158	1296	1023	10.0
P04	1	1393	230	1358	1566	1293	5.5
	2	1173	70	1148	1258	985	10.75
P05	1	1333	450	1301	1518	1245	6.5
P08	2	1223	210	1196	1351	1078	9.0
P10	1	1473	270	1249	1518	1244	6.75
	2	1278	160	1320	1266	993	10.50
P11	1	1353	240	1320	1518	1244	6.75
	2	1173	90	1148	1266	993	10.50
P23S	1	1338	235	1305	1497	1224	6.75

6.7 Application of the Bastien et al (68) Model to CGESW of A36 Plate

The grain size for the plate welds produced by consumable electroslag welding was optically determined at 100X magnification by use of a comparative transparent ASTM grain size overlay. The grain size number was also calculated and determined using the method of Bastien et al (68). The calculated grain size method is presented in Appendix C and the results presented in Table 20.

The comparable number for the experimental grain size and the calculated grain size are presented in Table 11. The correlation between the grain size numbers is felt to be good and actually the same when the experimental error possible is taken into account. However, there is a deviation that is constant and may be the result of the electroslag process. The actual (experimental) grain size is smaller than the predicted grain size when the grain size is large (i.e., for small grain size numbers) and the actual grain size is larger than predicted when the grain size is smaller. This could be visualized as a result of the applicable nomogram having a shallower slope than in figure 14.

It should be noted that the grain sizes measured and predicted are approximately the same and the variation across the distance of 1.27 cm is very large. This gives rise to the impact strength problems. It also leads to the unfortunate result, that continuous cooling curves (C.C.T.) are not applicable throughout this region. Two or more C.C.T. curves would be required to account for the extreme change in grain size. In order to evaluate the changes in structures on the basis of the experimental or predicted thermal cycles a correction would have to be made for the grain size variation within the heat affected zone.

CHAPTER 7

CONCLUSIONS

- 1) The technique of investigating electroslog welding by use of a hollow cylinder has been found to be useful in investigating the process variables. This technique removes the problems associated with cooling water and a slag skin. In effect, the cylinder could be used as a temperature/time simulator for the high temperature history of electroslog parent metal.
- 2) Hardness traverse data are useful in determining the depth of penetration and extent of the HAZ. This technique could be used with a section through the cut-off run-out block assembly used in many welding shops.
- 3) It has been shown, from the oxide inclusion and consequent weld metal impact strength, that the DC reverse polarity and AC modes of welding are preferable for electroslog welding.
- 4) The slag temperature distributions indicate the maximum temperature is approximately 1700°C and DCRP has the steepest gradient and AC the shallowest.
- 5) It can be concluded, from the maxima in the penetration and immersion versus specific power input data, that the DCSP mode requires more

energy due to the lower resistivity of the slag when welding in this mode.

- 6) It has been concluded there is little mixing in the liquid pool because the nickel from the stainless steel nozzle did not distribute to any degree through the weldment.
- 7) The slag depth and immersion (interelectrode gap) would appear to have the greatest effect on the rate of heating and cooling as plotted on the temperature/time profiles. Thus, these two parameters have the greatest effect on the degree of penetration and the size of the HAZ.
- 8) The DCRP mode has the greatest degree of penetration for equivalent welding conditions and thus, the largest grain size and lowest impact strength.
- 9) AC is the best welding mode to achieve penetration with a modest thermal profile while producing the lowest degree of grain growth.
- 10) When the consumable guide technique is utilized, the welding current is found to be distributed over the depth of the slag pool and approximately 50% the current passes to the molten liquid pool. This is significant in that most of the literature assumes more than 80% of the current passes through the liquid metal/slag interface. The current distribution is confirmed by the temperature distribution.
- 11) The bar electrode method of electroslag welding when compared to consumable guide electrode welding has the following features:
 - low specific power requirements.
 - shallow electrode immersion.

- high deposition rates.
 - shallow slag depth requirements.
 - greater degree of penetration.
 - greater loss of impact strength.
- 12) The analytical model is not very useful when applied to the CGESW experiments in the present research. It is, however, useful for welding schedules incorporating thicker plates up to 200 cm.
 - 13) The Pertsovskii electrode immersion equation is applicable to CGESW.
 - 14) The Bastien et al austenitising parameter is useful in determining the grain size of the austenite in the HAZ adjacent to the fusion boundary and thus the effect on the impact strength in the HAZ.

CHAPTER 8

SUGGESTIONS FOR ADDITIONAL RESEARCH

- 1) The analytical model used in this research has not been found to be of practical value for the prediction of the penetration or extent of the HAZ for consumable guide electroslag welding of thin plates. The use of the hollow cylinder technique allows use of cylindrical symmetry and thus heat flows only in the longitudinal and radial directions. A finite difference technique could be developed and would probably be useful in predicting many of the steady state welding conditions.
- 2) The electrode immersion, interelectrode gap and slag depth interrelationships could be investigated utilizing a single slag, a non-consumable electrode and a cylindrical parent metal. In the steady state condition the temperature and current distributions could also be investigated.
- 3) It would also be enlightening to study the effect of adding a large percentage of the filler metal as a powder. This would decrease the temperature of the slag pool and allow for chemistry changes in the weldment.

- 4) Investigation of lower melting point slags and slags that react vigorously with the parent metal surface chemically or by wetting would be useful. These slags would allow for penetration without excessive austenite grain growth.

REFERENCES

1. Patton, B.E., "Electroslag Welding", American Welding Society, 1962.
2. Coplestone, F.W., paper to Commission XII of the International Institute of Welding, 1965.
3. Harvyoshi Suzuki et al, U.S. Patent 3,352,993, Nov. 14, 1967.
4. Matsuoka; Araki, Suzuki and Murai, British Welding Journal, June, 1967, pp. 287-298.
5. Linde, Electric Welding Instructions, publication F-51-220, Feb., 1969.
6. Paton, B.E., Welding Journal, Dec., 1962, pp. 1115-1123.
7. Saffonnikov, A.N., Avtomaticheskaya Svarka, No. 12, 1967, p. 69.
8. Malysheuskaya, E.G., and Andrew, V.P., Avtomaticheskaya Svarka, No. 3, 1968, pp. 5-7.
9. Ruklin, P.N. and Fokin, N.I., Avtomaticheskaya Svarka, No. 4, 1968, pp. 49-51.
10. Medovar et al, Federal Republic of Germany Patent 1,917,861, April 8, 1968.
11. Saffonnikov et al, Avtomaticheskaya Svarka, No. 7, 1963, pp. 29-33.
12. Lefevre, M., Arcos, vol. 45, 1968, pp. 4205-4216.
13. Miska, H.K., Materials Engineering, vol. 73, 5, pp. 25-28.
14. Hrivnak, I., Metal Construction, 1, Feb., 1969, pp. 74-77, (discussion pp. 128-129).
15. Mel'bard, S.N., Svarocnoe Proizvodstvo, No. 9, 1960, pp. 5-7.
16. Pugin, A.I., and Pertsovskii, G.C., Avtomaticheskaya Svarka, No. 6, 1963, pp. 14-23.

17. Sharapov, Yu. V., *Avtomaticeskaya Svarka*, No. 6, 1965, pp. 32-37.
18. Sharapov, Yu. V., *Svarocnoe Proizvodstvo*, No. 6, 1968, pp. 13-15.
19. Trepov, P.V., *Avtomaticeskaya Svarka*, No. 9, 1969, pp. 15-17.
20. Shvartser, A. Ya., and Zolotarceuskii, D.B., *Avtomaticeskaya Svarka*, No. 4, 1968, pp. 16-19.
21. Eregin, L.P., *Svarocnoe Proizvodstvo*, No. 7, 1970, pp. 25-27.
22. Makara, A.M. et al, *Avtomaticeskaya Svarka*, No. 6, 1963, pp. 24-29.
23. Rote, R.S., *Welding Journal*, May, 1964, pp. 421-426.
24. Zeke, J., *British Welding Journal*, May, 1969, pp. 258-268.
25. Woodley, C.C., and Burdekin, F.M., *British Welding Journal*, June, 1966, pp. 387-397.
26. Naumchenkov, N.E., *Svarocnoe Proizvodstvo*, No. 5, 1967, pp. 12-14.
27. Woodley, C.C., Burdekin, F.M. and Wells, A.A., *British Welding Journal*, March, 1966, pp. 165-173.
28. Malinovska, E. and Hrivnak, I., *British Welding Journal*, Oct., 1967, pp. 527-532.
29. Belen'kii, A.M., Toshchev, A.M., and Parkheta, V.K., *Avtomaticeskaya Svarka*, No. 12, 1967, pp. 56-59.
30. Pokataev, S.E., Gudov, I.I., Chernykh, V.V., Malai, A.E., and Eregin, L.P., *Svarocnoe Proizvodstvo*, No. 5, 1968, pp. 5-7.
31. Bentley, K.P., *British Welding Journal*, August, 1968, pp. 408-410.
32. Zeke, J., and Malinovska, E., *British Welding Journal*, December, 1968, pp. 621-626.
33. Braun, M.P., et al., *Avtomaticeskaya Svarka*, No. 10, 1969, pp. 7-10.
34. Makara, A.M., Yegorova, S.V., and Novikov, I.V., *Avtomaticeskaya Svarka*, No. 12, 1969, pp. 1-5.

35. Makara, A.M., Egorova, S.V., and Novikov, I.I., *Avtomaticeskaya Svarka*, No. 3, 1971, pp. 52-55.
36. Novikov, V.N., Tutov, I.E., and Kondrashev, A.I., *Metallovedenie i Obrbotka Metallov*, No. 8, August 1958, pp. 38-43.
37. Eichhorn, F., and Shabeeb, A.R., *Schweissen und Schneiden*, vol. 25, No. 5, 1973, pp. 174-177.
38. Ikeno, T. et al. and Takahashi, Y., et al, *Tetsu to Hagane*, vol. 59, No. 4, 1973, Lectures 146-149, pp. S148-S151.
39. Voloshkevich, G.Z., *Avtomaticeskaya Svarka*, Vol. 6, No. 6, 1953, pp. 3-10.
40. Gotal'skii, Yu. N., *Avtomaticeskaya Svarka*, Vol. 7, No. 5, 1954, pp. 38-43.
41. Gotal'skii, Yu. N., *Avtomaticeskaya Svarka*, Vol. 8, No. 5, 1955, pp. 47-49.
42. Gotal'skii, Yu. N., *Svarocnoe Proizvodstvo*, No. 3, 1957, pp. 1-3.
43. Ostrovskaya, S.A., *Avtomaticeskaya Svarka*, Vol. 10, No. 4, 1957, pp. 33-47.
44. Zaitsev, Yu. M., and Tyagun-Belous, G.S., *Avtomaticeskaya Svarka*, Vol. 11, No. 11, 1958, pp. 57-60.
45. Muller, R., *Schweissen and Schneiden*, Vol. 10, No. 9, pp. 359-367.
46. Poznyak, L.A., Zaitsev, Yu. M., and Tikhonovskii, A.L., *Avtomaticeskaya Svarka*, Vol. 11, No. 10, 1958, pp. 67-74.
47. Kozulin, M.G., Syatishev, A.P., and Emel'yanov, Y.V., *Avtomaticeskaya Svarka*, No. 5, 1969, pp. 47-49.
48. Dubovetskii, V., Ya., et al, and Bronshtein, L.M., and Sigarev, V.S., *Avtomaticeskaya Svarka*, No. 8, 1969, pp. 44-47.

49. Ivochkin, I.I., and Sosedov, A.F., Svarocnoe Proizvodstvo, No. 11, 1969, pp. 18-19.
50. Yushchenko, K.A., et al, Avtomaticheskaya Svarka, No. 5, 1970, pp. 72-73.
51. Makara, A.M., Egorova, S.V., Novikov, I.V., and Bronshtein, L.M., Avtomaticheskaya Svarka, No. 10, 1970, pp. 43-46.
52. Ando, K., and Wada, H., The Welding Journal, (Japanese), Vol. 39, No. 7, 1970, pp. 62-76.
53. Ando, K., Nakata, S., and Wada, H., The Welding Journal (Japanese), Vol. 40, No. 10, 1971, pp. 62-71.
54. Ando, K., Nakata, S., and Wada, H., The Welding Journal (Japanese), Vol. 40, No. 11, 1971, pp. 28-34.
55. Feldman, M. et al, Soudage et Techniques connexes Paris, Vol. 25, No. 9/10, Sept.-Oct., 1971, pp. 359-377.
56. Zeke, J., Slabon, I. and Mosny, J., Welding Research Abroad, Vol. XXIII, No. 2, Feb., 1972, pp. 18-31.
57. Lanyie, L., and Zeke, J., Welding Research Abroad, Vol. XXIII, No. 2, Feb., 1972, pp. 32-45.
58. Shaheeb, A.R., Schweissen und Scheiden, Vol. 25, No. 6, 1973, pp. 223-224.
59. Sharapov, Yu. V., Svarocnoe Proizvodstvo, No. 7, 1967, pp. 21-24.
60. Shcherbina, M., Ya. et al, Avtomaticheskaya Svarka, No. 9, 1970, pp. 45-48.
61. Rosenthal, D., Transactions ASME, Vol. 68, 1946, pp. 849-866.
62. Rosenthal, D. and Cameron, R.H., Transactions ASME, Vol. 69, 1947, pp. 961-968.

63. Rykalin, N.N., "Calculation of Heat Flow in Welding", translated by Z. Paley and C.M. Adams, U.S. contract number UC-19-060-001-3817, 1951.
64. Rosenthal, D., 2-eme Congres National des Sciences, 1935, pp. 1277-1292.
65. Goldack, J.A., Burbridge, G., and Bibby, M.J., Canadian Metallurgical Quarterly, Vol. 9, No. 3, 1971, pp. 459-466.
66. Goldack, J.A., Burbridge, G. and Bibby, M.J., Canadian Metallurgical Quarterly, Vol. 9, No. 3, 1971, pp. 467-473.
67. Pertsovskii, G.A., Svarka, Vol. 1, 1958, pp. 187-193.
68. Bastien, P.G., Dollet, J. and Maynier, Ph., Metal Construction, Vol. 2, No. 1, Jan., 1970, pp. 9-14.
69. Rykalin, N.N., Soudage et Techniques Connexes, Vol. 15, 1961, p. 5.
70. Haveri, J., Moffat, W.G. and Adams, C.M., Welding Journal, Jan., 1962, p. 125.
71. Maynier, Ph., Martin, P.F., and Bastien, P., Soudage et Techniques Connexes, May-June, 1966, pp. 197-218.
72. Etienne, M., Ph.D. Thesis, University of British Columbia, 1970.
73. Burel, B.C., M.A.Sc. Thesis, University of British Columbia, 1969.
74. Joshi, S.V., Ph.D. Thesis, University of British Columbia, 1971.
75. Vinokurov, V.A., Avtomaticheskaya Svarka, No. 4, 1966, pp. 18-21.
76. Dilawari, A.H. and Szekely, J., Metallurgical Transactions B, Vol. 8B, June, 1977, pp. 227-236.
77. Beynon, G. T., Ph.D. Thesis, University of British Columbia, 1971

APPENDIX A

CALCULATION OF IMMERSION

A.1 The Equation

The equation to be used is

$$R = \frac{\rho}{2\pi L} \ln \left(\frac{2L}{r} \right)$$

where: R is the apparent resistance in ohms, ρ is the specific resistance in ohms cm.⁻¹, L is the electrode immersion in cm. and r is the radius in cm.

A.2 Determination of the Parameters

The apparent resistance is found by dividing the overall voltage by the overall amperage. The specific resistance can either be calculated or can be used to calculate the immersion by use of a computer program. The radius is a constant 0.12 cm. (diameter is 3/32 inch. or 0.24 cm.). Thus if the immersion is known, then the specific resistance can be calculated. The apparent resistance and measured immersions are presented in Table 9.

A.3 Calculation of the Specific Resistance

If the measured immersion for the first experiment in each mode is used (i.e., P04 for AC, P13 for DCRP and P16 for DCSP) the specific resistance is:

1) for AC,

$$\rho = \frac{2\pi LR}{\ln\left(\frac{2L}{r}\right)} = \frac{2\pi(1.10)(.078)}{\ln\left[\frac{2(1.10)}{.12}\right]} = 0.185 \text{ ohm cm.}^{-1}$$

2) for DSRP,

$$\rho = \frac{2\pi(1.42)(.047)}{\ln\left[\frac{2(1.42)}{.12}\right]} = 0.133 \text{ ohm cm.}^{-1}$$

3) for DCSP,

$$\rho = \frac{2\pi(1.62)(.049)}{\ln\left[\frac{2(1.62)}{.12}\right]} = .151 \text{ ohm cm.}^{-1}$$

These specific resistances are then utilized to calculate further immersions.

A.4 Calculation of Immersions

The immersions of each mode were calculated using the above specific resistances. The calculation involves a solution using a IBM program and the following derivation:

$$L = \frac{\rho}{2\pi R} \ln \left(\frac{2L}{r} \right) \quad (A.1)$$

$$f(X_0) = \frac{\rho}{2\pi L} \ln \left(\frac{2L}{r} \right) - R$$

$$\frac{\partial f(X_0)}{\partial L} = \frac{\rho}{2\pi L^2} \left(1 - \ln \frac{2L}{r} \right)$$

$$X_1 = X_0 - f(X_0) / f'(X_0) \quad (A.2)$$

Equation [A.2] can be solved by an iterative process until the solution converges to a value. The immersions calculated by this method are presented in Table 18.

APPENDIX B

GRAIN SIZE CALCULATION

B.1 Introduction

The calculation of the austenitizing parameter, P, requires two experimentally determined values. These values are the maximum temperature attained and the time above the austenitizing temperature, 850°C. Figures 61-73, the temperature/time relationships for CGESW of A36 plates, are used to directly obtain the maximum temperature for the position and the time above the austenitizing temperature.

B.2 The Equivalent Maximum Temperature

An equivalent maximum temperature must be calculated because the temperature/time relationship is not rectangular. The calculation allows for the heating and cooling cycle portions of the temperature/time relationship.

Mathematically the equivalent maximum temperature, T_E is calculated as follows:

$$T_M - T_E = \frac{RT_M^2}{\Delta H} \quad [B.1]$$

where

T_M = the maximum temperature experimentally
achieved, °K.

R = the universal gas constant, $1.98 \text{ cal.mol.}^{-1} \text{ °K}^{-1}$.

ΔH = the activation energy for austenite grain growth.

and rewriting [C.1],

$$T_E = T_M - [(RT_M^2)/(\Delta H)] \quad [\text{B.2}]$$

and for P04 (see Table 20),

$$\begin{aligned} T_E &= (970 + 273) - [(1.98)(1243)^2/110,000] \text{ °K} \\ &= 1215 \text{ °K} \end{aligned}$$

B.3 The Austenizing Parameter

The austenizing parameter, P , is calculated as follows for P04:

$$\begin{aligned} P &= \left[\frac{1}{T_E} - \frac{R}{\Delta H} \ln \left(\frac{t}{t_0} \right) \right]^{-1} \quad [\text{B.3}] \\ &= \left[\frac{1}{1215} - \frac{1.98 \ln \left(\frac{165}{1} \right)}{110,000} \right]^{-1} \\ &= [0.000823 - 0.00018 (5.1059)]^{-1} \\ &= [(0.000823) - (0.000919)]^{-1} \\ &= (0.000731)^{-1} \\ &= 1368 \text{ °K or } 1095 \text{ °C} \end{aligned}$$

where $t = 165$ sec. is the time above 850°C from the temperature/time relationship and $t_0 = 1$ sec. is used so figure 14 can be used directly (figure 14 is plotted for $(t_0 = 1$ sec. only).

B.4 Grain Size Determination

The grain size is determined from the nomogram, figure 14, where the austenitizing temperature is obtained by calculation as in C.3 and the AFNOR grain size number is read. The AFNOR grain size is the same as the ASTM Micrograin Size Number from ASTM E-112. The Grain Size Number is equal to the number of nominal grains per square inch at 100X magnification. The results of the above calculations and grain size determinations are presented in Table 20.

APPENDIX C

COMPUTER CALCULATIONS AND OUTPUT

C.1 Introduction

The temperature at any position in the plate and any time are calculated using equation (2.16) and the relative positions are calculated using equation (2.17). The computer programs written and used to solve these two equations are THEORY and DROG respectively and are presented below.

C.2 THEORY Program

This program was used to solve equation (2.16) with the input data from Table 17. The program generates the data required to characterize the welding procedure. This data is stored in a permanent file titled "run number - S" (e.g., 05S). The program also generates the time temperature relationship data required to plot thermal profiles and isothermal profiles. Some of this data is stored in a permanent file titled "run number - S1" (e.g., 05S1). Two printed plotter outputs are also generated to evaluate the input data and calculations before the final plotting and contour mapping is undertaken.

An example THEORY program is:

```
DIMENSION QS (3), Y (10), TIME (200), POSN (3), EXTERM (3), RADIUS (3)
DIMENSION SQTERM (3), BESTER (3), BFUN (3), CONTER (3), TEMP (10, 200)
DIMENSION S (3), POSIT (200), T (3), TT (3), TEMPI (200, 4)
READ (5, 1) NUMRDN
READ (5, 2) PREH, VOLT, AMP, VEL, AK, CEPE, RHO, DTIME, THICK, EFF
READ (5, 3) SLDEP, AIMMER, POOLDP, SORS1, SORS2, SORS3,
1 RTGAP, SHTC, START
Y (1) = 3
DO 35 J = 2, 8
Y (J) = Y (J - 1) + 1.
CONTINUE
POWER = 0.24 * VOLT * AMP * EFF
SPWR = POWER / THICK
TPK = 1. / (2. * 3.14159264 * AK)
PWRS1 = SORS1 * SPWR / 100.
PWRS2 = SORS2 * SPWR / 100.
PWRS3 = SORS3 * SPWR / 100.
QS (1) = PWRS1 * TPK
QS (2) = PWRS2 * TPK
QS (3) = PWRS3 * TPK
BEE = 2. * SHTC / (THICK * RHO * CEPE)
DIFPUS = AK / (RHO * CEPE)
BEYA = BEE / DIFPUS
SEP1 = (SLDEP + AIMMER) / 2.
SEP2 = SLDEP + (POOLDP / 2.)
X1 = START * VEL
TIME (1) = START
S (1) = -SEP1
S (2) = 0.
S (3) = SEP2 - SEP1
TT (1) = -SEP1 / VEL
TT (2) = 0.
TT (3) = (SEP2 - SEP1) / VEL
ELGAP = SLDEP - AIMMER
Q44 = POWER / (EFF * VEL * 1000.)
WRITE (6, 5) NUMRDN
WRITE (6, 6)
WRITE (6, 7) RHO
WRITE (6, 8) AK
WRITE (6, 9) CEPE
WRITE (6, 10) DIFPUS
WRITE (6, 11)
WRITE (6, 12) VOLT
WRITE (6, 13) AMP
WRITE (6, 14) SPWR
WRITE (6, 15) THICK
WRITE (6, 16) Q44
WRITE (6, 17) EFF, POWER
WRITE (6, 18) SHTC
WRITE (6, 19)
WRITE (6, 20) (QS (I), I = 1, 3)
WRITE (6, 21) VEL
WRITE (6, 22) SLDEP
WRITE (6, 23) POOLDP
WRITE (6, 24) AIMMER
WRITE (6, 25) ELGAP
WRITE (6, 26)
WRITE (6, 27) S (1), S (2), S (3)
```

35

WRITE (6,29) TT (1), TT (2), TT (3)

WRITE (7,30)

WRITE (7,31)

DO 60 K=1,200

 POSN (1) =X1-SEP1

 POSN (2) =X1

 POSN (3) =POSN (1) +SEP2

DO 50 J=1,8

 DO 40 I=1,3

 EXTERM (I) =(-0.5*VEL*POSN (I)) /DIFFUS

 RADIUS (I) =SQRT (POSN (I) *POSN (I) +Y (J) *Y (J))

 SQTERM (I) = (((VEL*VEL) / (4.*DIFFUS*DIFFUS)) +BBYA)

 BESTER (I) =RADIUS (I) *SQRT (SQTERM (I))

 BFUN (I) =BESSKO (BESTER (I))

 CONTER (I) =QS (I) *EXP (EXTERM (I)) *BFUN (I)

40 CONTINUE

 TEMP (J,K) =PREH+CONTER (1) +CONTER (2) +CONTER (3)

50 CONTINUE

 TIME (K+1) =TIME (K) +DTIME

 X1=X1-VEL*DTIME

 T (2) =TIME (K)

 POSIT (K) =POSN (2)

 WRITE (7,32) T (2), POSIT (K), (TEMP (J,K), J=1,8)

60 CONTINUE

AA=.5

CALL DRAWC (TEMP,POSIT,J,Y)

CALL ALABL (NUMRUN,VOLT,AMP,SLDEP,AIMMER,POOLDP,VEL,AA,THICK,Q44)

CALL OUTPLT (TEMP,POSIT,VEL)

CALL ALABL (NUMRUN,VOLT,AMP,SLDEP,AIMMER,POOLDP,VEL,AA,THICK,Q44)

CALL PLOTND

STOP

1 FORMAT (I4)

2 FORMAT (8F10.5)

3 FORMAT (8F10.5)

4 FORMAT (4F10.5)

5 FORMAT ('*****', //, 1X, I4, //, 1X, '*****', //)

6 FORMAT (1X, '**** THE FOLLOWING ARE THE THERMOPHYSICAL PROPERTIES **

1**' //)

7 FORMAT (1X, 'DENSITY =', 3X, F10.2, 'GM.-CM.-3', //)

8 FORMAT (1X, 'THERMAL CONDUCTIVITY =', F10.5, 'CAL. SEC.-1CM.-1 DEG. C.-1'

1 //)

9 FORMAT (1X, 'SPECIFIC HEAT =', 6X, F10.5, 'CAL. GM.-1 DEG. C.-1' //)

10 FORMAT (1X, 'THERMAL DIFFUSIVITY =', 1X, F10.5, 5X, 'CM.2 SEC.-1', //)

11 FORMAT (1X, '**** THE FOLLOWING ARE THE WELDING CONDITIONS ****', //)

1 //)

12 FORMAT (1X, 'VOLTAGE =', 13X, F10.1, 5X, 'VOLTS', //)

13 FORMAT (1X, 'AMPERAGE =', 12X, F10.0, 5X, 'AMPS', //)

14 FORMAT (1X, 'HEAT INPUT PER UNIT THICKNESS', 2X, F10.0, 'CAL. SEC.-1', //)

15 FORMAT (1X, 'PLATE THICKNESS =', 5X, F10.2, 5X, 'CM.', //)

16 FORMAT (1X, 'SPECIFIC POWER INPUT =', F10.0, 'KCAL. CM.-1', //)

17 FORMAT (1X, 'HEAT INPUT AT', 2X, F4.2, 2X, '=' , 2X, F6.0, 2X, 'CAL. SEC.-1CM.

1-1', //)

18 FORMAT (1X, 'SURFACE HEAT TRANSFER COEFFICIENT =', F10.3, 5X, 'CAL. CM.

1-2. SEC.-1 DEG. C.-1', //)

```

19 FORMAT(1X,'THE THREE HEAT SOURCES IN CAL. CM.-1SEC.-1 ARE:',////)
20 FORMAT(1X,10X,'Q(1)',10X,'Q(2)',10X,'Q(3)',//,3P10.0)
21 FORMAT(1X,'WELDING VELOCITY = ',5X,F8.5,5X,'CM. SEC.-1',////)
22 FORMAT(1X,'SLAG DEPTH = ',10X,F4.2,5X,'CM',/)
23 FORMAT(1X,'POOL DEPTH = ',10X,F4.2,5X,'CM',/)
24 FORMAT(1X,'IMMERSION = ',10X,F4.2,5X,'CM',/)
25 FORMAT(1X,'ELECTRODE GAP = ',8X,F4.2,5X,'CM',////)
26 FORMAT(1X,'THE RELATIVE POSITION OF THE HEAT SOURCES :',////)
27 FORMAT(1X,'Q(1)',2X,F6.3,2X,'CM',/,1X,'Q(2)',2X,F6.3,2X,'CM',/,1
1 X,'Q(3)',2X,F6.3,2X,'CM',////)
28 FORMAT(1X,'THE RELATIVE TIMES OF THE HEAT SOURCES :',////)
29 FORMAT(1X,'Q(1)',2X,F6.1,2X,'SEC',/,1X,'Q(2)',2X,F6.1,2X,'SEC',/,
1 1X,'Q(3)',2X,F6.1,2X,'SEC',////)
30 FORMAT(1H1)
31 FORMAT(1X,'TIME',3X,'POSITION',5X,'THERMOCOUPLE POSITION',/,1X,'SE
1CONDS',3X,'CM',3X,' ONE CENTIMETER INTERVALS ',//)
32 FORMAT(1X,E10.2,4X,F8.3,4X,10F8.0)
END
SUBROUTINE DRAWC(TEMP, POSN, J, Y)
DIMENSION TEMP(4,200), POSN(200), T(4), Y(10), TEMPI(200,4)
C
C DO 20 K=1,200
C
C DO 10 J=1,8
C TEMPI(K,J)=TEMP(J,K)
10 CONTINUE
C
C 20 CONTINUE
C
C XMIN=POSN(1)
C
C DO 30 K=1,200
C POSN(K)=POSN(K)-XMIN
30 CONTINUE
C
C XMIN=POSN(1)
C XMAX=POSN(200)
C DX=(XMAX-XMIN)/10.
C YMIN=0.0
C YMAX=5.0
C AMELT1=723.
C AMELT2=1450.
C
C DY=5./7.
C DO 40 K=1,200
C POSN(K)=(POSN(K)-XMIN)/DX
40 CONTINUE
C
C DO 45 J=1,4
C Y(J)=Y(J)/DY
45 CONTINUE
C CALL AXIS(0.,0.,'POSITION ALONG WELD CENTERLINE',-30,10.,0.,
1 XMIN,-DX)
C CALL AXIS(0.,0.,'DISTANCE FROM WELD CENTERLINE',29,7.,90.,YMIN,
1 DY)
C CALL CNTOUR(POSN,200,Y,4,TEMPI,200,AMELT1,4.,AMELT1)
C CALL CNTOUR(POSN,200,Y,4,TEMPI,200,AMELT2,4.,AMELT2)
C DO 70 K=1,200

```

```
      POSN (K) = POSN (K) * DX
70  CONTINUE
      DO 80 J=1,4
      Y (J) = Y (J) * DY
80  CONTINUE
      RETURN
      END
      SUBROUTINE ALABL (NUMRUN, V, AMP, SD, E, PD, VW, AA, DELTA, Q44)
      RUNNUM = FLOAT (NUMRUN)
      HT = .07
      BE = AA + 2.25
      CC = BB + 0.5
      CALL SYMBOL (AA, 6.5, HT, 'EXP NUMBER', 0., 10)
      CALL NUMBER (BB, 6.5, HT, RUNNUM, 0., - 1)
      CALL SYMBOL (AA, 6.25, HT, 'VOLTAGE', 0., 7)
      CALL SYMBOL (CC, 6.25, HT, 'VOLTS', 0., 5)
      CALL NUMBER (BB, 6.25, HT, V, 0., - 1)
      CALL SYMBOL (AA, 6.0, HT, 'AMPERAGE', 0., 8)
      CALL SYMBOL (CC, 6.0, HT, 'AMPS', 0., 4)
      CALL NUMBER (BB, 6.0, HT, AMP, 0., - 1)
      CALL SYMBOL (AA, 5.75, HT, 'SLAG DEPTH', 0., 10)
      CALL SYMBOL (CC, 5.75, HT, 'CM.', 0., 3)
      CALL NUMBER (BB, 5.75, HT, SD, 0., 2)
      CALL SYMBOL (AA, 5.5, HT, 'IMMERSION', 0., 9)
      CALL SYMBOL (CC, 5.5, HT, 'CM.', 0., 3)
      CALL NUMBER (BB, 5.5, HT, E, 0., 2)
      CALL SYMBOL (AA, 5.25, HT, 'POOL DEPTH', 0., 10)
      CALL SYMBOL (CC, 5.25, HT, 'CM.', 0., 3)
      CALL NUMBER (BB, 5.25, HT, PD, 0., 2)
      CALL SYMBOL (AA, 5.0, HT, 'WELD VELOCITY', 0., 13)
      CALL SYMBOL (CC, 5.0, HT, 'CM. SEC-1', 0., 8)
      CALL NUMBER (BB, 5.0, HT, VW, 0., 3)
      CALL SYMBOL (AA, 4.75, HT, 'THICKNESS', 0., 9)
      CALL SYMBOL (CC, 4.75, HT, 'CM.', 0., 3)
      CALL NUMBER (BB, 4.75, HT, DELTA, 0., 2)
      CALL SYMBOL (AA, 4.5, HT, 'SPECIFIC POWER INPUT', 0., 20)
      CALL SYMBOL (CC, 4.5, HT, 'KCAL. CM.-1', 0., 10)
      CALL NUMBER (BB, 4.5, HT, Q44, 0., - 1)
      RETURN
      END
      SUBROUTINE OUTPLT (TEMP, POSN, VW)
      DIMENSION TEMP (10, 200), POSN (200), Y (10), TIME (200), W (200)
C
      DO 10 K=1, 200
          TIME (K) = POSN (K) / VW
10  CONTINUE
C
      XMIN = TIME (1)
      XMAX = TIME (200)
C
      DO 20 K=1, 200
          TIME2 (K) = TIME (K) - XMIN
20  CONTINUE
C
      XMIN = TIME (1)
      XMAX = TIME (200)
      DX = (XMAX - XMIN) / 10.
```

C

```
DO 30 K=1,200  
    TIME(K)=TIME(K)/DX
```

30 CONTINUE

C

```
YMIN=0.0  
YMAX=1400.  
DY=200.  
CALL PLOT(14.,0., - 3)  
CALL AXIS(0.,0., 'TIME IN SECONDS', - 15,10.,0.,XMIN,DX)  
CALL AXIS(0.,0., 'TEMP. IN DEG. C.', 15,7.,90.,YMIN,DY)
```

C

```
DO 50 J=1,8
```

C

```
    DO 40 K=1,200  
        W(K)=TEMP(J,K)/DY
```

40

```
    CONTINUE
```

C

```
        CALL LINE(TIME,W,200, + 1)
```

50 CONTINUE

C

```
RETURN  
END
```

C.3 THEORY Program Output

The complete output data from a computer run of THEORY results in the creation of two files and two printer plotter outputs. The listing of two example files 05S and 05S1 and the corresponding printer plottings follow below (this output is for experiment P05).

1	*****
2	
3	5
4	
5	*****
6	
7	
8	
9	
10	**** THE FOLLOWING ARE THE THERMOPHYSICAL PROPERTIES ****
11	
12	
13	
14	
15	DENSITY = 7.50GM.CM.-3
16	
17	
18	
19	
20	THERMAL CONDUCTIVITY = 0.1000CAL.SEC.-1CM.-1CEG.C.-1
21	
22	
23	
24	
25	SPECIFIC HEAT= 0.16300CAL.GM.-1CEG.C.-1
26	
27	
28	
29	
30	THERMAL DIFFUSIVITY = 0.08180 CM.2 SEC.-1
31	
32	
33	
34	
35	**** THE FOLLOWING ARE THE WELDING CONDITIONS ****
36	
37	
38	
39	
40	VOLTAGE = 42.0 VOLTS
41	
42	
43	
44	
45	AMPERAGE = 490. AMPS
46	
47	
48	
49	
50	HEAT INPUT PER UNIT THICKNESS 575.CAL.SEC.-1
51	

52	PLATE THICKNESS =	3.18	CM.
53			
54			
55			
56			
57	SPECIFIC POWER INPUT =	353.	KCAL.CM.-1
58			
59			
60			
61			
62	HEAT INPUT AT C.37 =	1828.	CAL.SEC.-1CM.-1
63			
64			
65			
66			
67	SURFACE HEAT TRANSFER COEFFICIENT =	0.500E-03	CAL.CM.-2.SEC.-1 DEG.C.-1
68			
69			
70			
71			
72	THE THREE HEAT SOURCES IN CAL.CM.-1SEC.-1 ARE:		
73			
74			
75			
76			
77		Q(1)	Q(2)
78			Q(3)
79		229.	457.
80	WELDING VELOCITY =	0.01400	CM.SEC.-1
81			
82			
83			
84			
85	SLUG DEPTH =	3.18	CM
86			
87	POOL DEPTH =	1.60	CM
88			
89	IMMERSION =	0.93	CM
90			
91	ELECTRODE GAP =	2.25	CM
92			
93			
94			
95			
96	THE RELATIVE POSITION OF THE HEAT SOURCES :		
97			
98			
99			
100			
101	Q(1)	-2.055	CM
102	Q(2)	0.0	CM.
103	Q(3)	1.525	CM.
104			
105			
106			
107			
108	THE RELATIVE TIMES OF THE HEAT SOURCES :		
109			
110			
111			

112
 113 Q(1) -146.8 SEC
 114 Q(2) C.O SEC
 115 Q(3) 137.5 SEC
 116
 117

118
 119
 ENC OF FILE

BL C551						
1	2	3	4	5	6	7
	TIME	POSITION	THERMOCOUPLE POSITION			
	SECONDS	CM	ONE CENTIMETER INTERVALS			
4						
5						
6	0.15E+C4	21.000	40.	40.	40.	40.
7	0.15E+C4	20.720	41.	41.	41.	40.
8	0.15E+C4	20.440	42.	42.	42.	41.
9	0.16E+C4	20.160	43.	43.	43.	42.
10	0.16E+C4	19.880	44.	44.	44.	43.
11	0.16E+C4	19.600	45.	45.	45.	45.
12	0.16E+C4	19.320	46.	46.	46.	46.
13	0.16E+C4	19.040	48.	48.	47.	47.
14	0.17E+C4	18.760	49.	49.	49.	48.
15	0.17E+C4	18.480	51.	50.	50.	50.
16	0.17E+C4	18.200	52.	52.	52.	51.
17	0.17E+C4	17.920	54.	54.	53.	53.
18	0.17E+C4	17.640	56.	55.	55.	55.
19	0.18E+C4	17.360	58.	57.	57.	56.
20	0.18E+C4	17.080	60.	59.	59.	58.
21	0.18E+C4	16.800	62.	61.	61.	60.
22	0.18E+C4	16.520	64.	64.	63.	62.
23	0.18E+C4	16.240	66.	66.	65.	65.
24	0.19E+C4	15.960	69.	69.	68.	67.
25	0.19E+C4	15.680	72.	71.	71.	70.
26	0.19E+C4	15.400	75.	74.	73.	73.
27	0.19E+C4	15.120	78.	77.	76.	76.
28	0.19E+C4	14.840	81.	80.	80.	79.
29	0.20E+C4	14.560	85.	84.	83.	82.
30	0.20E+C4	14.280	88.	88.	87.	85.
31	0.20E+C4	14.000	92.	92.	91.	89.
32	0.20E+C4	13.720	97.	96.	95.	93.
33	0.20E+C4	13.440	101.	100.	99.	98.
34	0.21E+C4	13.160	106.	105.	104.	102.
35	0.21E+C4	12.880	111.	110.	109.	107.
36	0.21E+C4	12.600	117.	116.	114.	112.
37	0.21E+C4	12.320	123.	121.	120.	117.
38	0.21E+C4	12.040	129.	128.	126.	123.
39	0.22E+C4	11.760	136.	134.	132.	129.
40	0.22E+C4	11.480	143.	141.	139.	136.
41	0.22E+C4	11.200	151.	149.	146.	143.
42	0.22E+C4	10.920	159.	157.	154.	151.
43	0.22E+C4	10.640	168.	166.	162.	159.
44	0.22E+C4	10.360	177.	175.	171.	167.
45	0.23E+C4	10.080	188.	185.	181.	176.
46	0.23E+C4	9.800	196.	195.	191.	186.
47	0.23E+C4	9.520	210.	206.	202.	196.

48	0.23E+04	9.240	223.	215.	213.	207.
49	0.24E+04	8.660	236.	231.	226.	219.
50	0.24E+04	8.680	290.	245.	239.	231.
51	0.24E+04	8.400	266.	260.	253.	245.
52	0.24E+04	8.120	283.	276.	268.	259.
53	0.24E+04	7.640	300.	253.	284.	274.
54	0.25E+04	7.560	320.	312.	302.	290.
55	0.25E+04	7.280	341.	331.	320.	308.
56	0.25E+04	7.000	363.	353.	340.	328.
57	0.25E+04	6.720	387.	375.	361.	345.
58	0.25E+04	6.440	413.	400.	384.	366.
59	0.26E+04	6.160	442.	426.	408.	388.
60	0.26E+04	5.880	472.	455.	434.	411.
61	0.26E+04	5.600	505.	485.	462.	436.
62	0.26E+04	5.320	541.	516.	491.	462.
63	0.26E+04	5.040	580.	553.	522.	490.
64	0.27E+04	4.760	622.	591.	555.	519.
65	0.27E+04	4.480	668.	631.	591.	550.
66	0.27E+04	4.200	718.	674.	628.	582.
67	0.27E+04	3.920	772.	720.	667.	615.
68	0.27E+04	3.640	829.	768.	708.	650.
69	0.28E+04	3.360	891.	819.	750.	685.
70	0.28E+04	3.080	957.	872.	793.	722.
71	0.28E+04	2.800	1025.	926.	838.	755.
72	0.28E+04	2.520	1095.	982.	883.	796.
73	0.28E+04	2.240	1164.	1037.	928.	833.
74	0.29E+04	1.960	1232.	1091.	972.	870.
75	0.29E+04	1.680	1297.	1145.	1016.	906.
76	0.29E+04	1.400	1360.	1196.	1058.	942.
77	0.29E+04	1.120	1420.	1249.	1098.	975.
78	0.29E+04	0.840	1475.	1291.	1136.	1007.
79	0.30E+04	0.560	1533.	1334.	1171.	1037.
80	0.30E+04	0.280	1580.	1371.	1203.	1064.
81	0.30E+04	-0.000	1618.	1403.	1230.	1088.
82	0.30E+04	-0.280	1644.	1428.	1254.	1110.
83	0.30E+04	-0.560	1659.	1446.	1272.	1128.
84	0.31E+04	-0.840	1665.	1456.	1287.	1143.
85	0.31E+04	-1.120	1663.	1464.	1297.	1154.
86	0.31E+04	-1.400	1655.	1465.	1302.	1163.
87	0.31E+04	-1.680	1642.	1460.	1304.	1168.
88	0.31E+04	-1.960	1622.	1451.	1301.	1170.
89	0.32E+04	-2.240	1596.	1437.	1296.	1170.
90	0.32E+04	-2.520	1565.	1415.	1287.	1167.
91	0.32E+04	-2.800	1531.	1395.	1275.	1161.
92	0.32E+04	-3.080	1494.	1376.	1261.	1154.
93	0.32E+04	-3.360	1456.	1351.	1246.	1145.
94	0.33E+04	-3.640	1419.	1325.	1229.	1135.
95	0.33E+04	-3.920	1382.	1295.	1211.	1123.
96	0.33E+04	-4.200	1347.	1273.	1192.	1110.
97	0.33E+04	-4.480	1314.	1247.	1173.	1097.
98	0.33E+04	-4.760	1282.	1222.	1154.	1083.
99	0.34E+04	-5.040	1251.	1197.	1135.	1069.
100	0.34E+04	-5.320	1223.	1173.	1116.	1054.
101	0.34E+04	-5.600	1195.	1150.	1097.	1040.
102	0.34E+04	-5.880	1169.	1128.	1079.	1025.
103	0.34E+04	-6.160	1144.	1106.	1061.	1010.
104	0.35E+04	-6.440	1120.	1085.	1043.	996.
105	0.35E+04	-6.720	1097.	1065.	1026.	982.
106	0.35E+04	-7.000	1075.	1046.	1009.	967.
107	0.35E+04	-7.280	1055.	1027.	993.	953.

108	0.35F+C4	-7.560	1035.	1065.	577.	940.
109	0.36E+C4	-7.840	1015.	961.	561.	926.
110	0.37E+C4	-8.120	937.	975.	546.	913.
111	0.38E+C4	-8.400	975.	558.	522.	900.
112	0.39E+C4	-8.680	962.	942.	517.	886.
113	0.39F+C4	-8.560	948.	527.	503.	873.
114	0.37E+04	-5.240	930.	818.	856.	863.
115	0.37E+C4	-5.520	915.	898.	877.	852.
116	0.37F+C4	-5.000	500.	864.	864.	840.
117	0.37E+04	-10.080	886.	871.	852.	825.
118	0.37E+C4	-10.360	872.	858.	840.	818.
119	0.38E+C4	-10.540	859.	842.	829.	807.
120	0.38F+04	-10.520	846.	832.	816.	796.
121	0.38E+C4	-11.200	833.	821.	805.	786.
122	0.38E+C4	-11.480	821.	810.	794.	776.
123	0.38F+C4	-11.760	810.	798.	764.	764.
124	0.39E+C4	-12.040	798.	787.	773.	756.
125	0.39E+04	-12.320	787.	777.	763.	747.
126	0.39E+C4	-12.600	776.	766.	753.	738.
127	0.39E+C4	-12.880	766.	756.	744.	729.
128	0.39E+C4	-13.160	755.	744.	734.	720.
129	0.40E+04	-13.440	745.	737.	725.	711.
130	0.40E+C4	-13.720	736.	727.	716.	703.
131	0.40F+04	-14.000	726.	718.	707.	694.
132	0.40E+C4	-14.280	717.	709.	699.	686.
133	0.40E+C4	-14.560	708.	700.	690.	678.
134	0.41E+C4	-14.840	699.	692.	682.	671.
135	0.41E+C4	-15.120	690.	683.	674.	663.
136	0.41E+C4	-15.400	682.	675.	666.	655.
137	0.41E+04	-15.680	674.	667.	658.	648.
138	0.41E+C4	-15.960	666.	659.	651.	641.
139	0.42E+C4	-16.240	658.	652.	644.	634.
140	0.42E+C4	-16.520	650.	644.	636.	627.
141	0.42E+C4	-16.800	643.	637.	629.	620.
142	0.42E+04	-17.080	635.	630.	622.	613.
143	0.42E+C4	-17.360	628.	623.	615.	607.
144	0.43E+C4	-17.640	621.	616.	608.	600.
145	0.43E+04	-17.920	614.	609.	602.	594.
146	0.43E+C4	-18.200	607.	602.	596.	588.
147	0.43E+04	-18.480	600.	595.	588.	582.
148	0.43E+C4	-18.760	594.	589.	583.	576.
149	0.44E+C4	-19.040	588.	583.	577.	570.
150	0.44E+C4	-19.320	581.	577.	571.	564.
151	0.44E+C4	-19.600	575.	571.	565.	558.
152	0.44E+04	-19.880	569.	565.	559.	553.
153	0.44E+C4	-20.160	563.	559.	554.	547.
154	0.45E+C4	-20.440	557.	553.	548.	542.
155	0.45E+C4	-20.720	551.	547.	543.	536.
156	0.45E+04	-21.000	546.	542.	537.	531.
157	0.45E+C4	-21.280	540.	537.	532.	526.
158	0.45E+04	-21.560	535.	531.	526.	521.
159	0.46E+C4	-21.840	530.	526.	521.	516.
160	0.46E+C4	-22.120	524.	520.	515.	511.
161	0.46E+04	-22.400	519.	515.	512.	506.
162	0.46E+C4	-22.680	514.	511.	507.	501.
163	0.46E+04	-22.960	509.	506.	502.	497.
164	0.47E+04	-23.240	504.	501.	497.	492.
165	0.47E+C4	-23.520	499.	496.	492.	488.
166	0.47E+04	-23.800	495.	492.	488.	483.
167	0.47E+04	-24.080	490.	487.	483.	478.

168	0.47E+04	-24,360	485.	482.	475.	474.
169	0.48E+04	-24,640	481.	476.	474.	470.
170	0.48E+04	-24,520	476.	474.	470.	466.
171	0.48E+04	-25,200	475.	469.	466.	462.
172	0.48E+04	-25,480	467.	465.	462.	457.
173	0.48E+04	-25,760	463.	461.	457.	453.
174	0.49E+04	-26,040	459.	457.	453.	449.
175	0.49E+04	-26,320	455.	452.	449.	445.
176	0.49E+04	-26,600	451.	448.	445.	442.
177	0.49E+04	-26,880	447.	444.	441.	438.
178	0.49E+04	-27,160	443.	441.	438.	436.
179	0.50E+04	-27,440	439.	437.	434.	430.
180	0.50E+04	-27,720	435.	433.	430.	427.
181	0.50E+04	-28,000	431.	428.	426.	423.
182	0.50E+04	-28,280	427.	425.	423.	419.
183	0.50E+04	-28,560	424.	422.	418.	416.
184	0.51E+04	-28,840	420.	418.	415.	412.
185	0.51E+04	-29,120	416.	415.	412.	409.
186	0.51E+04	-29,400	413.	411.	409.	405.
187	0.51E+04	-29,680	409.	406.	405.	402.
188	0.51E+04	-29,960	406.	404.	402.	399.
189	0.52E+04	-30,240	403.	401.	398.	395.
190	0.52E+04	-30,520	399.	397.	395.	392.
191	0.52E+04	-30,800	396.	394.	392.	389.
192	0.52E+04	-31,080	393.	391.	389.	386.
193	0.52E+04	-31,360	389.	388.	385.	383.
194	0.53E+04	-31,640	386.	384.	382.	380.
195	0.53E+04	-31,920	383.	381.	379.	377.
196	0.53E+04	-32,200	380.	378.	376.	374.
197	0.53E+04	-32,480	377.	375.	373.	371.
198	0.53E+04	-32,760	374.	372.	370.	368.
199	0.54E+04	-33,040	371.	369.	367.	365.
200	0.54E+04	-33,320	368.	366.	364.	362.
201	0.54E+04	-33,600	365.	363.	361.	359.
202	0.54E+04	-33,880	362.	360.	359.	356.
203	0.54E+04	-34,160	359.	358.	356.	354.
204	0.55E+04	-34,440	356.	355.	353.	351.
205	0.55E+04	-34,720	353.	352.	350.	348.
206	0.55E+04	-35,000	351.	349.	348.	345.
207	0.55E+04	-35,280	348.	347.	345.	343.
208	0.55E+04	-35,560	345.	344.	342.	340.
209	0.56E+04	-35,840	343.	341.	340.	338.
210	0.56E+04	-36,120	340.	339.	337.	335.
211	0.56E+04	-36,400	337.	336.	335.	333.
212	0.56E+04	-36,680	335.	334.	332.	330.
213	0.56E+04	-36,960	332.	331.	329.	328.
214	0.57E+04	-37,240	330.	329.	327.	325.
215	0.57E+04	-37,520	327.	326.	325.	323.
216	0.57E+04	-37,800	325.	324.	322.	320.
217	0.57E+04	-38,080	322.	321.	320.	318.
218	0.57E+04	-38,360	320.	319.	317.	316.
219	0.58E+04	-38,640	317.	316.	315.	313.
220	0.58E+04	-38,920	315.	314.	313.	311.
221	0.58E+04	-39,200	313.	312.	310.	309.
222	0.58E+04	-39,480	310.	309.	308.	307.
223	0.59E+04	-39,760	308.	307.	306.	304.
224	0.59E+04	-40,040	306.	305.	304.	302.
225	0.59E+04	-40,320	304.	303.	301.	300.
226	0.59E+04	-40,600	302.	301.	299.	298.
227	0.59E+04	-40,880	299.	298.	297.	295.

228	0.55E+04	-41,160	291.	256.	255.	254.
229	0.60E+04	-41,440	295.	254.	253.	251.
230	0.66E+04	-41,720	293.	252.	251.	285.
231	0.60E+04	-42,000	291.	250.	248.	287.
232	0.66E+04	-42,280	289.	248.	247.	285.
233	0.60E+04	-42,560	287.	246.	245.	283.
234	0.61E+04	-42,840	285.	244.	243.	281.
235	0.61E+04	-43,120	283.	242.	241.	279.
236	0.61E+04	-43,400	281.	240.	239.	277.
237	0.61E+04	-43,680	279.	238.	237.	276.
238	0.61E+04	-43,960	277.	236.	235.	274.
239	0.65E+04	-44,240	275.	234.	233.	272.
240	0.62E+04	-44,520	273.	232.	231.	270.
241	0.62E+04	-44,800	271.	230.	229.	268.
242	0.62E+04	-45,080	269.	228.	227.	266.
243	0.63E+04	-45,360	267.	226.	225.	264.
244	0.63E+04	-45,640	265.	224.	223.	263.
245	0.63E+04	-45,920	263.	222.	221.	261.
246	0.63E+04	-46,200	261.	220.	219.	259.
247	0.63E+04	-46,480	259.	218.	217.	257.
248	0.63E+04	-46,760	257.	216.	215.	255.
249	0.64E+04	-47,040	255.	214.	213.	253.
250	0.64E+04	-47,320	253.	212.	211.	251.
251	0.64E+04	-47,600	251.	210.	209.	249.
252	0.64E+04	-47,880	249.	208.	207.	247.
253	0.64E+04	-48,160	247.	206.	205.	245.
254	0.65E+04	-48,440	245.	204.	203.	243.
255	0.65E+04	-48,720	243.	202.	201.	241.
256	0.65E+04	-49,000	241.	200.	199.	239.
257	0.65E+04	-49,280	239.	198.	197.	237.
258	0.65E+04	-49,560	237.	196.	195.	235.
259	0.66E+04	-49,840	235.	194.	193.	233.
260	0.66E+04	-50,120	233.	192.	191.	231.
261	0.66E+04	-50,400	231.	190.	189.	229.
262	0.66E+04	-50,680	229.	188.	187.	227.
263	0.66E+04	-50,960	227.	186.	185.	225.
264	0.67E+04	-51,240	225.	184.	183.	223.
265	0.67E+04	-51,520	223.	182.	181.	221.
266	0.67E+04	-51,800	221.	180.	179.	219.
267	0.67E+04	-52,080	219.	178.	177.	217.
268	0.67E+04	-52,360	217.	176.	175.	215.
269	0.68E+04	-52,640	215.	174.	173.	213.
270	0.68E+04	-52,920	213.	172.	171.	211.
271	0.68E+04	-53,200	211.	170.	169.	209.
272	0.68E+04	-53,480	209.	168.	167.	207.
273	0.68E+04	-53,760	207.	166.	165.	205.
274	0.69E+04	-54,040	205.	164.	163.	203.
275	0.69E+04	-54,320	203.	162.	161.	201.
276	0.69E+04	-54,600	201.	160.	159.	199.
277	0.69E+04	-54,880	199.	158.	157.	197.
278	0.69E+04	-55,160	197.	156.	155.	195.
279	0.70E+04	-55,440	195.	154.	153.	193.
280	0.70E+04	-55,720	193.	152.	151.	191.
281	0.70E+04	-56,000	191.	150.	149.	189.
282	0.70E+04	-56,280	189.	148.	147.	187.
283	0.70E+04	-56,560	187.	146.	145.	185.
284	0.71E+04	-56,840	185.	144.	143.	183.
285	0.71E+04	-57,120	183.	142.	141.	181.
286	0.71E+04	-57,400	181.	140.	139.	179.
287	0.71E+04	-57,680	179.	138.	137.	177.

288	0.71E+C4	-57.66C	200.	196.	199.	198.
289	0.72E+C4	-58.240	198.	198.	197.	157.
29C	0.72E+C4	-58.52C	197.	197.	196.	19C.
291	0.72E+C4	-58.80C	196.	19C.	155.	154.
292	0.72E+C4	-59.080	195.	194.	154.	153.
293	0.72E+C4	-59.360	194.	193.	193.	192.
294	0.73E+C4	-59.64C	192.	192.	192.	151.
295	0.73E+C4	-59.920	191.	191.	19C.	19C.
296	0.73E+C4	-60.20C	190.	19C.	189.	189.
297	0.73E+C4	-60.480	189.	189.	188.	188.
298	0.73E+C4	-60.760	188.	187.	187.	186.
299	0.74E+C4	-61.040	187.	186.	186.	185.
300	0.74E+C4	-61.320	186.	185.	185.	184.
301	0.74E+C4	-61.600	185.	184.	184.	183.
302	0.74E+C4	-61.880	183.	183.	183.	182.
303	0.74E+C4	-62.160	182.	182.	182.	181.
304	0.75E+C4	-62.440	181.	181.	180.	180.
305	0.75E+C4	-62.720	180.	18C.	175.	175.

END OF FILE

1R PFINAL1**PRPLOT 5=C5 6=C55 7=0551
EXECUTION BEGINS

** NOTE-- THE FOLLOWING STRING COULD NOT BE PRINTED DUE TO OVERCROWDING OF THE PLOT PAGE.
1450

Distance from Weld Centerline	200	400	600	800	1000	1200	1400	1600	1800	2000	2200	2400	2600	2800	3000	3200	3400	3600	3800	4000	4200	4400	4600	4800	5000		
5.0-																											
4.5-																											
4.0-																											
3.5-																											
3.0-																											
2.5-																											
2.0-																											
1.5-																											
1.0-																											
0.5-																											

0.01.....
 0.0 -5.582 -11.163 -16.744 -22.326 -27.507 -33.488 -39.070 -44.651 -50.232 -55.814 -61.395 -6
 POSITION ALONG WELD CENTERLINE

C.4 DROG Program

The DROG program was run in interactive *IF made of fortran and thus the output from this program was not in hard copy. The program is presented below.

```
C      THIS PROGRAM IS USED TO CALCULATE THE IMMERSION
C      THE ELECTRODE DURING ELECTROSLAG WELDING, IF THE
C      FOLLOWING PARAMETERS ARE KNOWN:
C
C          VOLTAGE
C          AMPERAGE
C          OVERALL RESISTANCE (V/I)
C          SLAG RESISTIVITY (RHO)
C          RADIUS OF THE ELECTRODE (RAD)
C
C
C      RHO=0.151
C      RAD=.238
75     READ(5,800,END=999) R,DELR
800    FORMAT(2F10.5)
76     N=0
1      N=N+1
      DP=RHO/(6.283*XL**2)*{1.-ALOG(2.*XL/RAD)}
      P=RHO/(6.283*XL)*ALOG(2.*XL/RAD)-R
      X1=XL-P/DP
      DX=X1-XL
      IF(ABS(DX/X1)-LT.0.01) GO TO 10
      IF(N.GT.50) GO TO 11
      XL=X1
      GO TO 1
10     WRITE(6,2) XL,N,R
2      FORMAT(1X,'IMMERSION IN CM. EQUALS',/F10.5,/, 'N',/I3,
15X,'RESISTANCE=',3X,F10.5)
      GO TO 19
11     WRITE(6,3)
3      FORMAT(1X,'TOO MANY ITERATIONS')
19     R=R+DELR
      IF(R.GT.-03) GO TO 999
      GO TO 76
999    STOP
      END
```

This data (i.e., immersion) was used to calculate the relative positions of the three heat sources and therefore became input data for THEORY. It could easily be incorporated in THEORY and be run simultaneously as a single program.

C.3 Computer Output Considerations

The computer generated data could have been used to generate cooling curves and then these curves could be plotted over a stored CCT curve and then the combined plots could have been used to predict the resultant expected microstructures. A major problem arose because there are few, if any, CCT curves available for the range of grain sizes observed. The cooling times for various temperature ranges for experiment P05 and two positions from the weld counterline are shown:

Temperature Range	Time (2 cm)	Time (4 cm)
900 - 500	1000 sec.	1000 sec.
700 - 500	700 sec.	680 sec.
700 - 600	360 sec.	280 sec.
800 - 500	820 sec.	860 sec.

The cooling rates are not significantly different for the 800-500^o C cooling time and are applicable to a curve that is shifted far to the right. Thus it would be expected that the transformation would not be affected as greatly for these slow cooling rates. Even though CCT curves are not available for the large grain sizes obtained in ESW,

the grain size effect on hardenability is obviously minimized. It should be noted that in the HAZ adjacent to the fusion boundary a bainitic structure was observed (also some retained austenite and some martensite) and thus the curve was shifted very far to the right for large grain sizes.

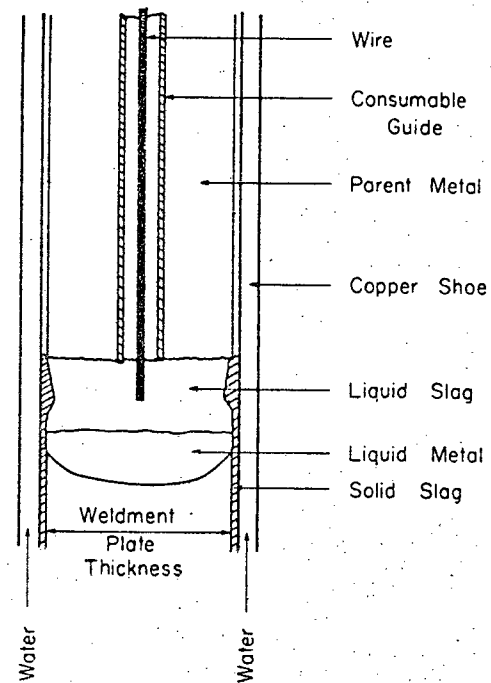
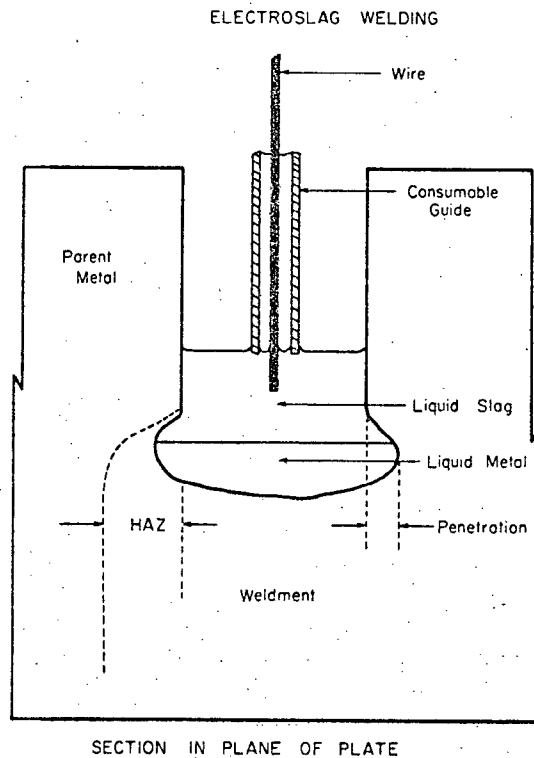


Figure 1 Schematic representations of Consumable Guide Electroslag Welding (CGESW)

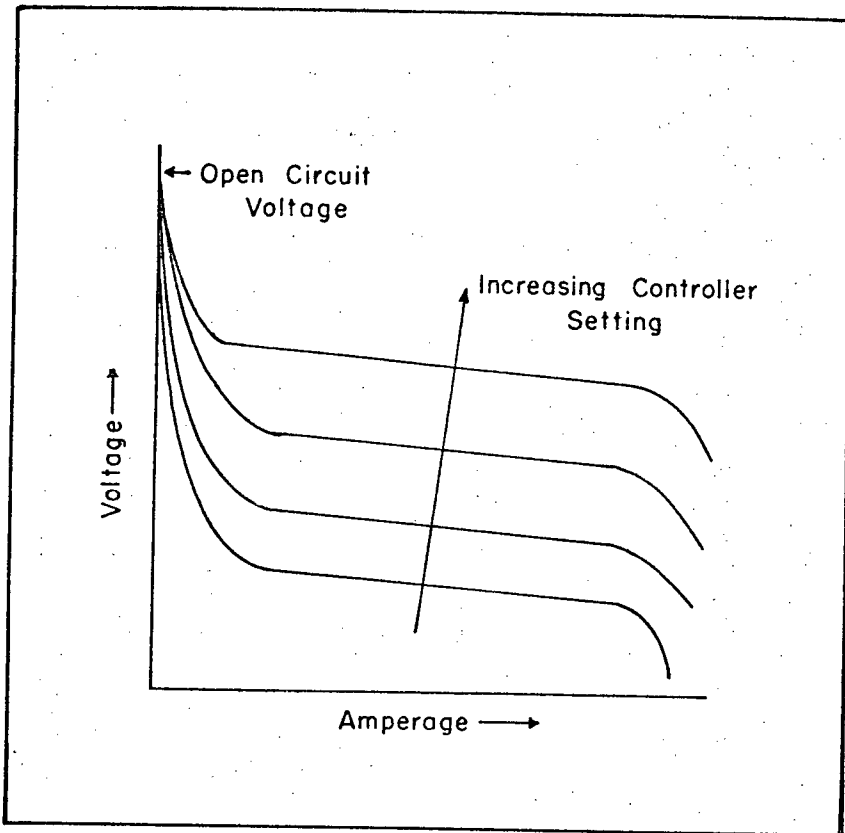
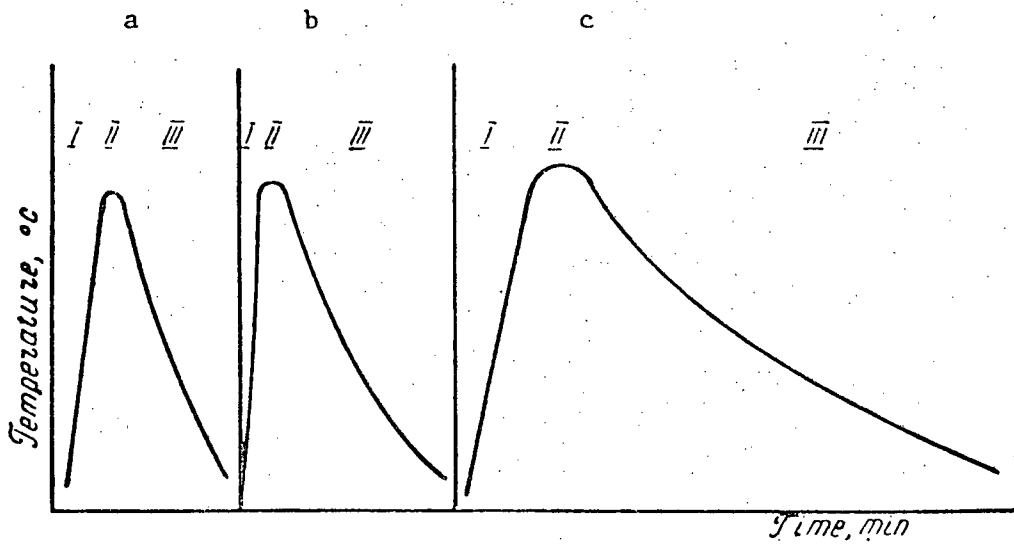


Figure 2 Schematic flat welding characteristic



Thermal cycles in welding with covered electrodes, by submerged arc, and electroslag welding: I—Heating; II—maximum temperature; III—cooling

Figure 3 Schematic comparison of thermal cycles; a, covered electrodes; b, submerged arc; c, ESW (Ref.6)

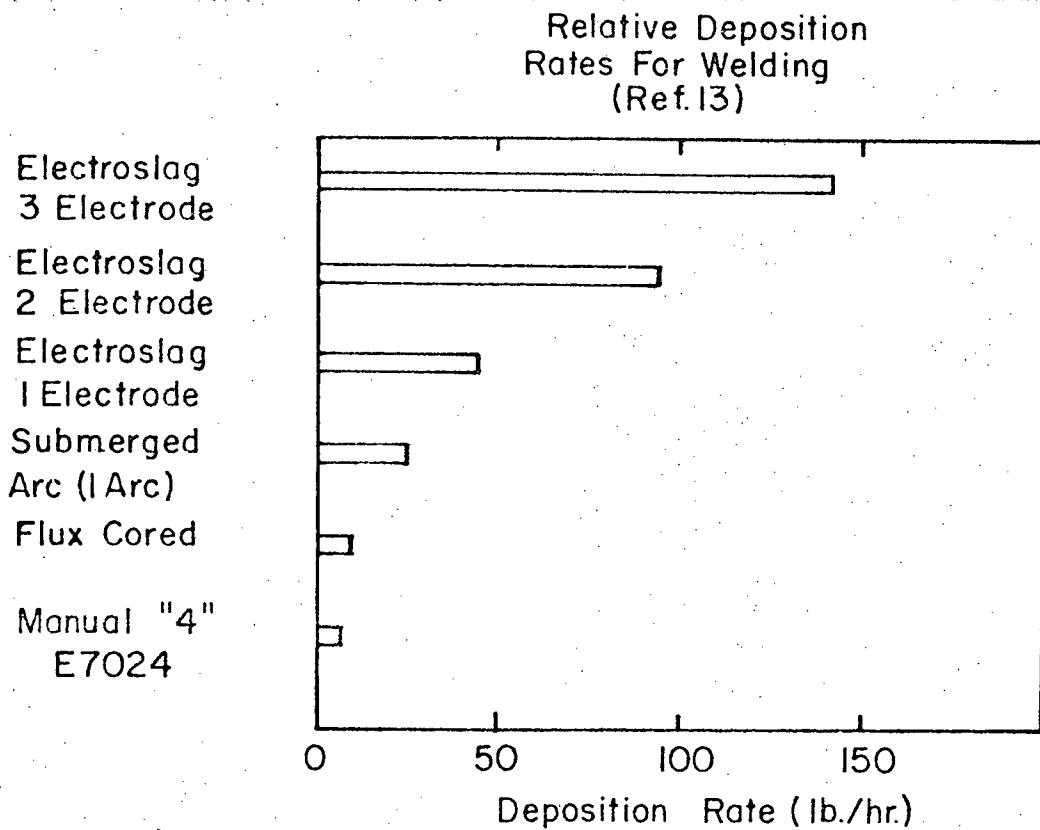
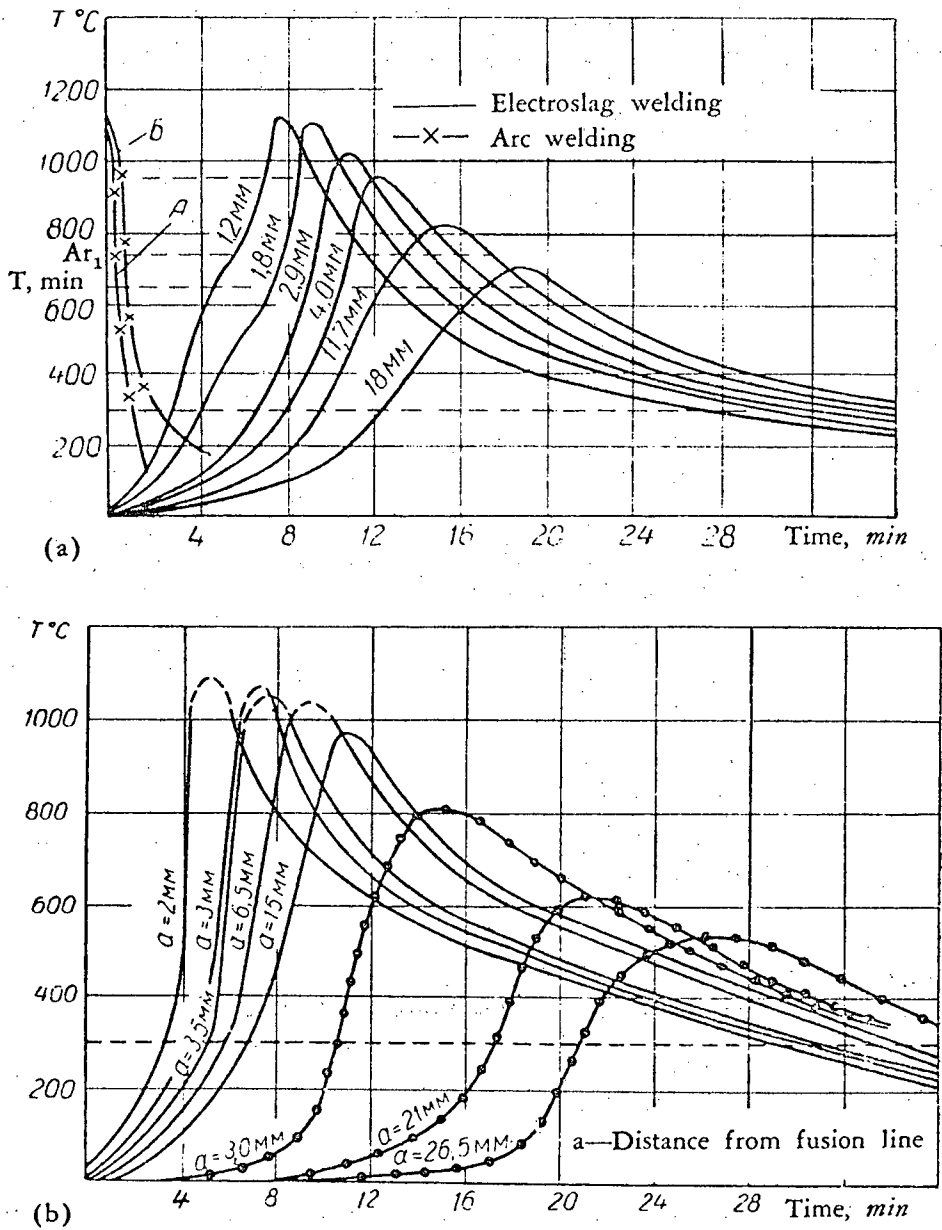


Figure 4 Relative deposition rates for various welding processes (Ref.13)



Thermal cycle: (a) arc and electroslag welding of steel, 100 mm thick, using one electrode; (b) electroslag welding of steel, 100 mm thick, using two electrodes (solid lines), and electroslag welding of same steel using a plate electrode (dotted lines)

Figure 5 Thermal cycles for welding conditions in Table 2 (Ref.1.)

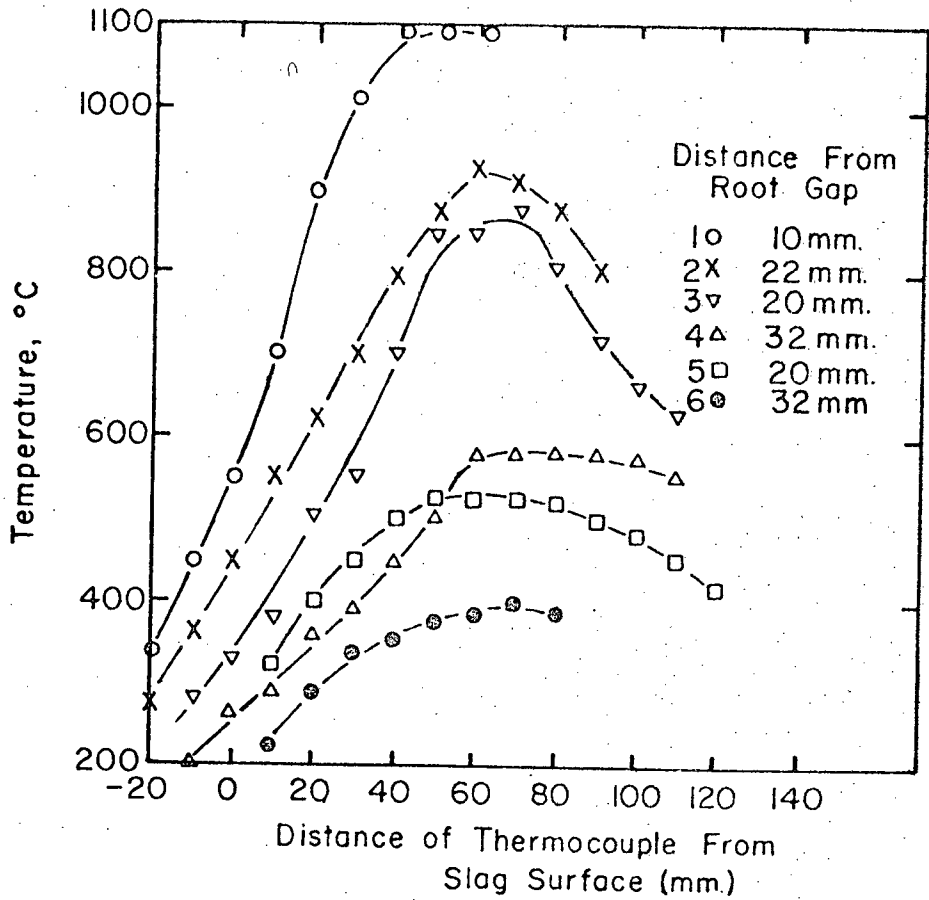


Figure 6 Thermal cycles from Mel-bard (Ref. 15)

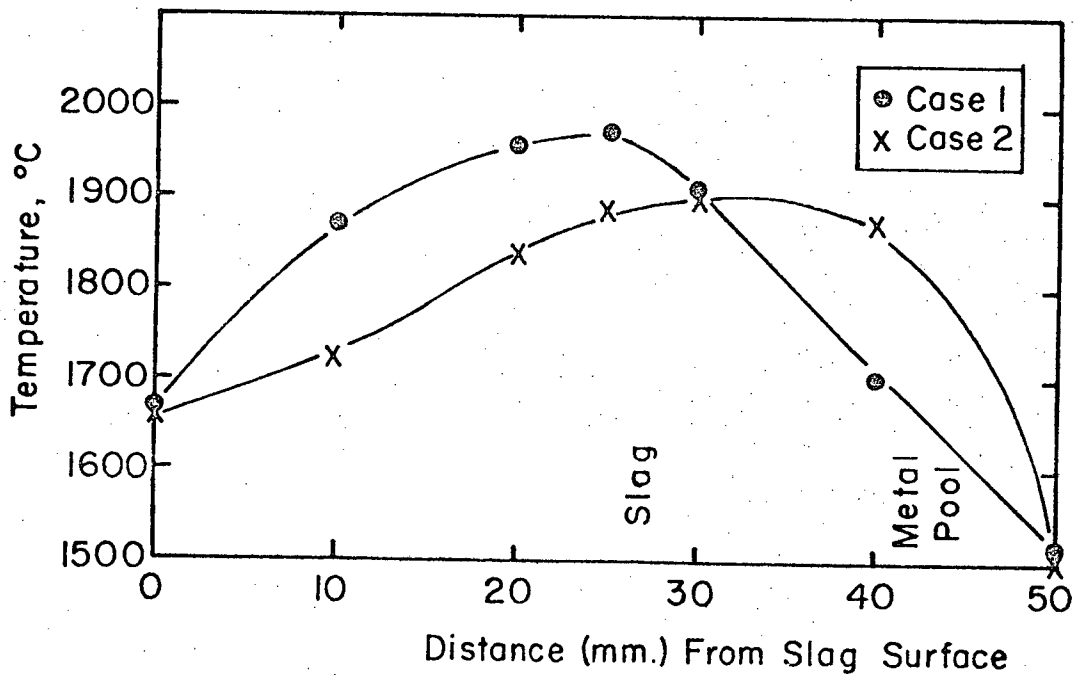
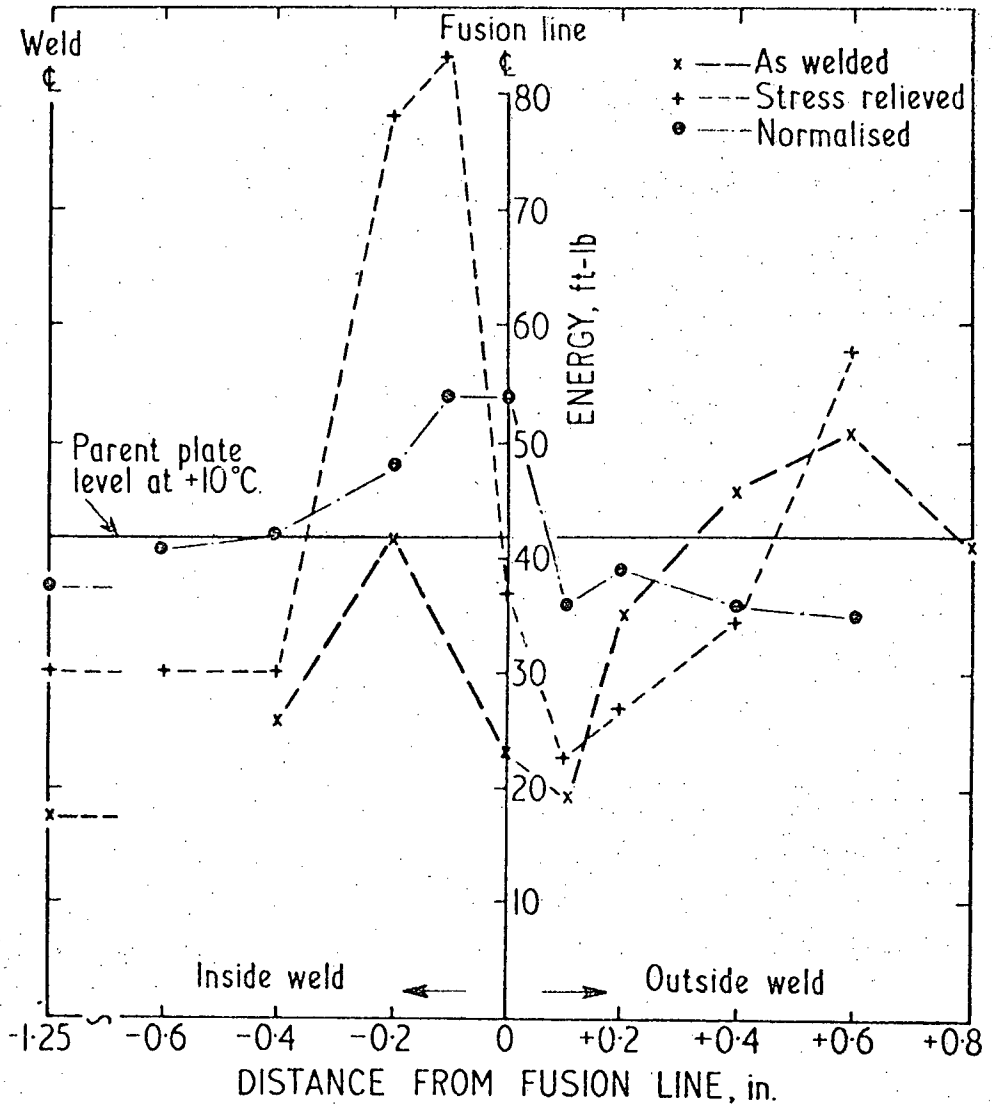


Figure 7 Slag temperatures from Mel-bard (Ref. 15)



Charpy V-notch impact test results for different regions of weld and HAZ, at +10°C.

Figure 8 Charpy impact traverse values for ESW from Woodley et al (Ref.17)

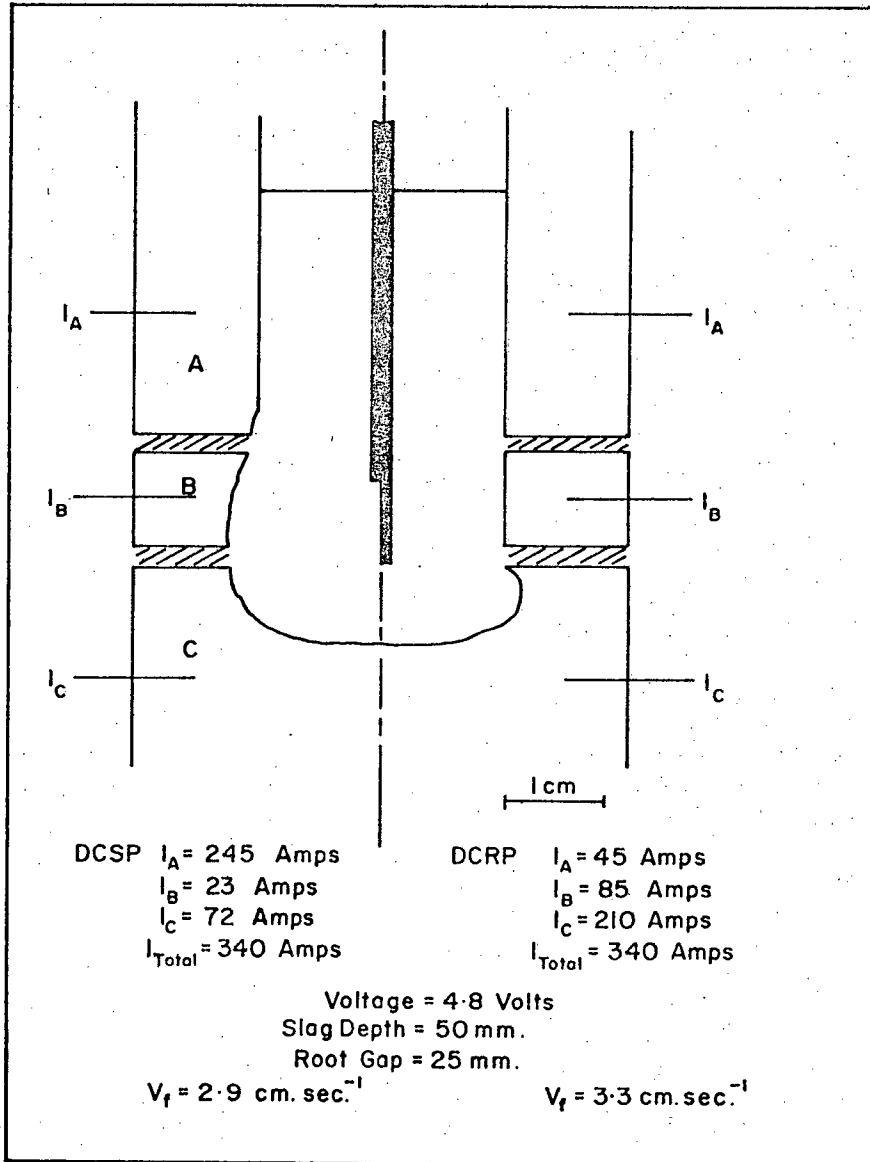


Figure 9 DCRP and DCSP immersion and electrical distribution (Ref. 53)

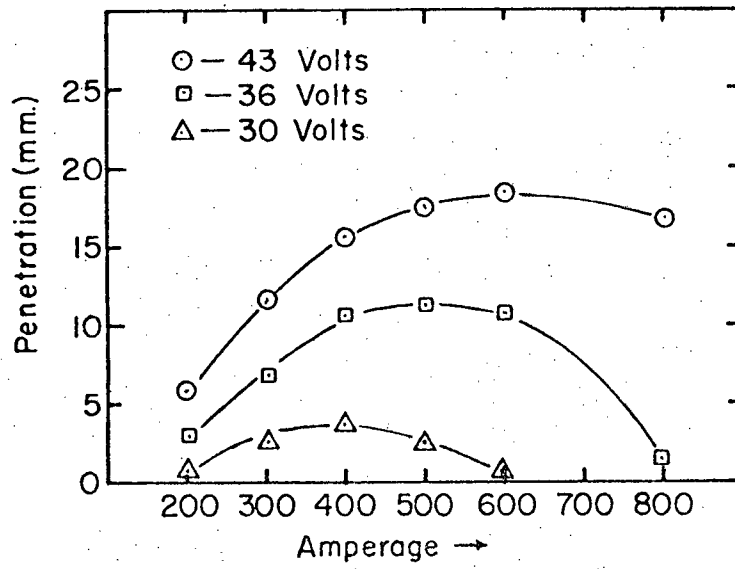


Figure 10 Penetration versus amperage for various voltages (Ref. 54)

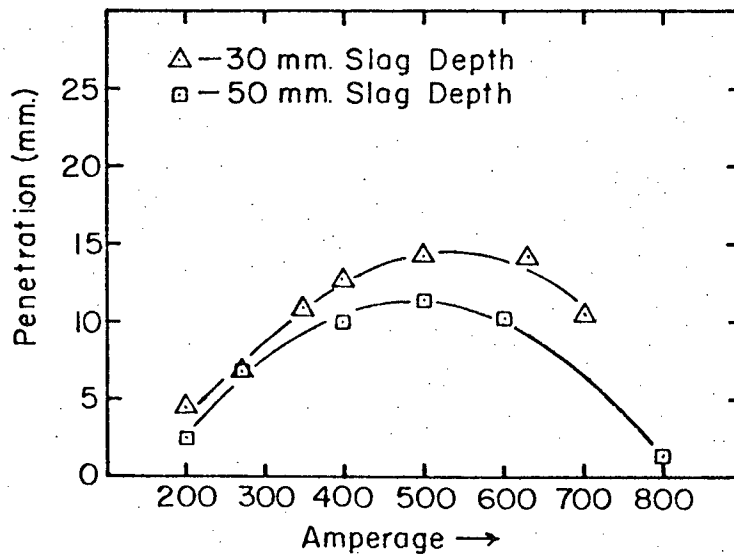


Figure 11 Penetration versus amperage for two slag depths (Ref. 54)

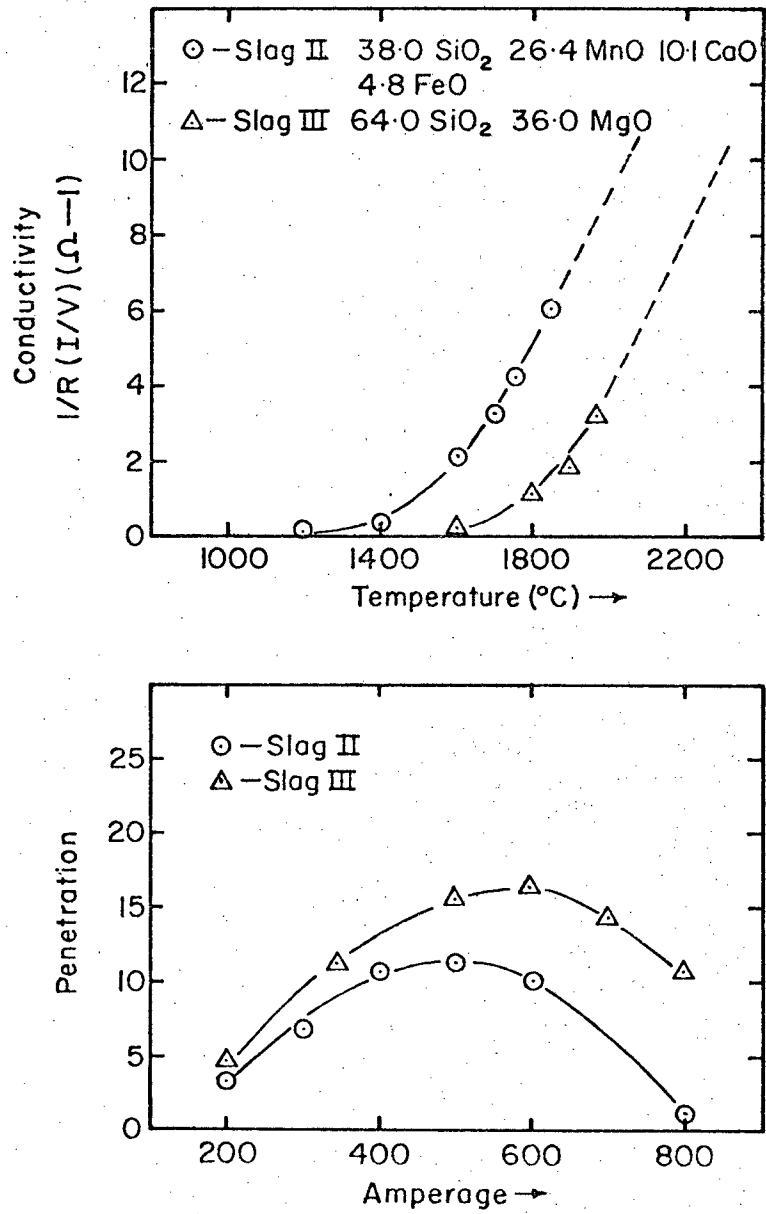


Figure 12 Penetration versus amperage for slags of different conductivity (Ref. 54)

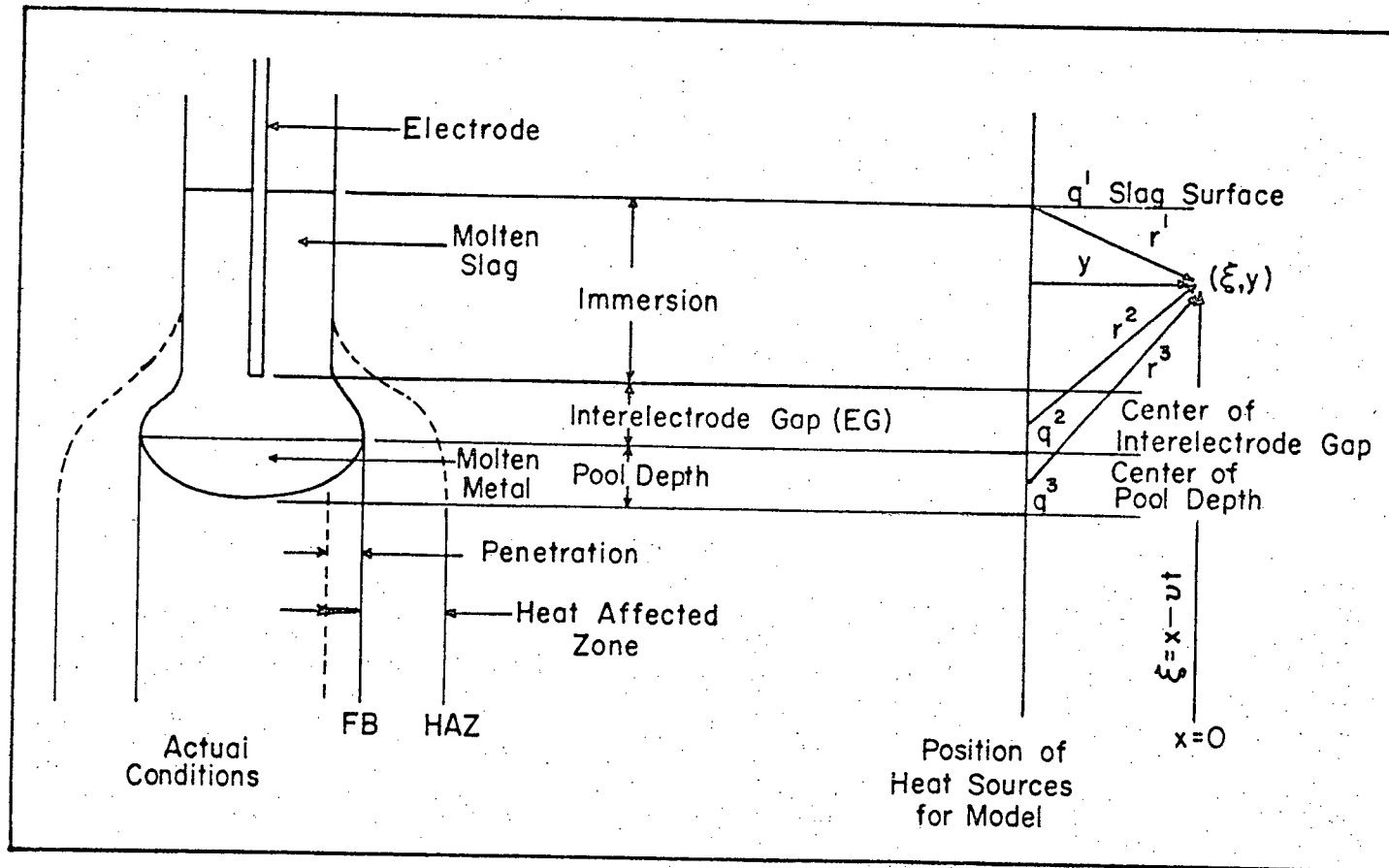
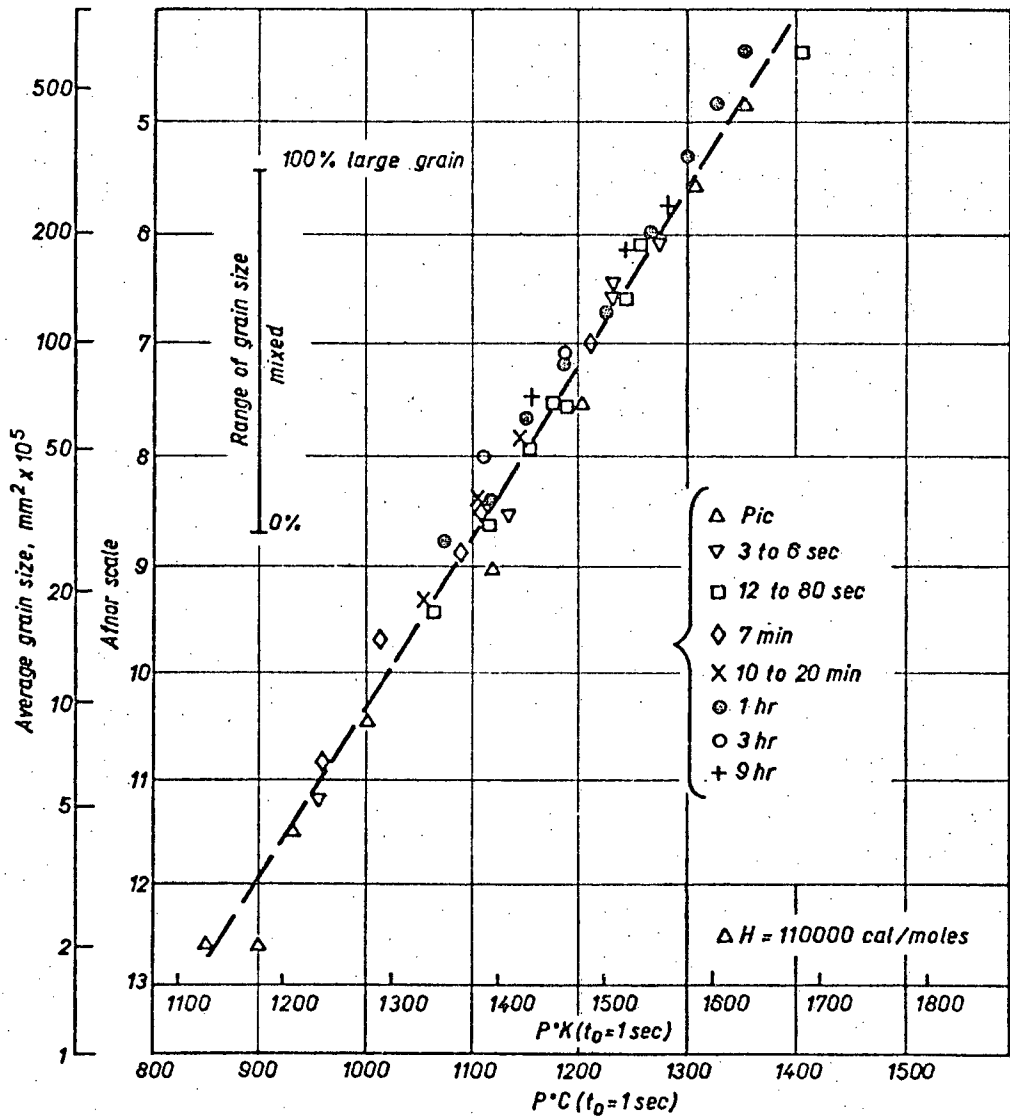


Figure 13 Schematic representation of the analytical model.



Influence of time and temperature on gamma grain size.

Figure 14 Nomograph for determining the austenite grain size

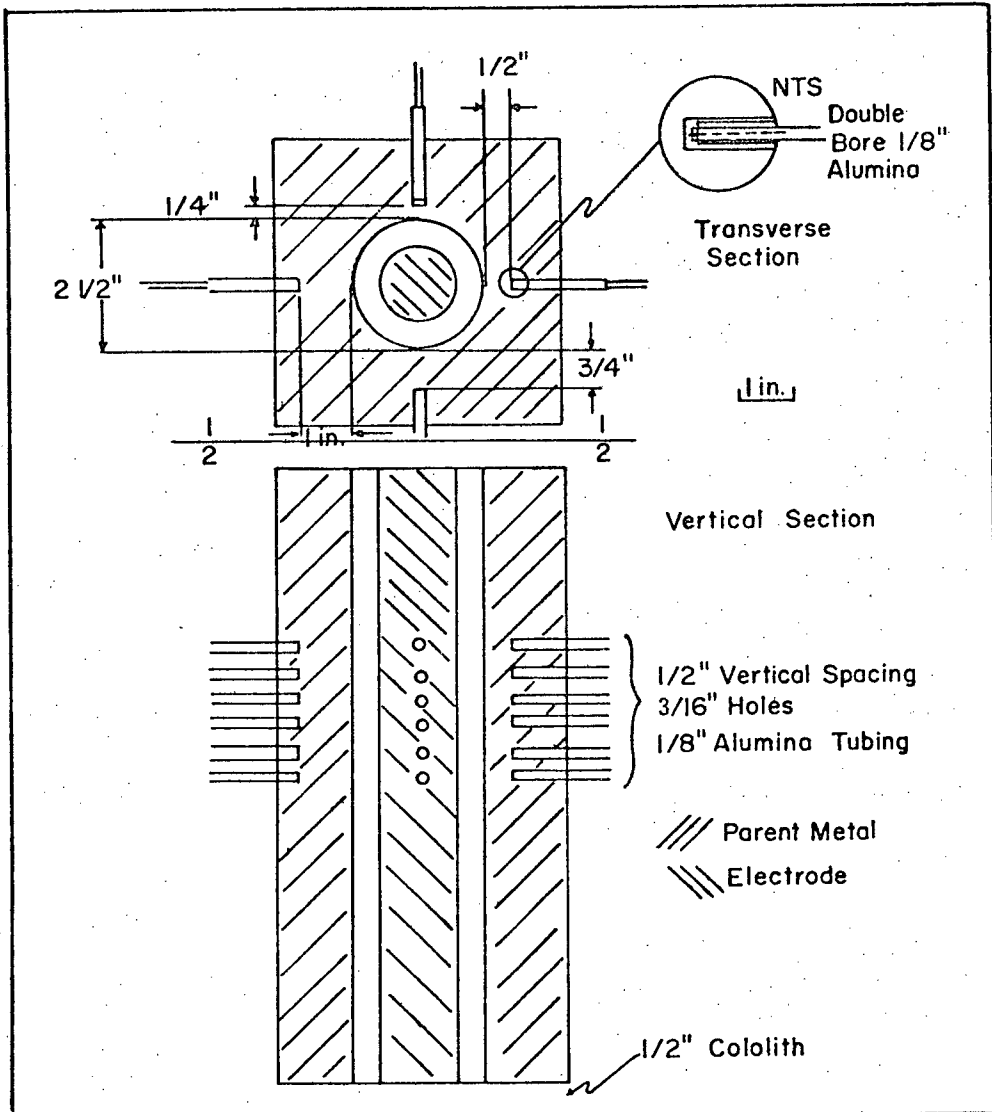


Figure 15 Thermocouple placement for initial block welds

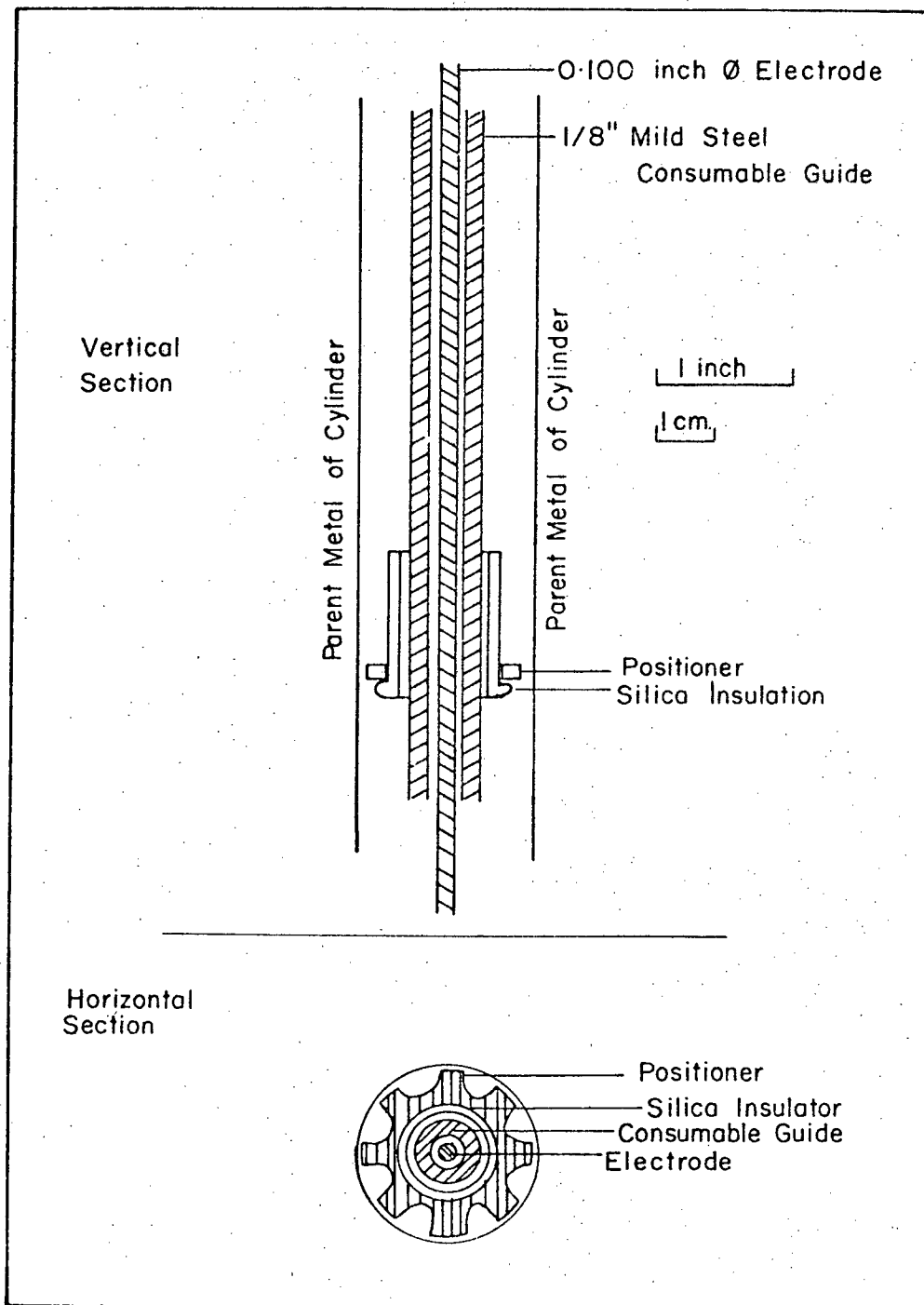


Figure 16 Silica guides for Consumable Guide Electroslag welding in cylinders.

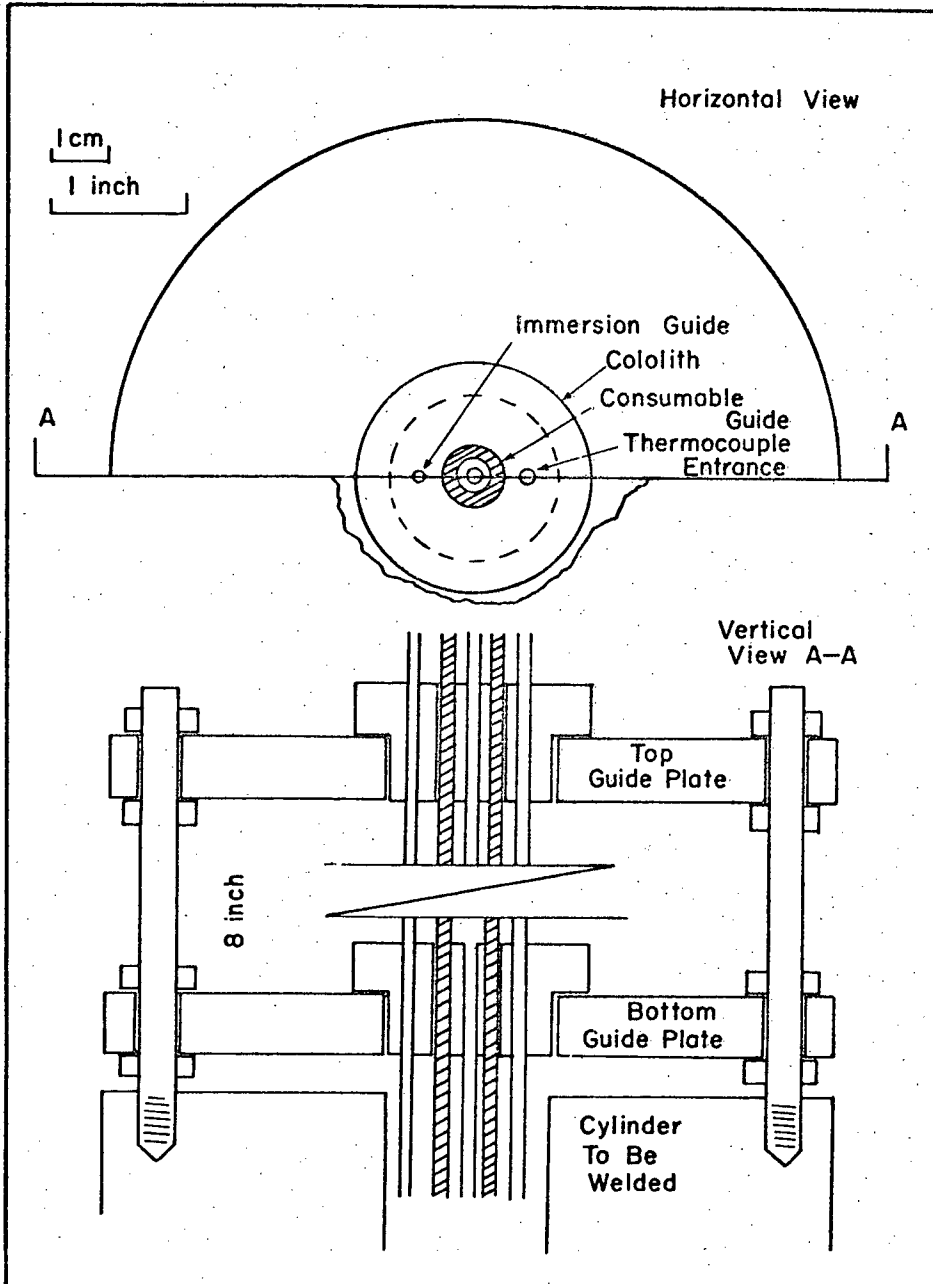


Figure 17 CGESW guiding head for welding and cylinders

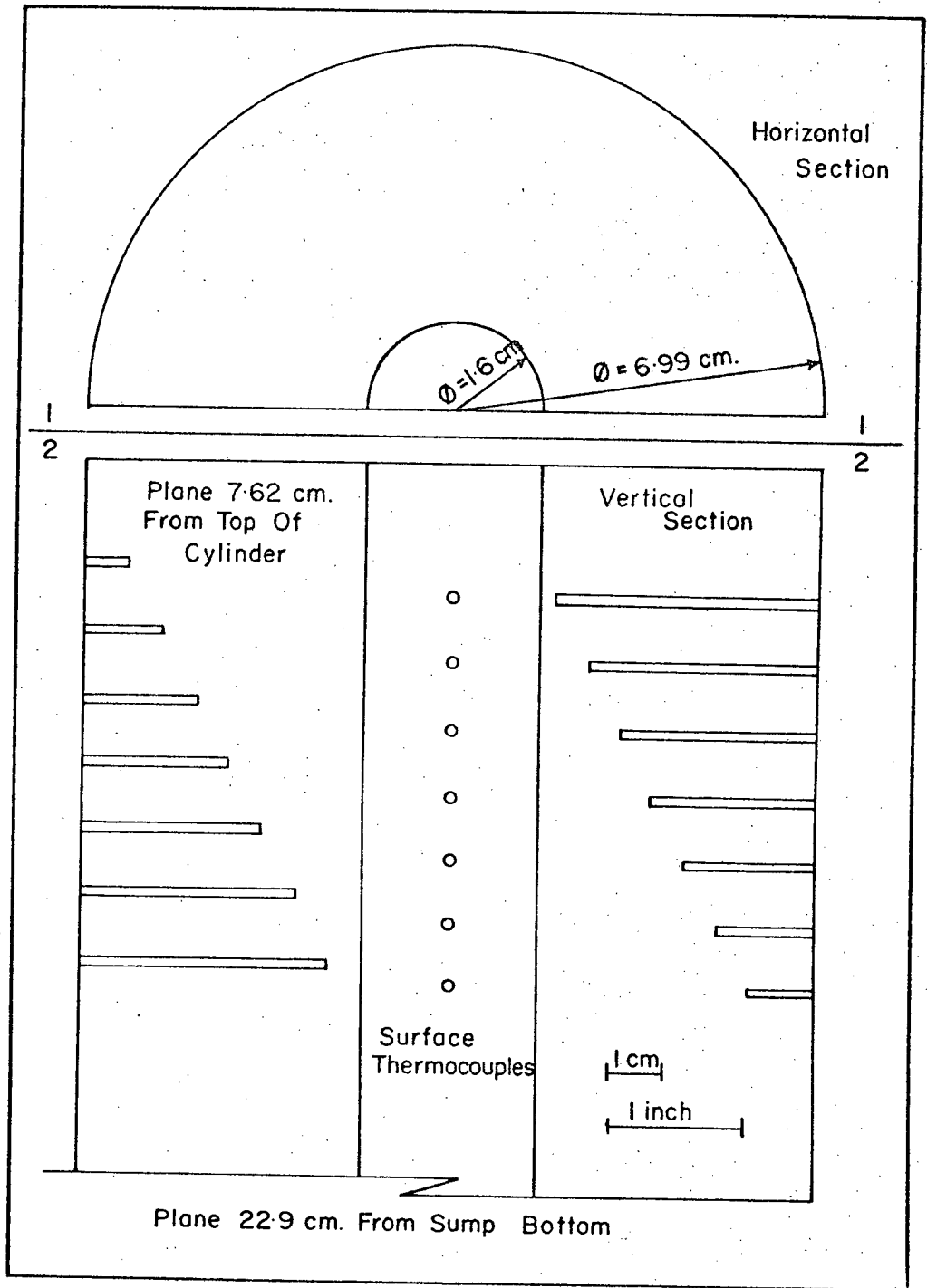


Figure 18 Initial thermocouple set-up for CGESW of cylinders.

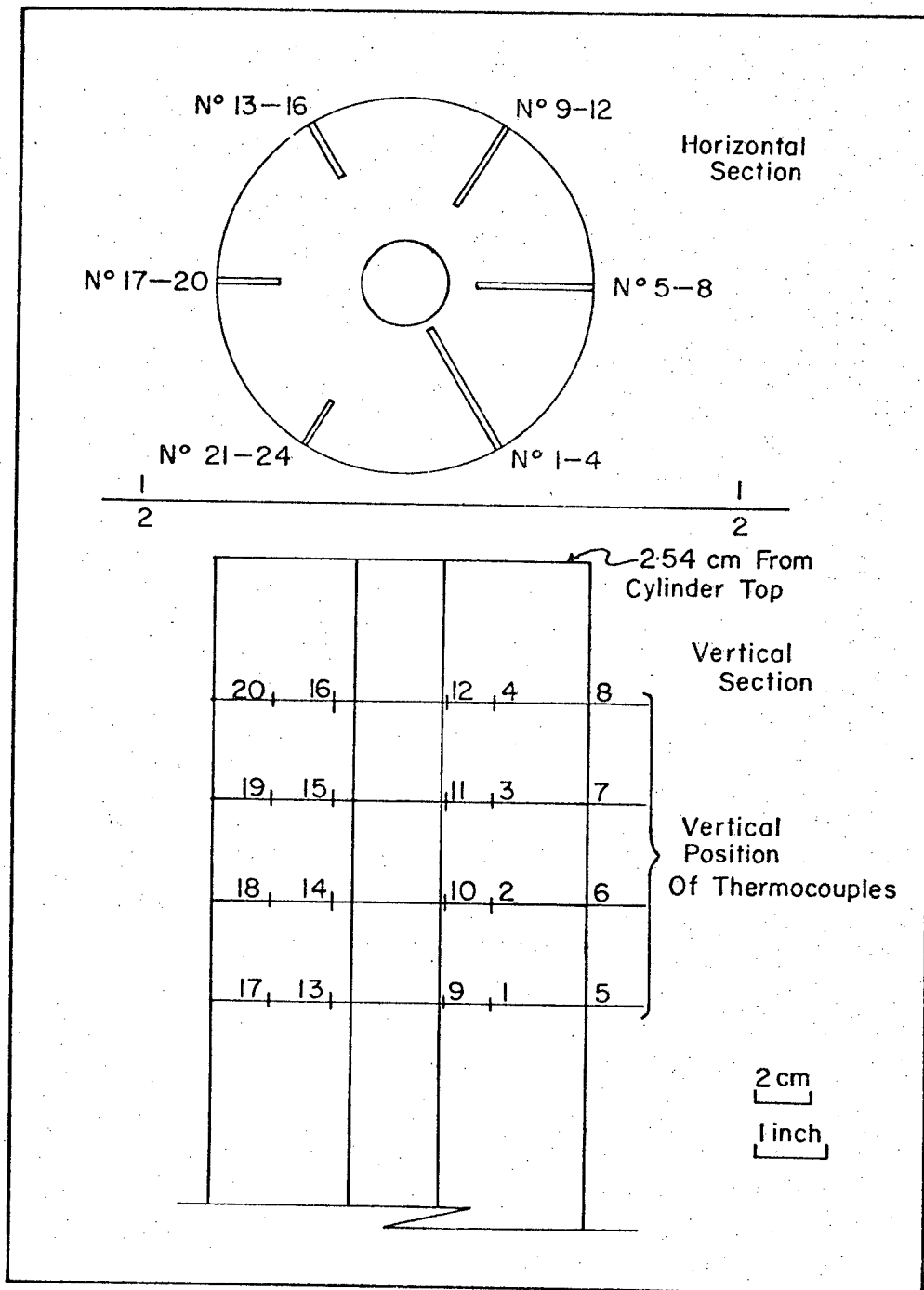


Figure 19 Final thermocouple set-up for CGESW of cylinders

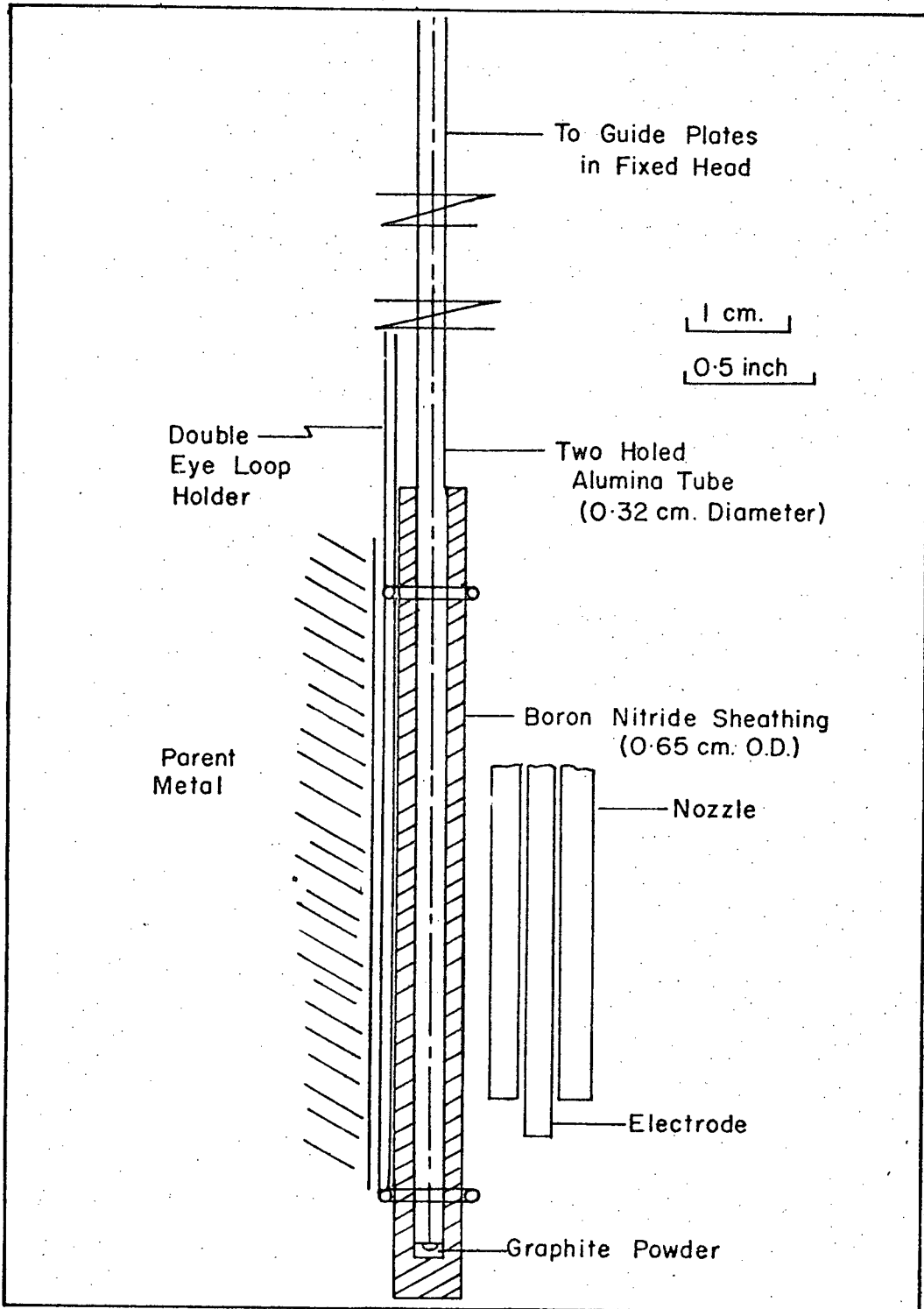


Figure 20 Slag temperature measuring thermocouple

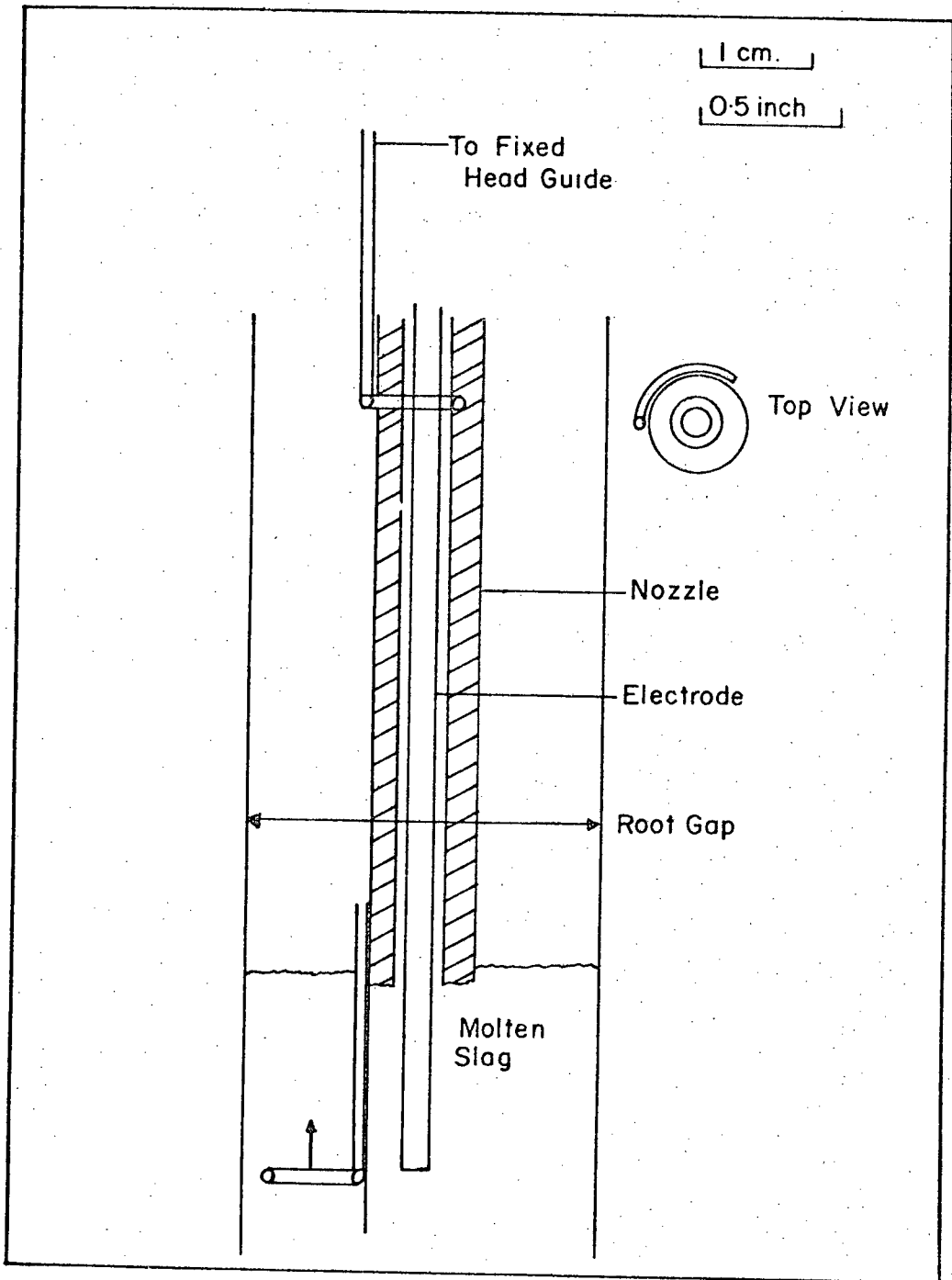


Figure 21 Immersion measuring loops

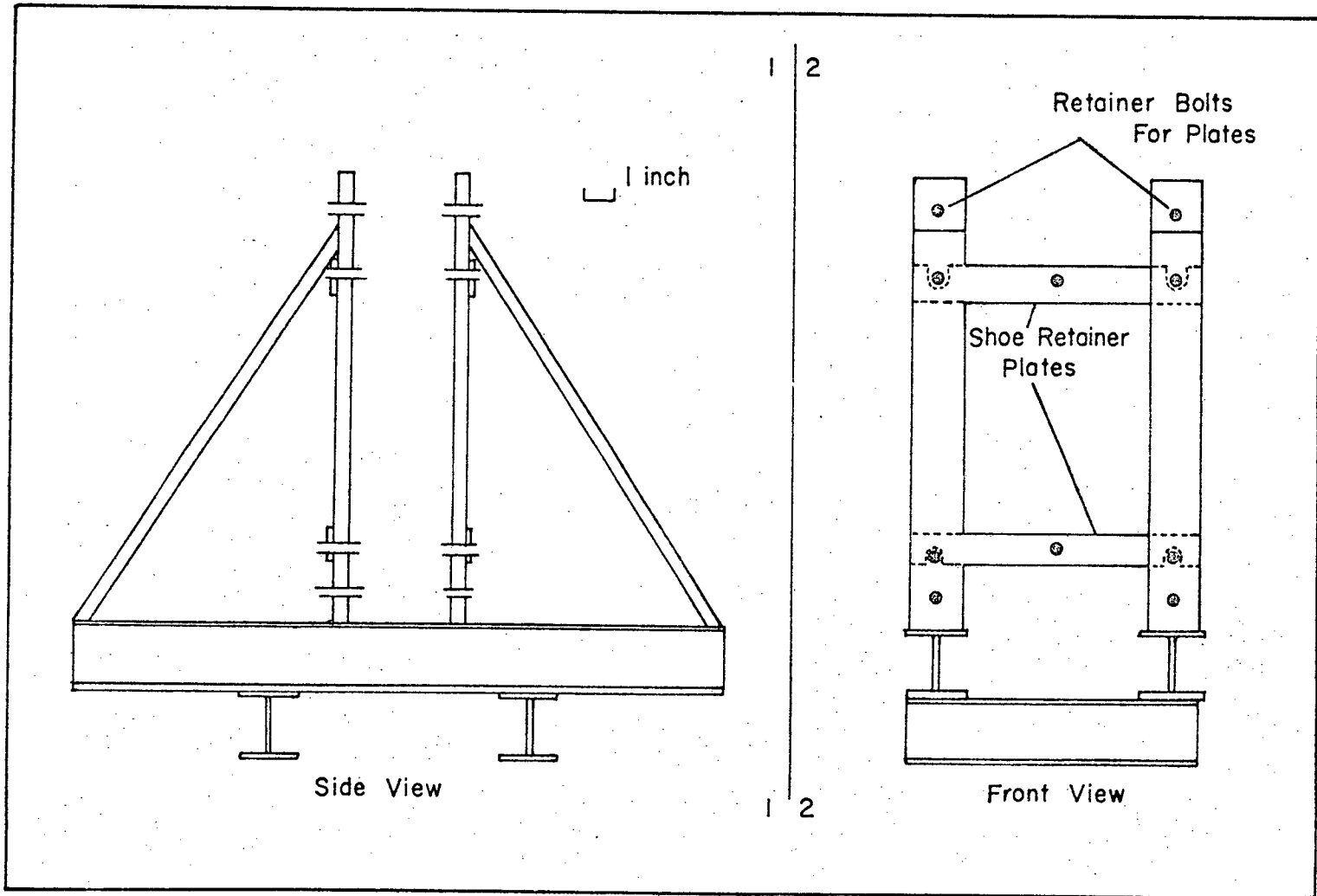


Figure 22 The welding jig for butt welding.

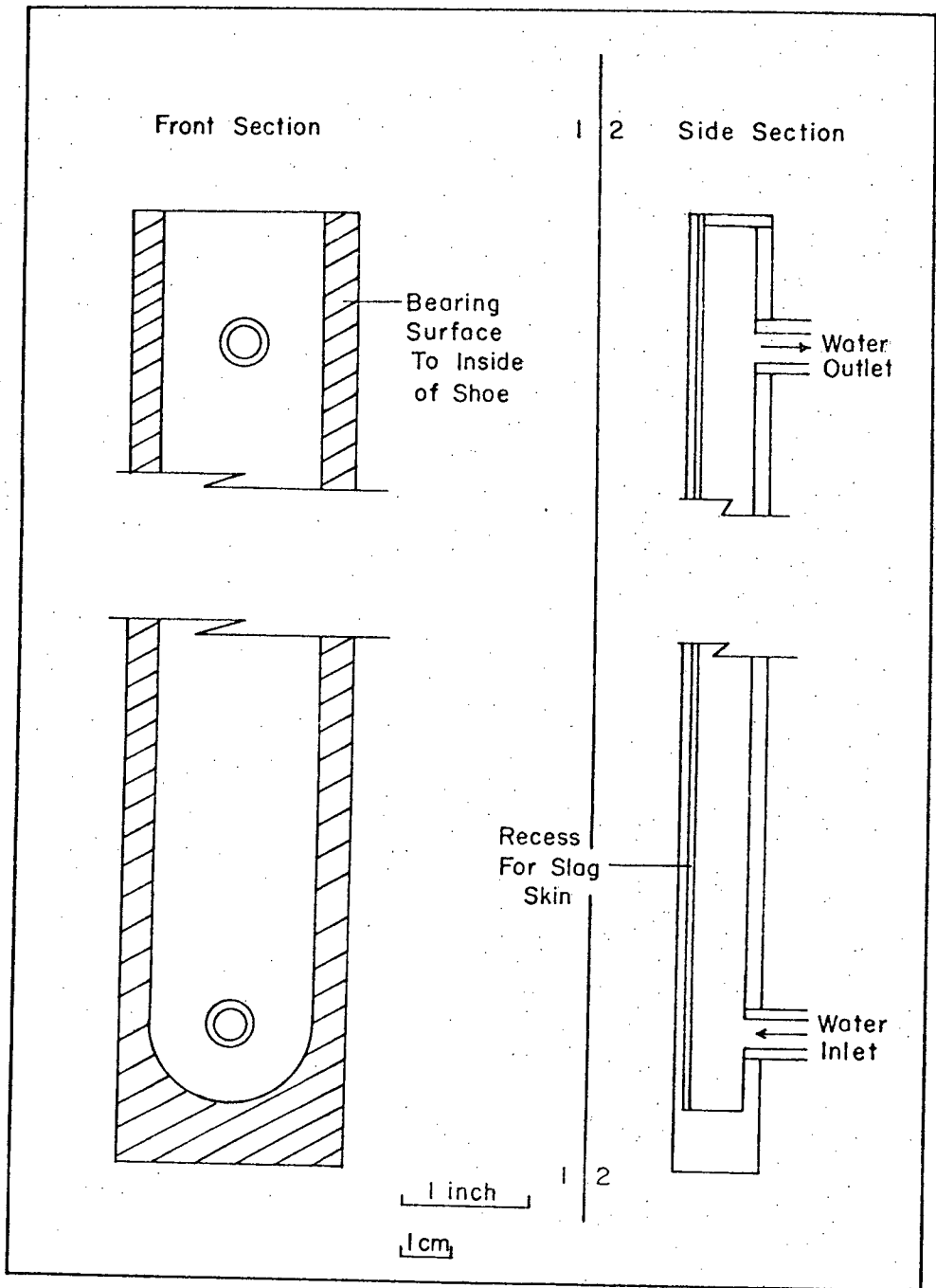


Figure 23 The cooling shoes

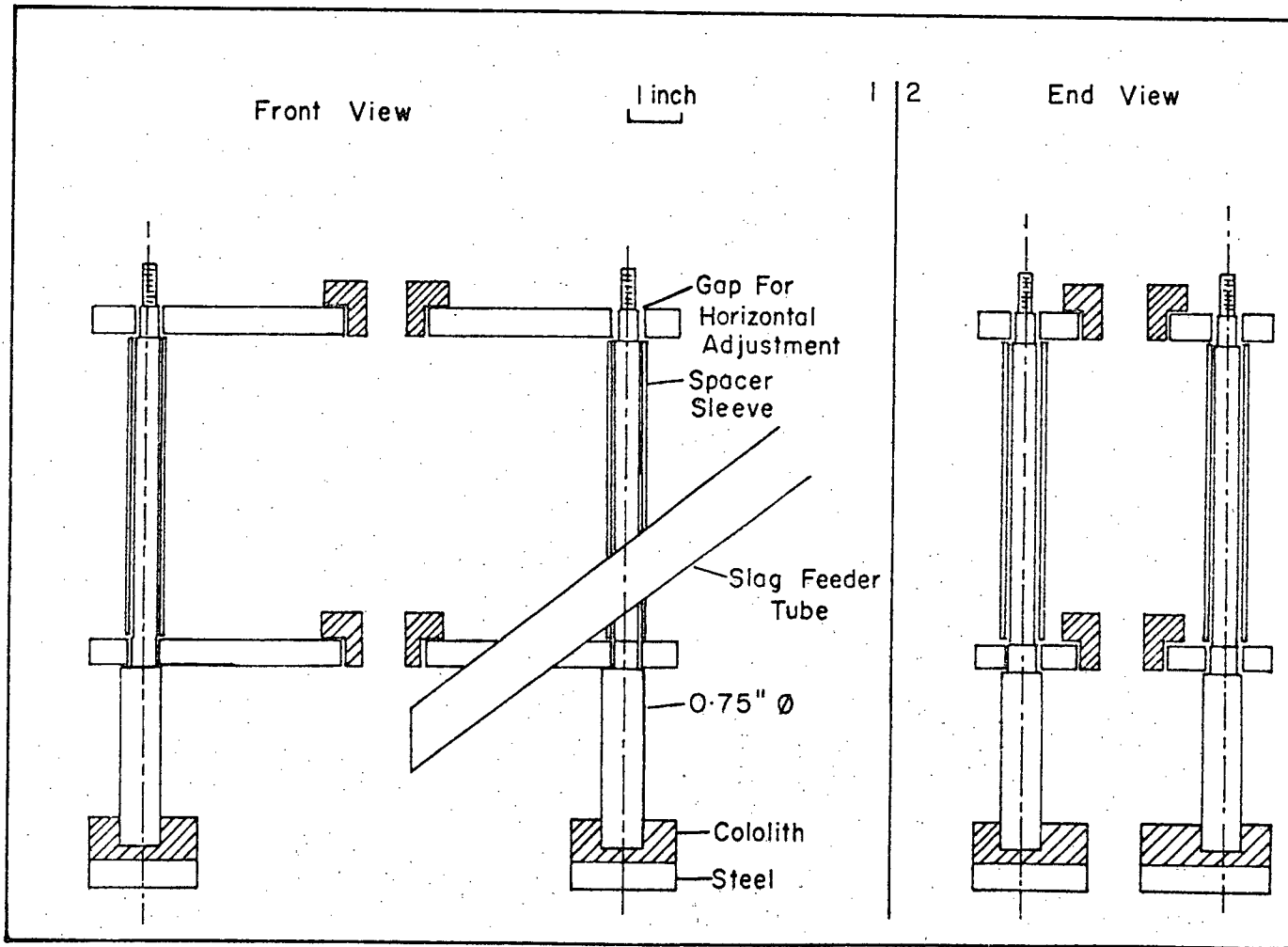


Figure 24 The consumable guide fixed head for butt welding.

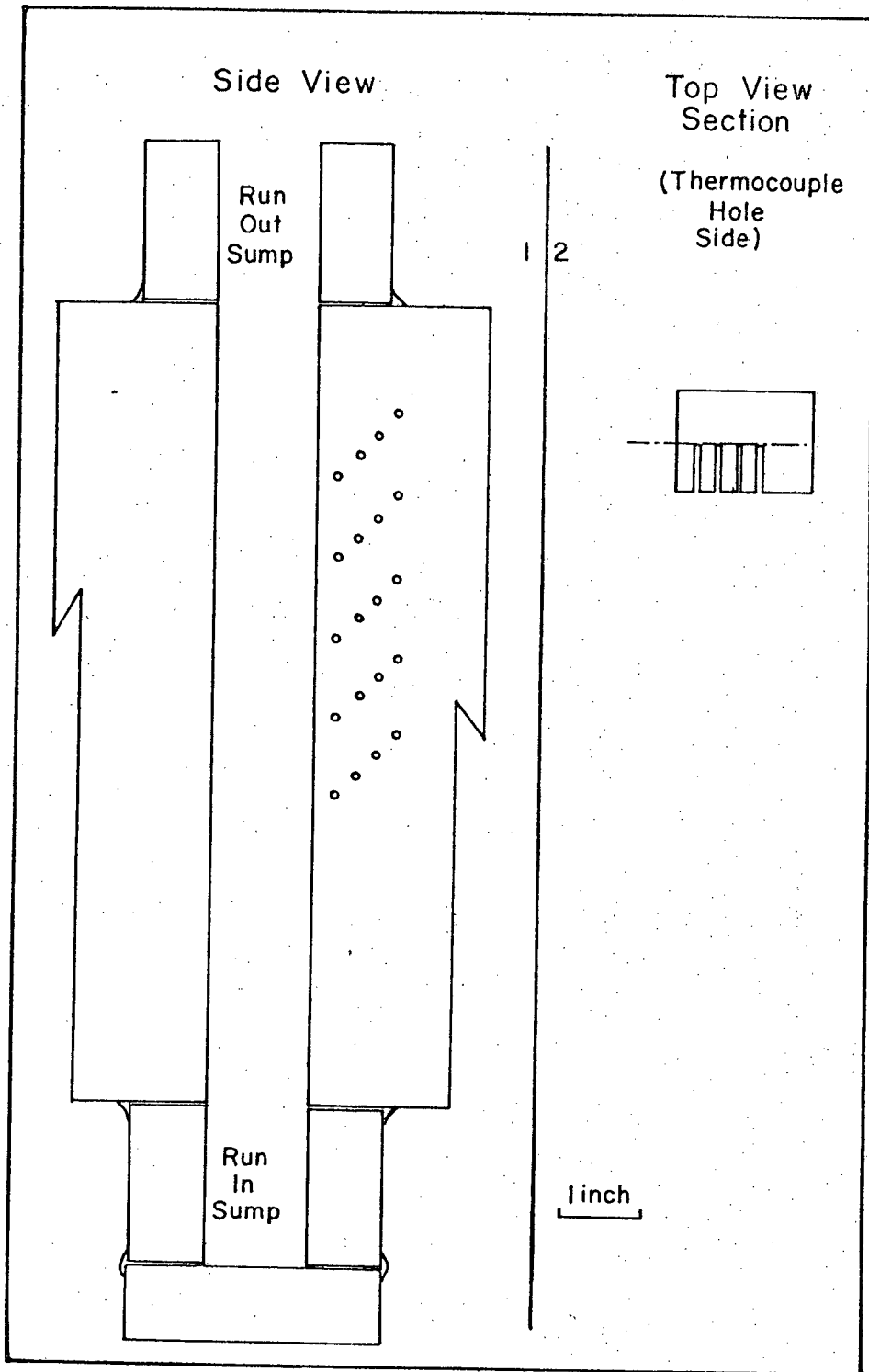


Figure 25 Thermocouple positioning in plate butt welding.

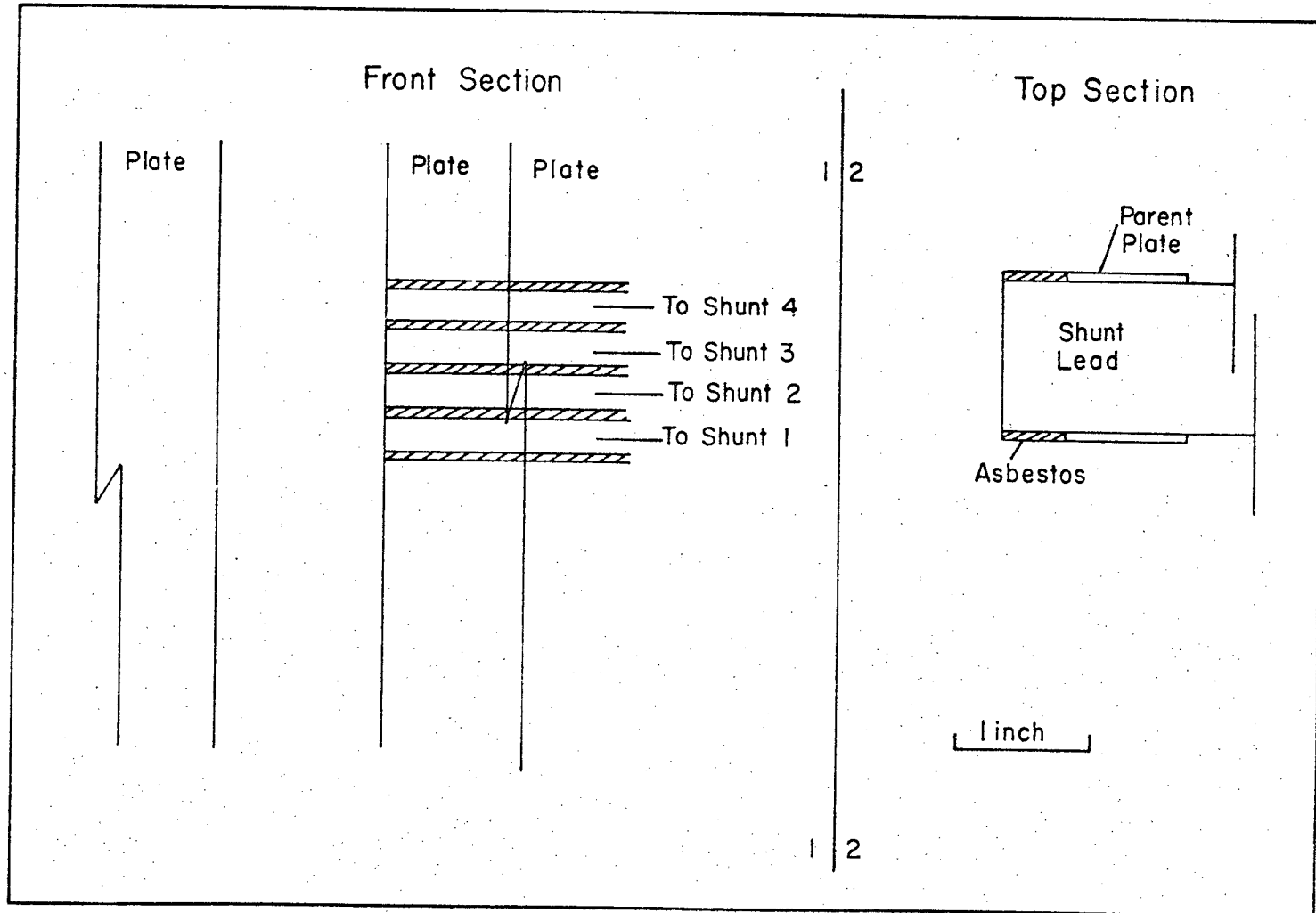


Figure 26 Shunt set-up for measuring the current distribution

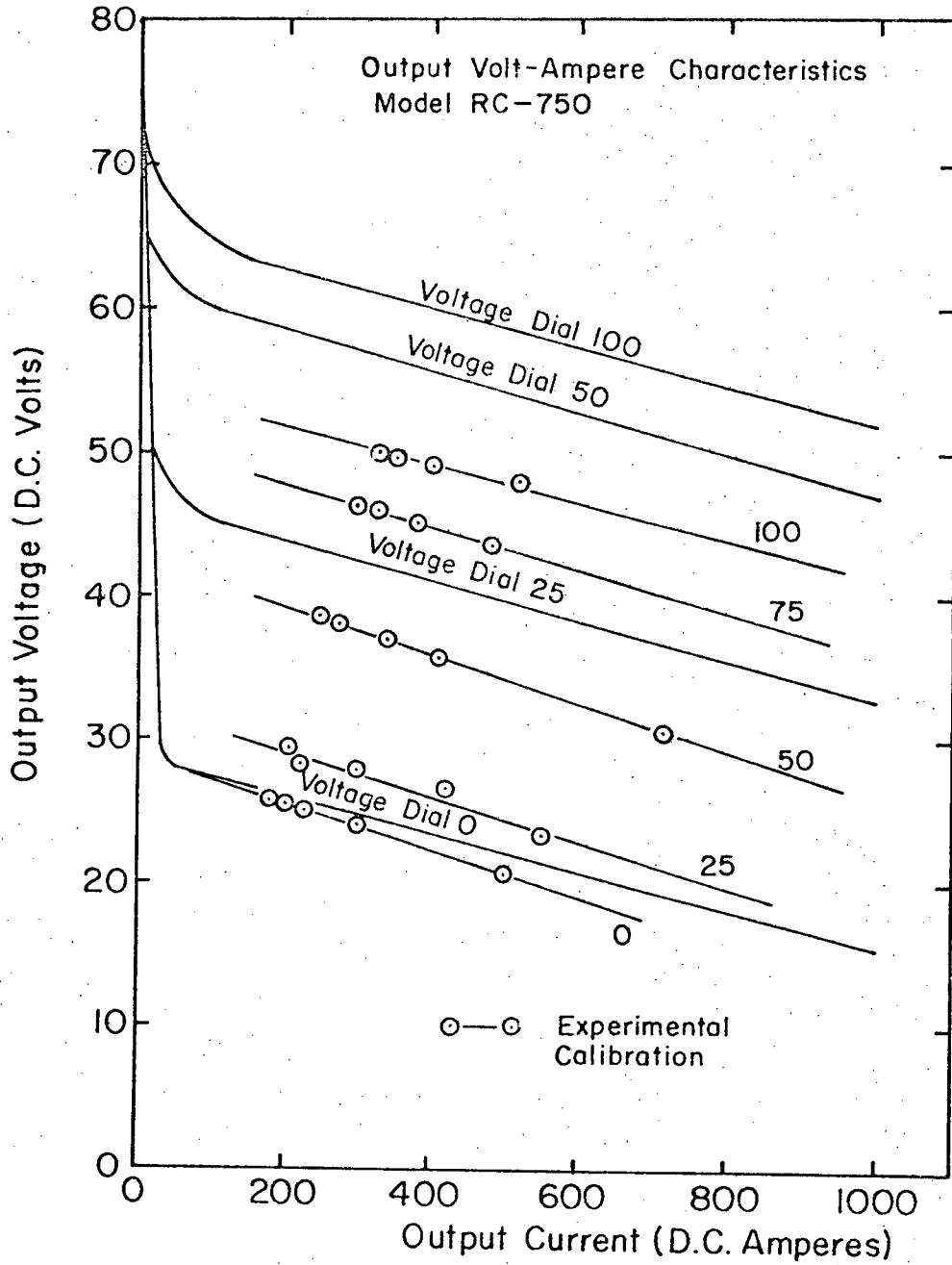


Figure 27 Hobart 750 direct current power characteristics

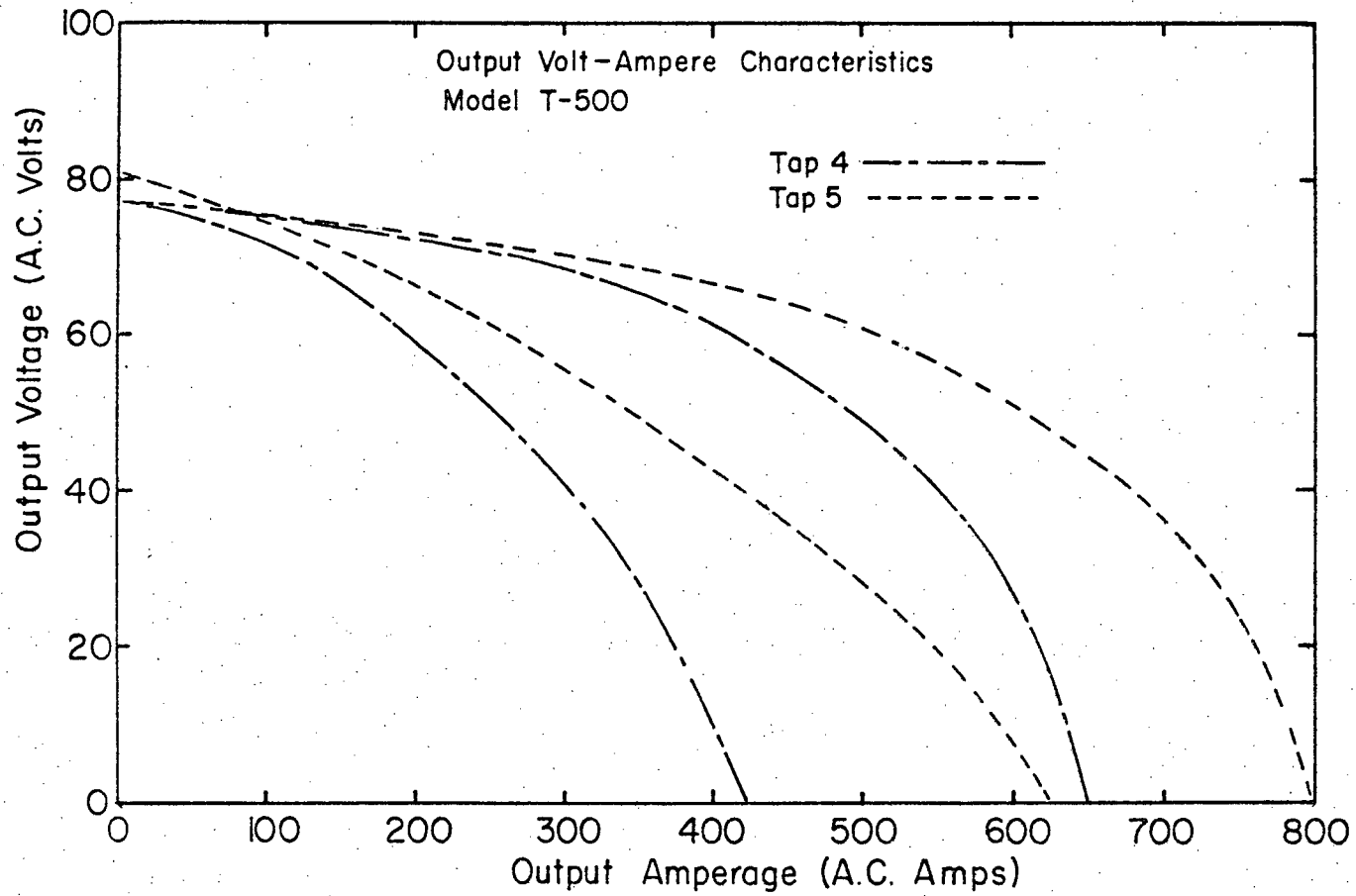


Figure 28 Hobart T-500 alternating current power characteristics

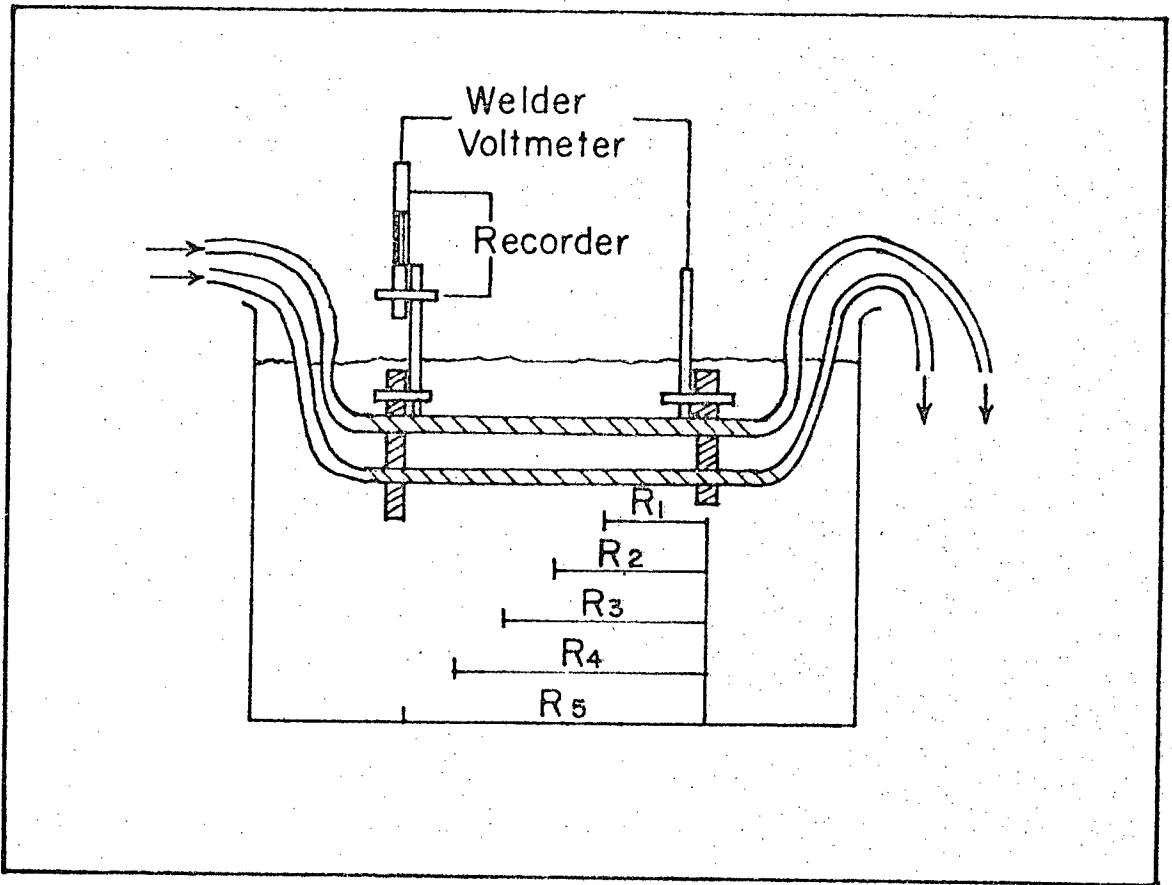


Figure 29 Variable resistance current measuring apparatus

INCLUSION DISTRIBUTION $1\frac{3}{4}$ " THICKNESS

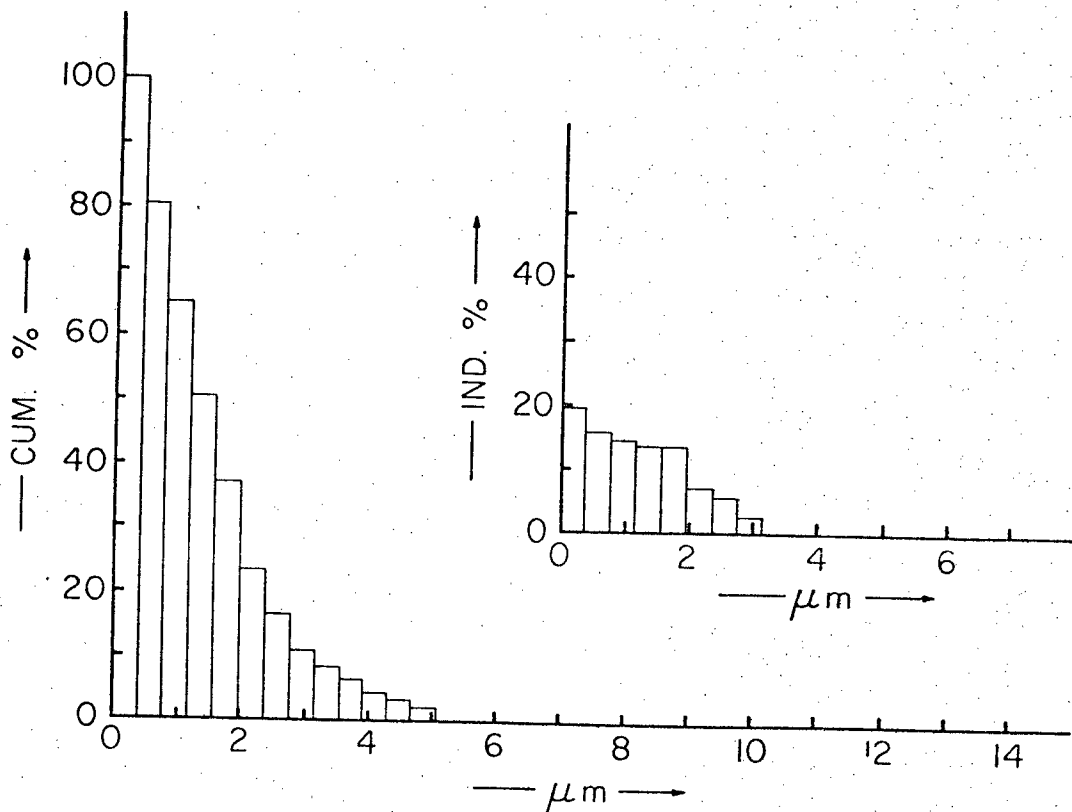


Figure 30 Typical Canron weld inclusion distribution

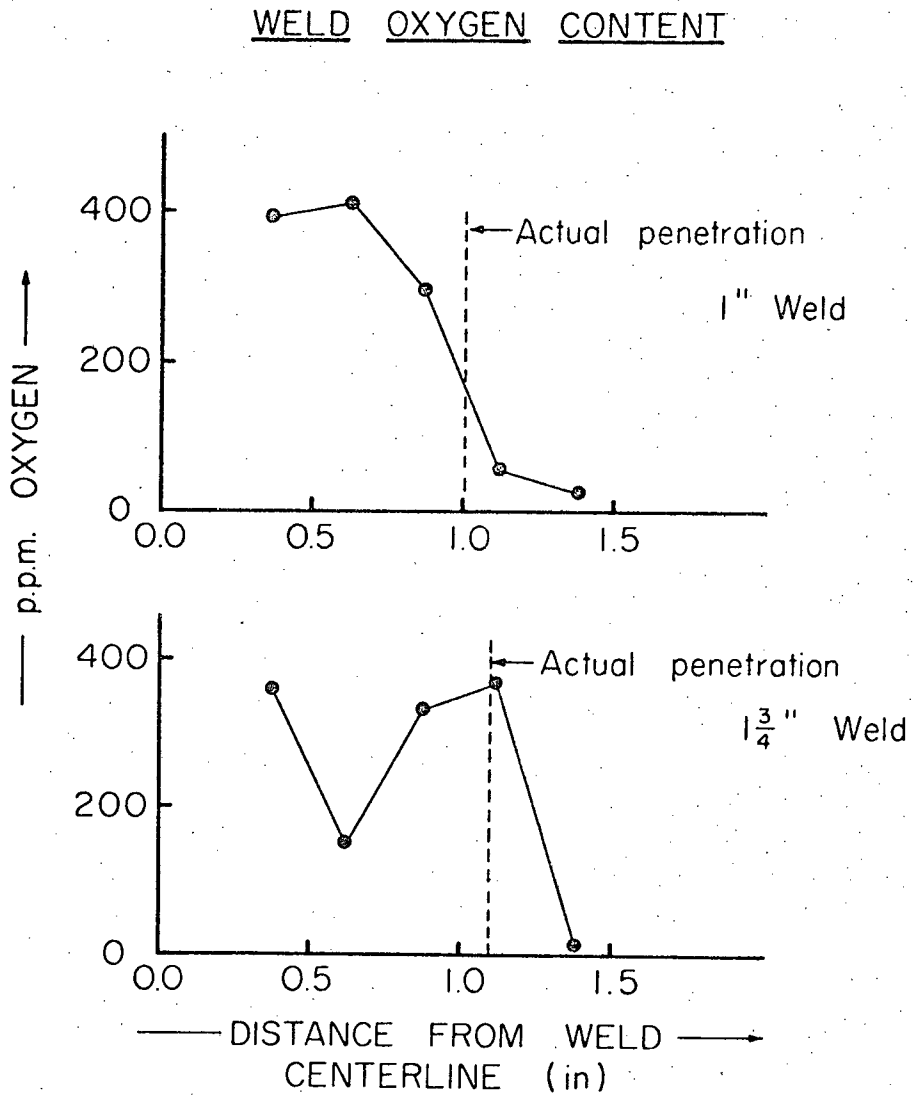


Figure 31 Cannon oxygen distribution and penetration

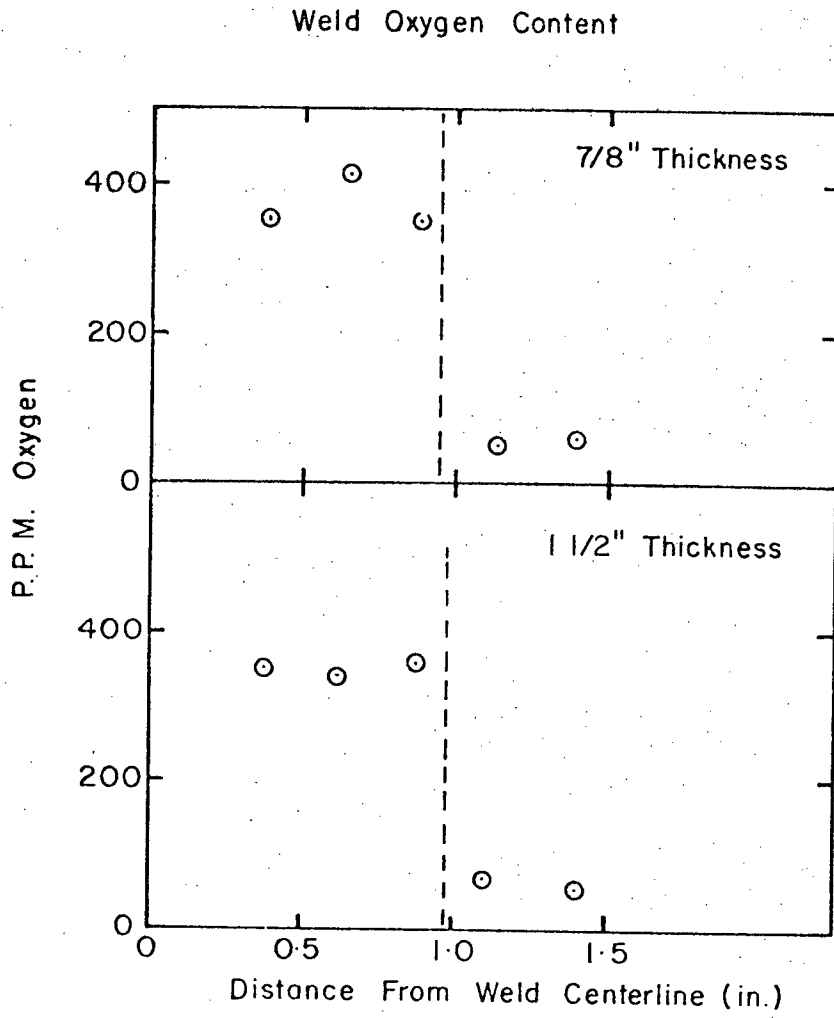


Figure 32 Cannon oxygen distribution and penetration

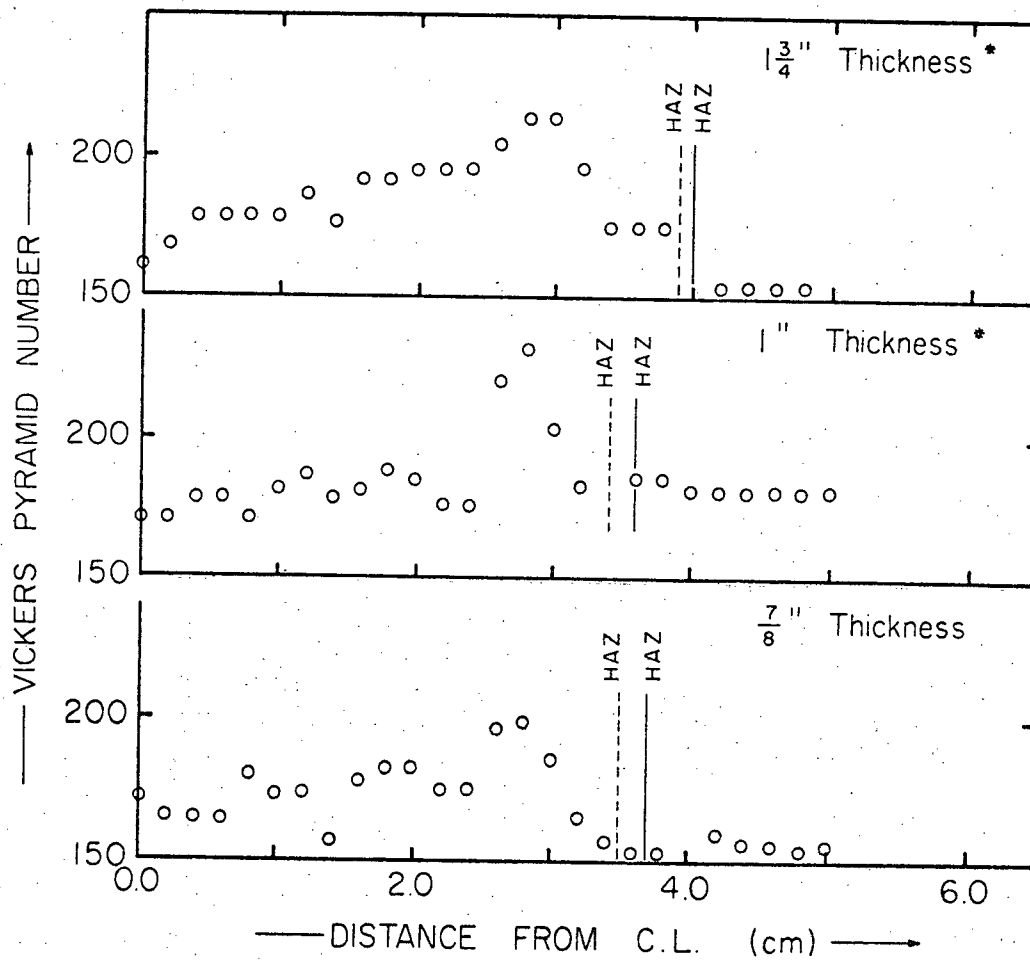


Figure 33 Canron weld, microstructurally determined (solid line) and hardness traverse determined (broken line) HAZ

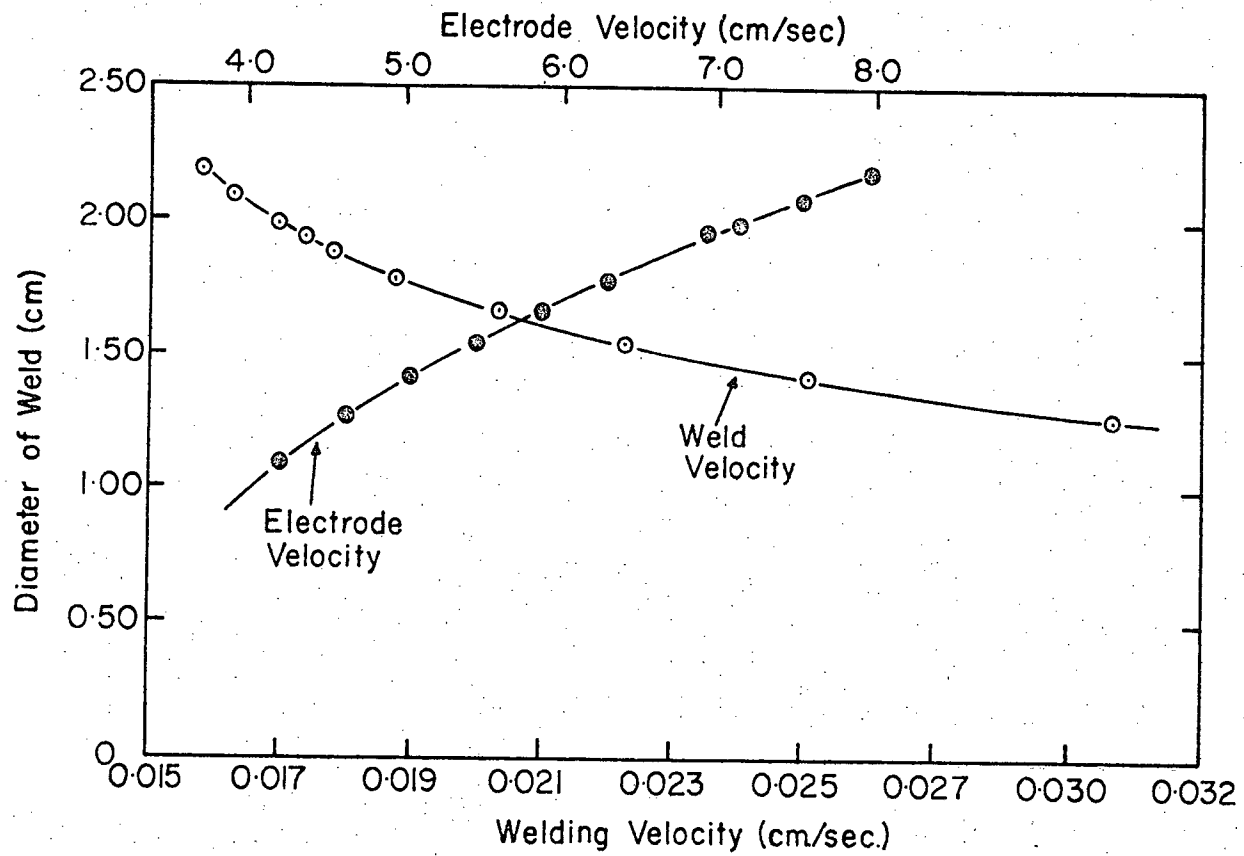


Figure 34 Electrode velocity and weld velocity for different weld sizes

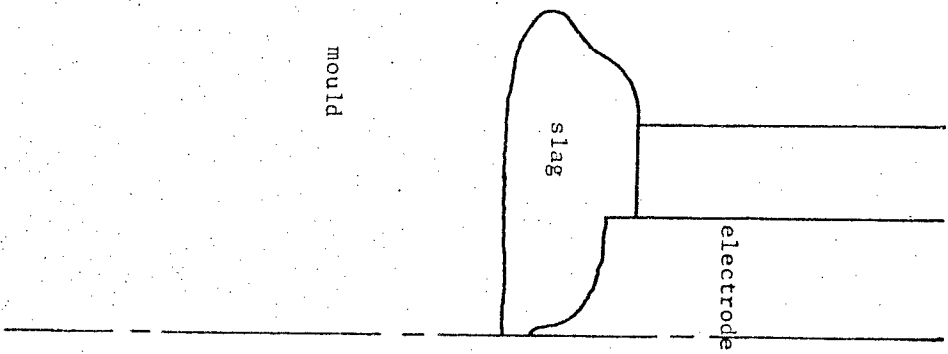
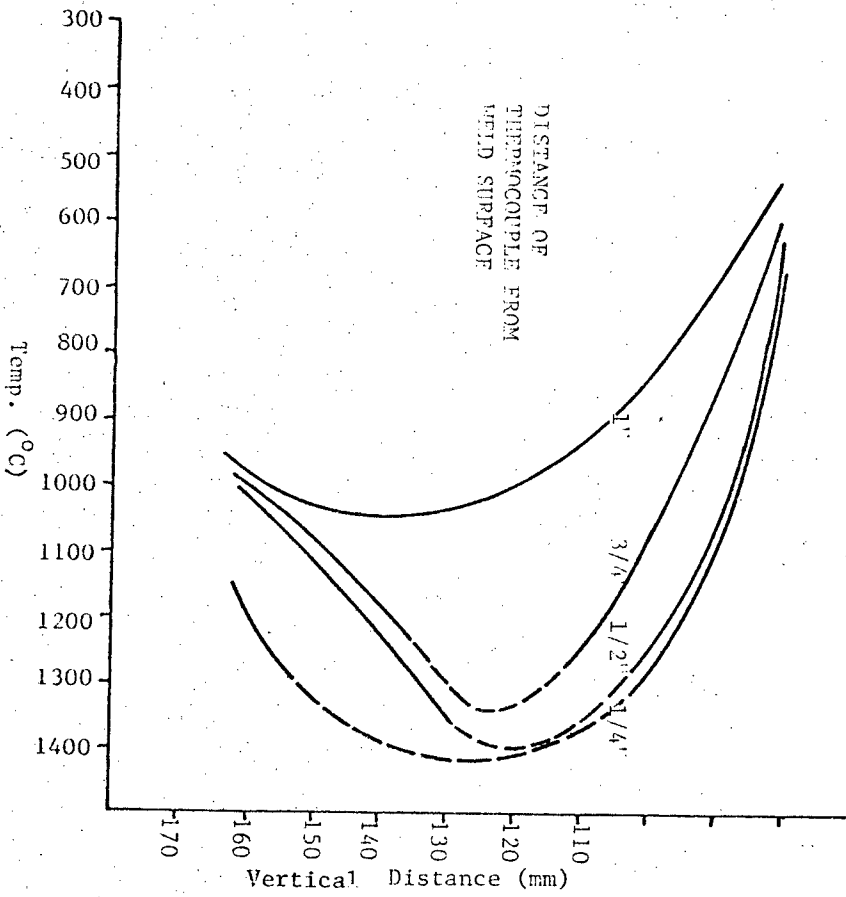


Figure 35 Thermal profile DCRP

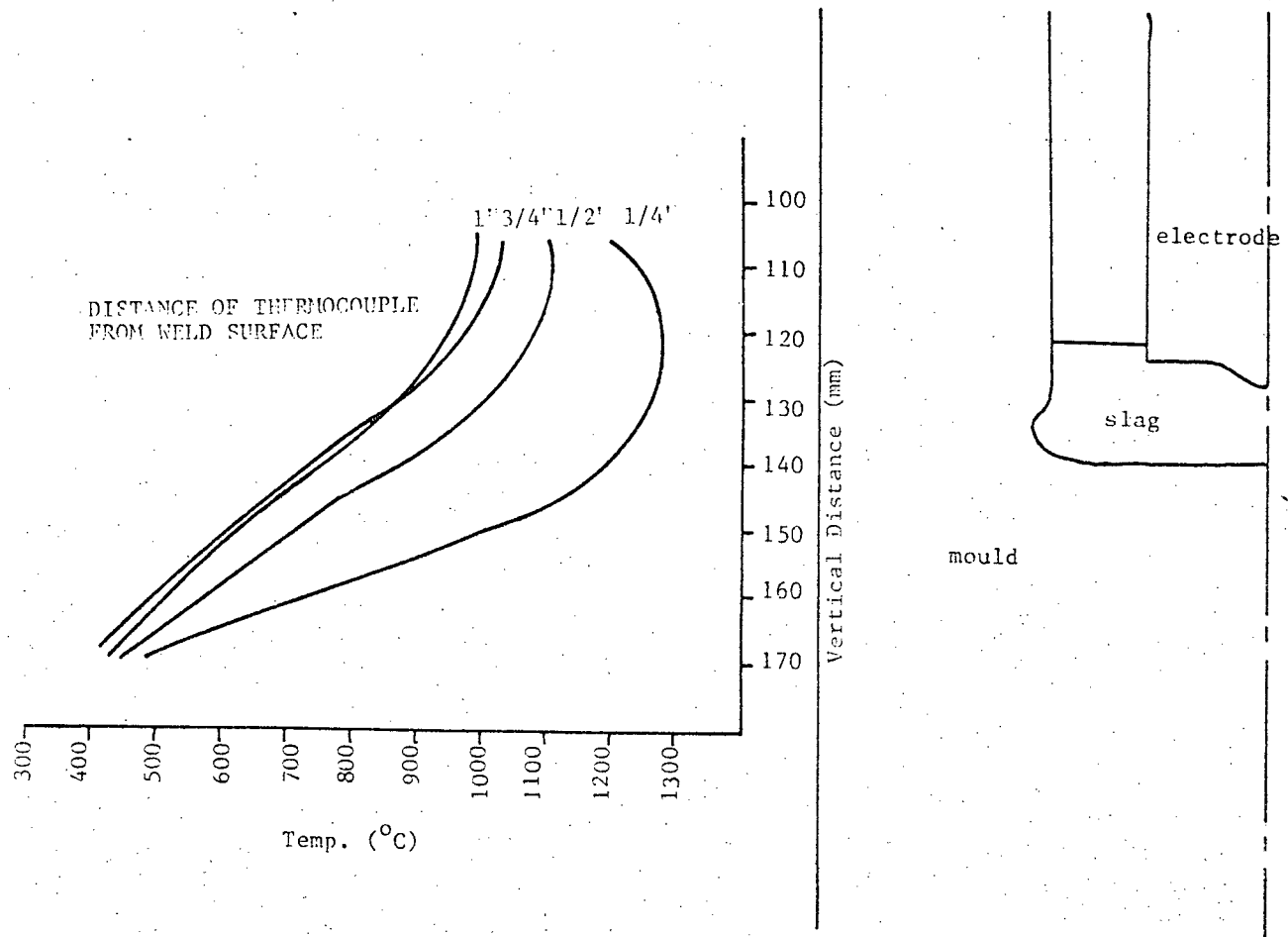


Figure 36 Thermal profile for DCSP

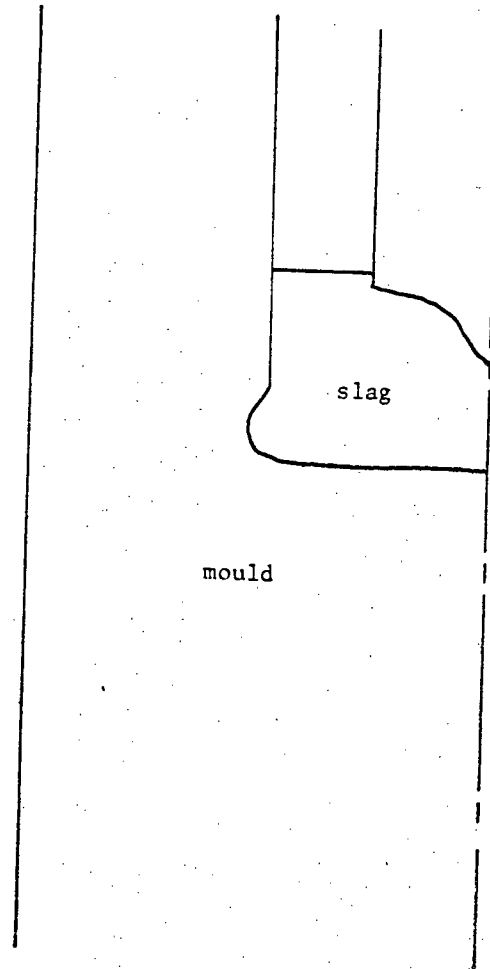
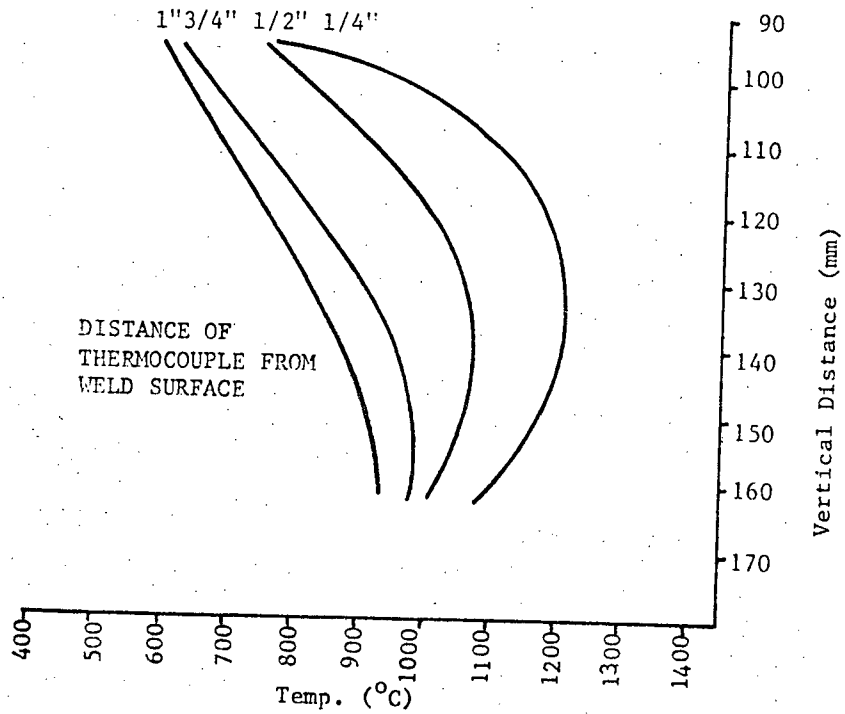


Figure 37 Thermal profile for AC

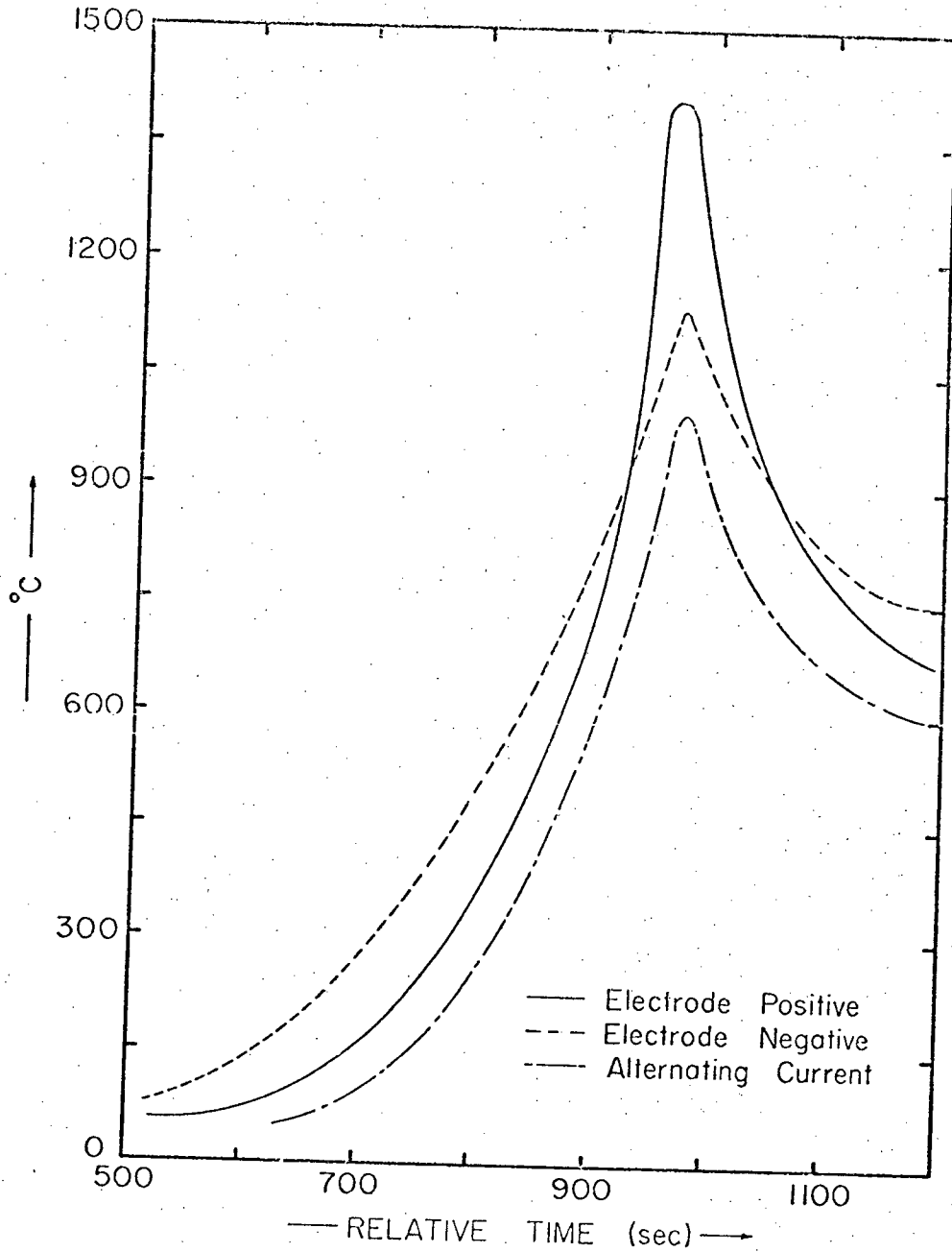


Figure 38 Thermal profile comparisons for large electrode experiments (each curve for a thermocouple 1/4 inch from original weld surface).

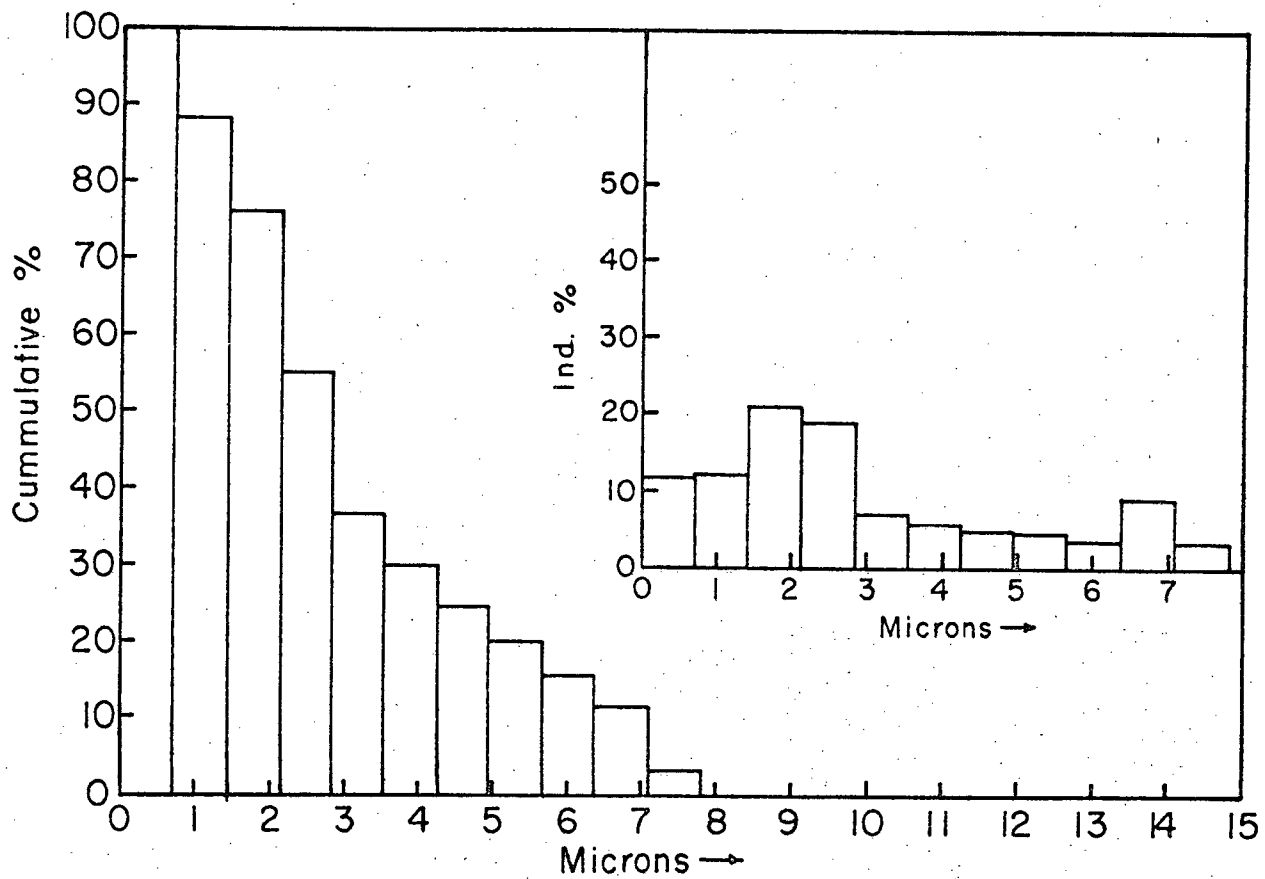


Figure 39 Inclusion distribution for DCRP

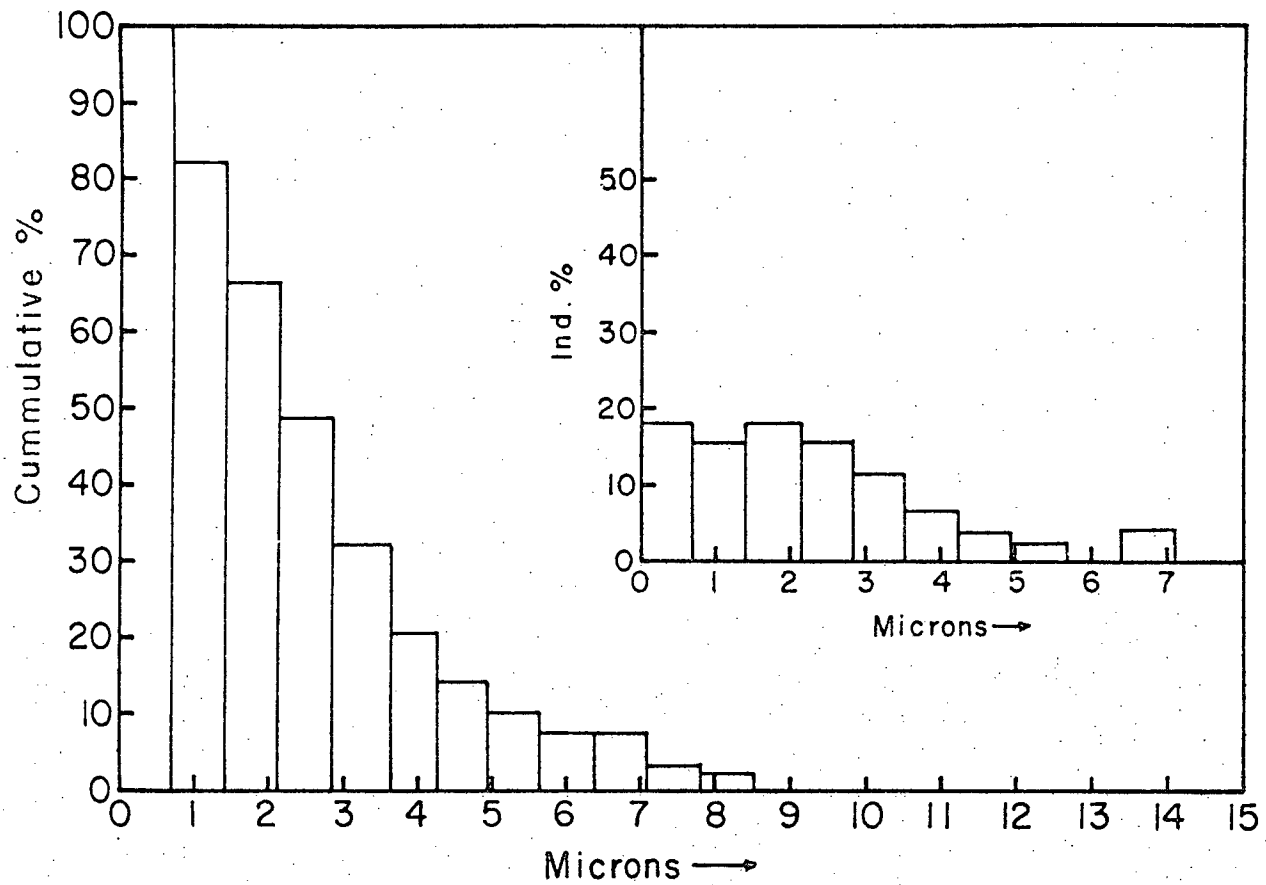


Figure 40 Inclusion distribution for DCSP

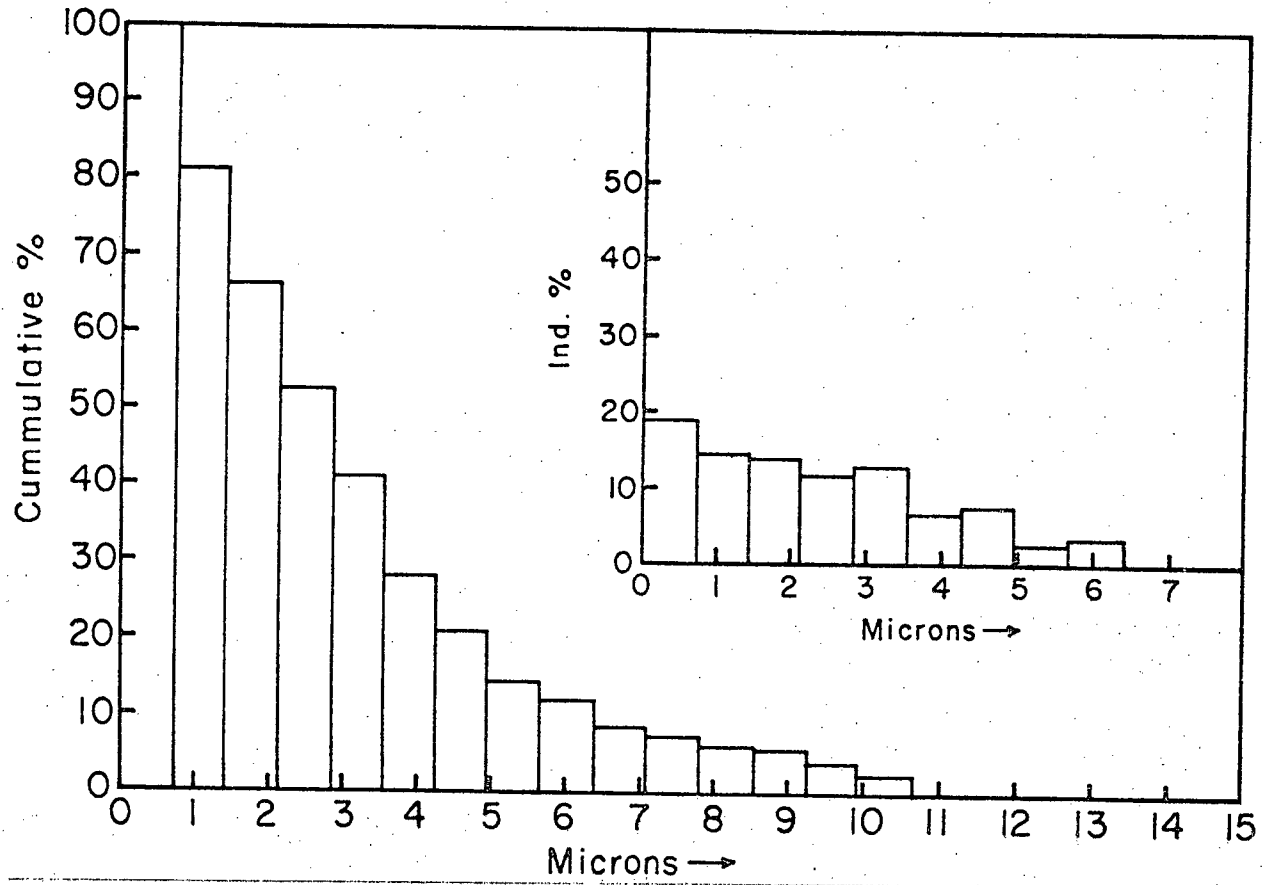


Figure 41 Inclusion distribution for AC

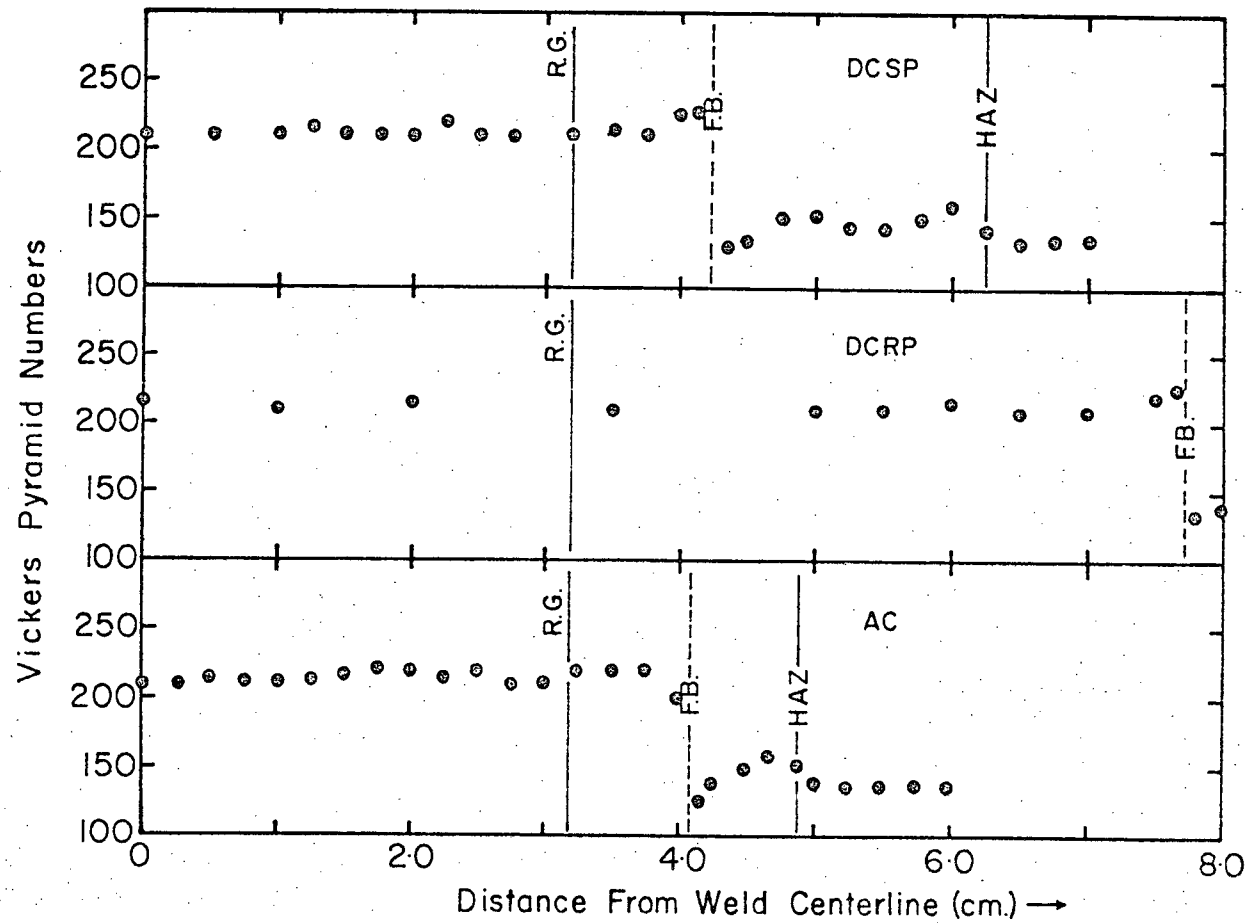


Figure 42 Hardness traverses for large electrode welds

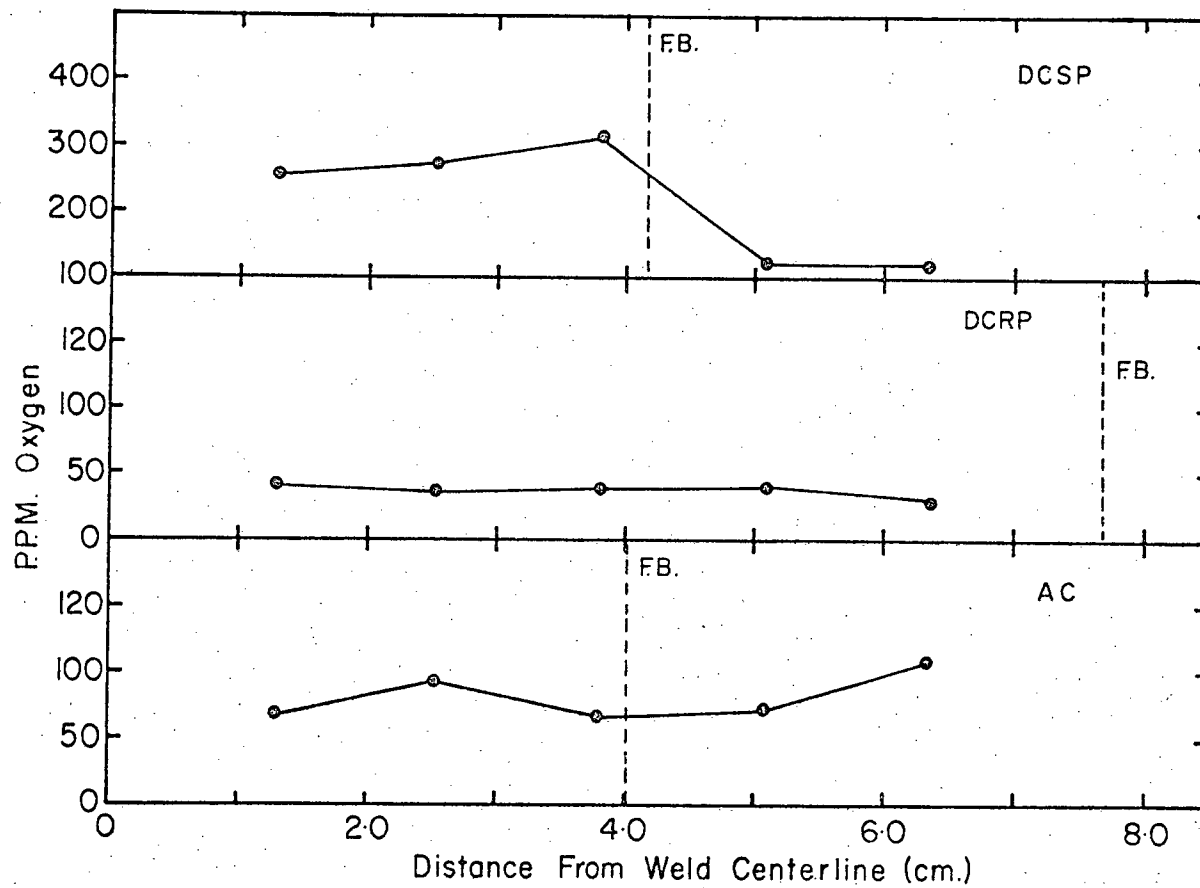


Figure 43 Oxygen content traverses for large electrode welds

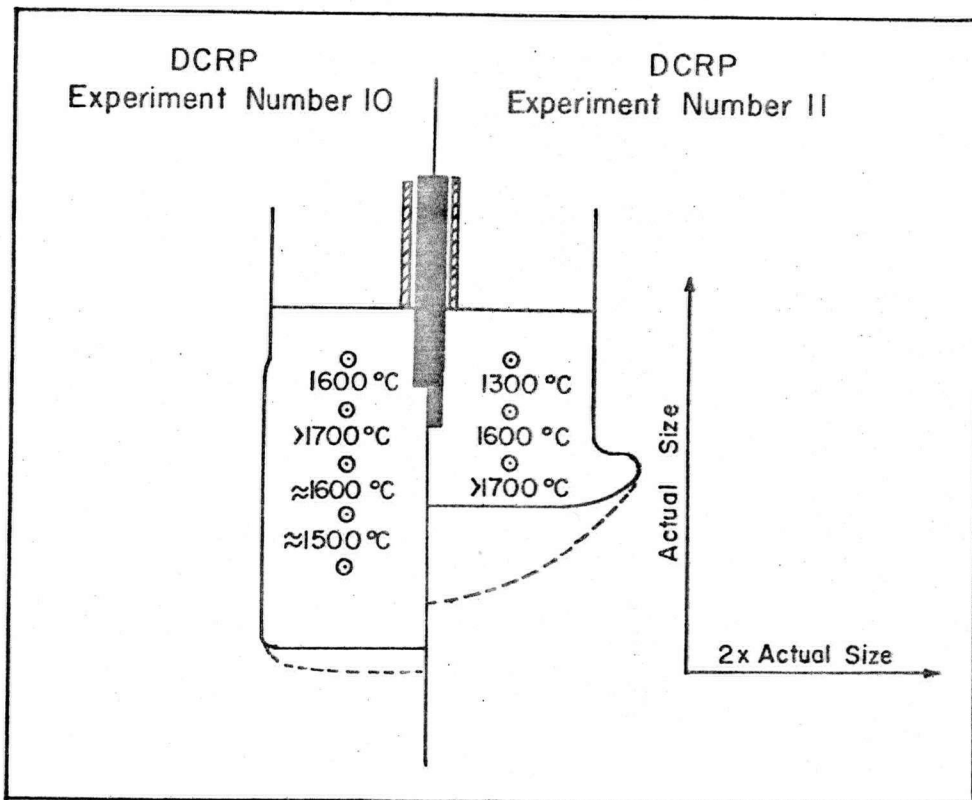


Figure 44 Slag temperatures for DCRP (experiment 10 and 11)

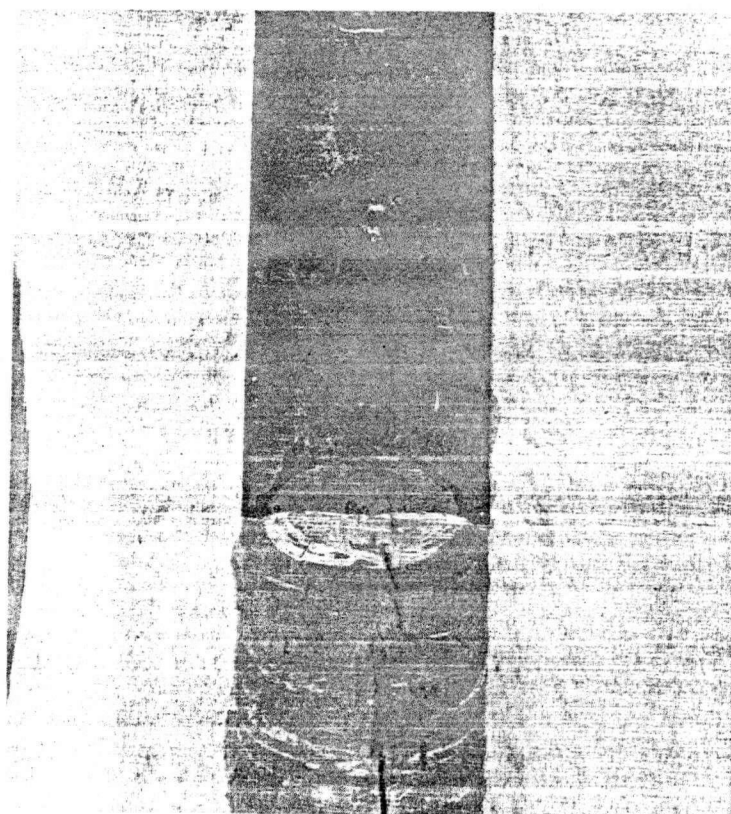


Figure 45 Experiment 10, vertical section macrograph (corresponding to above temperatures).

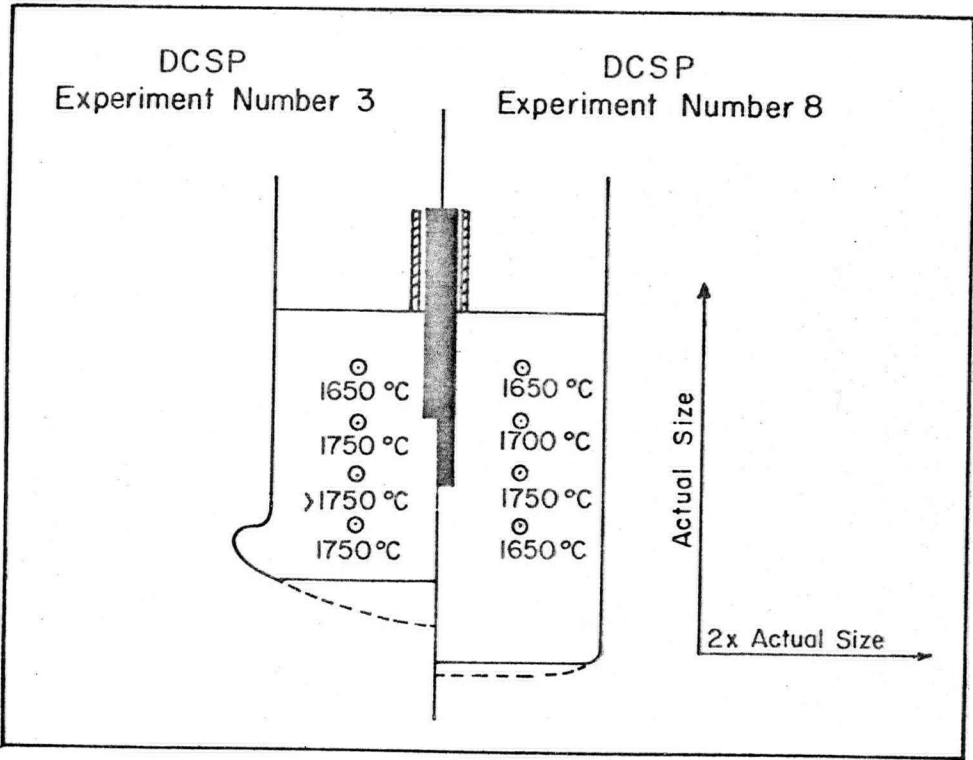


Figure 46 Slag temperatures for DCSP (experiment 3 and 8)



Figure 47 Experiment 3, vertical section macrograph (corresponding to above temperatures)

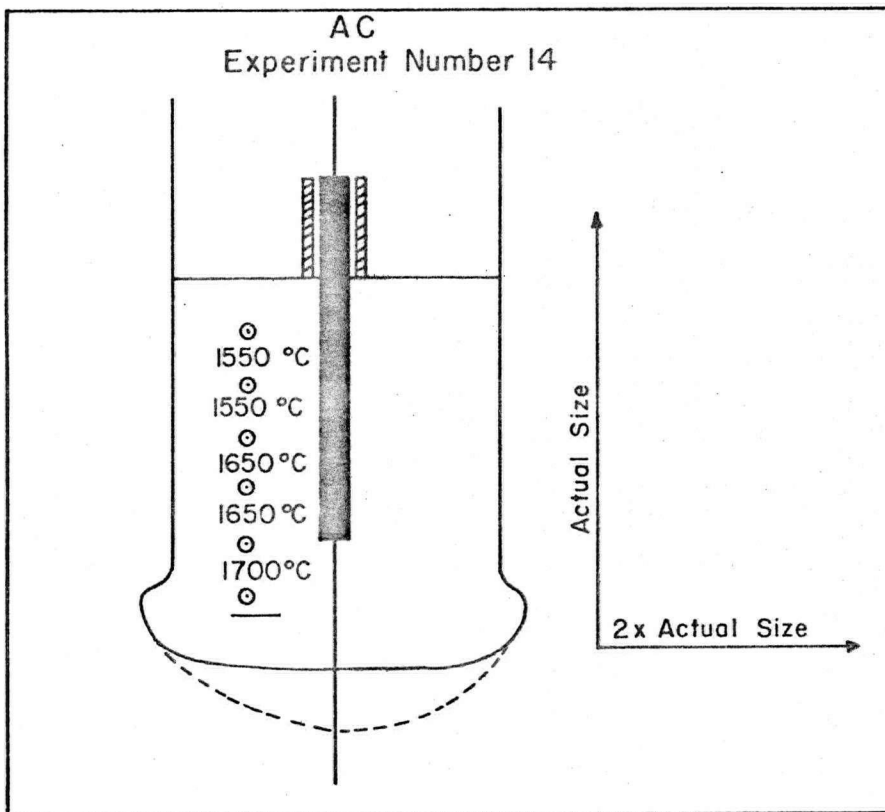


Figure 48 Slag temperatures for AC (experiment 14)

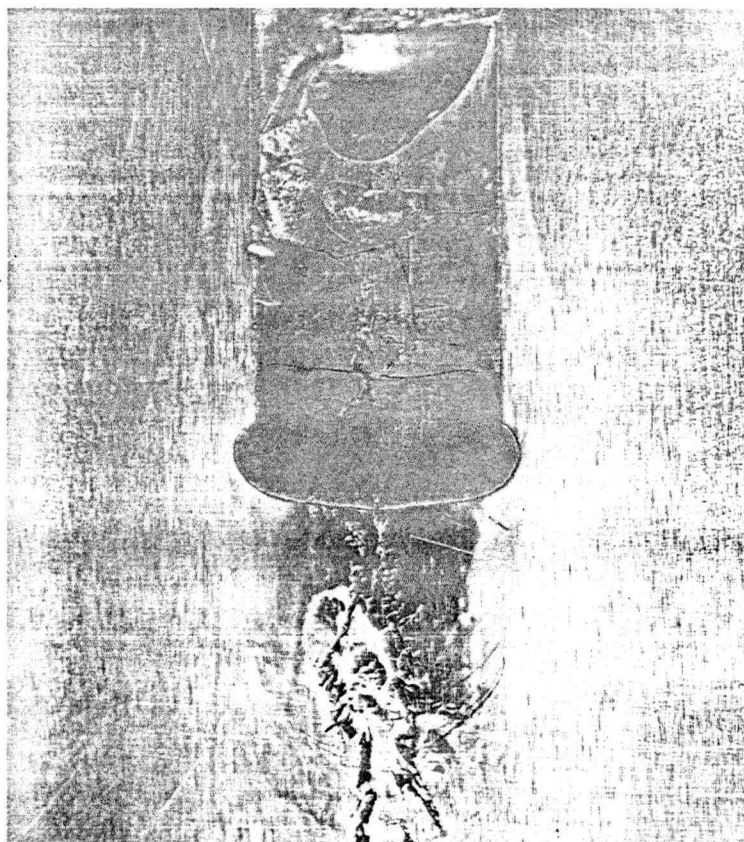


Figure 49 Experiment 14, vertical section macrograph (corresponding to above temperatures)

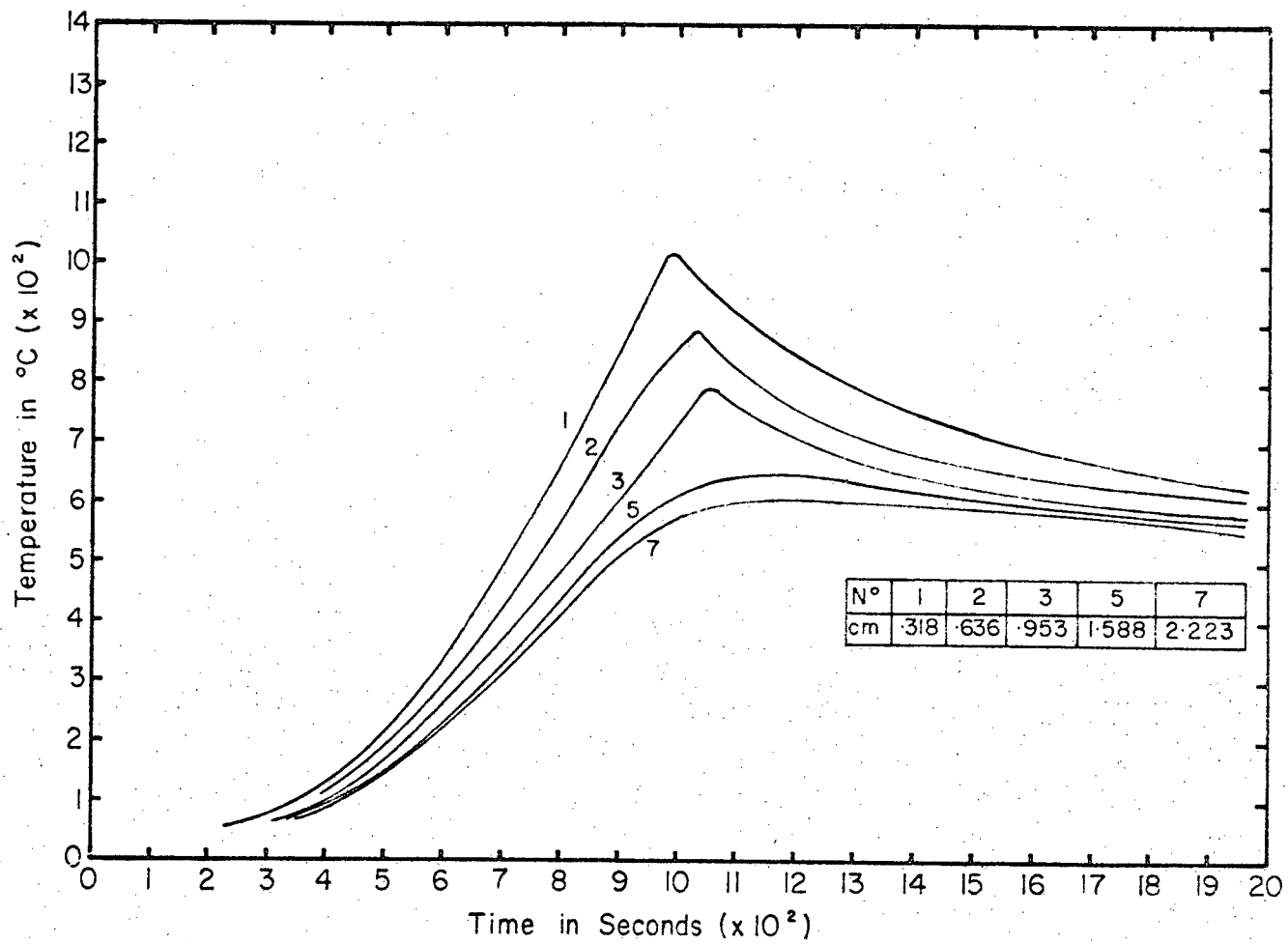


Figure 50 Thermal cycle for DCRP, experiment 10.

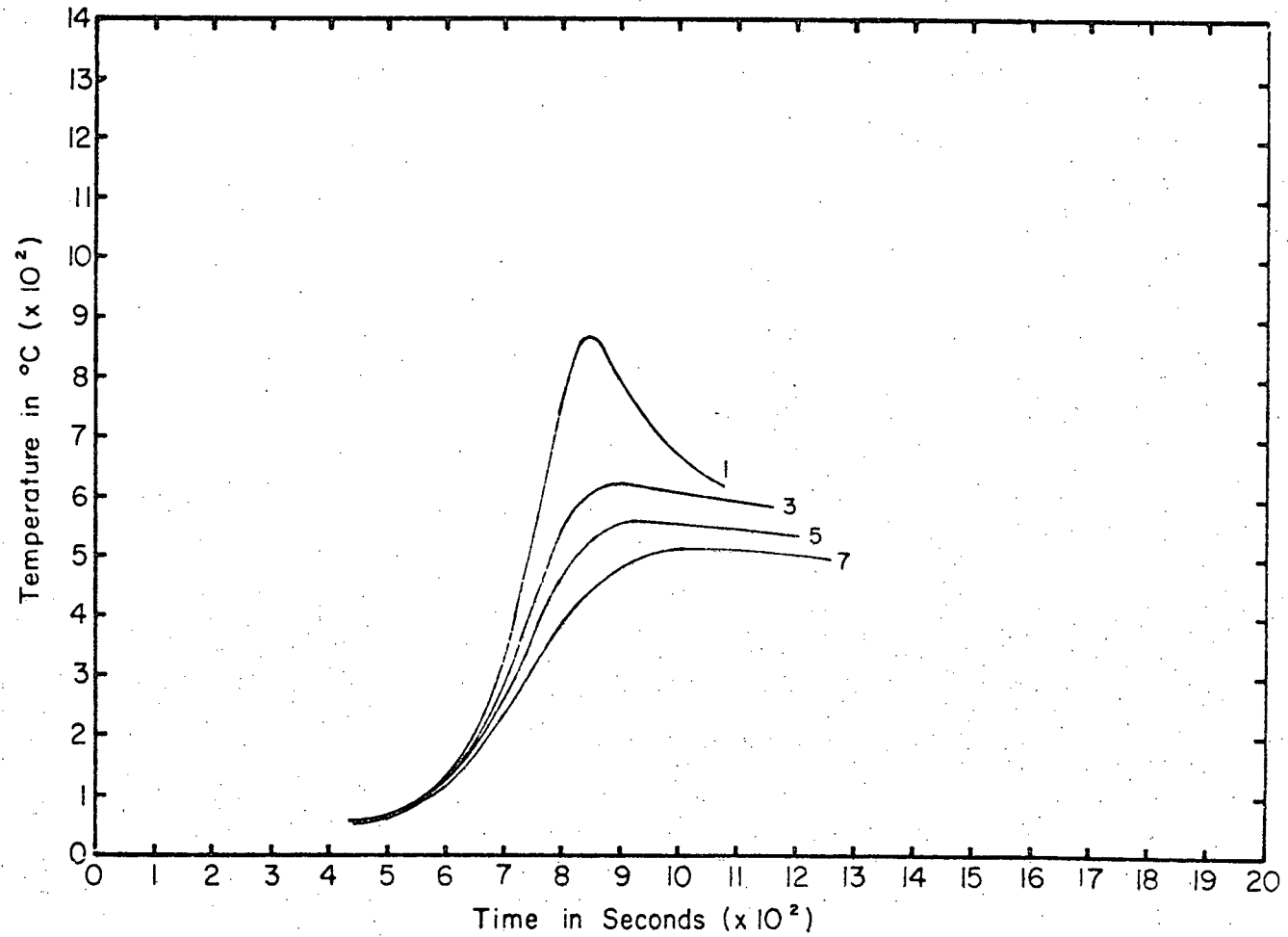


Figure 51 Thermal cycle for DCSP, experiment 8, same thermocouple positions as in Fig. 50.

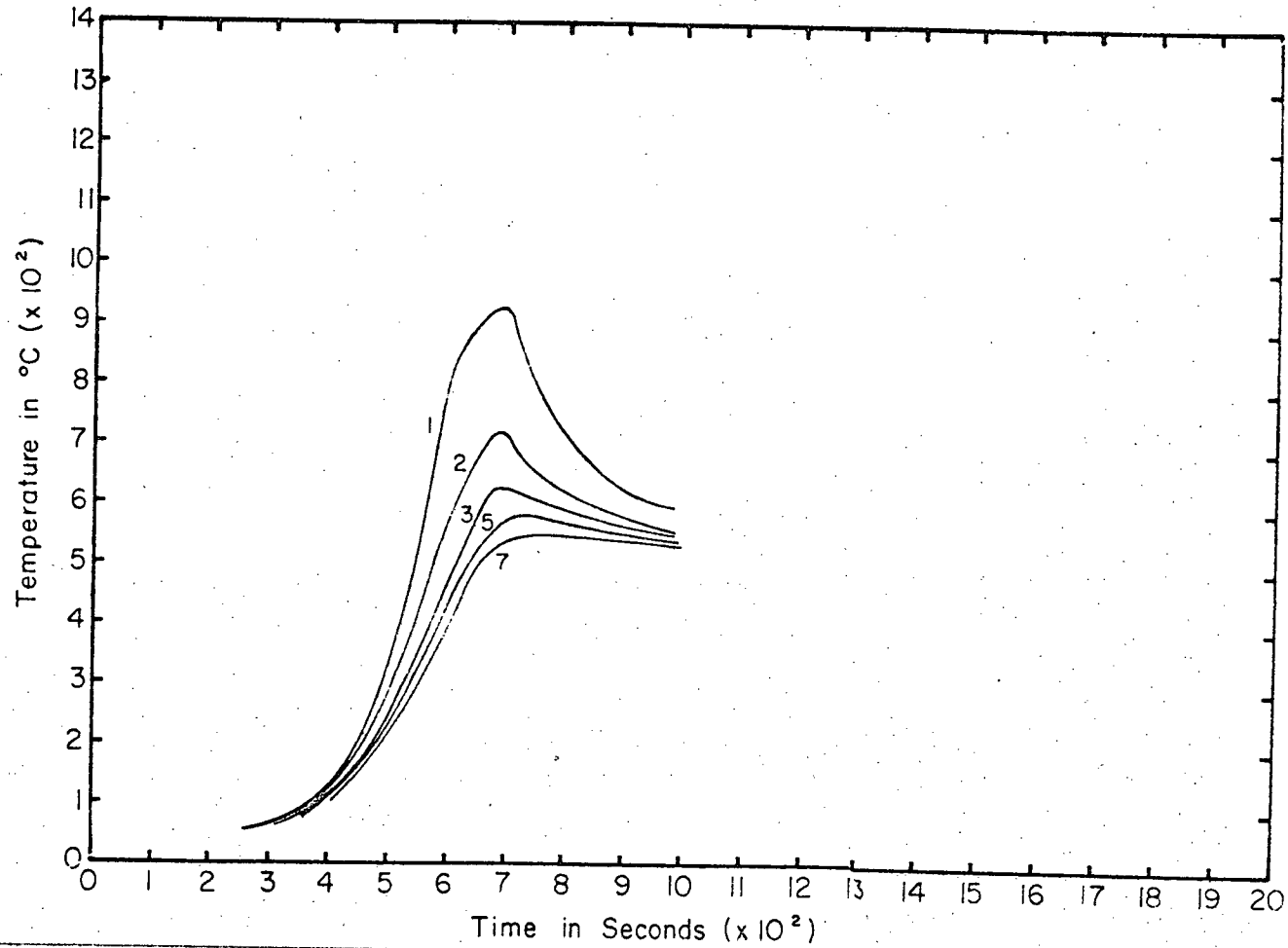


Figure 52 Thermal cycle for AC, experiment 14, same thermocouple positions as in Fig. 50.

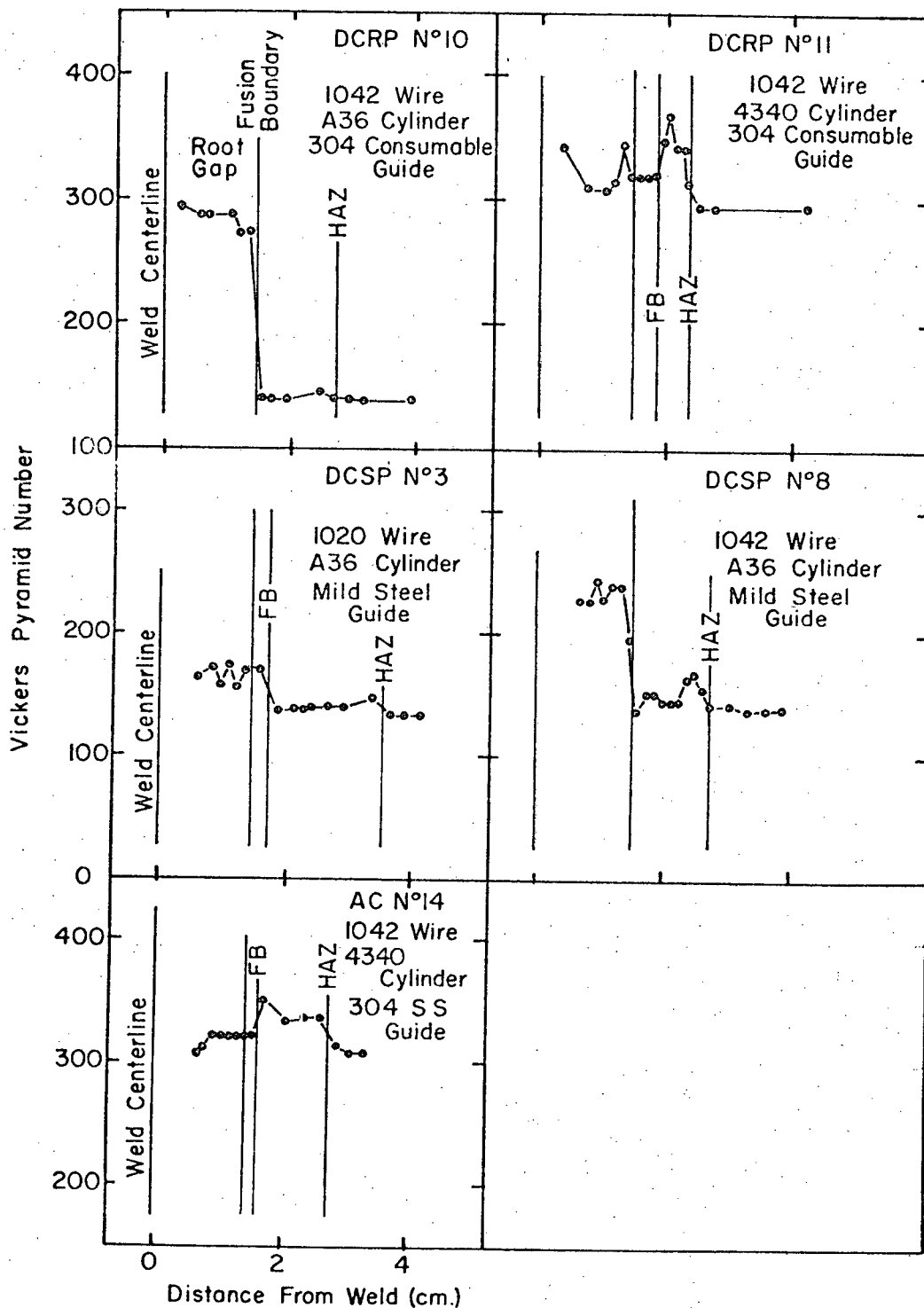


Figure 53 Example Vickers hardness traverses for CGESW cylinders

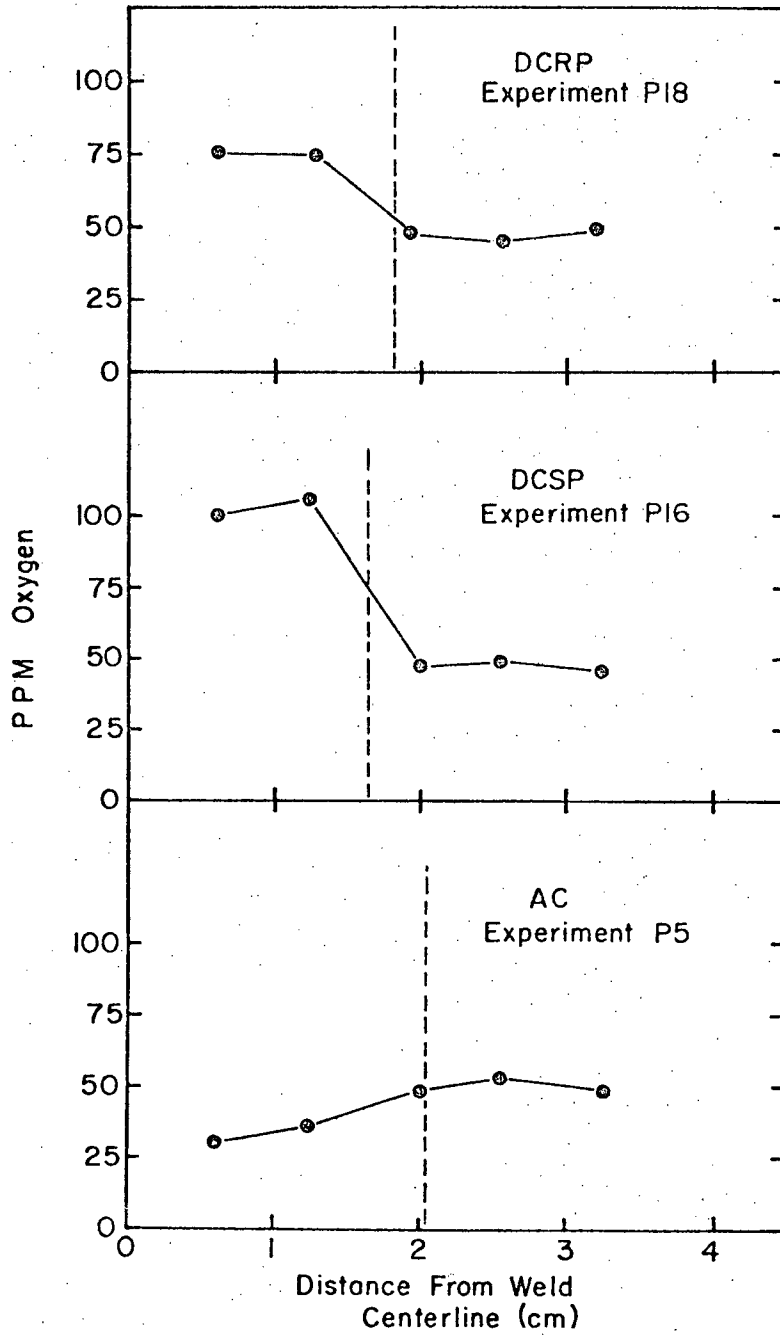


Figure 54 Representative oxygen values for CGESW cylinders



Figure 55 Macrograph of etched weld produced using a 304 S.S. consumable guide

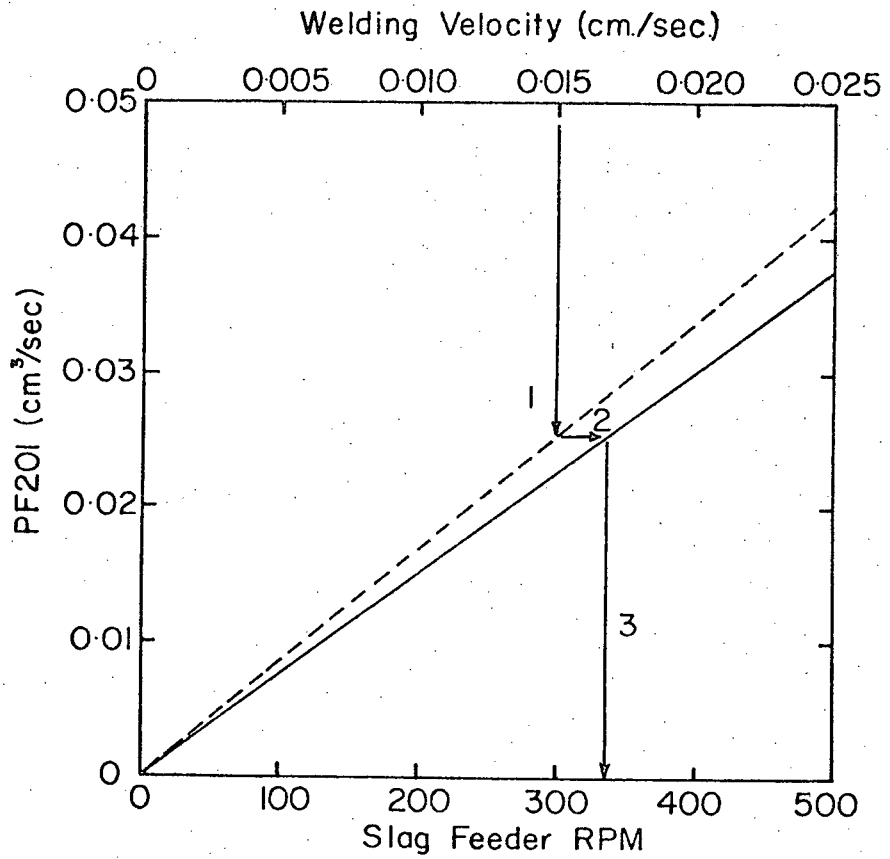


Figure 56 Calibration curve for slag feeder and method for determining slag addition rate

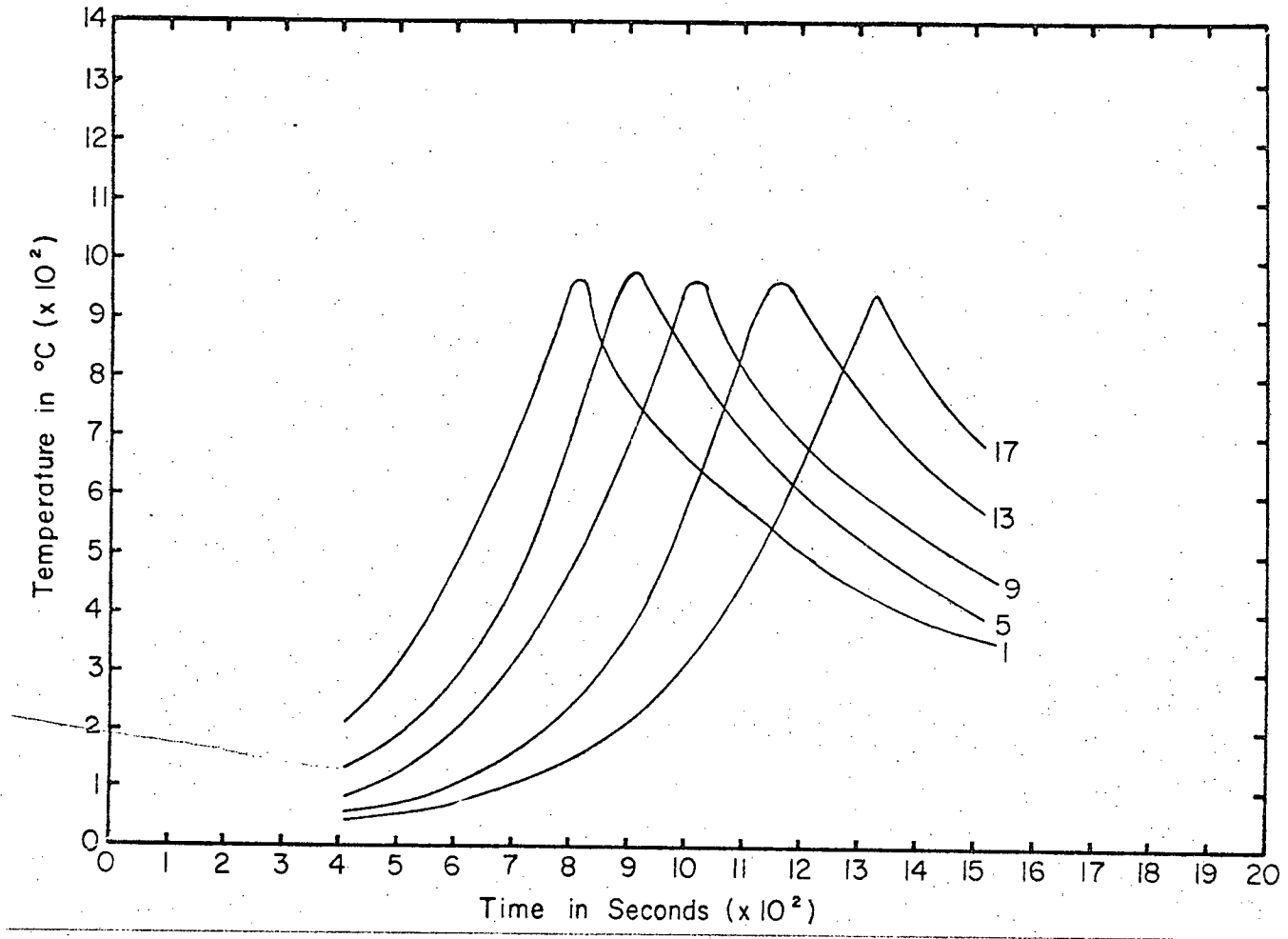


Figure 57 Thermal profiles for all thermocouples $\frac{1}{4}$ inch from the original surface for experiment P15.

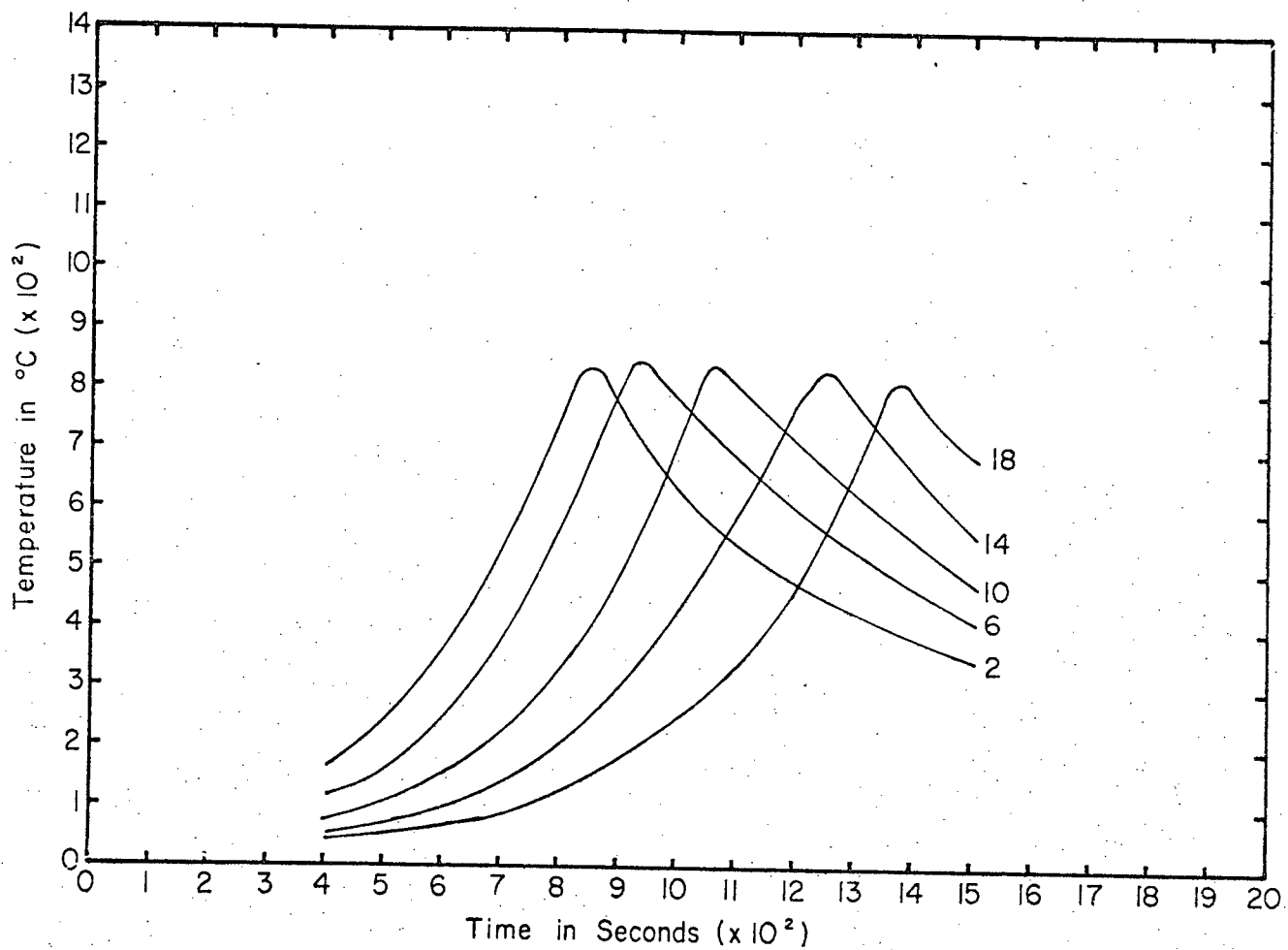


Figure 58 Thermal profiles for all thermocouples $\frac{1}{2}$ inch from the original surface for experiment P15.

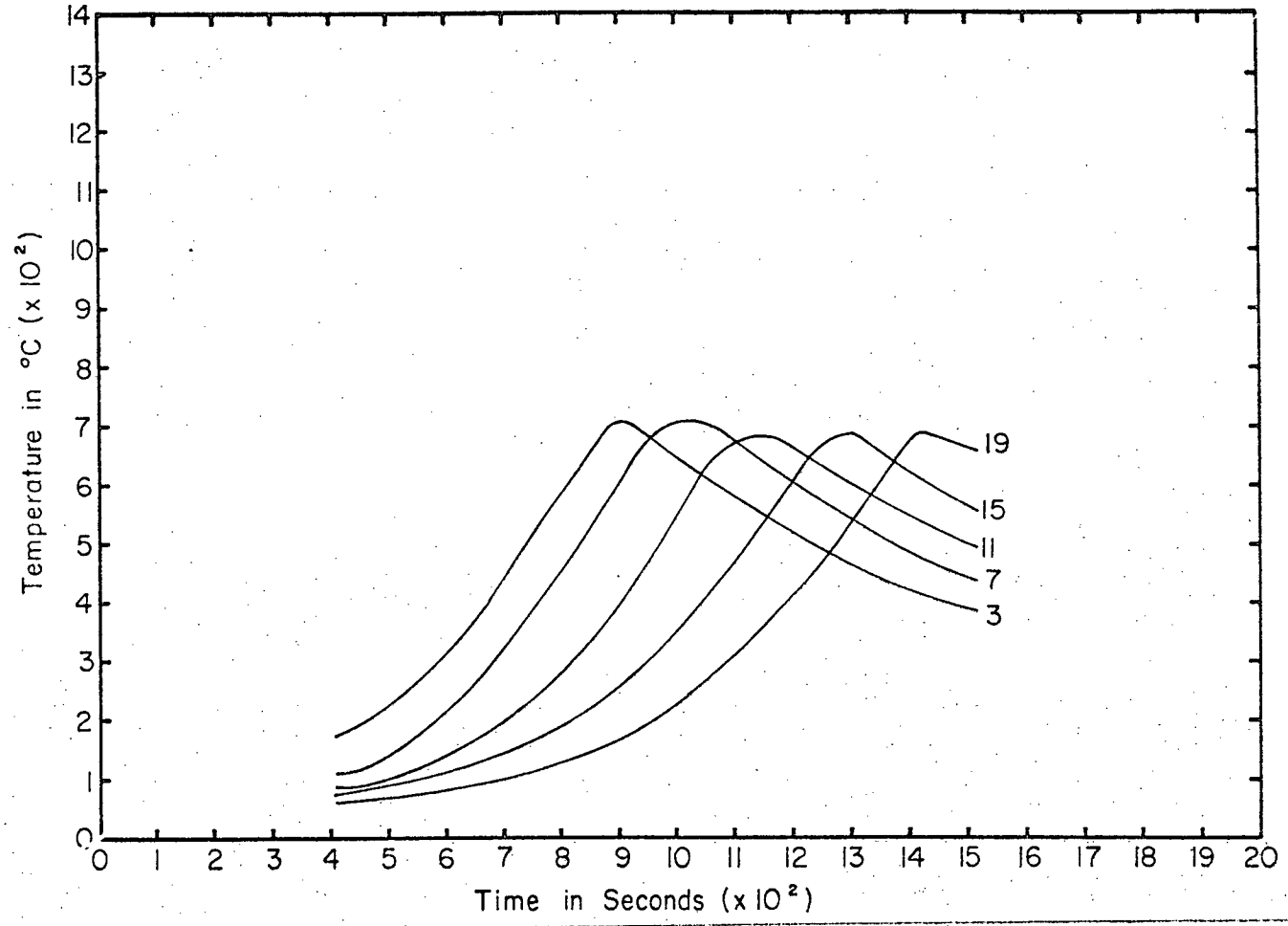


Figure 59 Thermal profiles for all thermocouples 3/4 inch from the original surface for experiment P15.

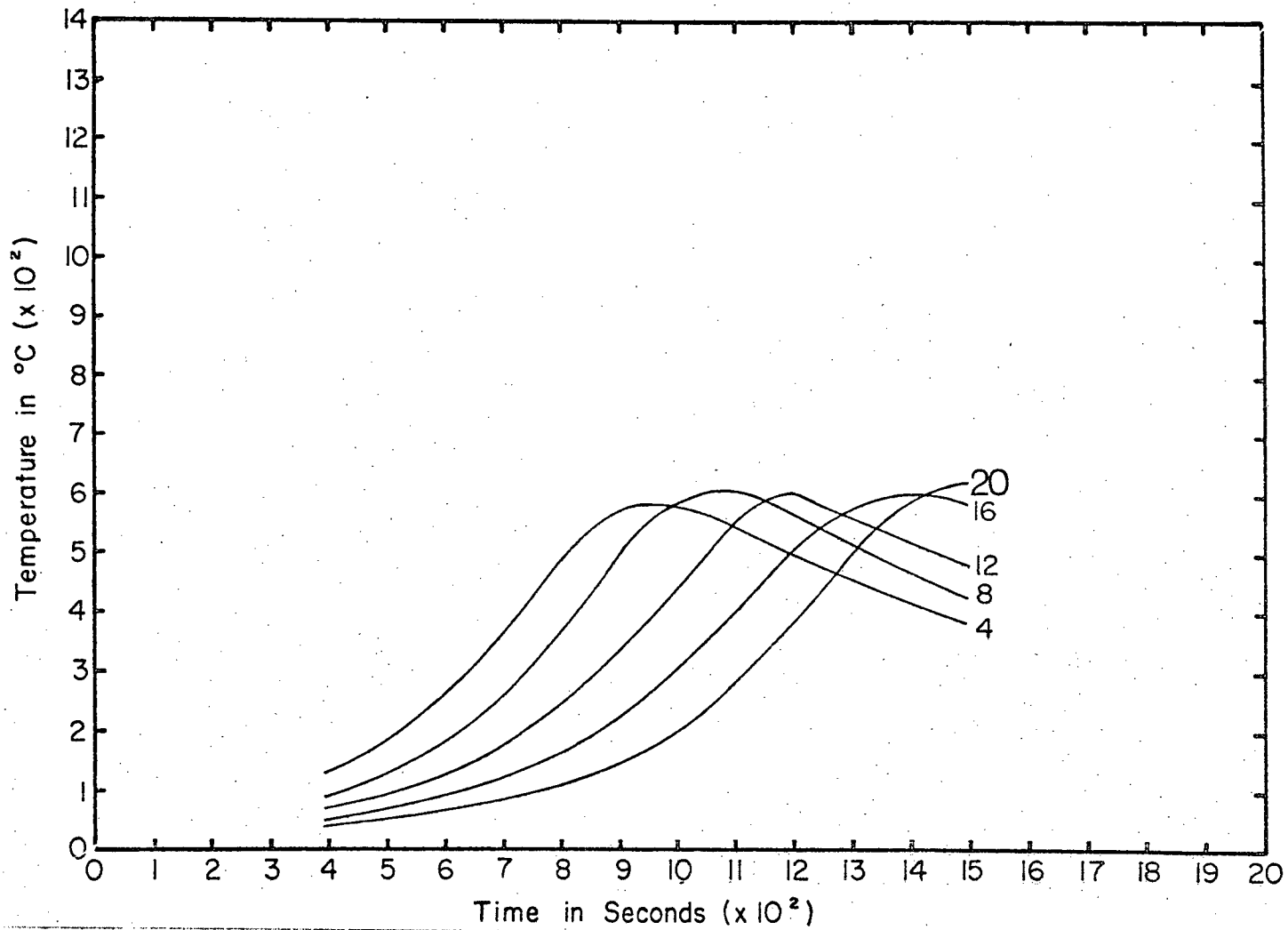
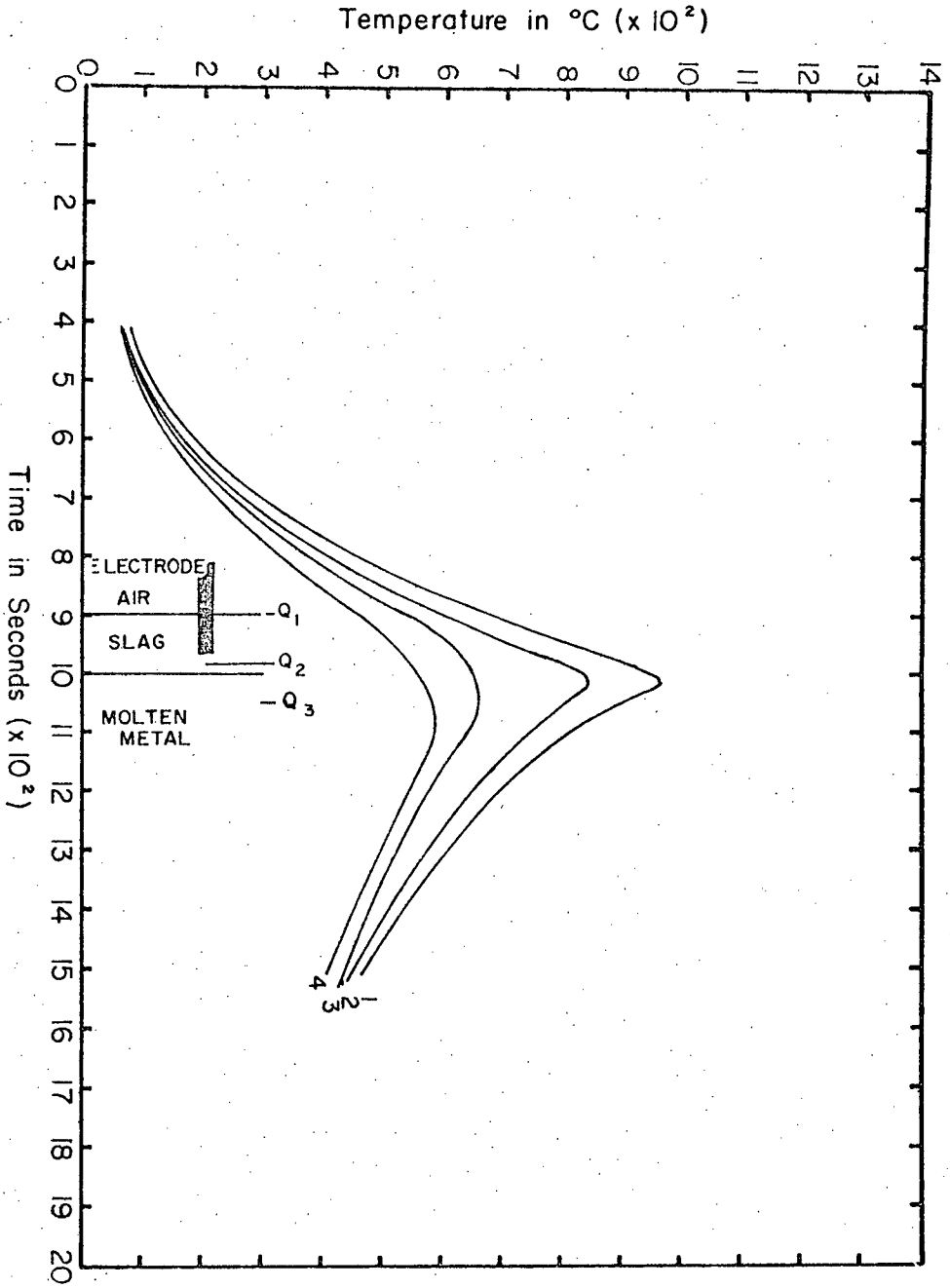


Figure 60 Thermal profiles for all thermocouples 1 inch from the original surface for experiment P15.

Figure 61 Thermal profiles for experiment P15.



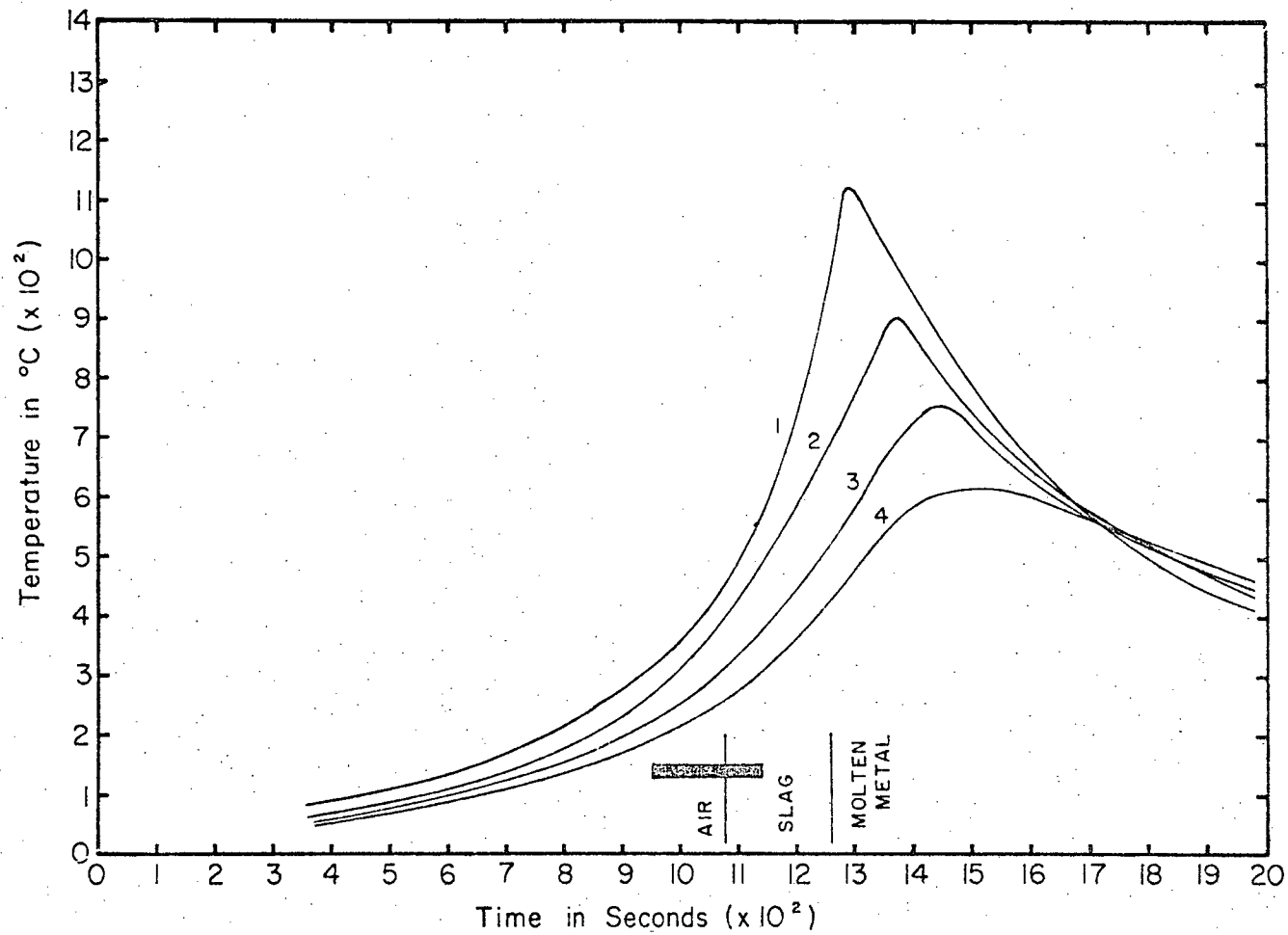
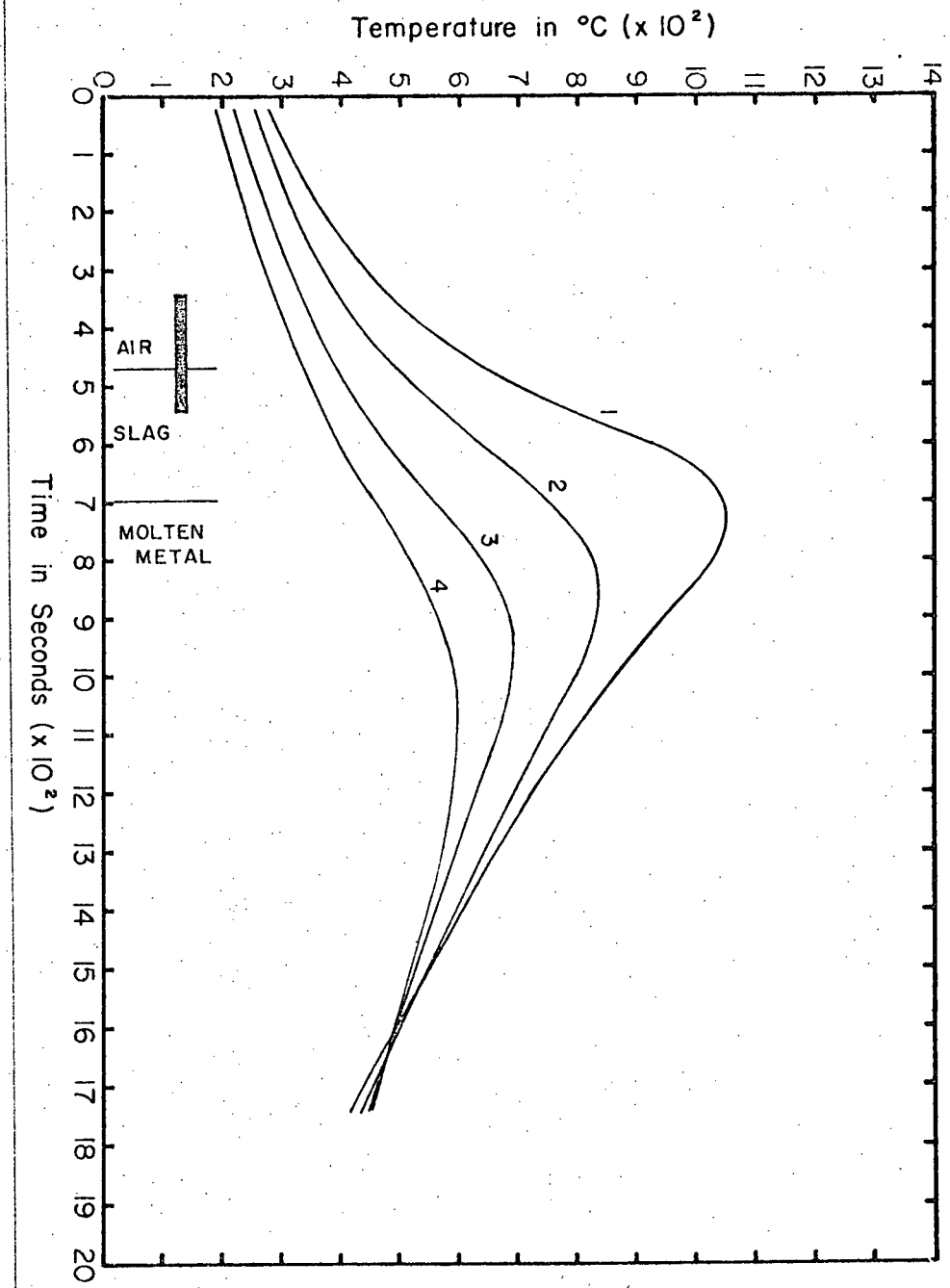


Figure 62 Thermal profiles for experiment P04.

Figure 63 Thermal profiles for experiment P05.



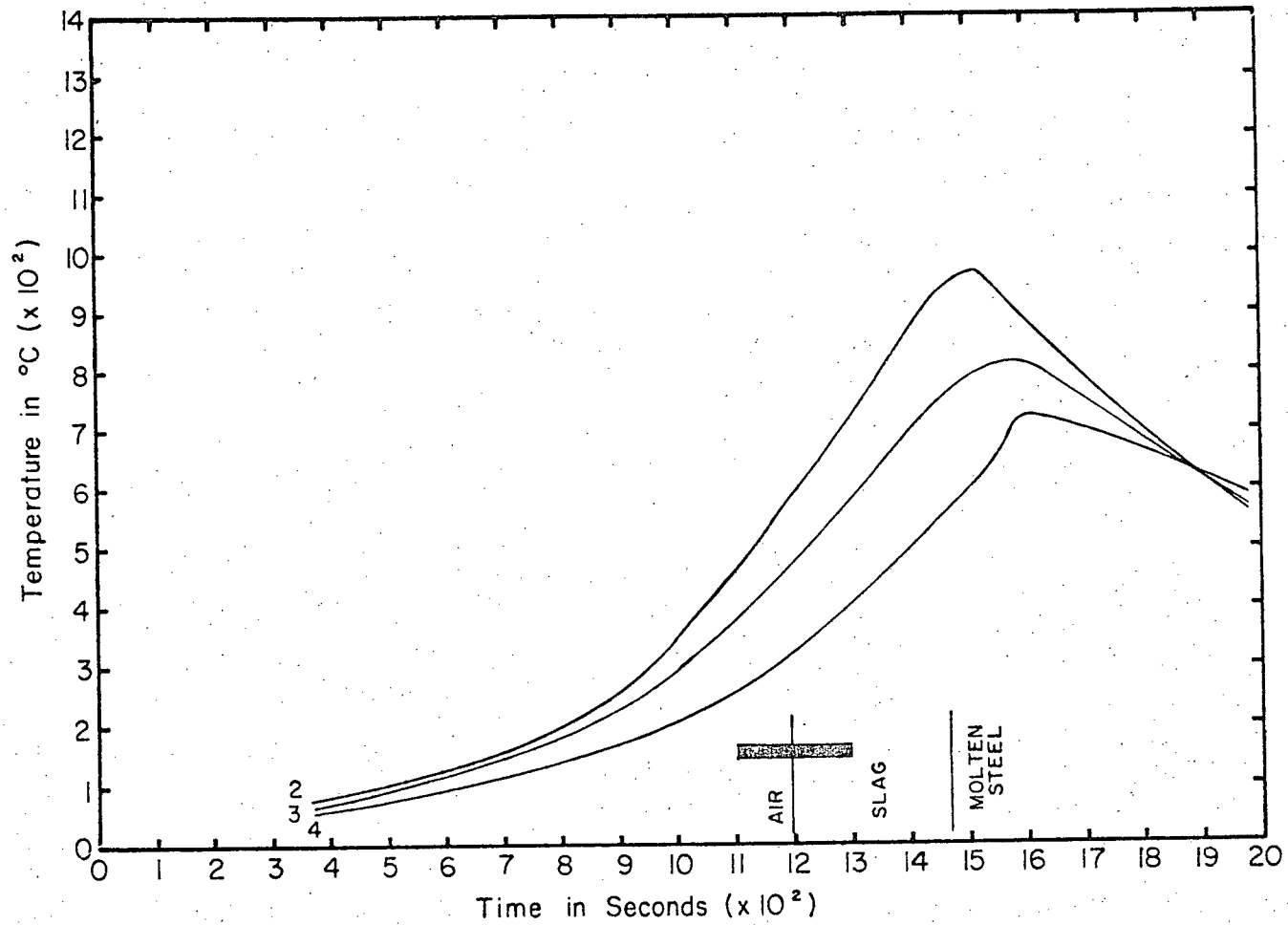


Figure 64 Thermal profiles for experiment P08.

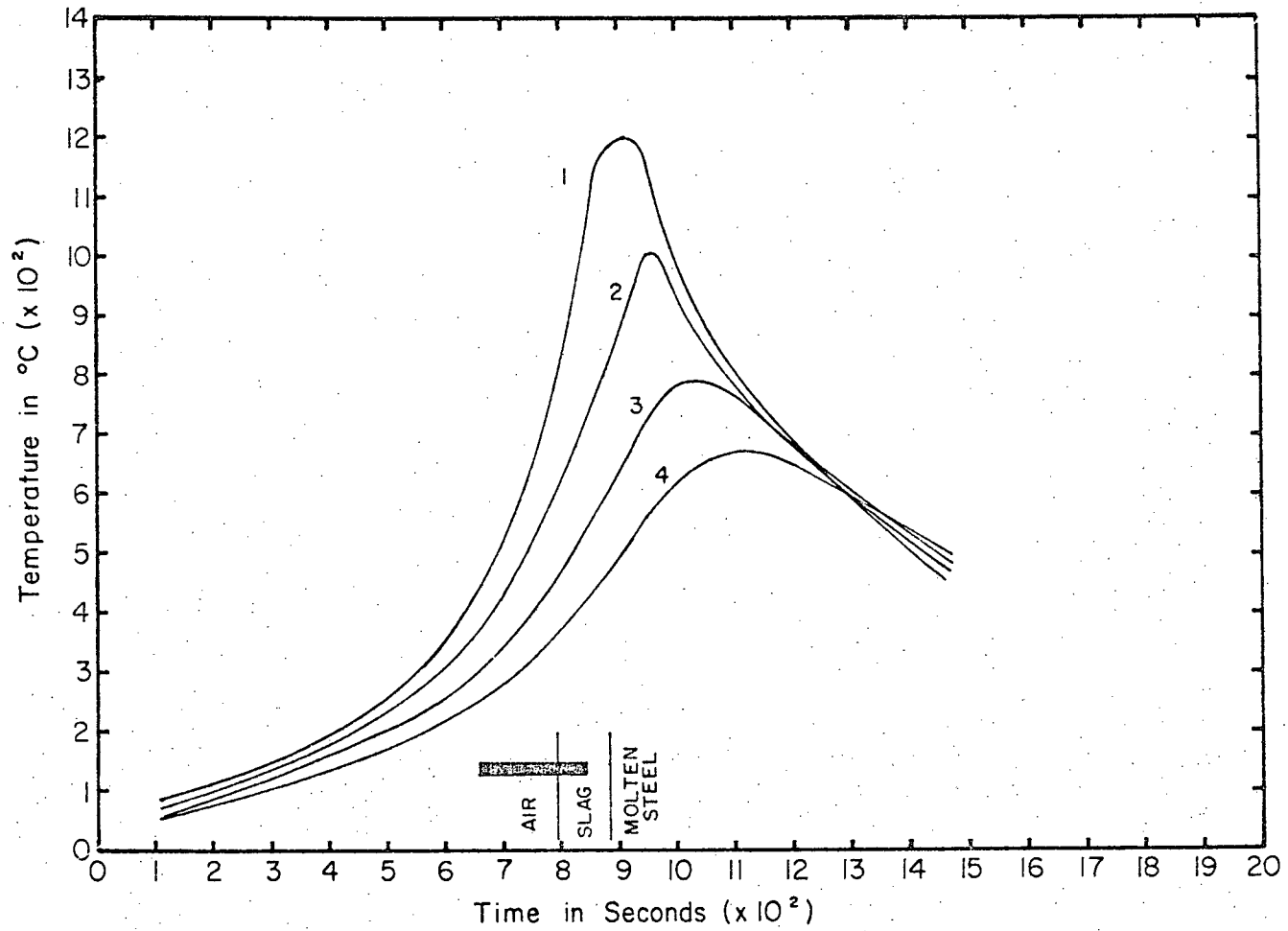


Figure 65 Thermal profiles for experiment P10.

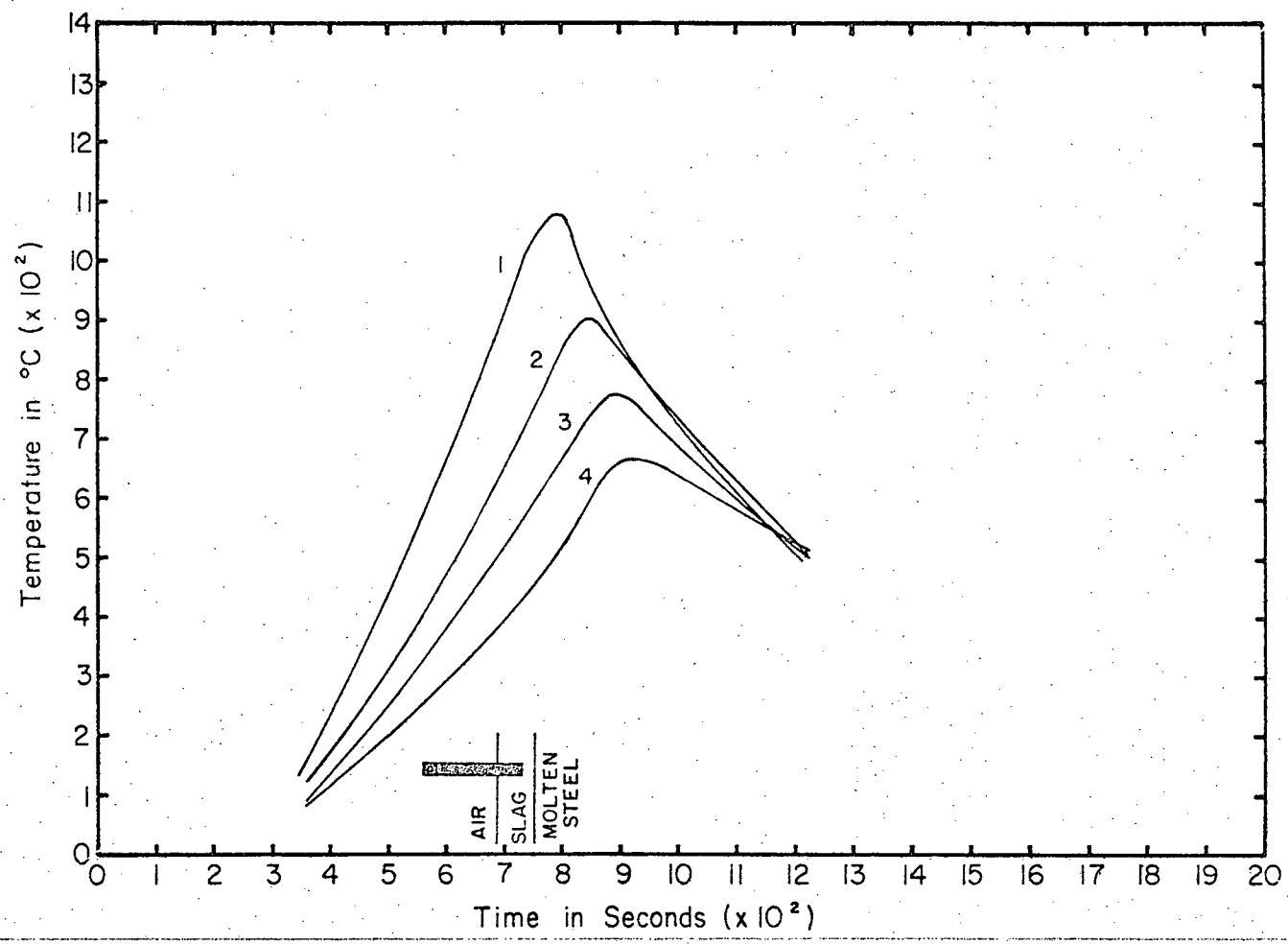


Figure 66 Thermal profiles for experiment P11.

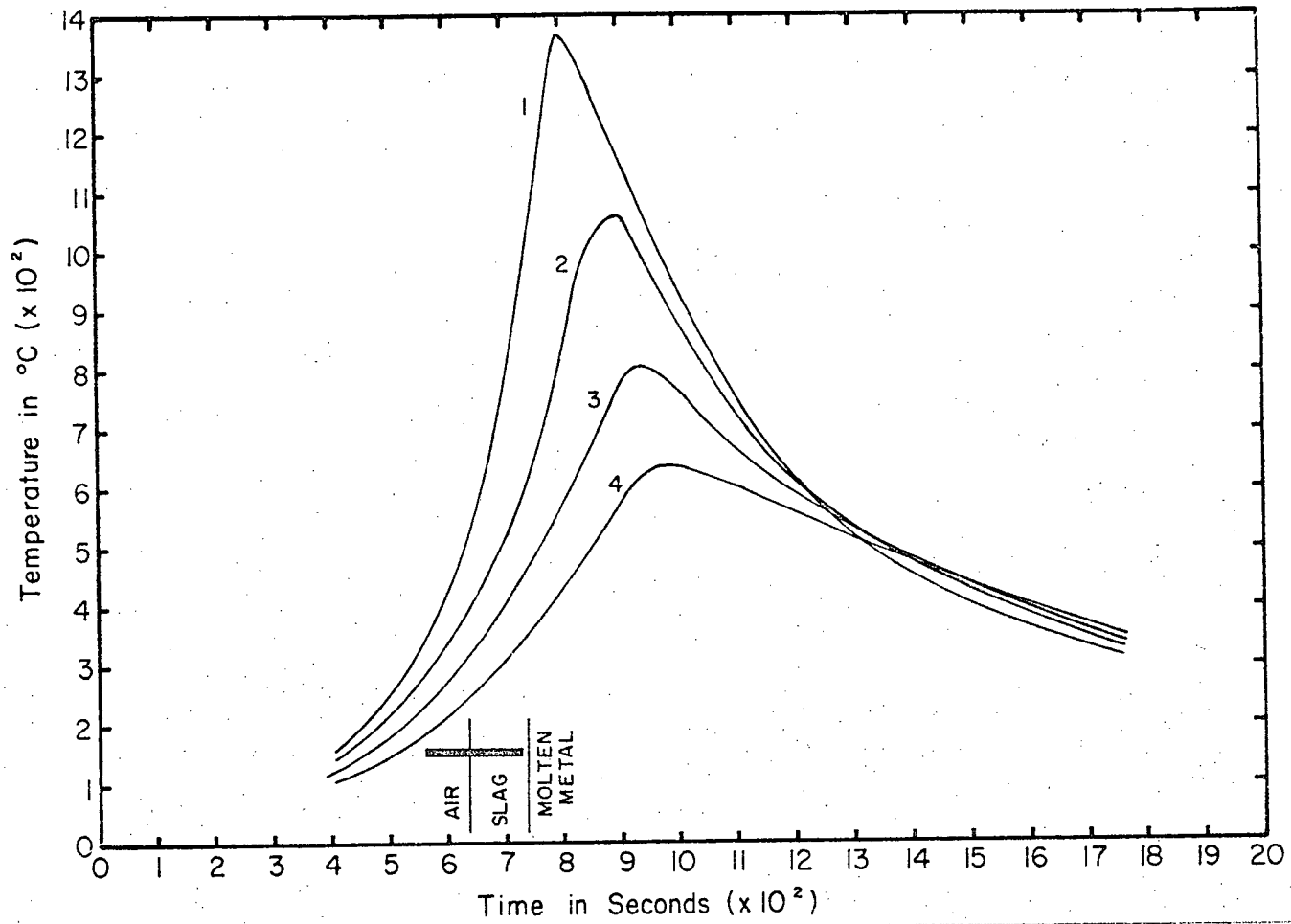


Figure 67 Thermal profiles for experiment P13.

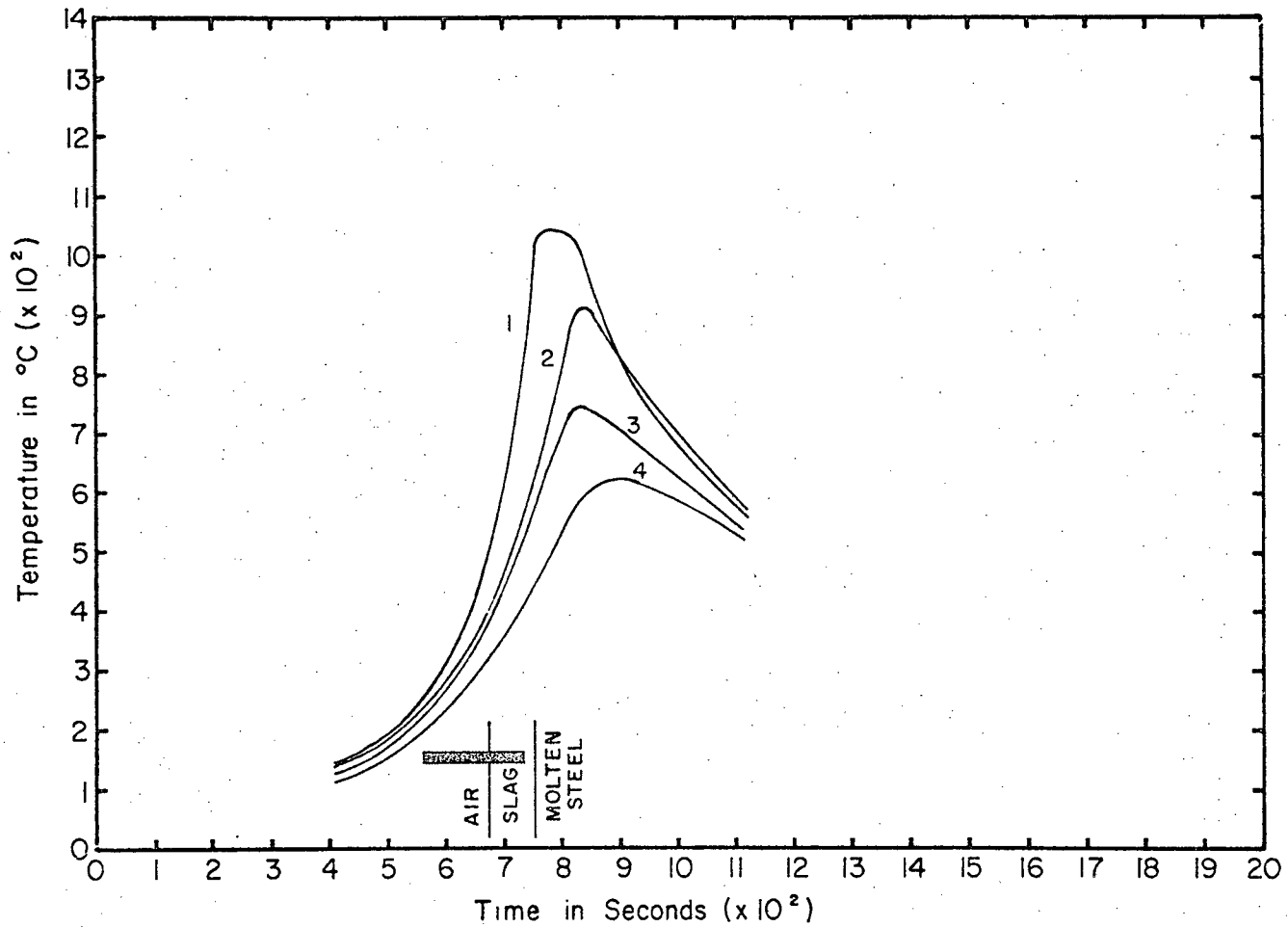
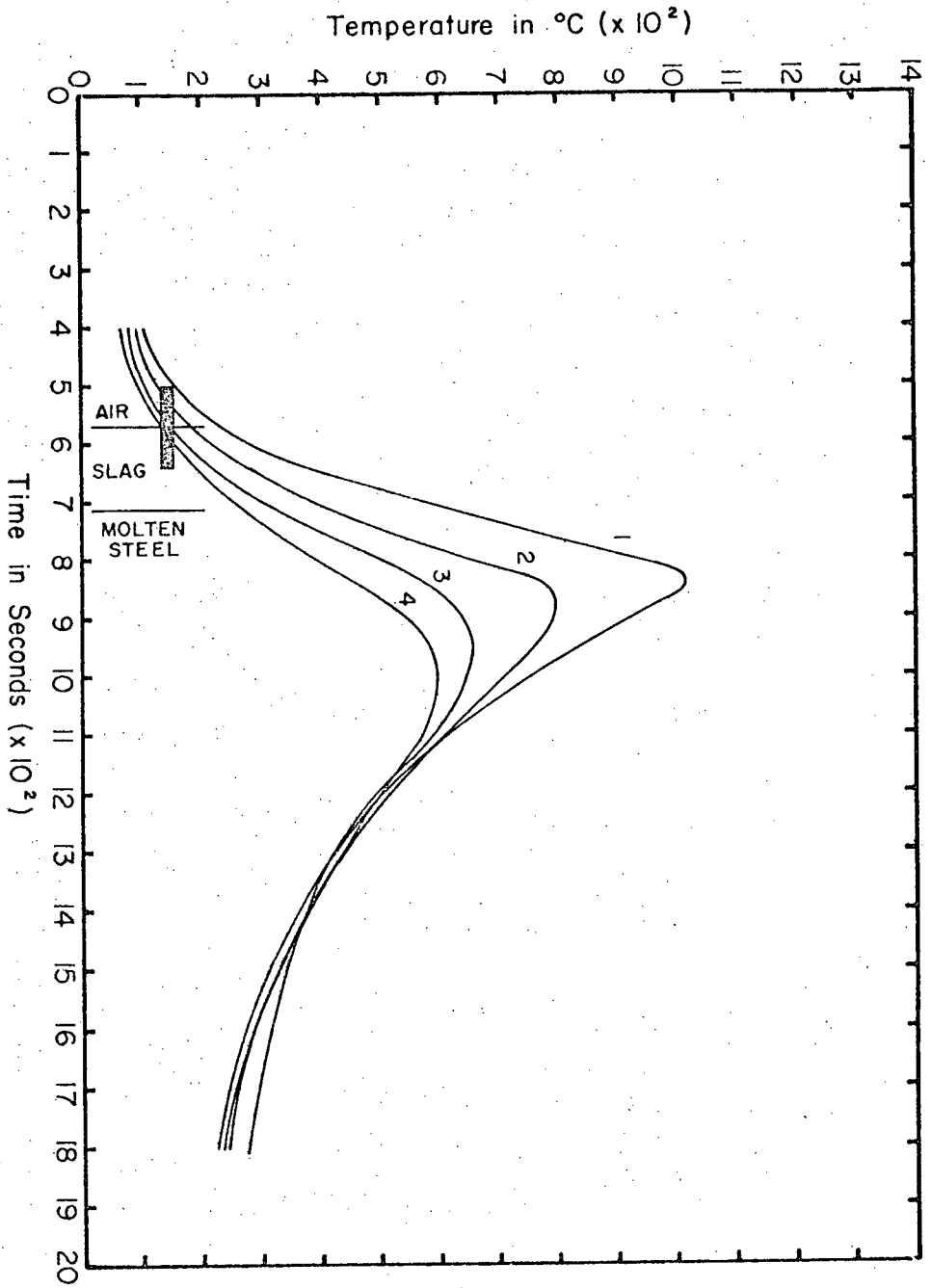


Figure 68 Thermal profiles for experiment P14.

Figure 69 Thermal profiles for experiment P16.



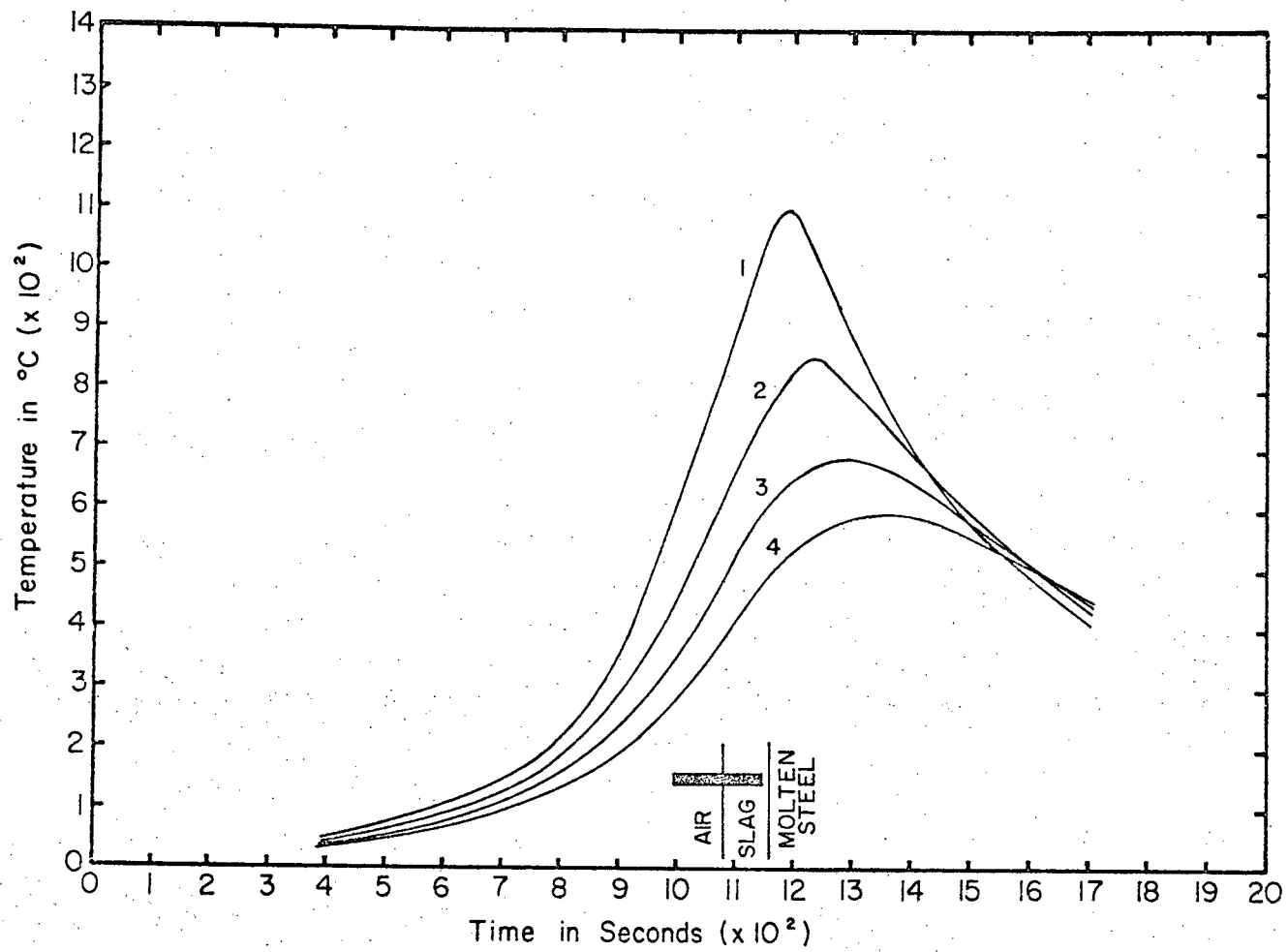
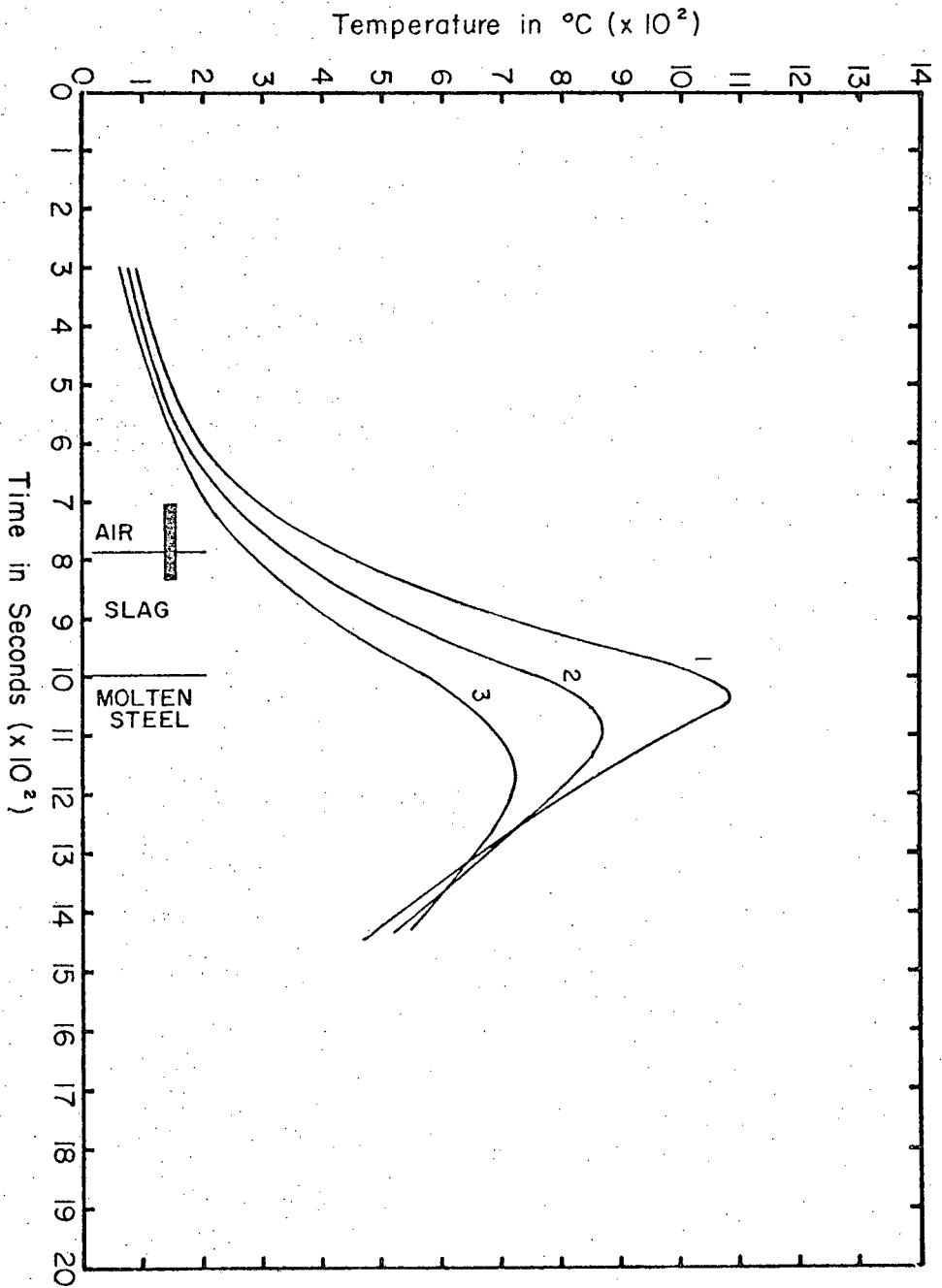


Figure 70 Thermal profiles for experiment P18.

Figure 71 Thermal profiles for experiment P21S.



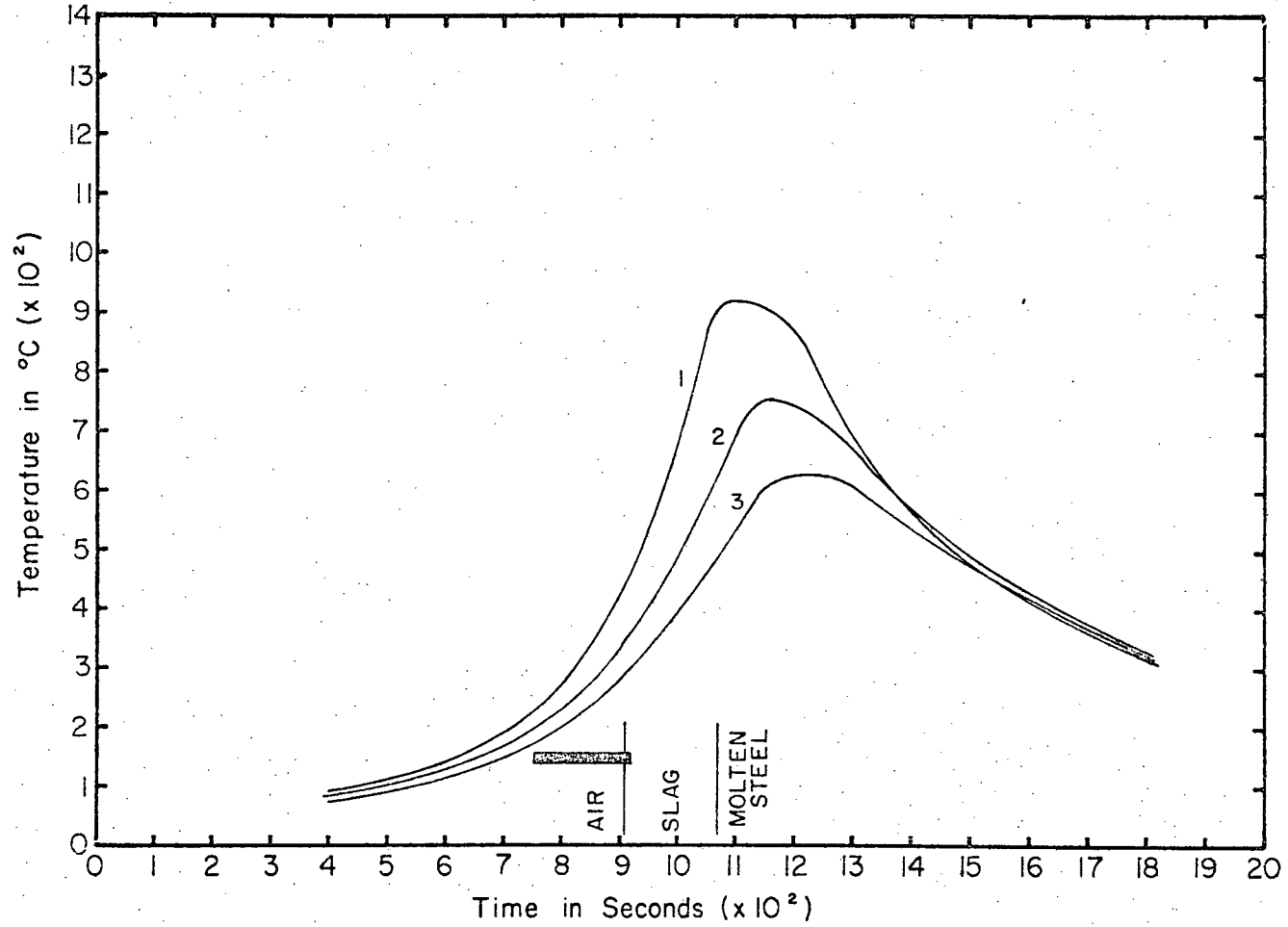
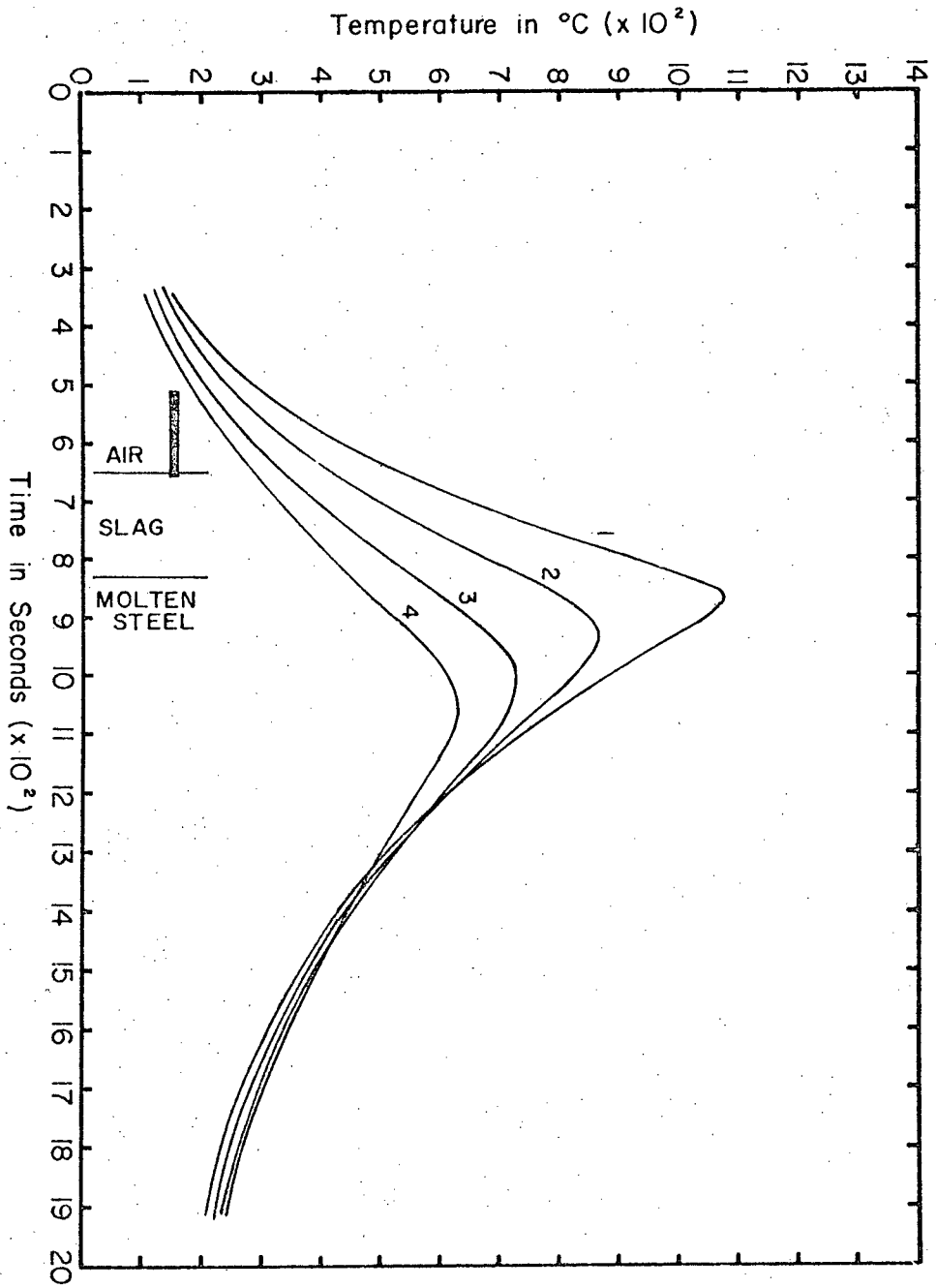


Figure 72 Thermal profiles for experiment P22S.

Figure 73 Thermal profiles for experiment P23S.



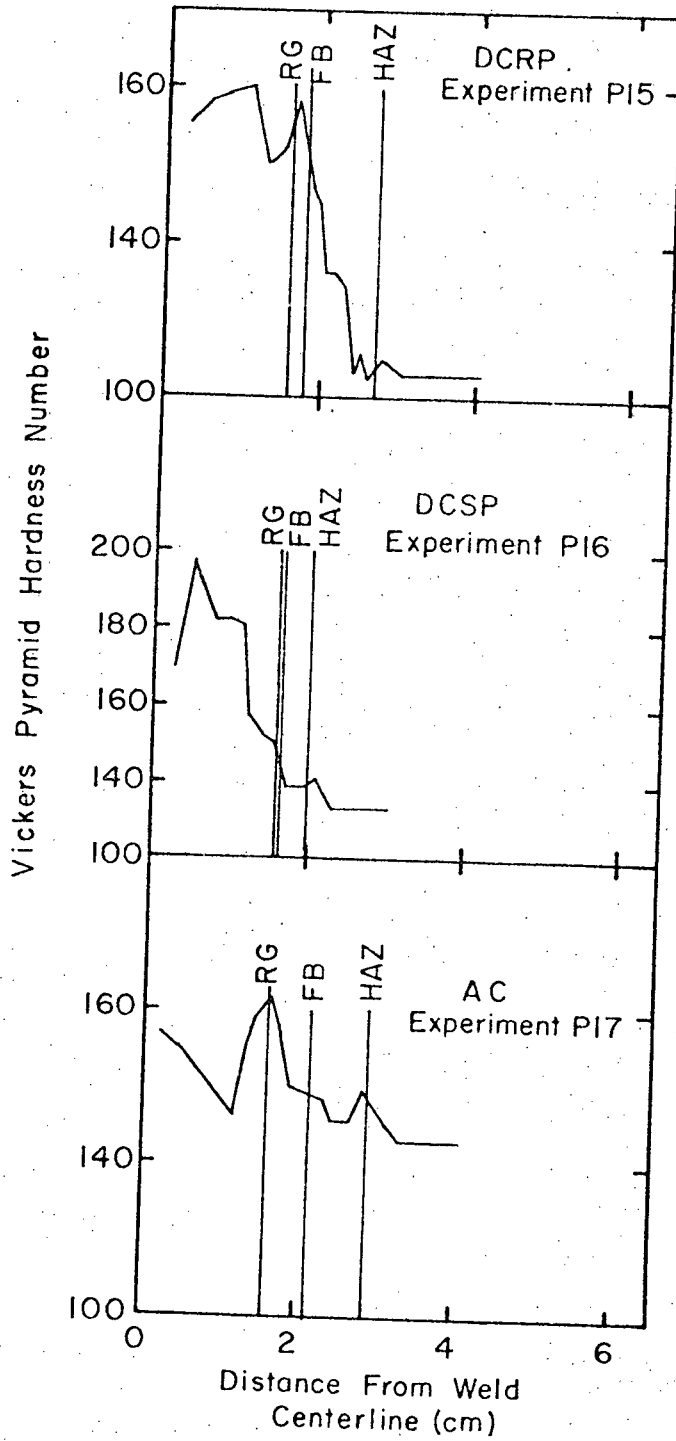


Figure 74 Typical hardness traverses for various degrees of fusion and modes of operation

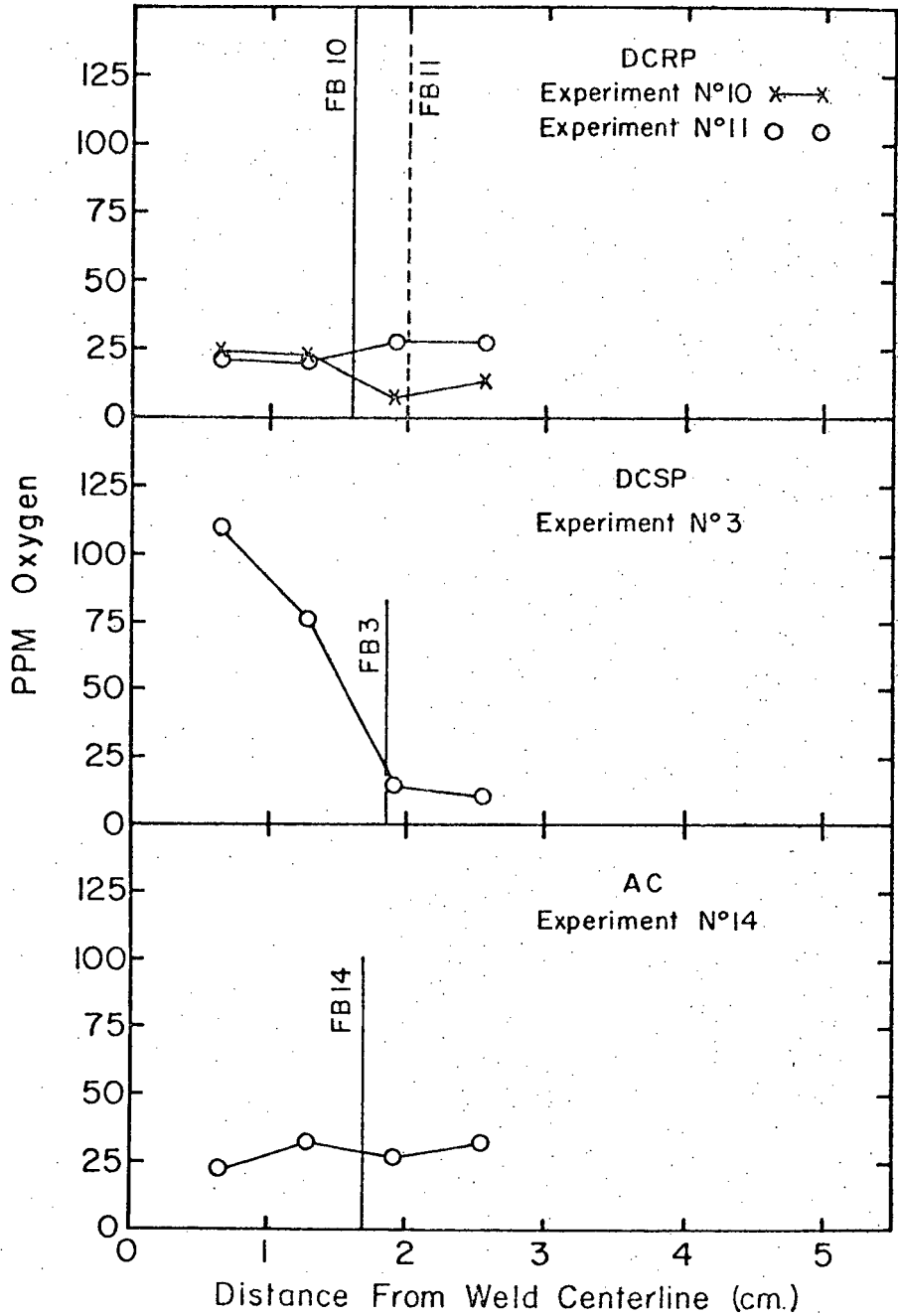


Figure 75 Oxygen values corresponding to the same traverses as Figure 74.

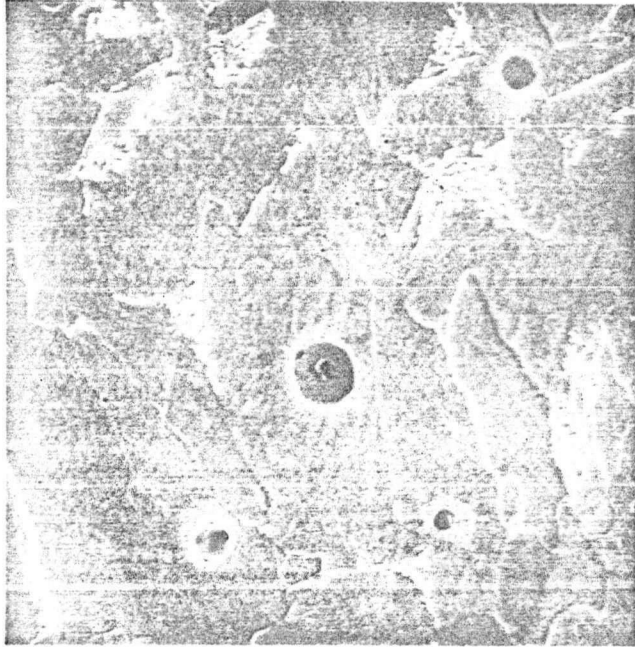


Figure 76 Inclusions in DCRP (≈ 3000 X magnification)

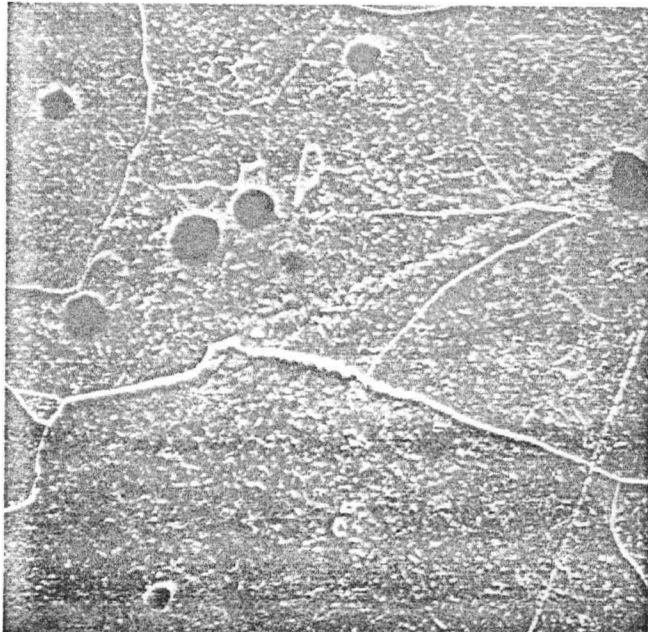


Figure 77 Inclusions in DCSP (≈ 3000 X magnification)

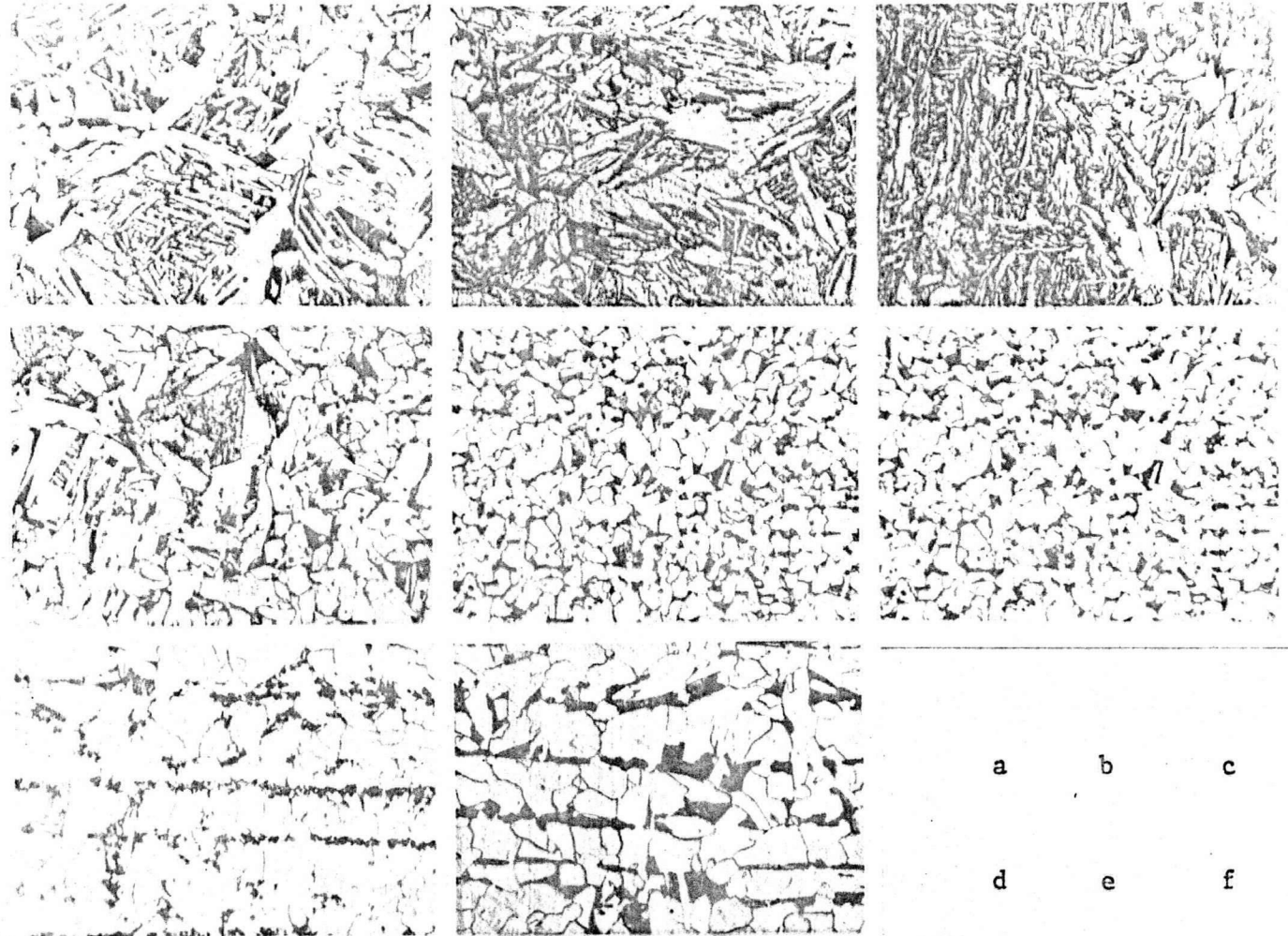


Figure 78

Micrographs of grain size variation with distance from fusion boundary in DCRP (P21); a, weld metal; b, adjacent to F.B.; c, 2mm; d, 4mm; e, 6mm; f, 10mm; g, 15mm; h, base metal. \approx 211X magnification

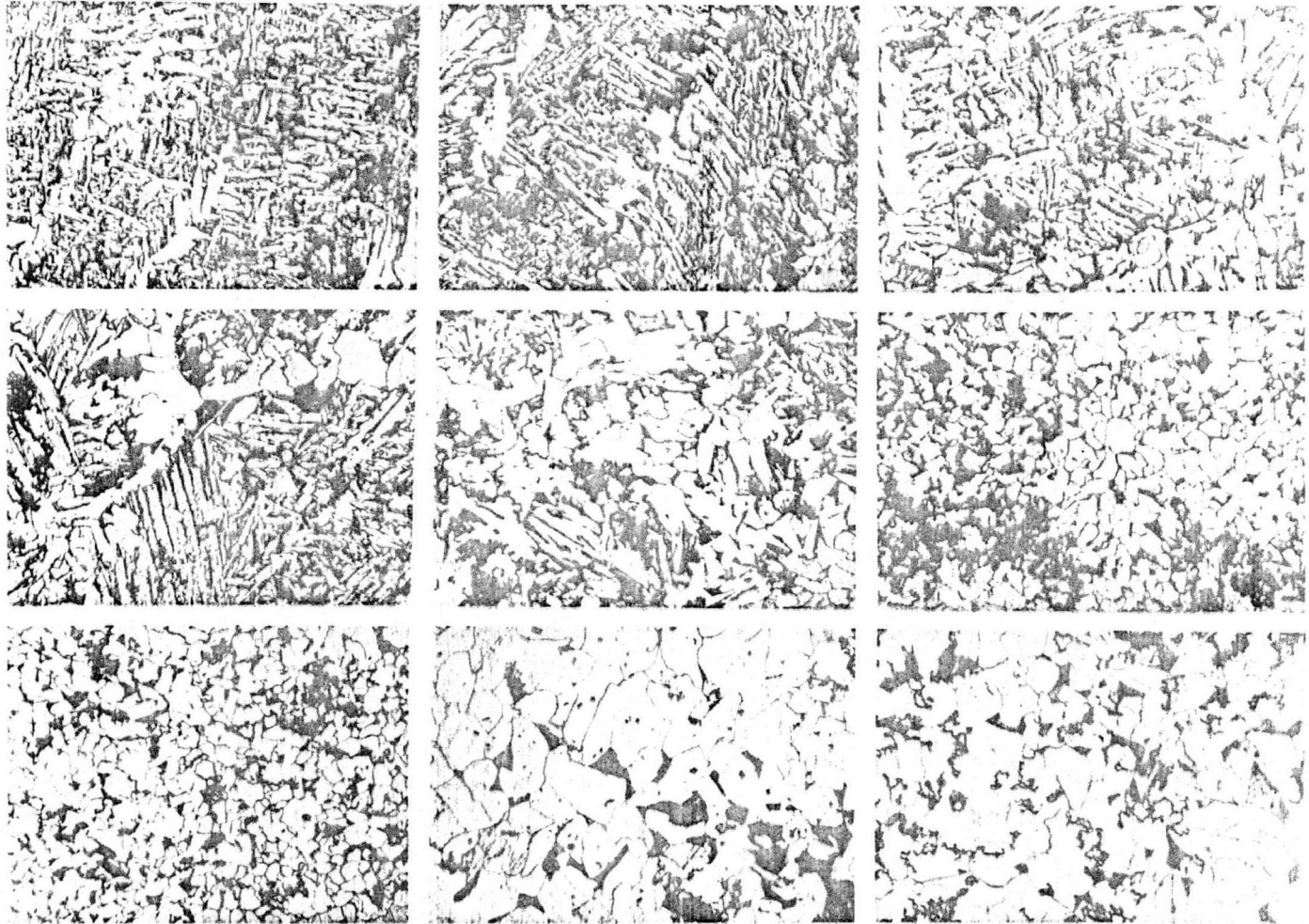
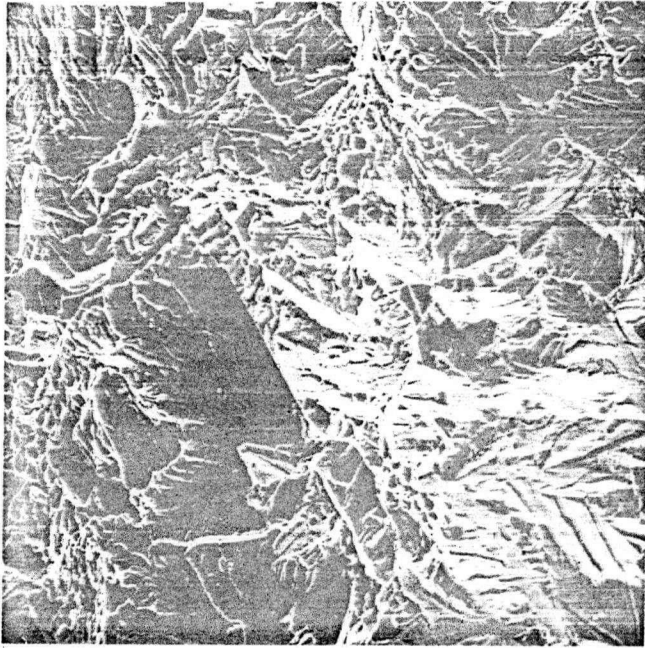
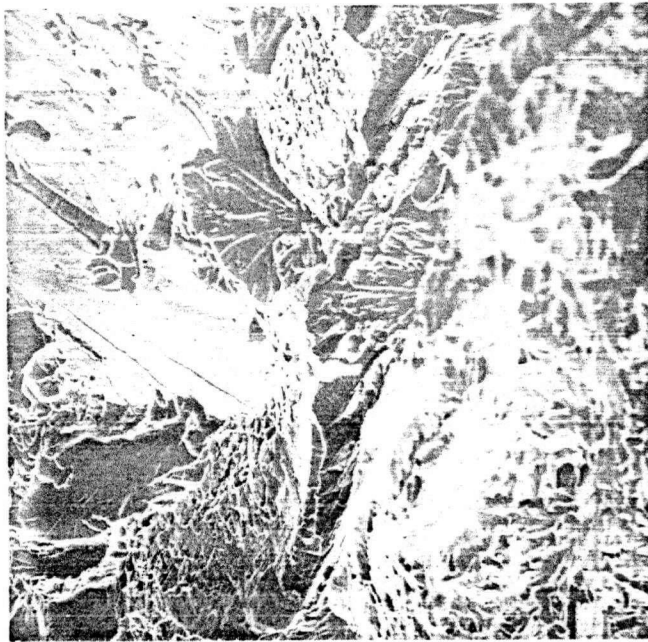


Figure 79 Micrographs of grain size variation with distance from fusion boundary in DCSP (P22); a, weld metal; b, adjacent to F.B.; c, 0.5mm; d, 1.0mm; e, 3.0mm; f, 6.0mm; g, 10mm; h, 15mm; i, parent metal. \approx 211X magnification



a, weld centerline $\times 200X$



b, 0.55mm into HAZ $\times 200X$

Figure 80 Fractograph of Charpy fracture surface (P21)

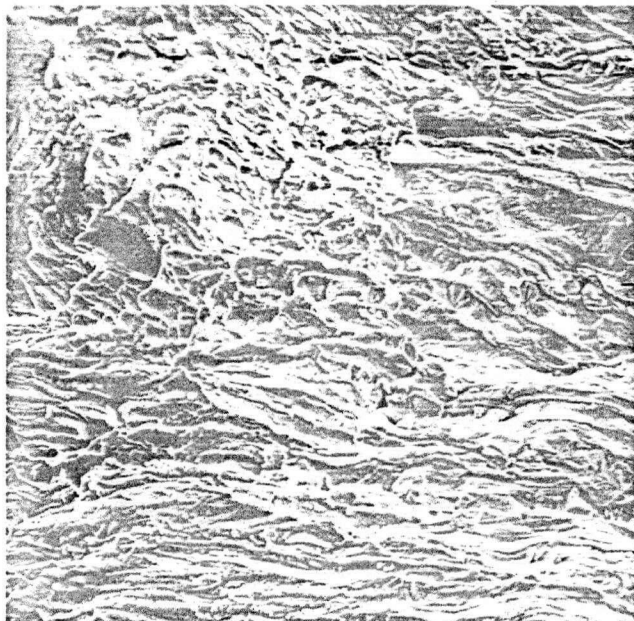


Figure 81 Fractograph of Charpy fracture surface 3.0mm into HAZ (P21) (\approx 200X)

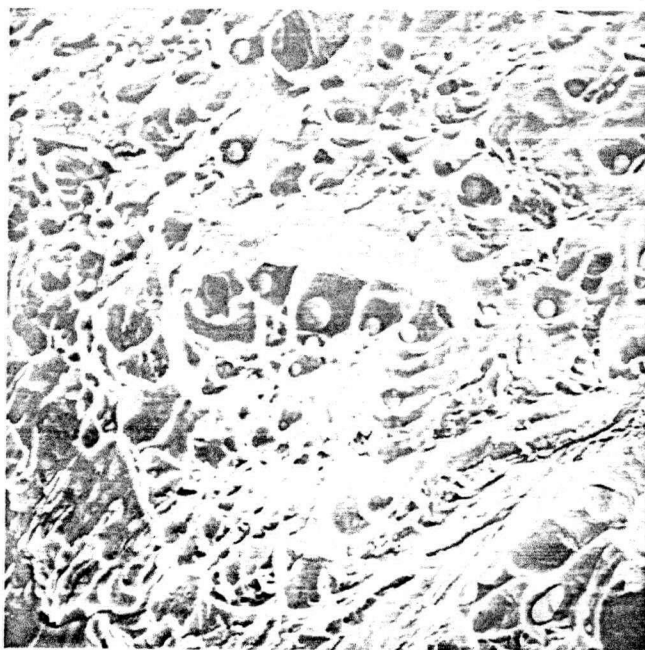


Figure 82 Fractograph of Charpy fracture surface in weld zone showing ductility and inclusions (P22) (\approx 1000X)



Figure 83 Fractograph of Charpy failure surface (P22) ($\approx 1000X$)

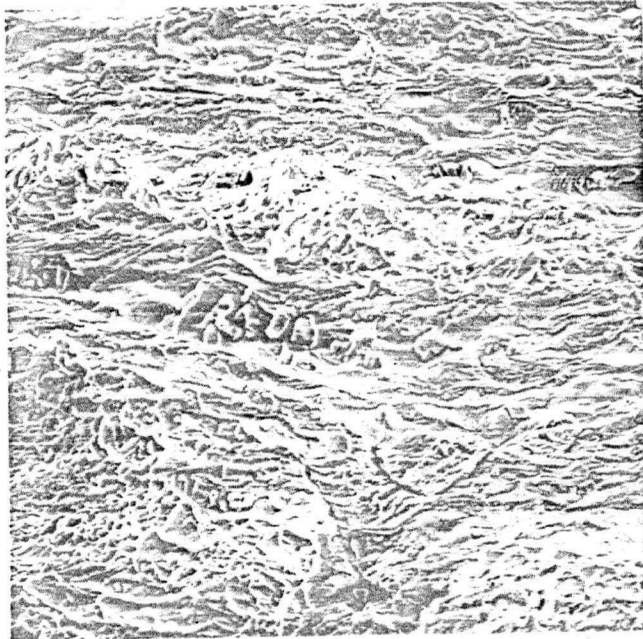
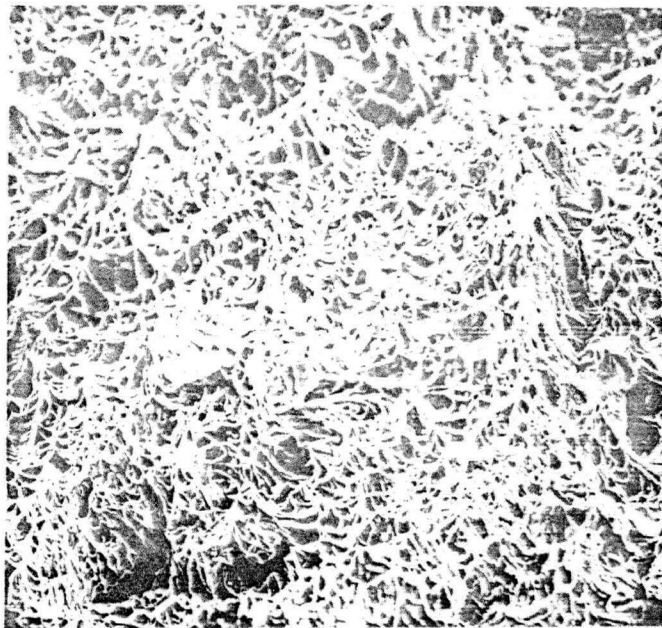


Figure 84 Fractograph of Charpy fracture surface in spheroidized zone (P22) (\approx 200X)

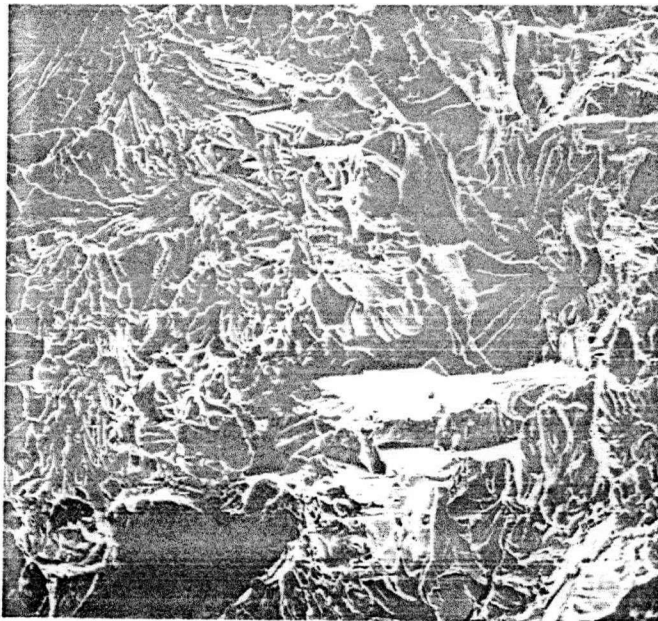


a. weld outline

Figure 85 Fractograph of Charpy fracture surface (P23) (\approx 200X)



b. Adjacent to F.B. in the HAZ ($\approx 200X$)



c. 1.5mm into HAZ from F.B.
Figure 85 Fractograph of Charpy fracture surface (P23) ($\approx 200X$)



Figure 86 Fractograph of Charpy surface 1.5mm into HAZ from F.B.
($\approx 100X$)

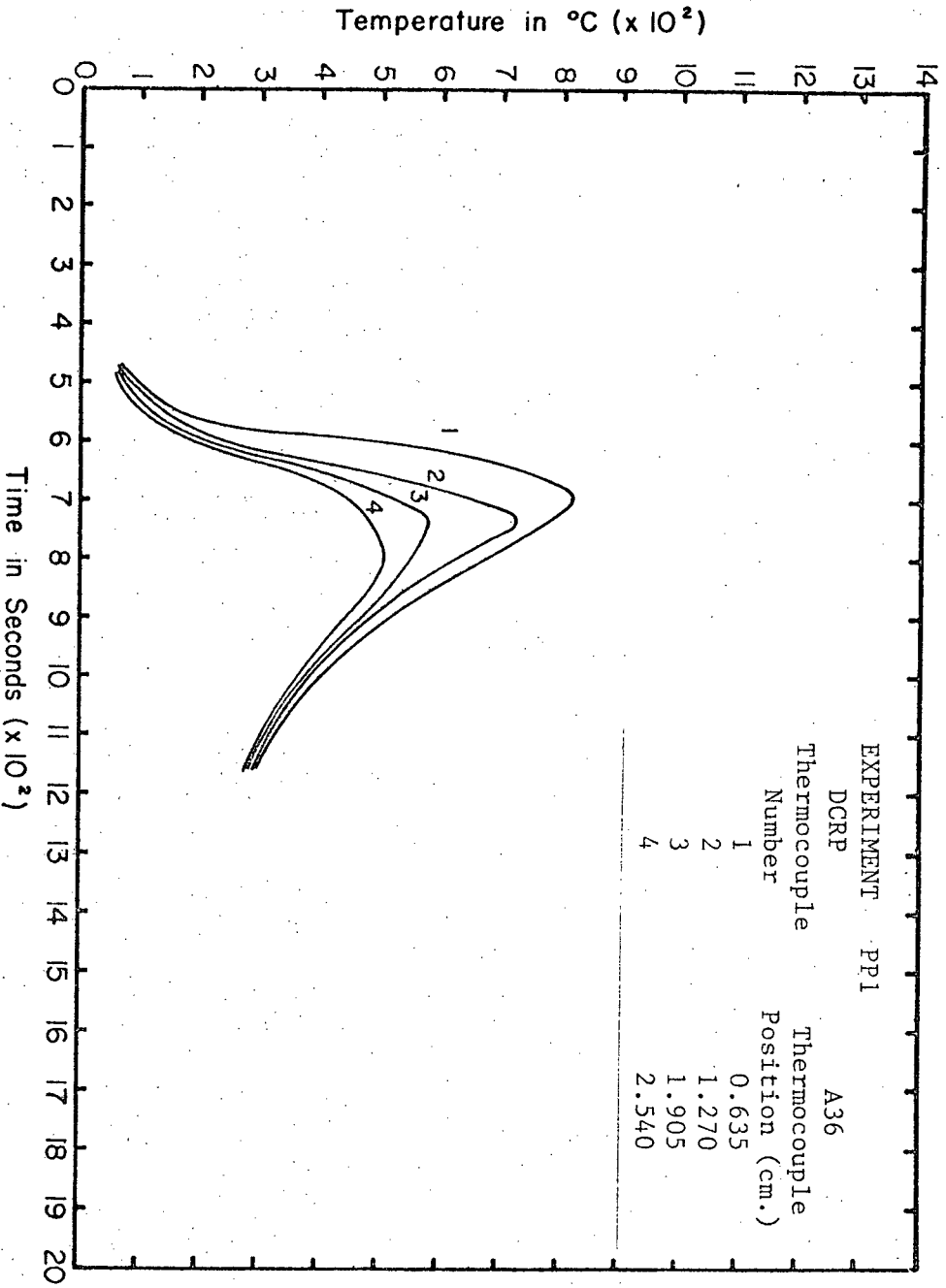


Figure 87 Thermal profile for PPI.

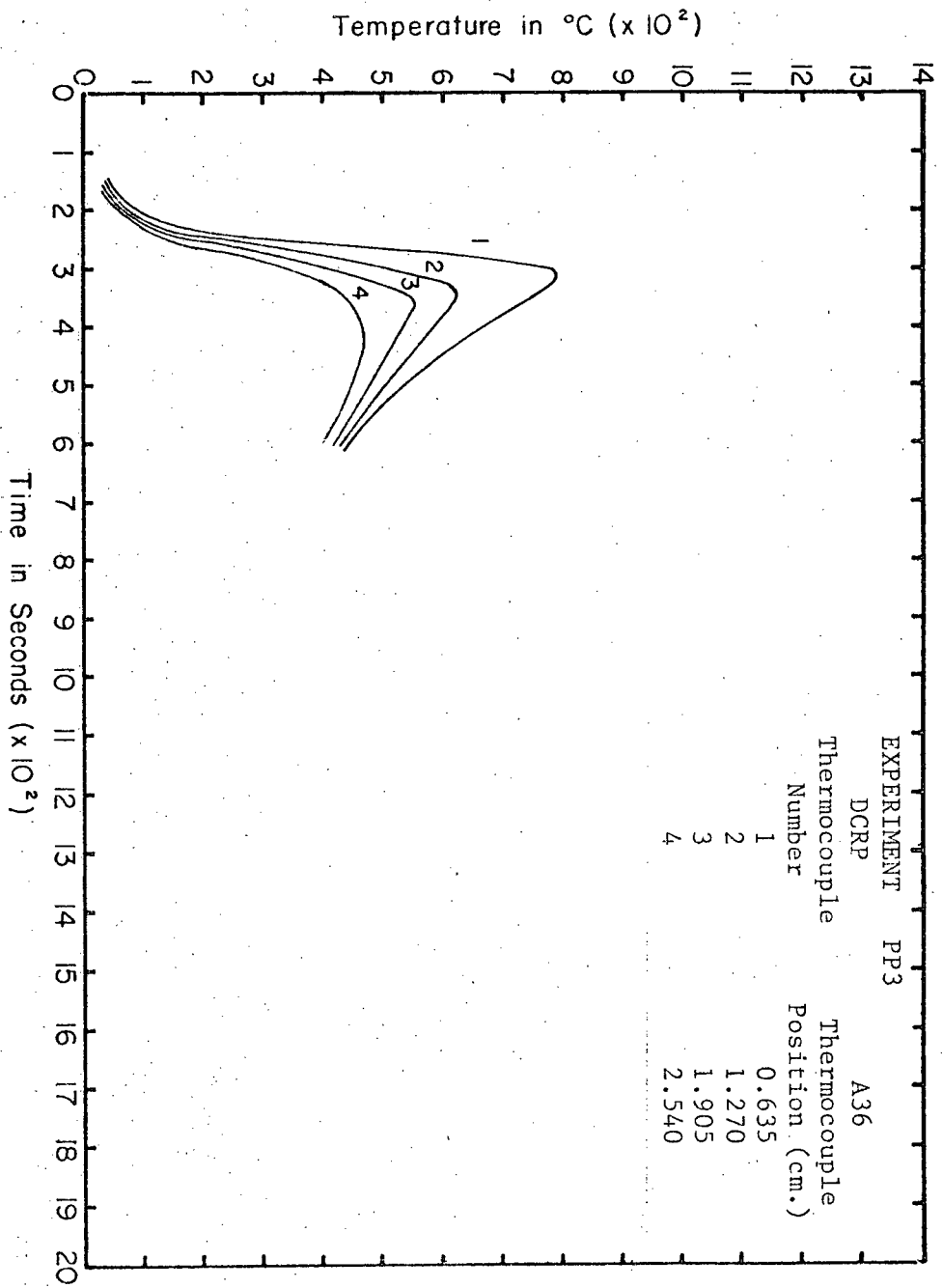


Figure 88 Thermal profile for PP3.

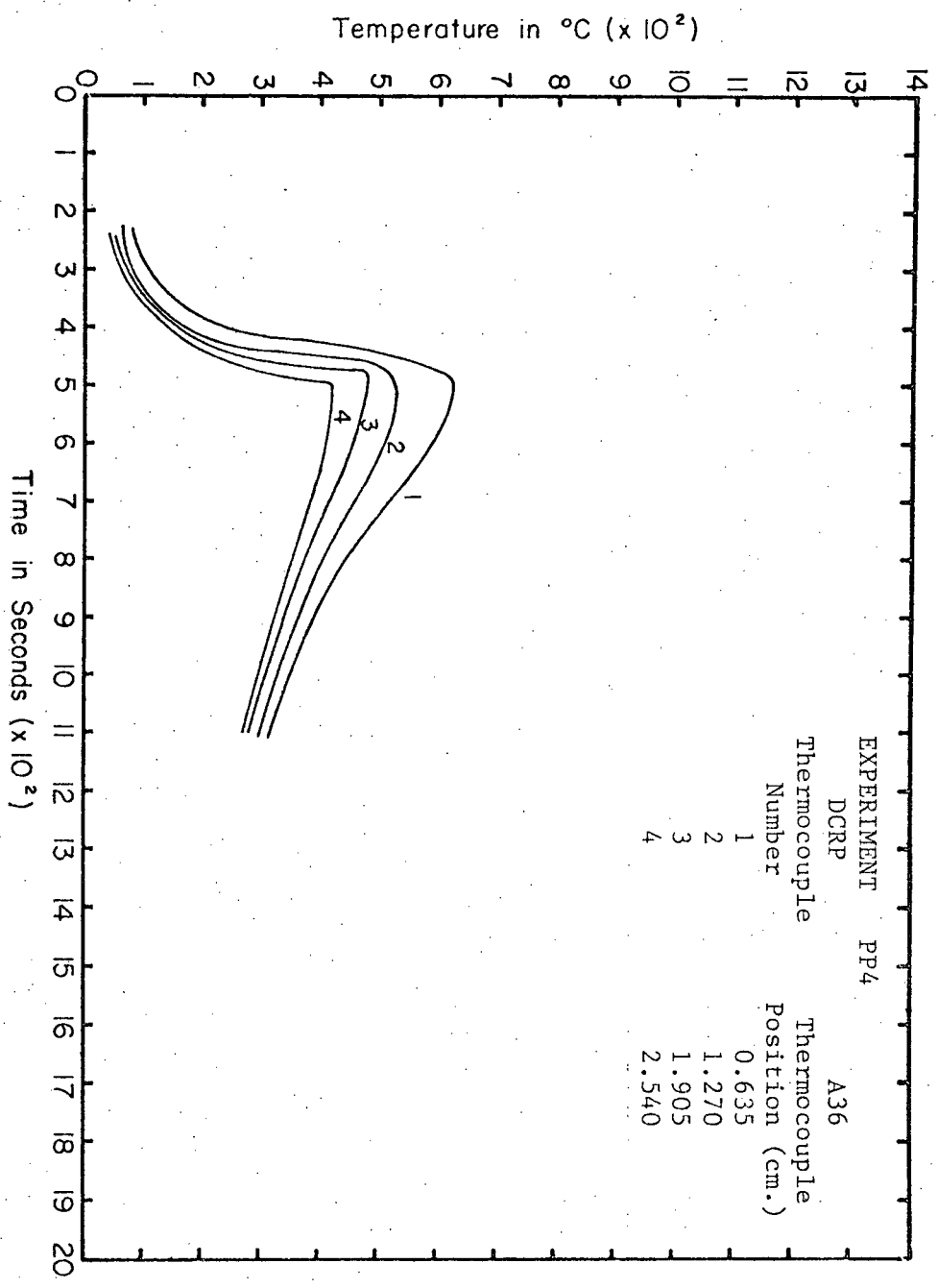


Figure 89 Thermal profile for PP4.

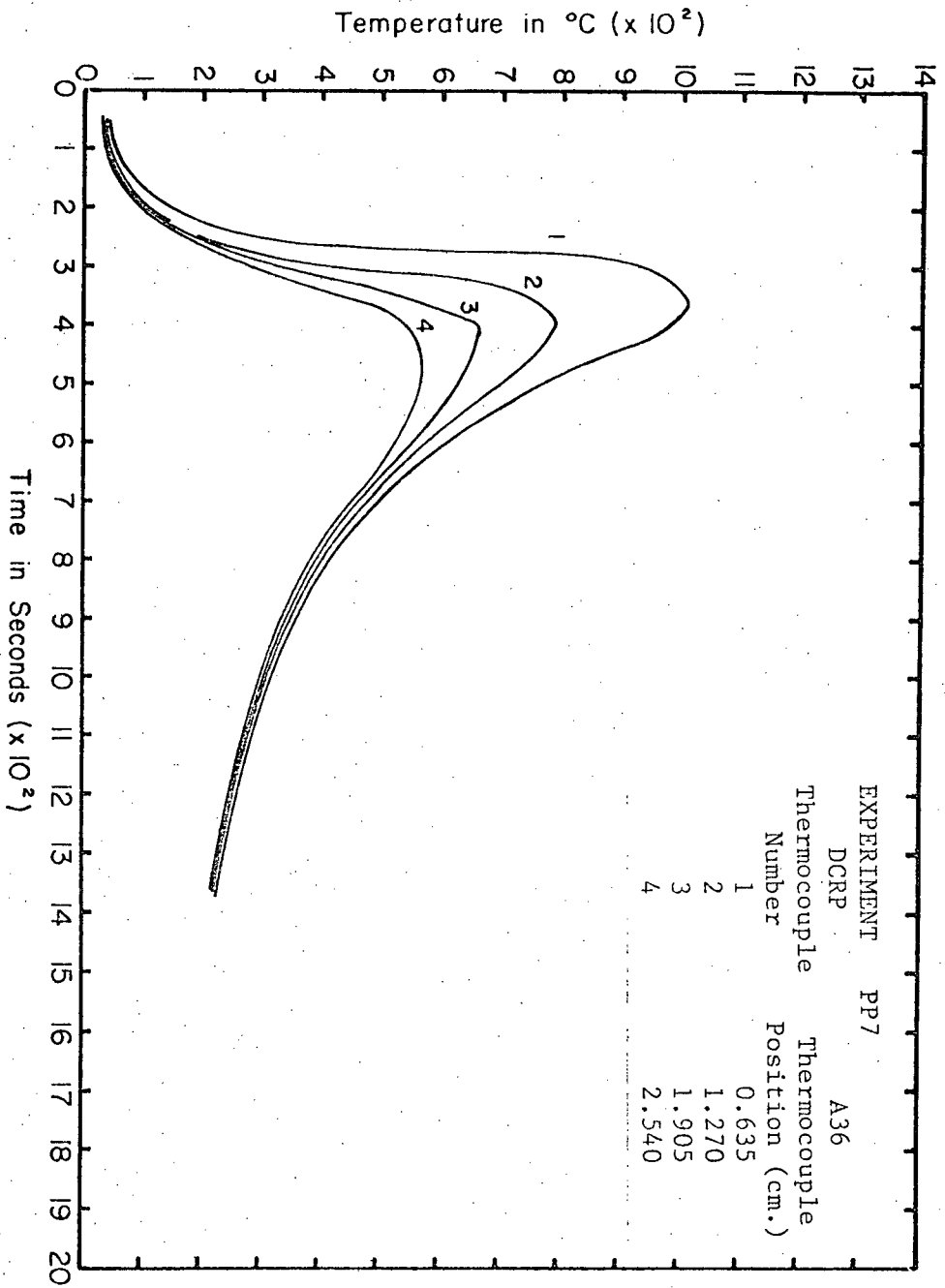


Figure 90 Thermal profile for PP7.

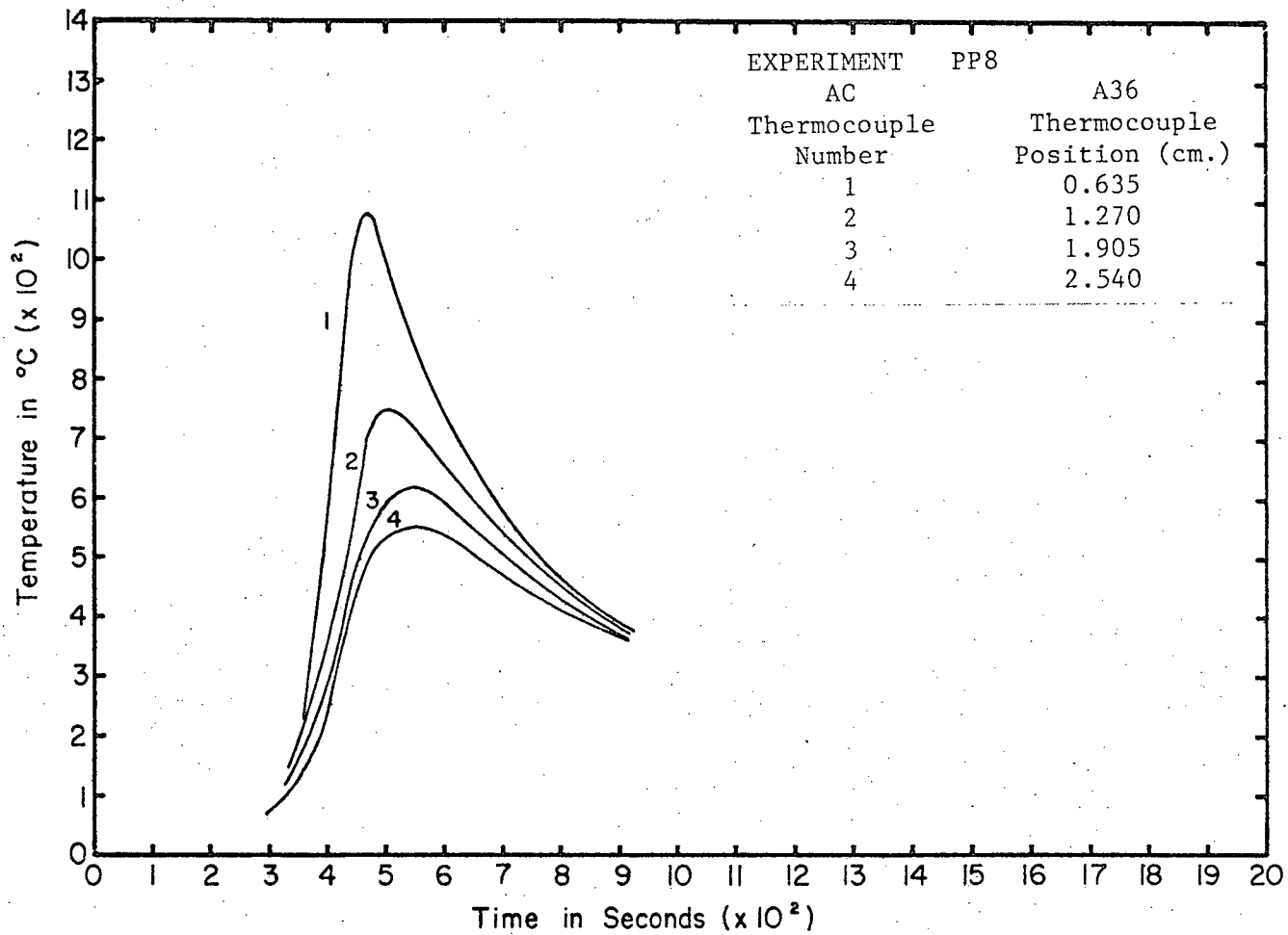


Figure 91 Thermal profile for PP8.

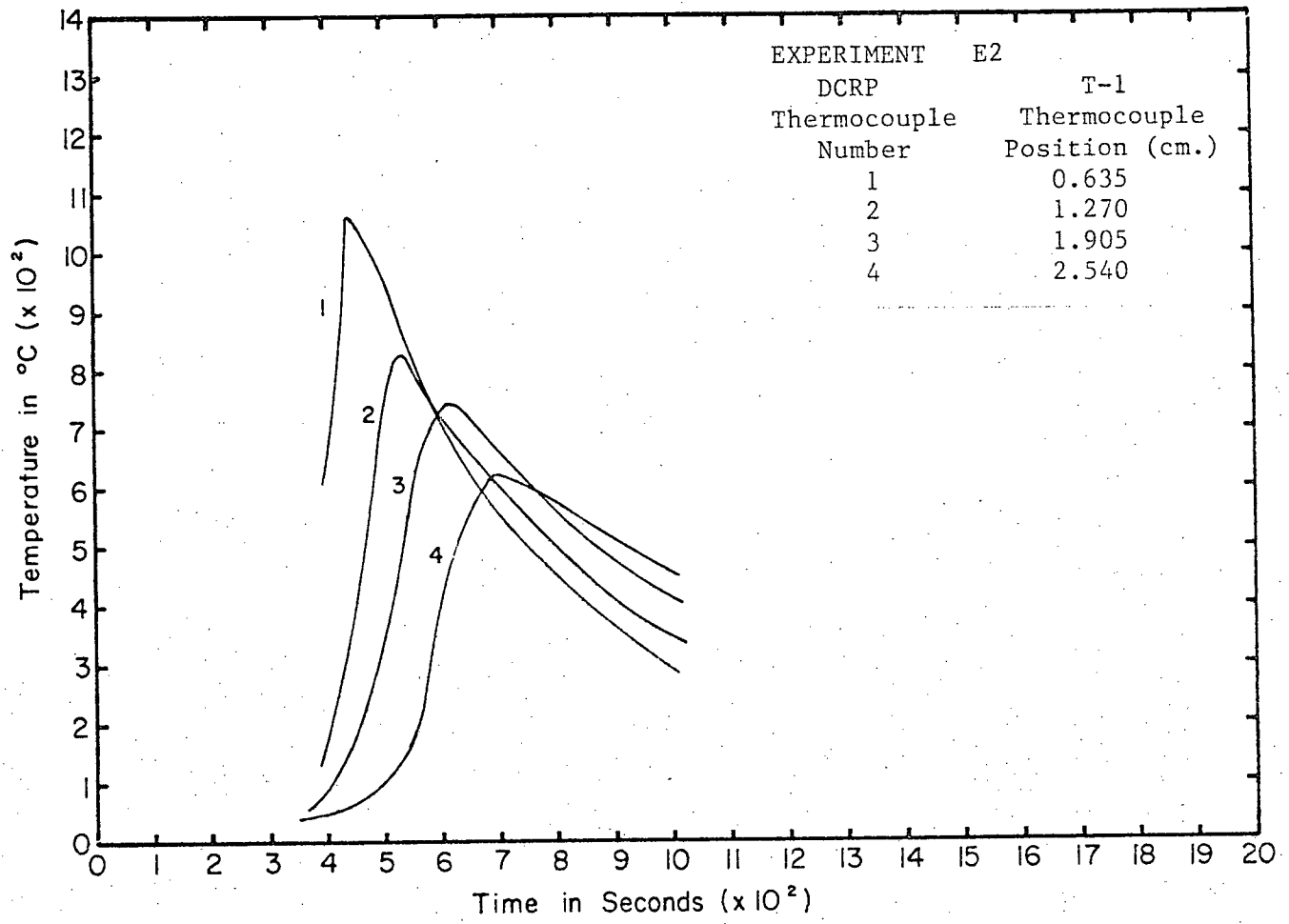


Figure 92 Thermal profile for E2.

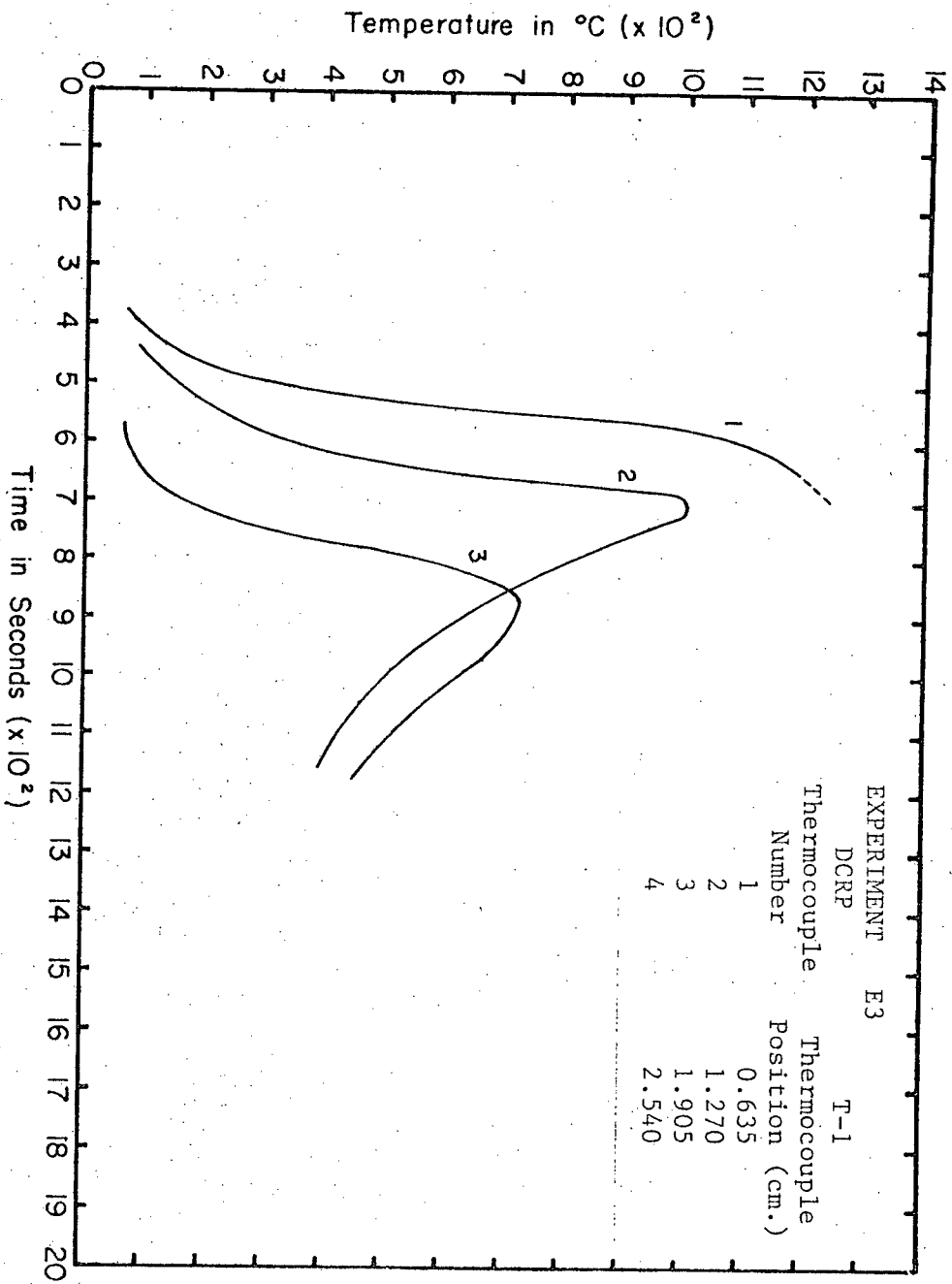


Figure 93 Thermal profile for E3.

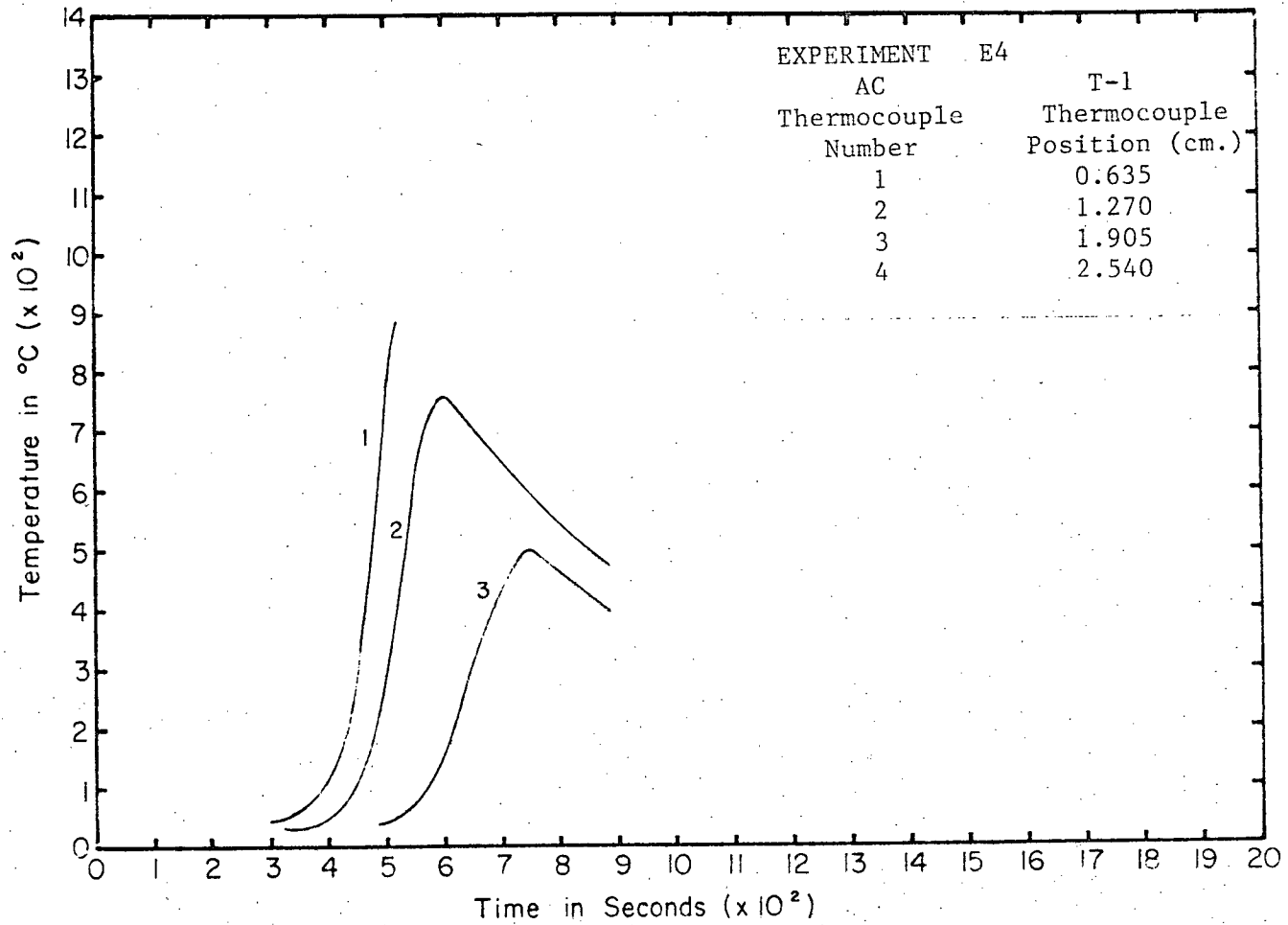


Figure 94 Thermal profile for E4.

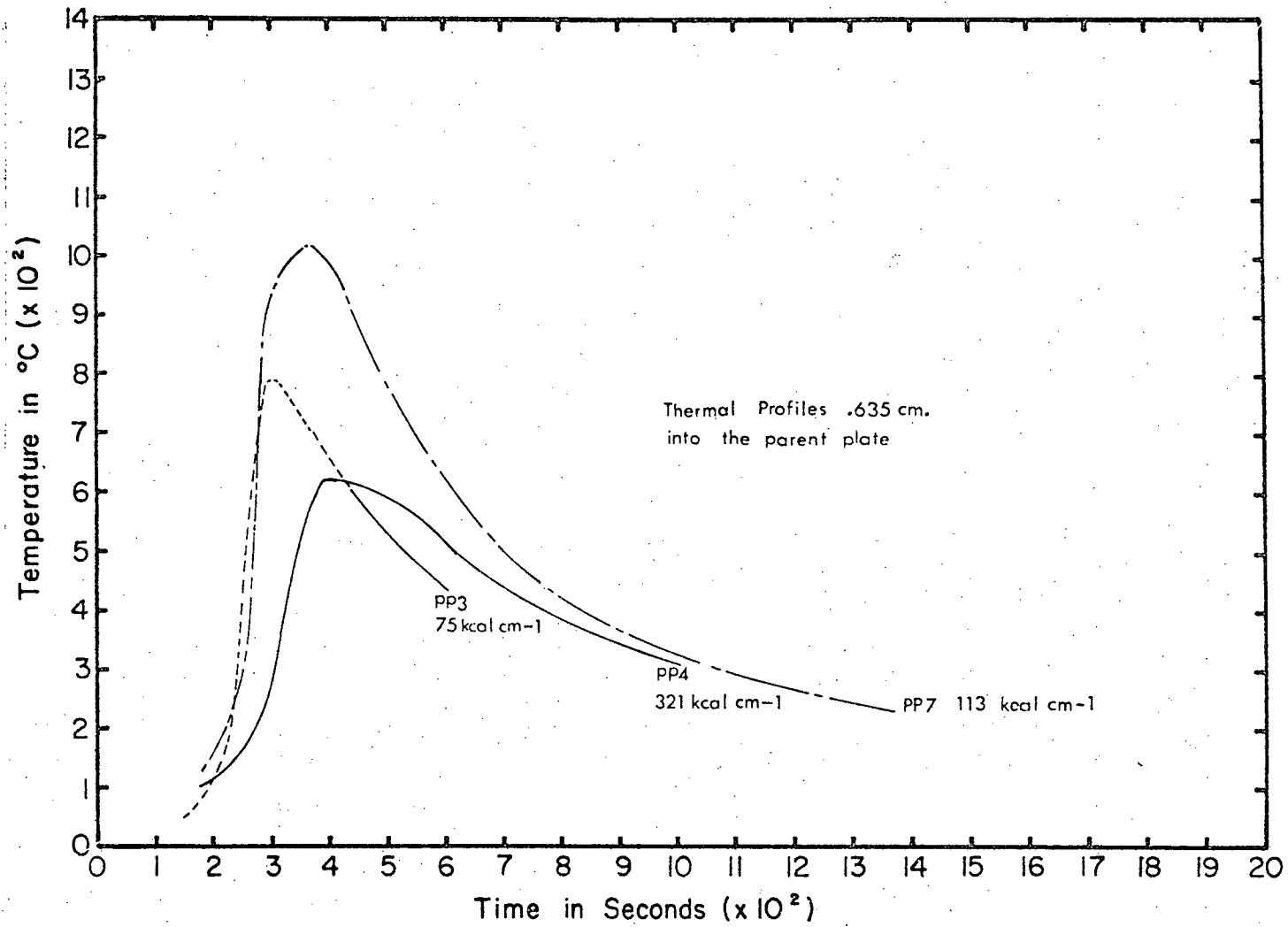


Figure 95 Comparison of thermal profiles for some specific power inputs

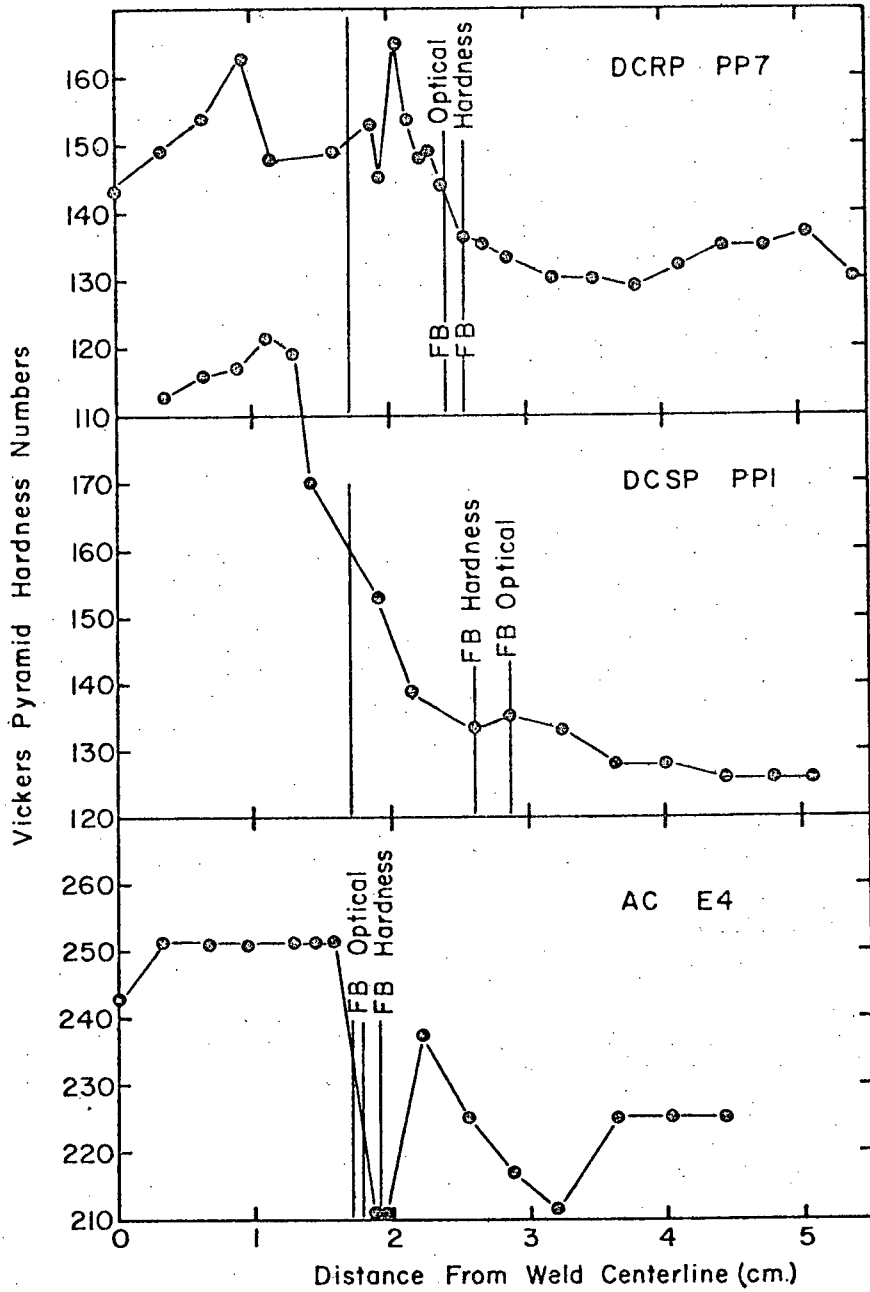


Figure 96 Hardness values for ESW utilizing bar electrodes. (PP7 A36, PPI A36, E4 T-1)

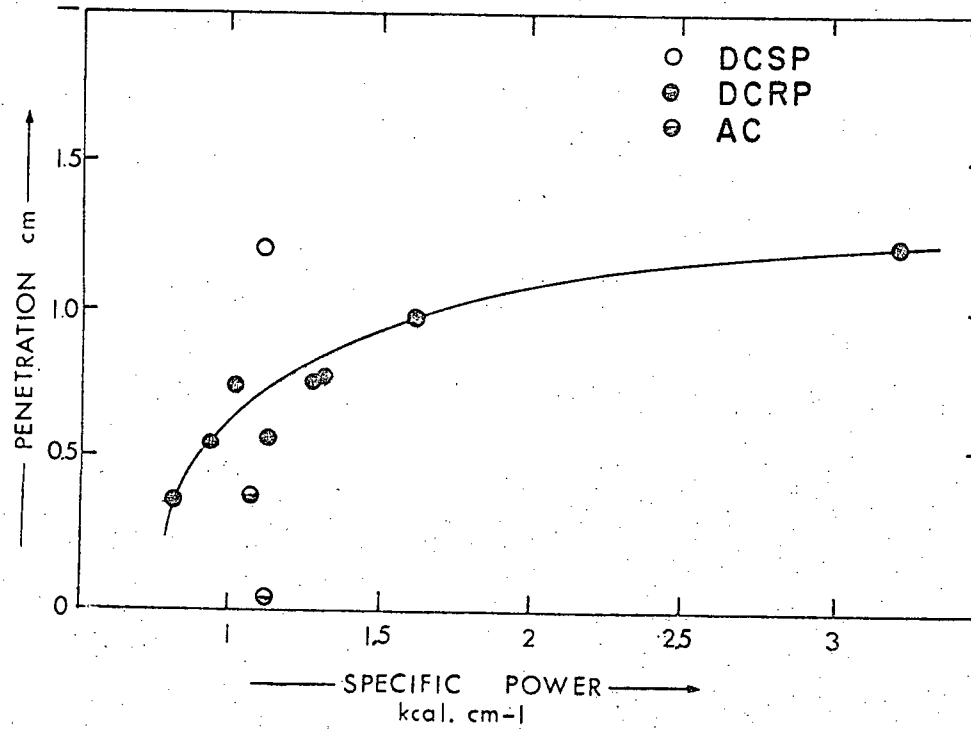


Figure 97 Penetration Versus specific power input, bar electrodes

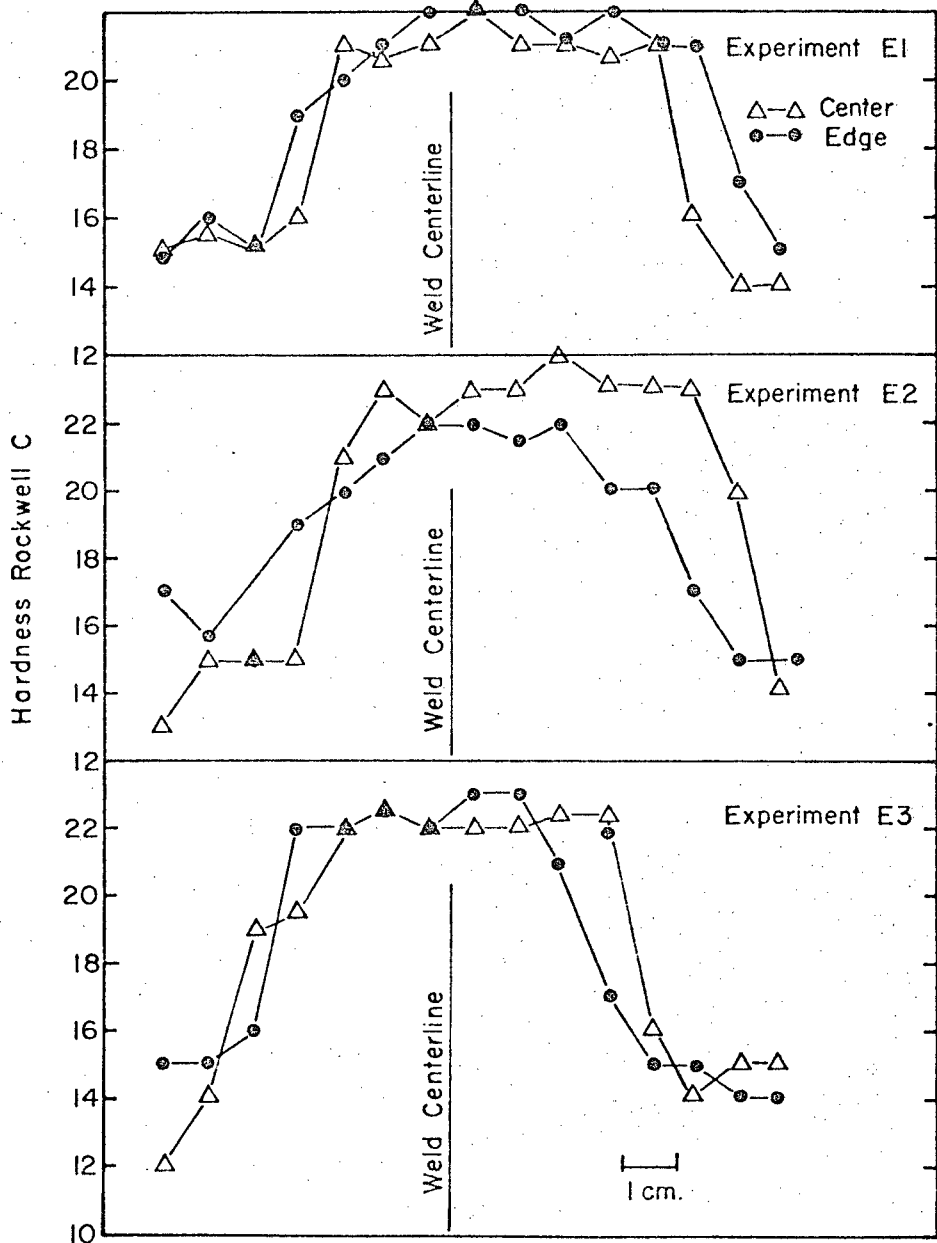


Figure 98 Hardness values along the centerline and near the surface of horizontal sections of T-1 equivalent cast plates.

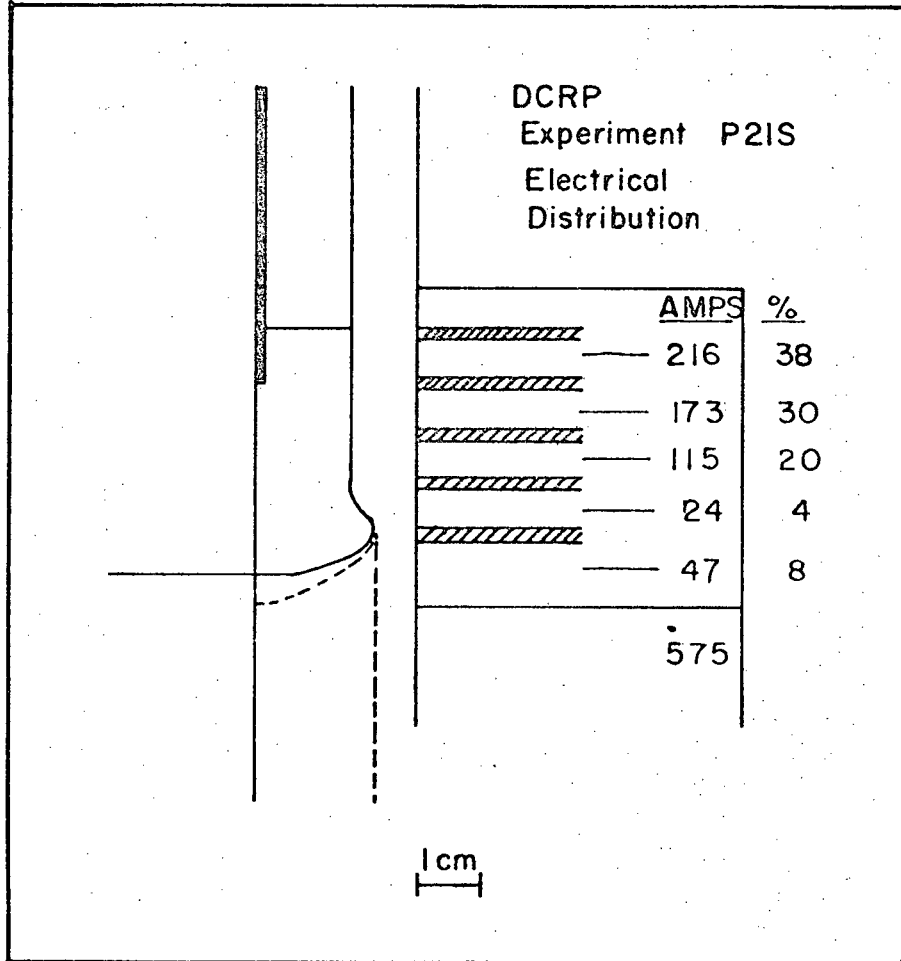


Figure 99 Electrical distribution in DCRP.

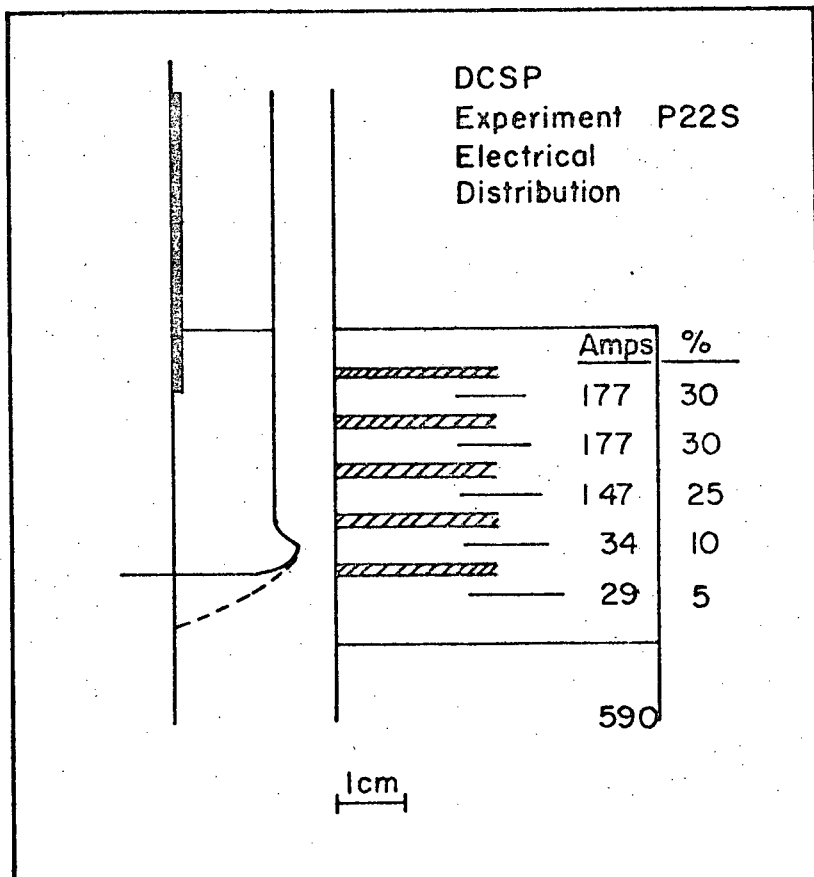


Figure 100 Electrical distribution in DCSP.

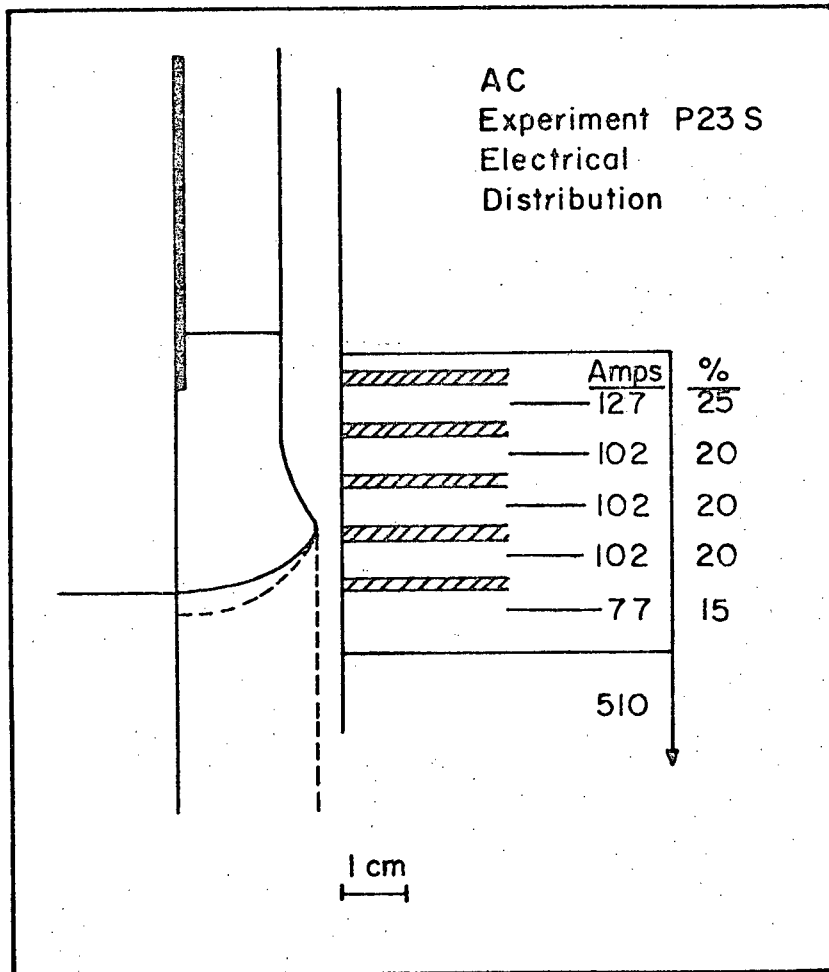


Figure 101 Electrical distribution in AC



Figure 102 Shunt set-up for P21S, DCRP

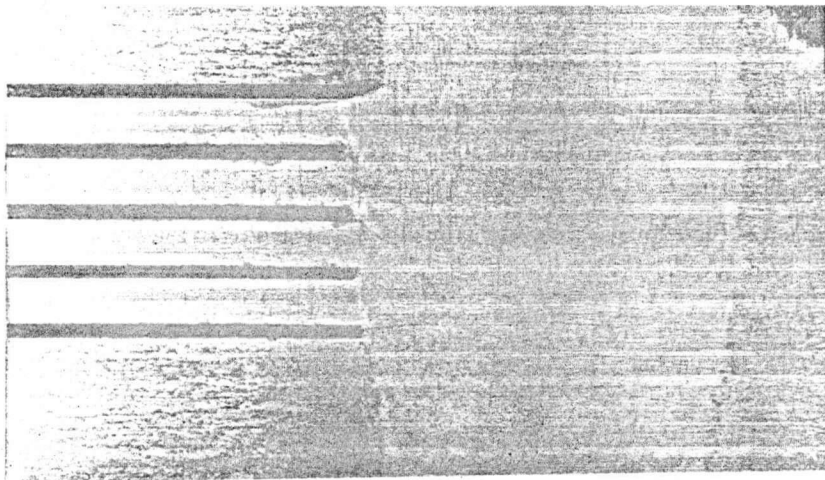


Figure 103 Shunt set-up for P22S, DCSP

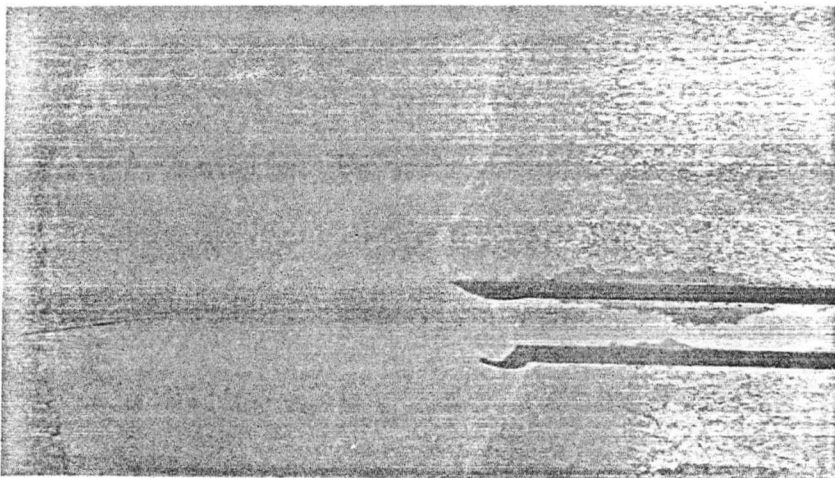


Figure 104 Shunt set-up for P23S, AC

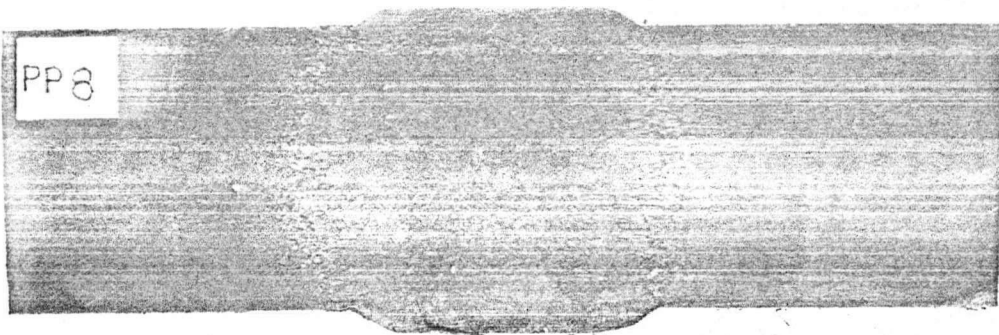
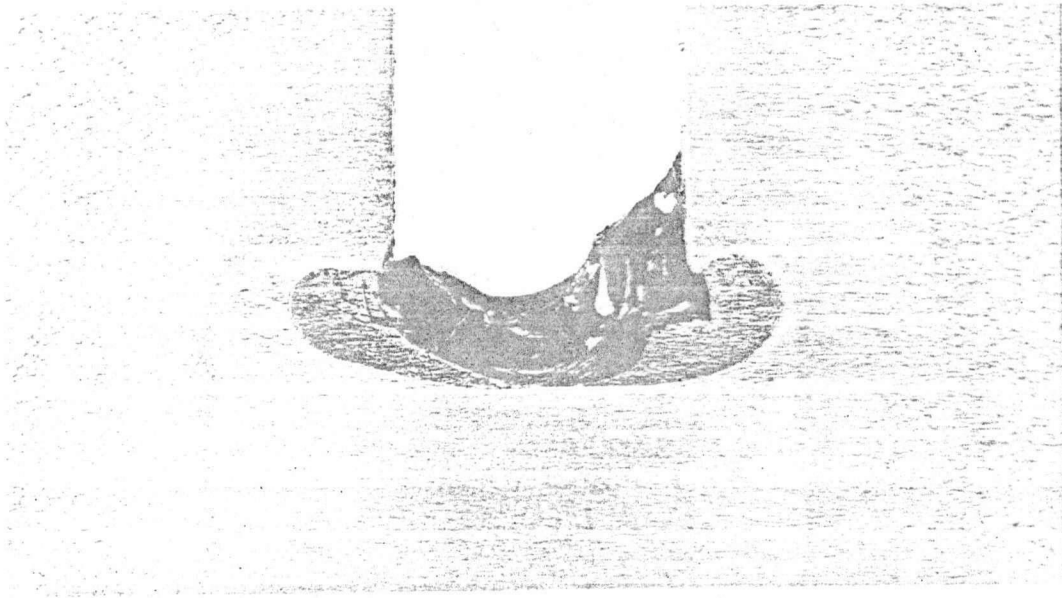


Figure 105 Typical horizontal and vertical sections of a CGESW weld.

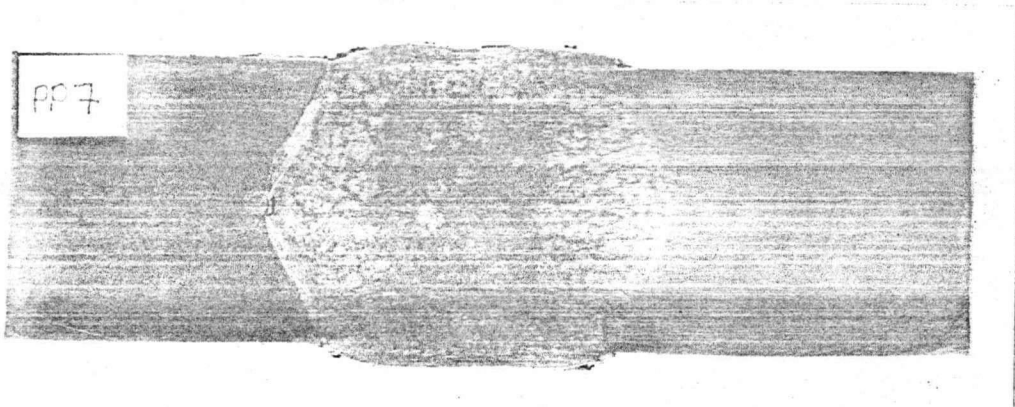
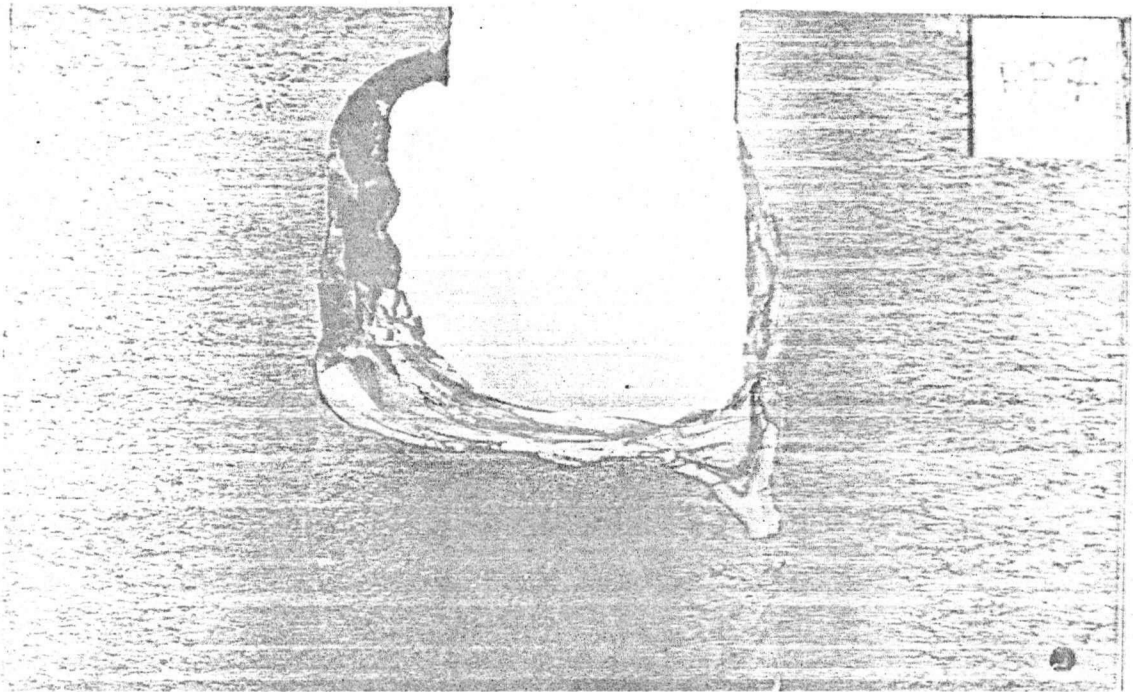


Figure 106 Penetration shape with bar electrodes in the DCRP mode.

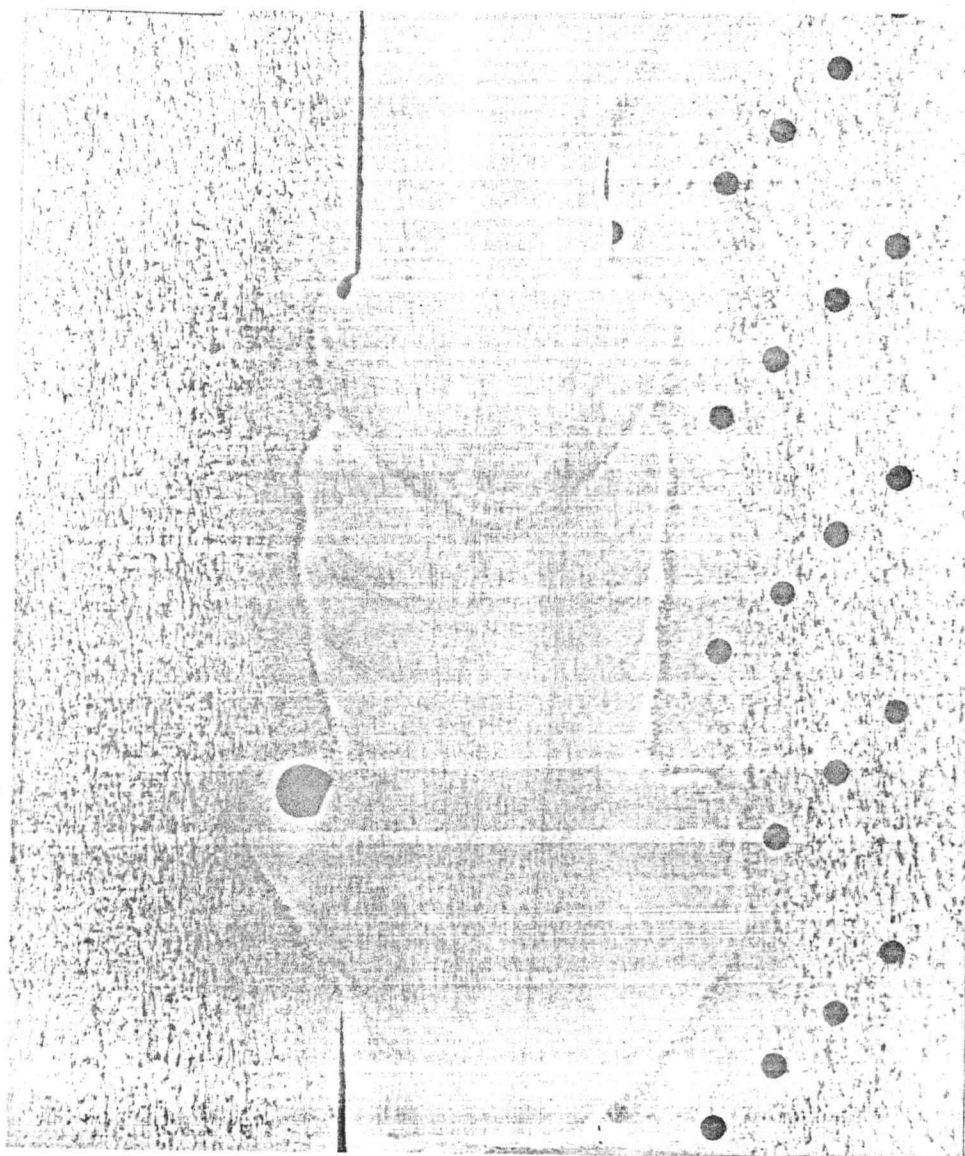


Figure 107 Macroetched longitudinal section of a weld produced during unstable welding conditions.



Figure 108 Macroetched longitudinal section of a weld produced during stable welding conditions.

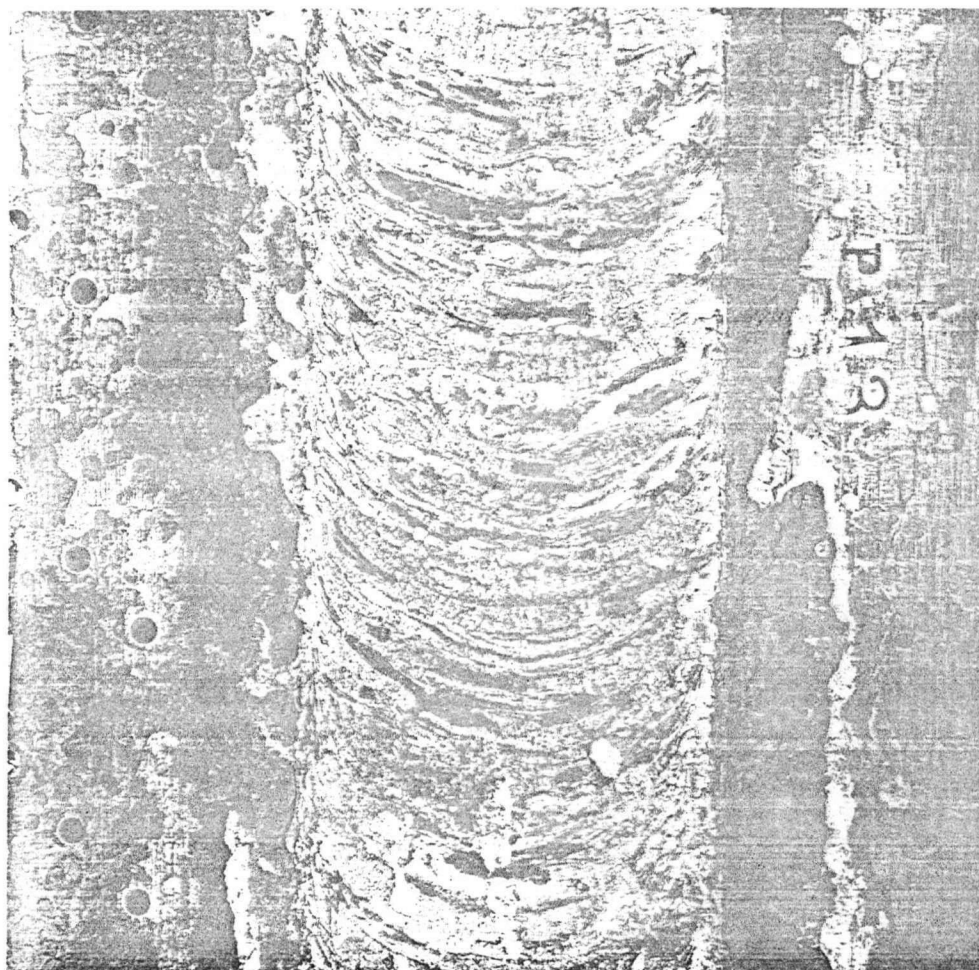


Figure 109 Typical electroslag weld surface.

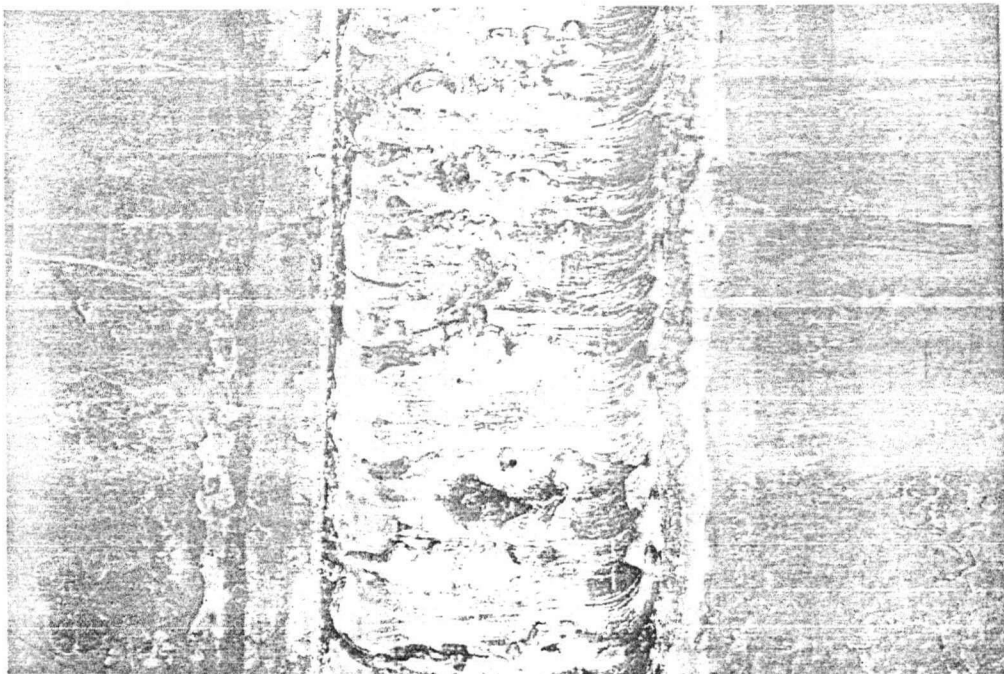


Figure 110 Electroslag surface for DCRP and AC.

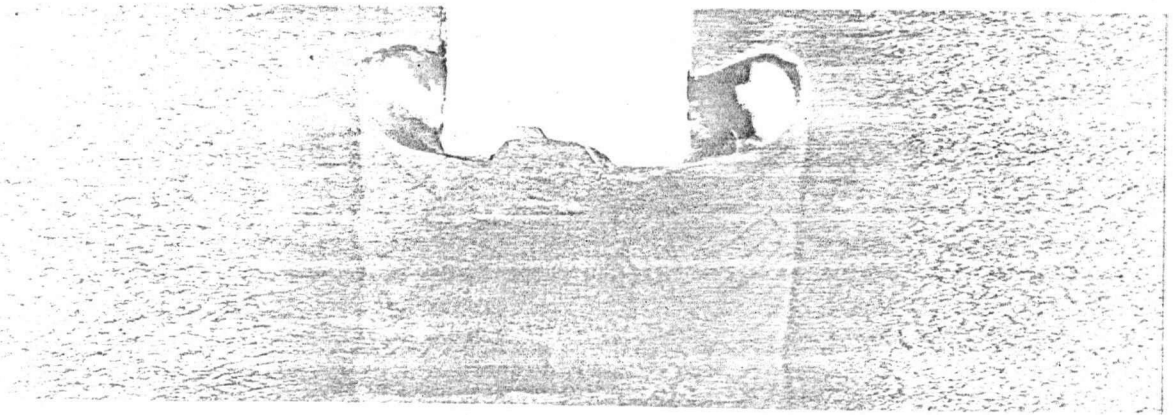


Figure 111 Weld run-out.

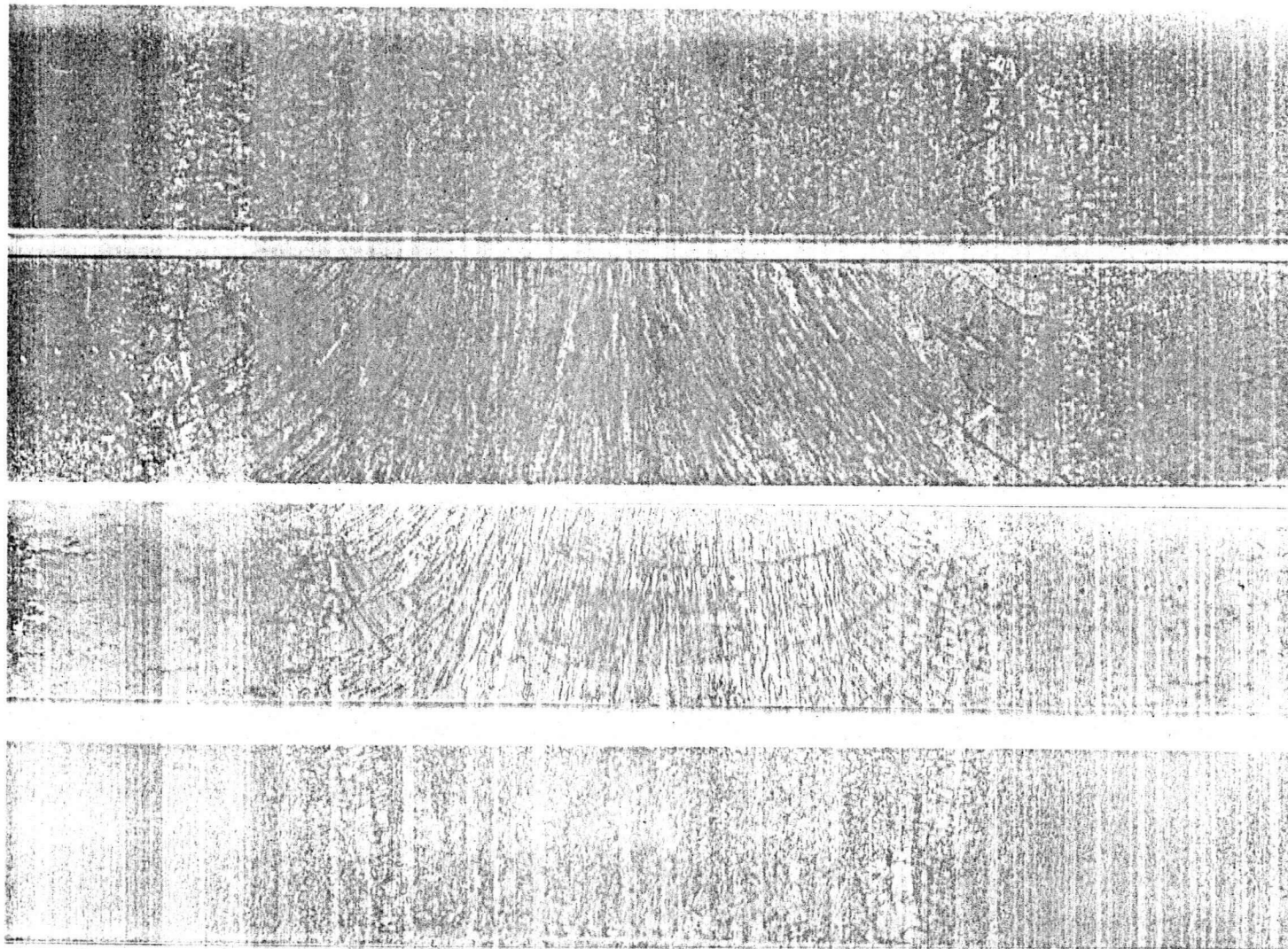


Figure 112 Horizontal and vertical sections of two typical welds, used for oxygen analysis, hardness traverses, grain size measurements and Charpy impact values.

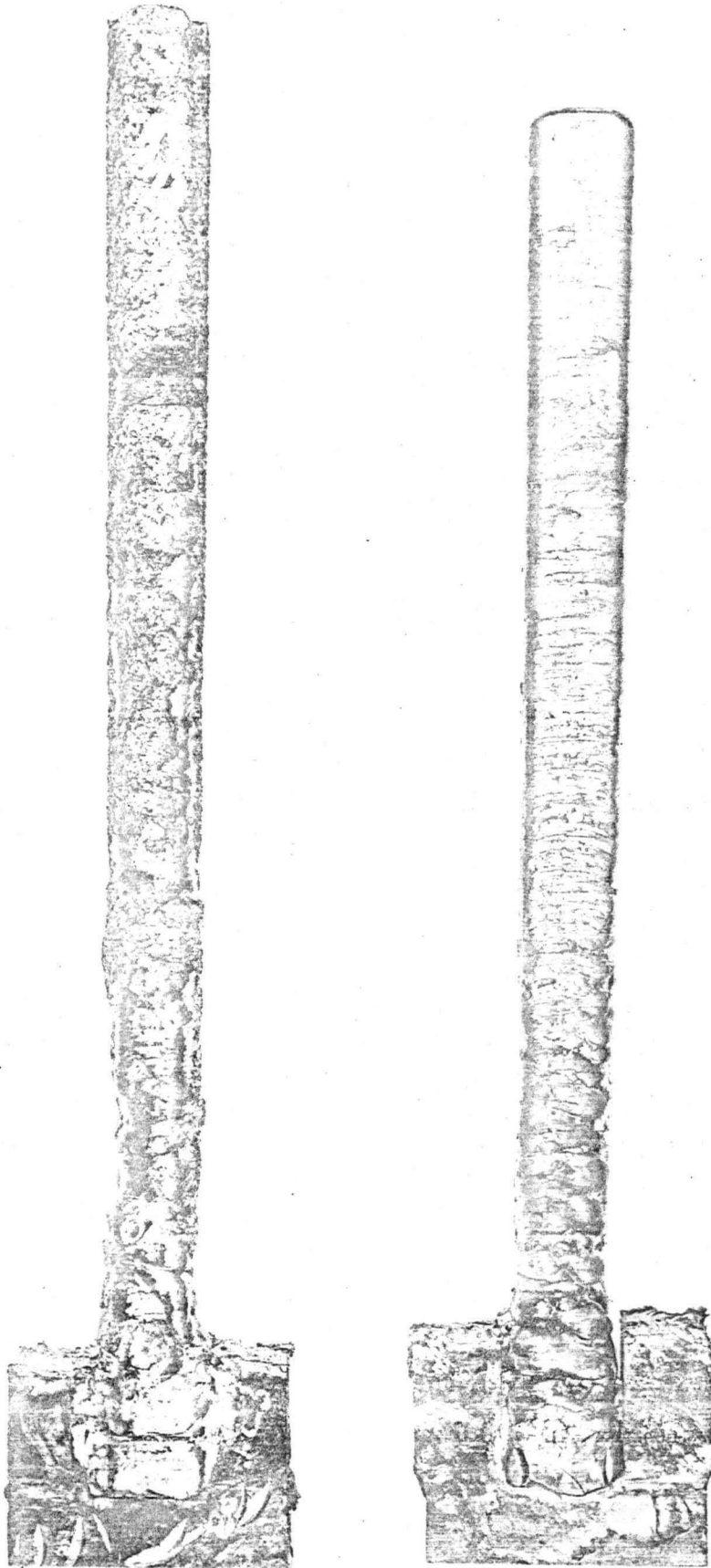


Figure 113 Casting produced when welding with too deep a slag.

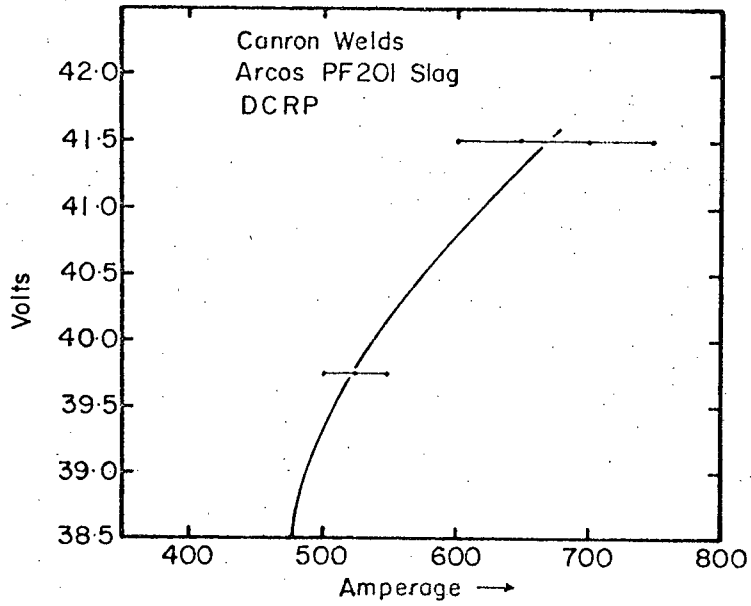


Figure 114 Voltage-amperage characteristics for Cannon welds.

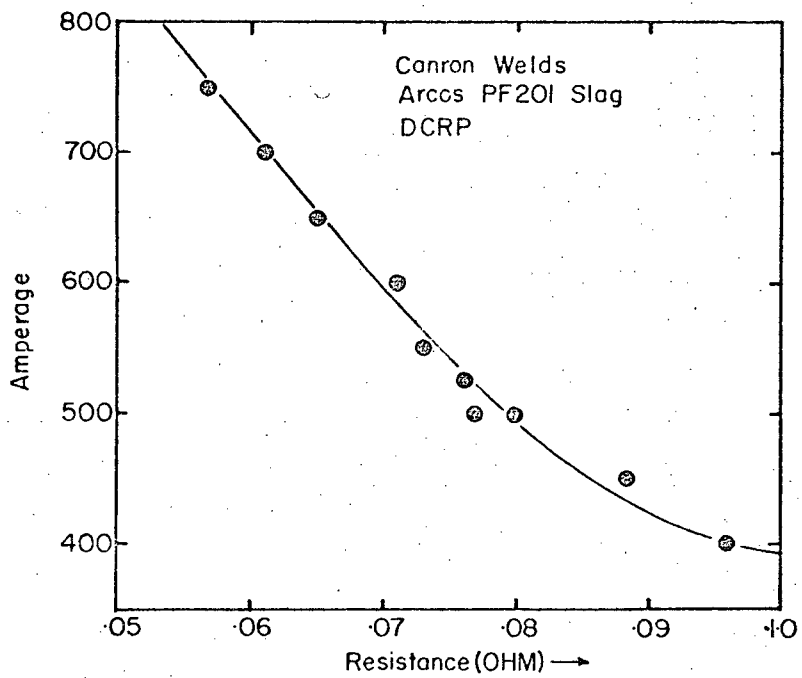


Figure 115 Amperage versus apparent resistance for Cannon welds.

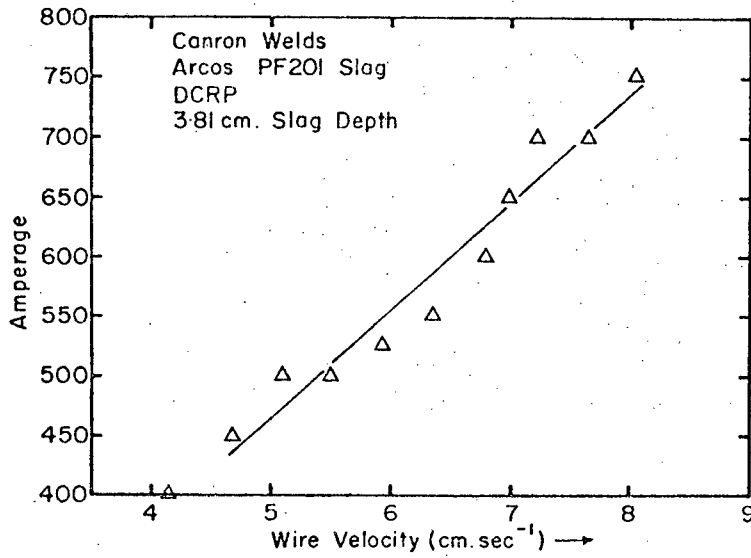


Figure 116 Amperage as a function of wire velocity.

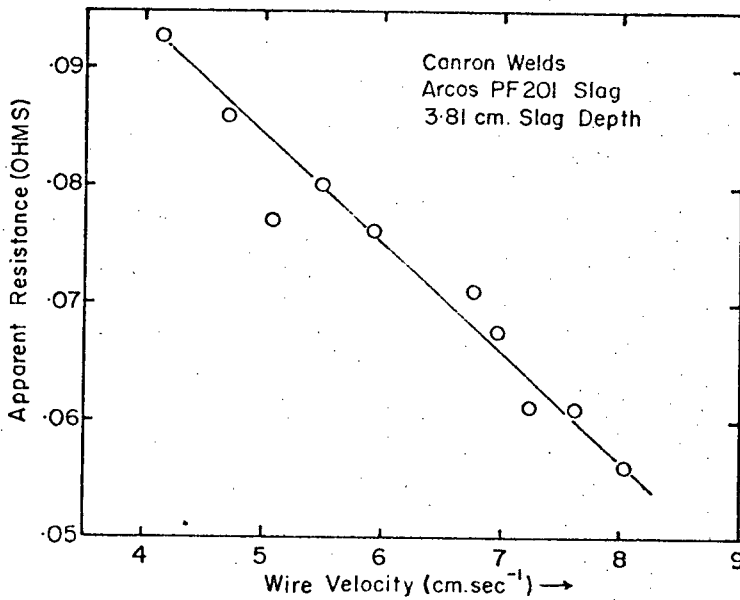


Figure 117 Apparent resistance as a function of wire velocity for Cannon welds.

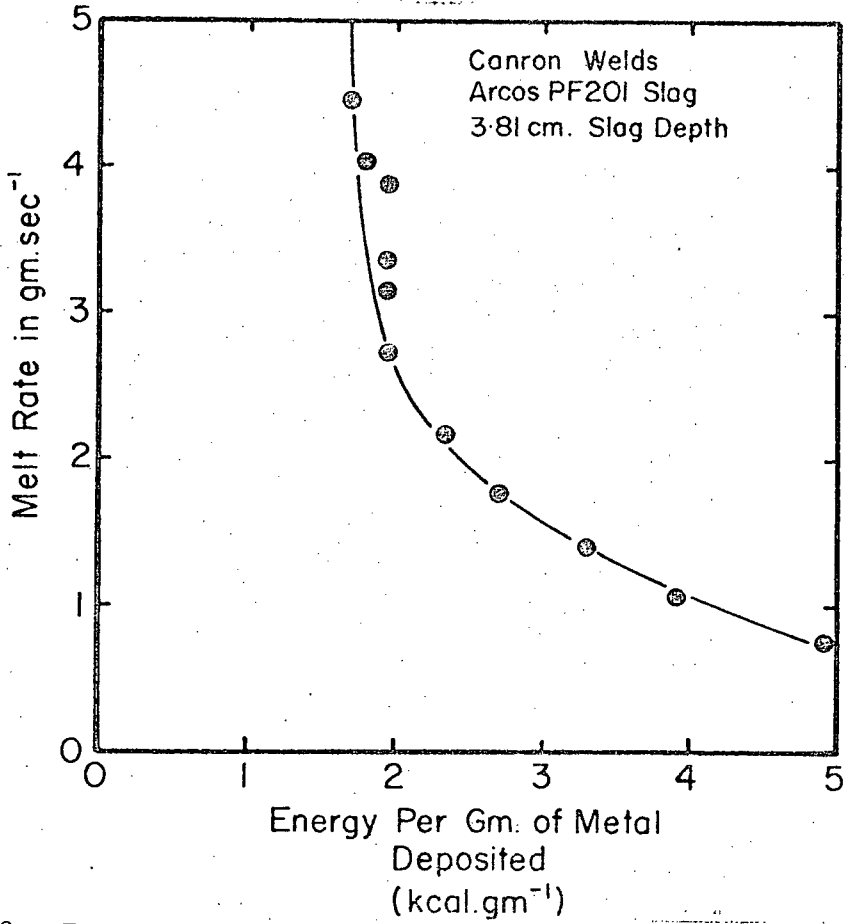


Figure 118 Energy per gram of metal deposit for Cannon welds.

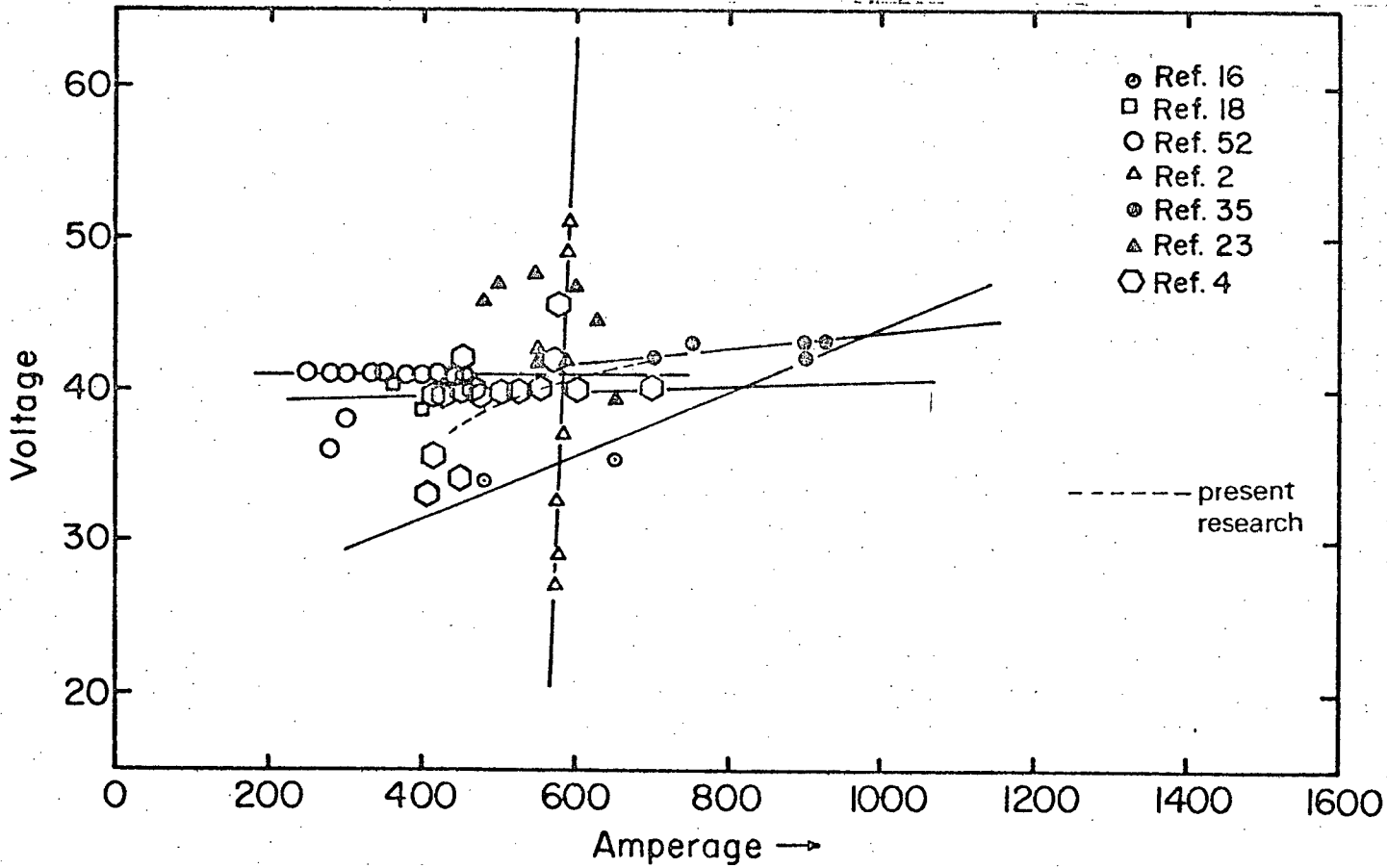


Figure 119 Literature cited voltage-amperage characteristics

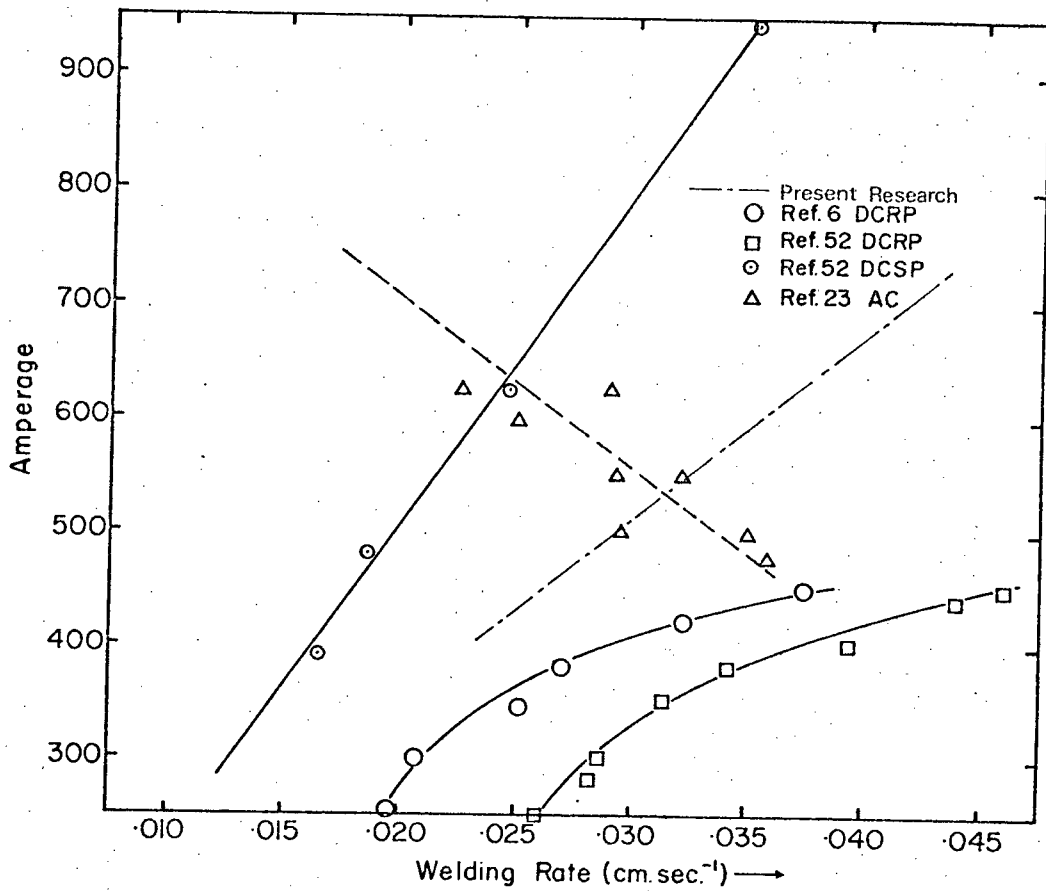


Figure 120 Literature cited amperage-welding rate relationships.

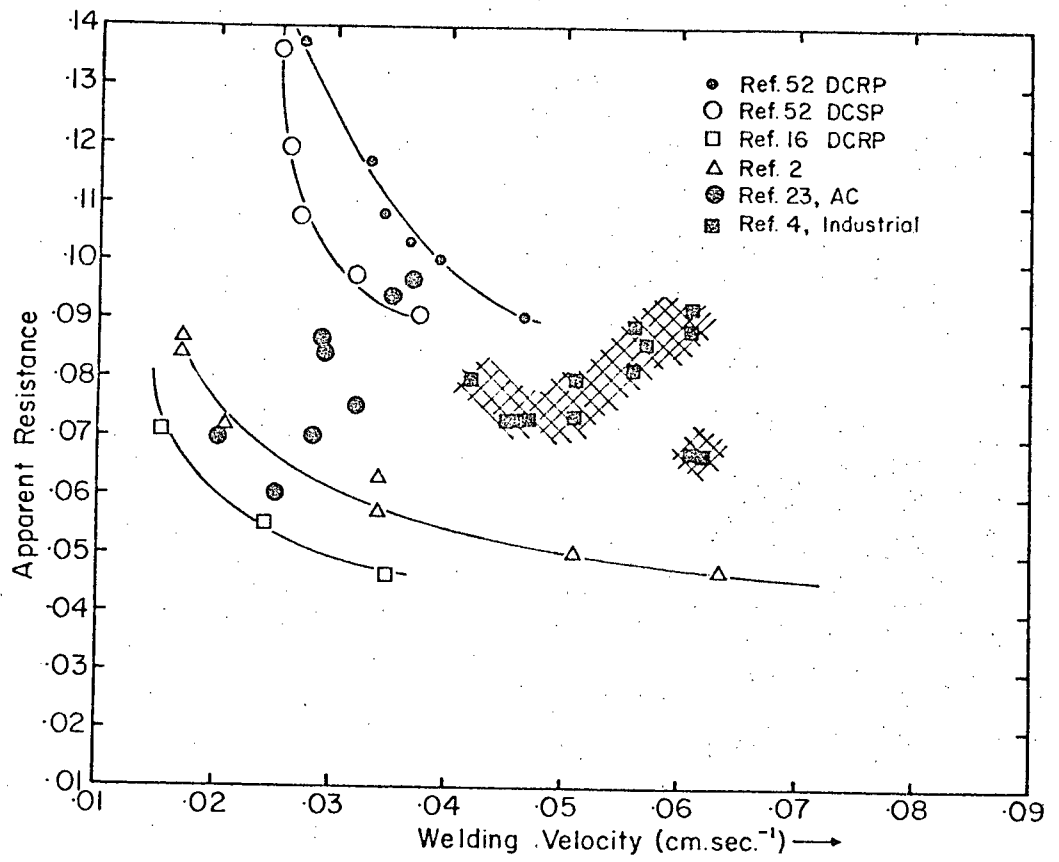


Figure 121 Literature cited apparent resistance dependence on welding velocity.

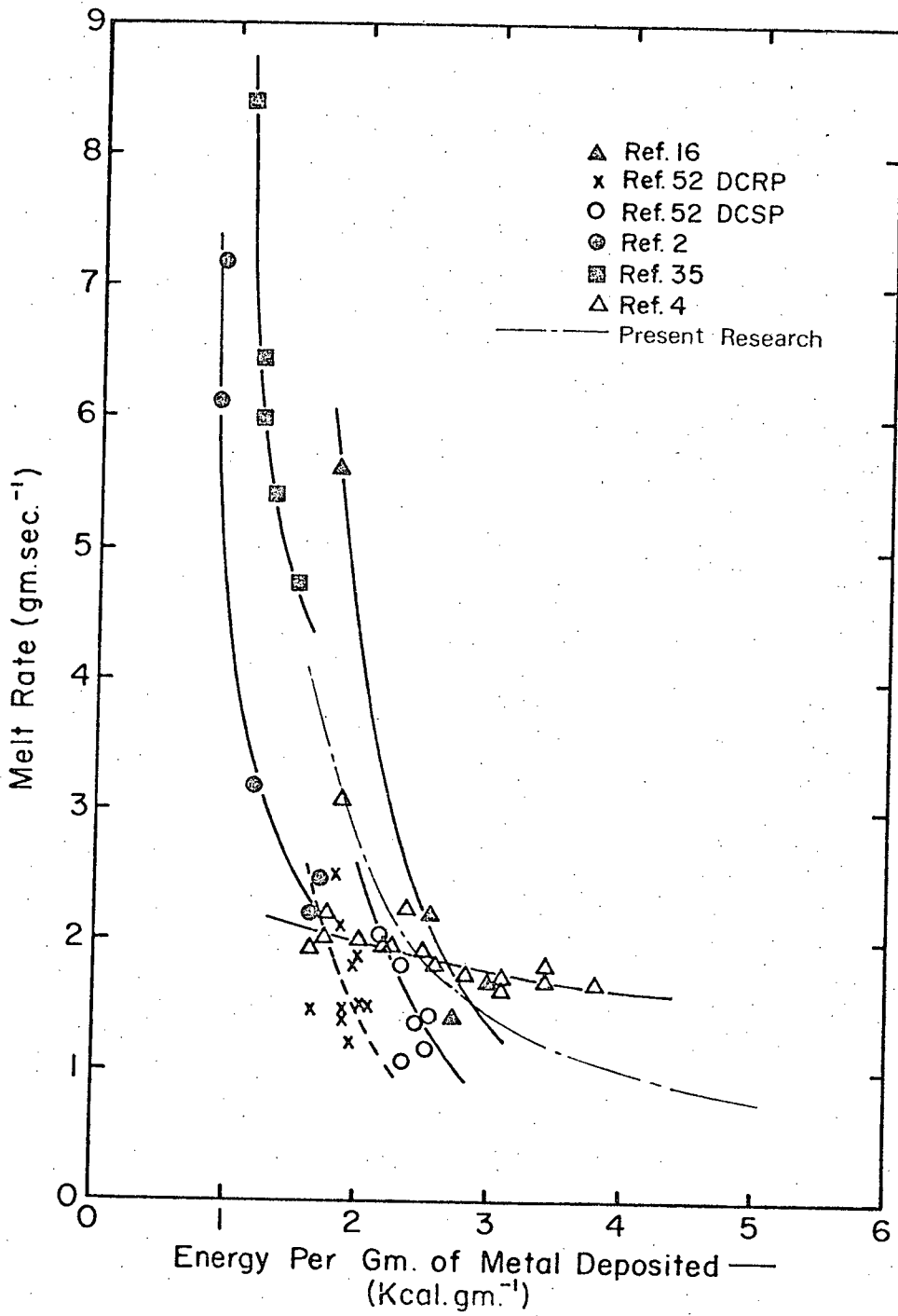


Figure 122 Literature cited energy requirements.

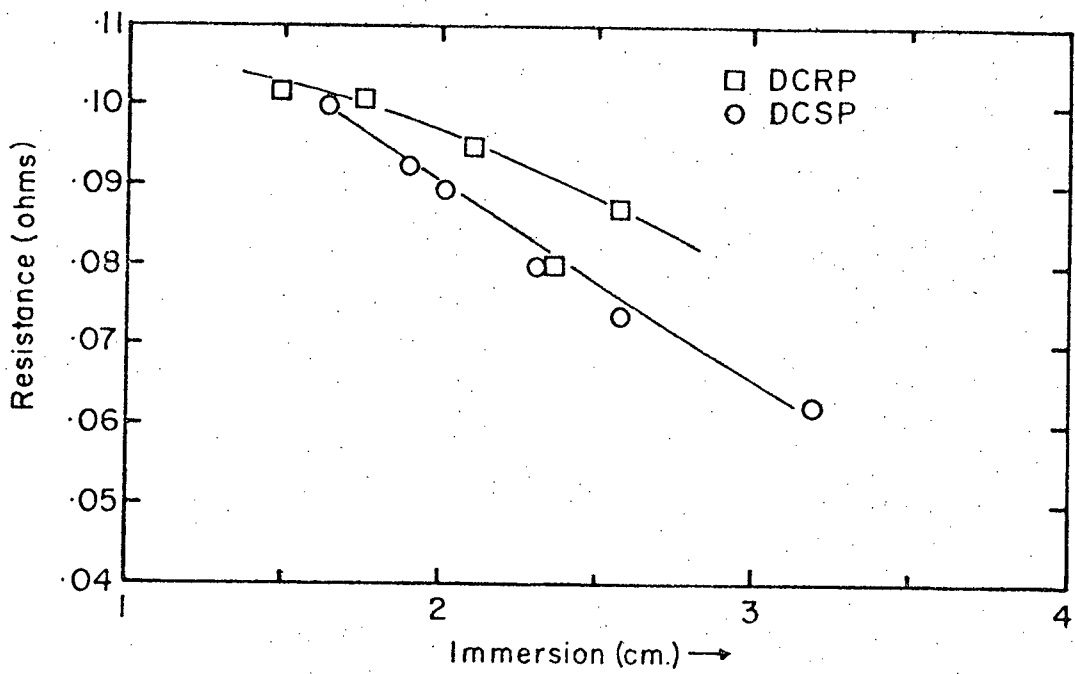


Figure 123 Electrode immersion versus apparent slag resistance.

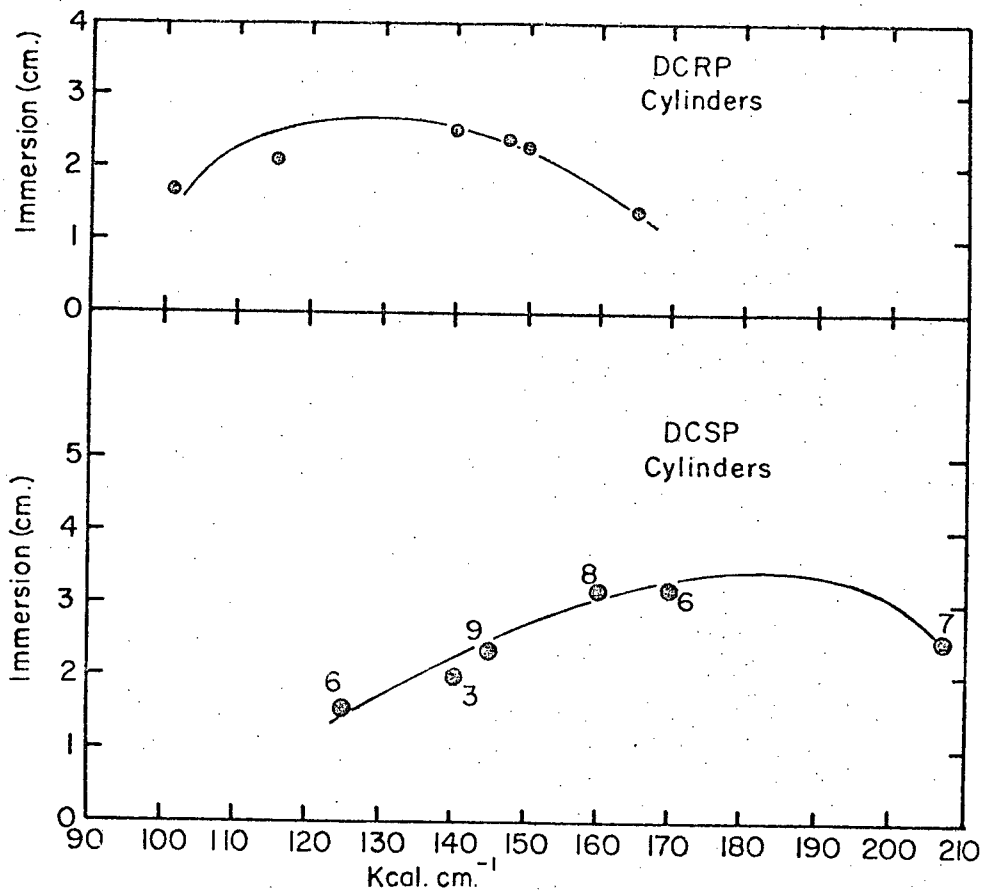


Figure 124 Electrode immersion versus energy input.

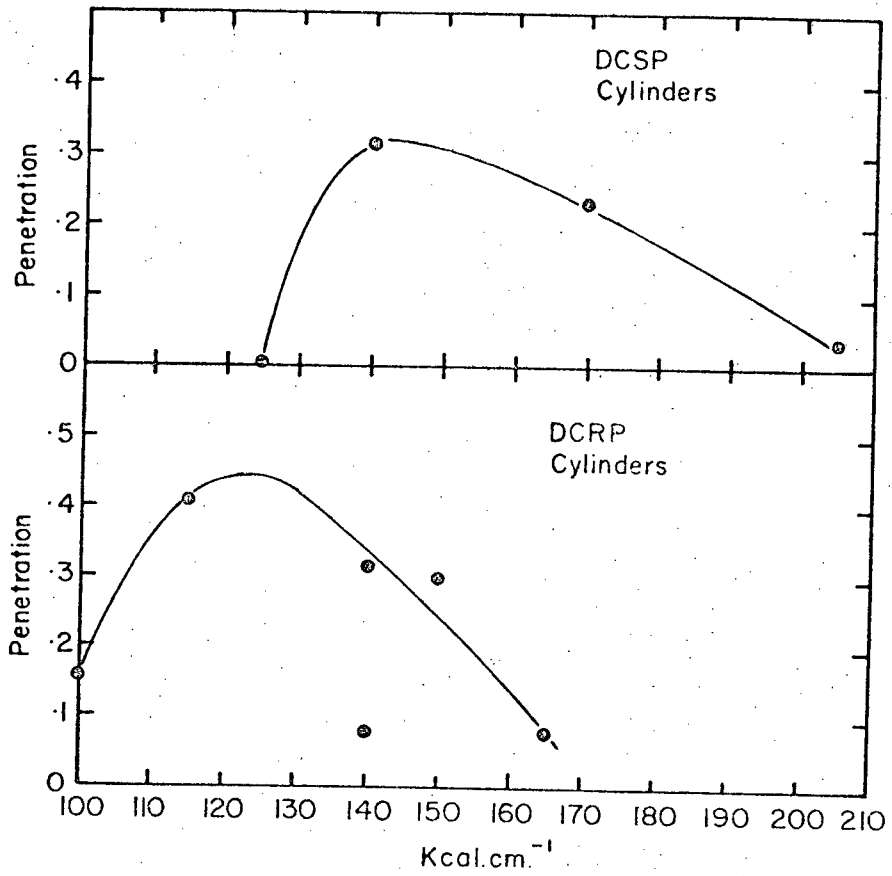


Figure 125 Penetration versus energy input

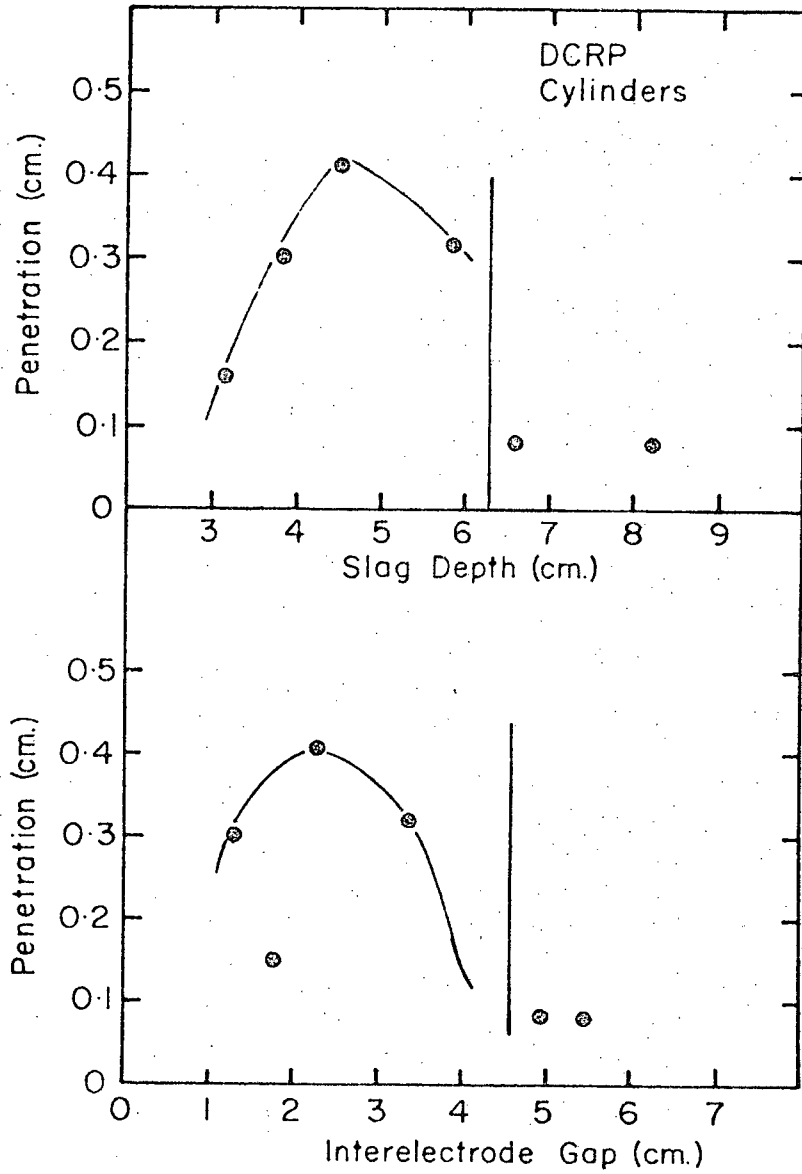


Figure 126 Penetration versus slag depth.

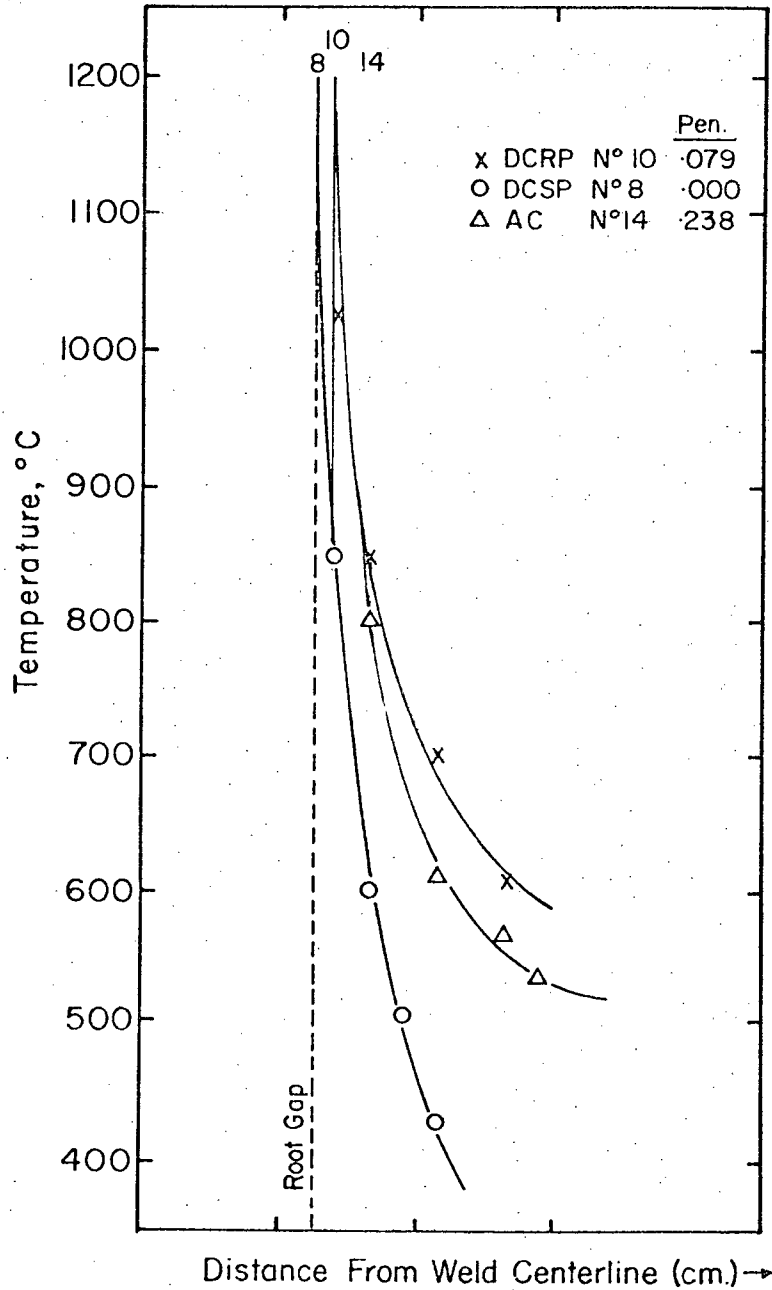


Figure 127 Temperature profile across weld sections

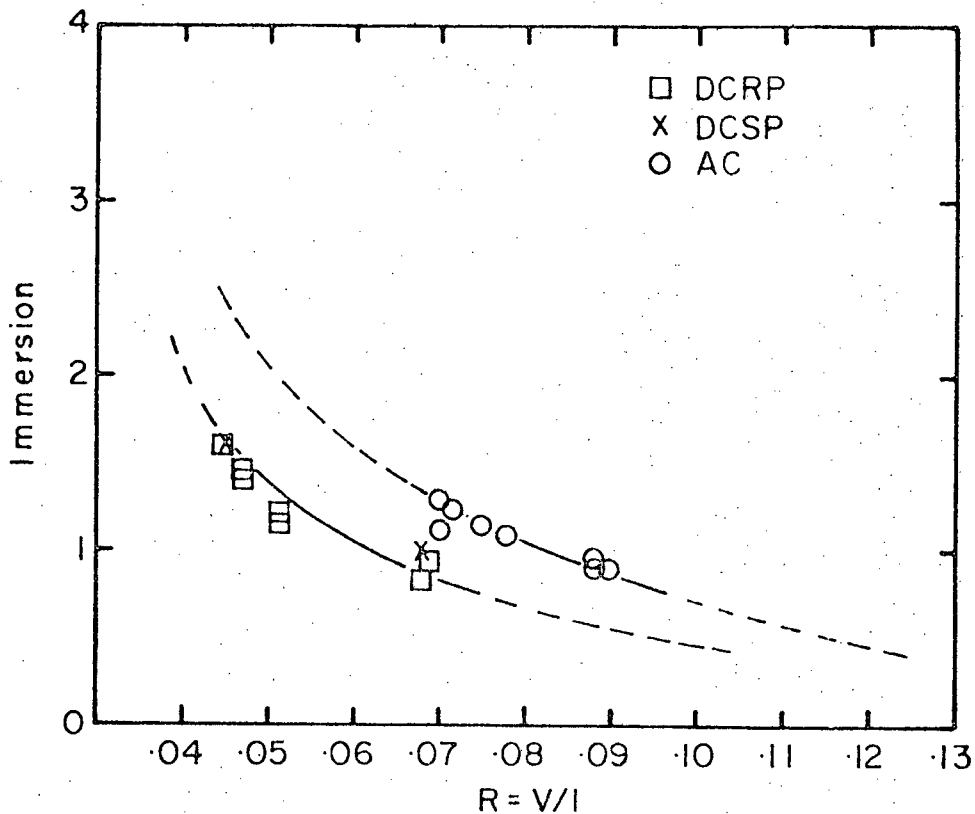


Figure 128 Immersion as a function of apparent resistance

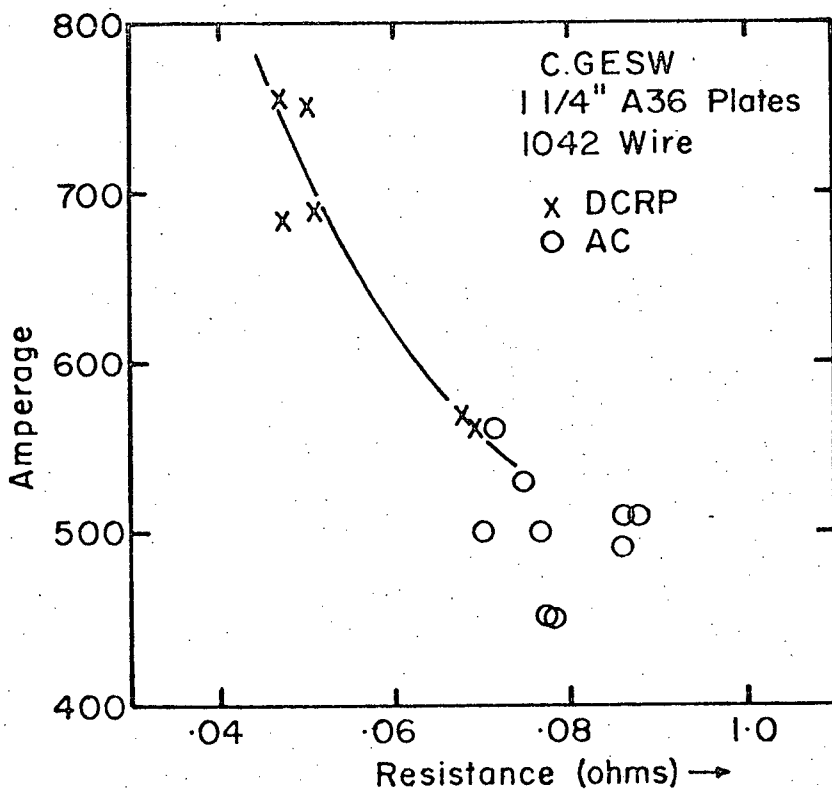
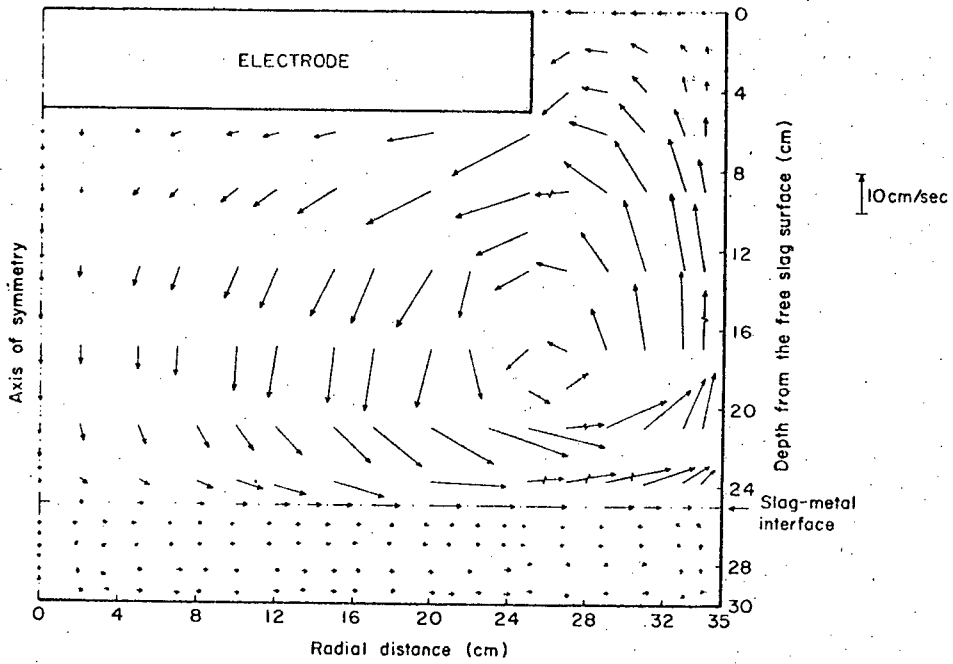


Figure 129 Amperage as a function of apparent resistance



The computed velocity field in an industrial scale ESR system

Figure 130 Theoretical slag flow pattern from Dilawari (75)

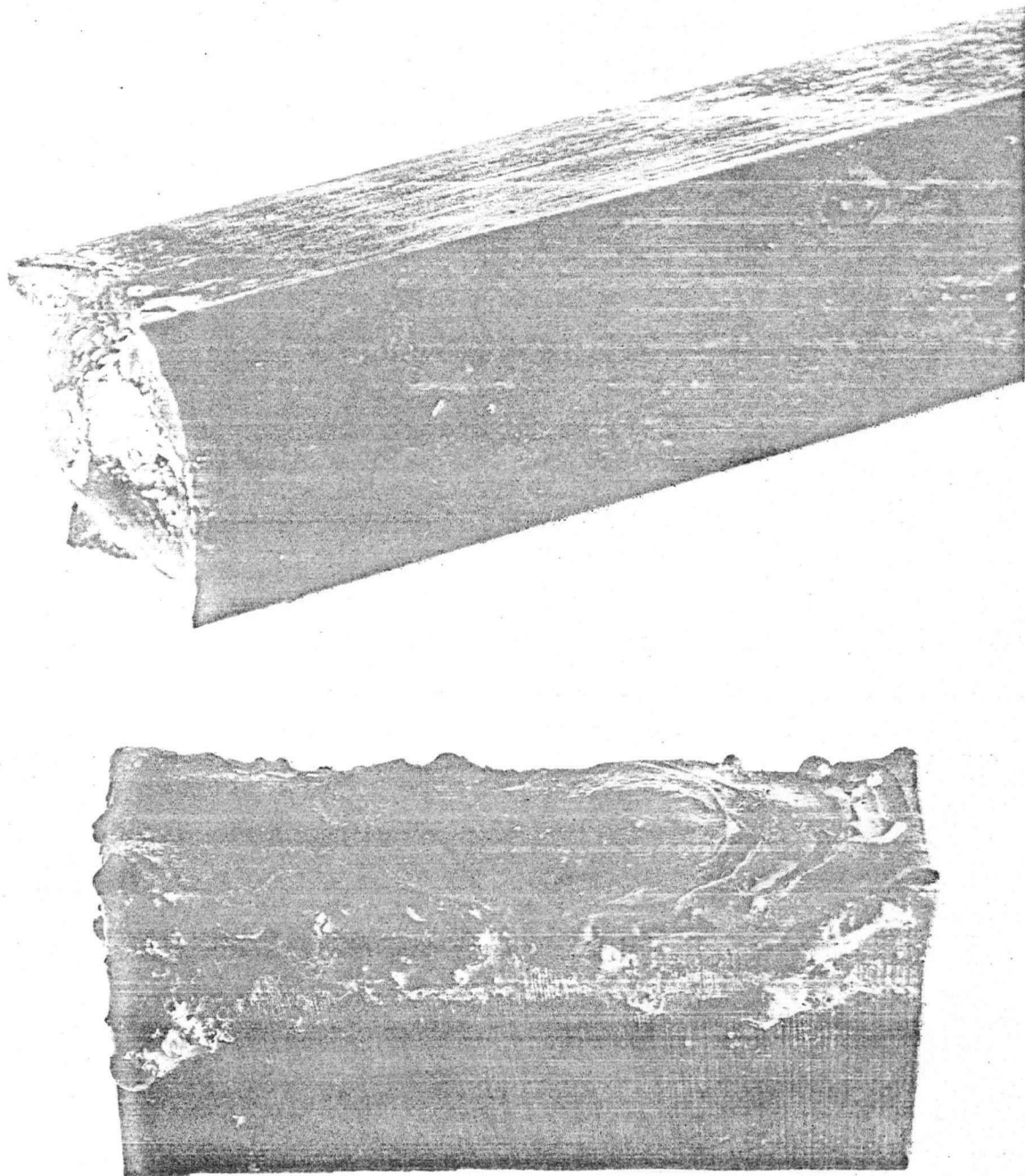


Figure 131 Typical bar electrode tips

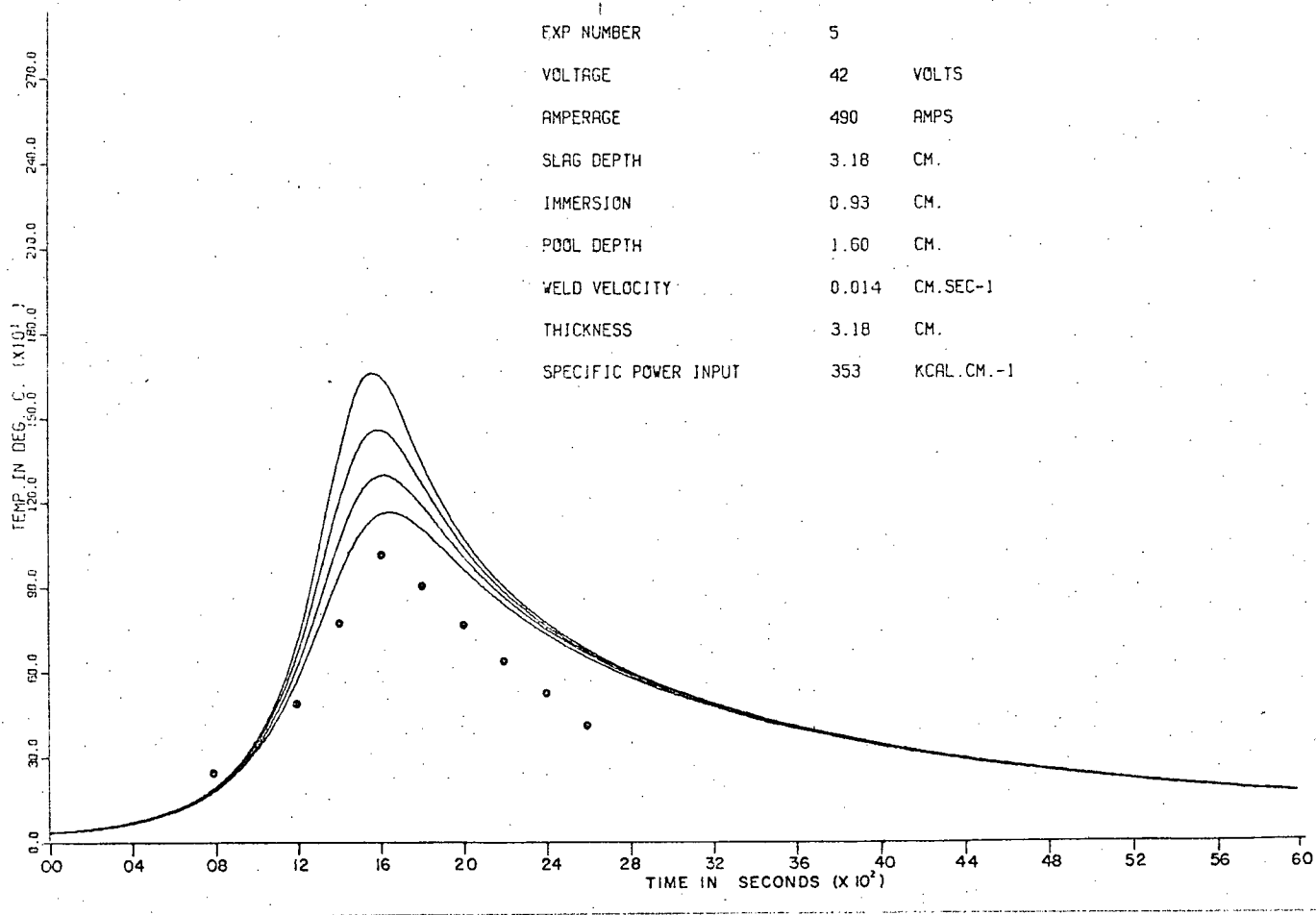


Figure 132 Model predicted thermal profile for P05.

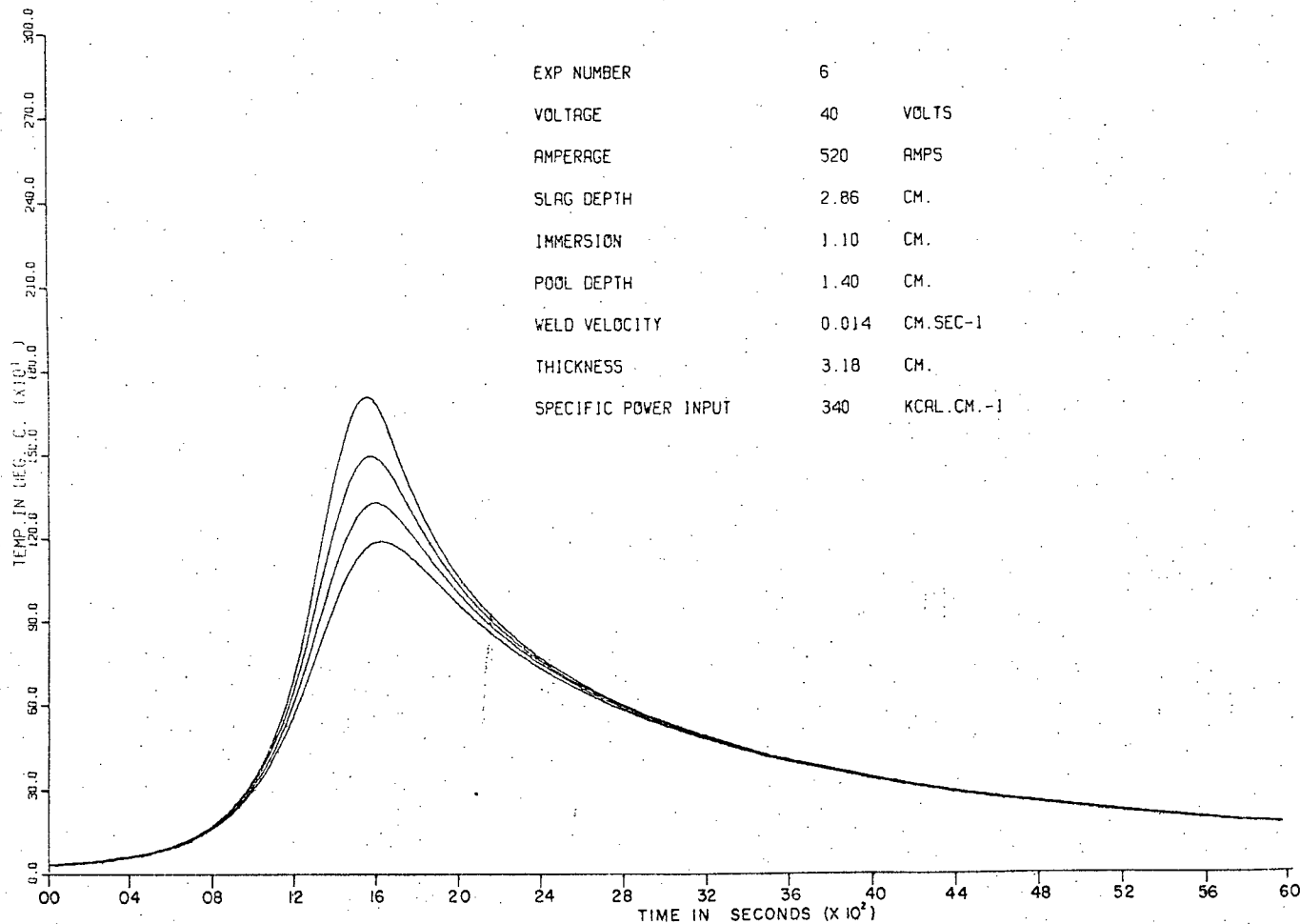
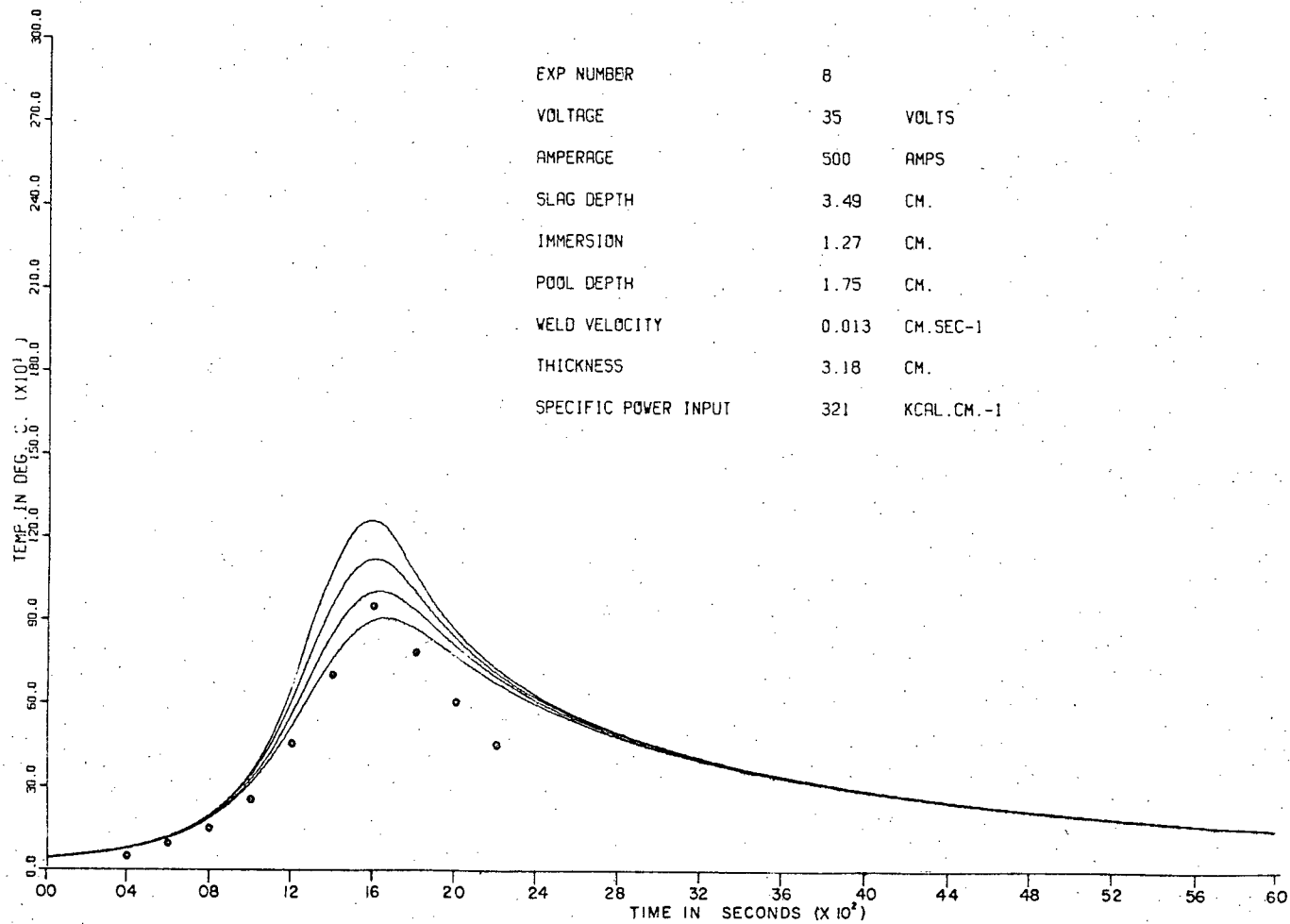
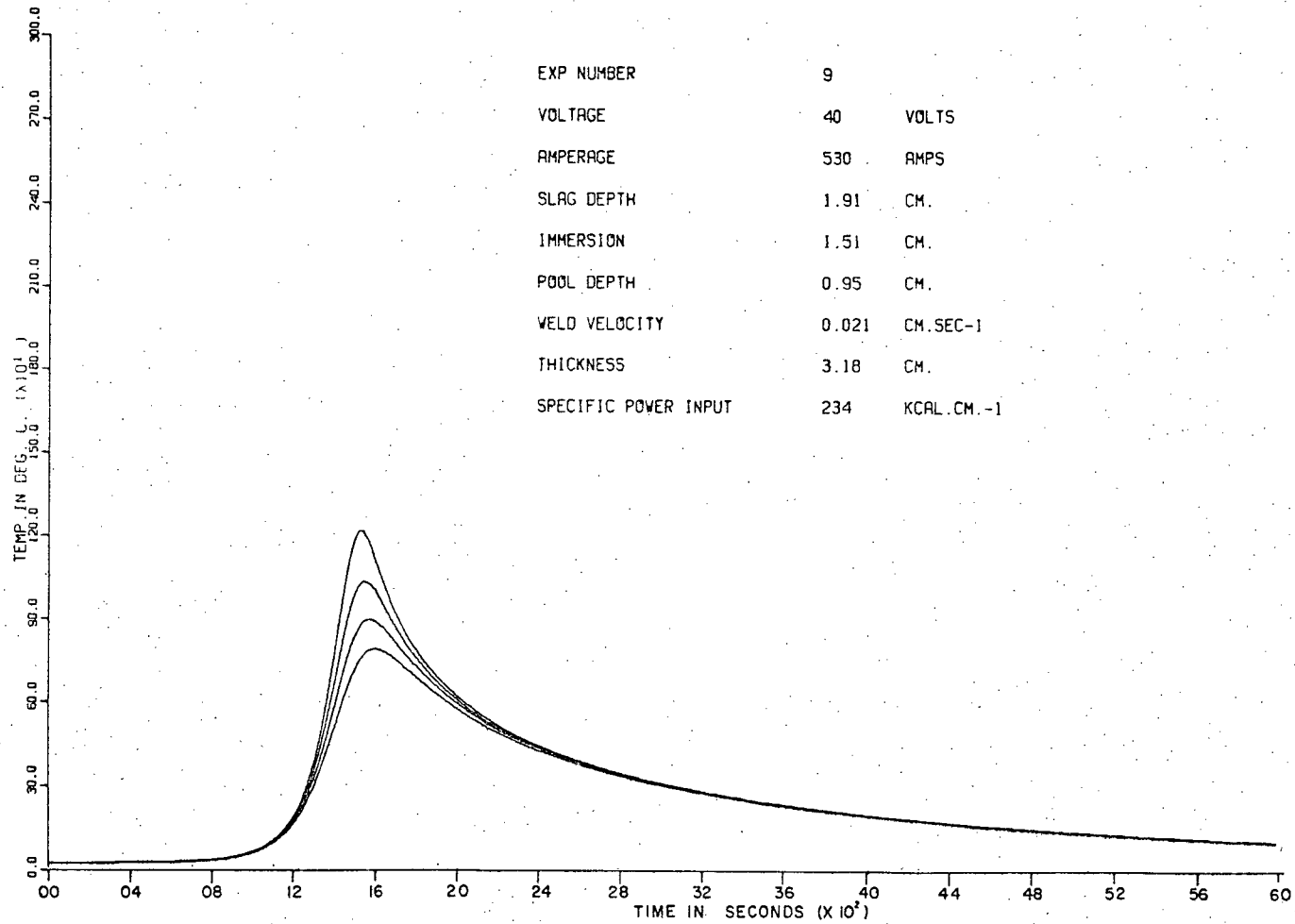


Figure 133 Model predicted thermal profile for P06.



EXP NUMBER	8	
VOLTAGE	35	VOLTS
AMPERAGE	500	AMPS
SLAG DEPTH	3.49	CM.
IMMERSION	1.27	CM.
POOL DEPTH	1.75	CM.
WELD VELOCITY	0.013	CM.SEC-1
THICKNESS	3.18	CM.
SPECIFIC POWER INPUT	321	KCAL.CM.-1

Figure 134 Model predicted thermal profile for P08.



EXP NUMBER	9	
VOLTAGE	40	VOLTS
AMPERAGE	530	AMPS
SLAG DEPTH	1.91	CM.
IMMERSION	1.51	CM.
POOL DEPTH	0.95	CM.
WELD VELOCITY	0.021	CM.SEC-1
THICKNESS	3.18	CM.
SPECIFIC POWER INPUT	234	KCAL.CM.-1

Figure 135 Model predicted thermal profile for P09.

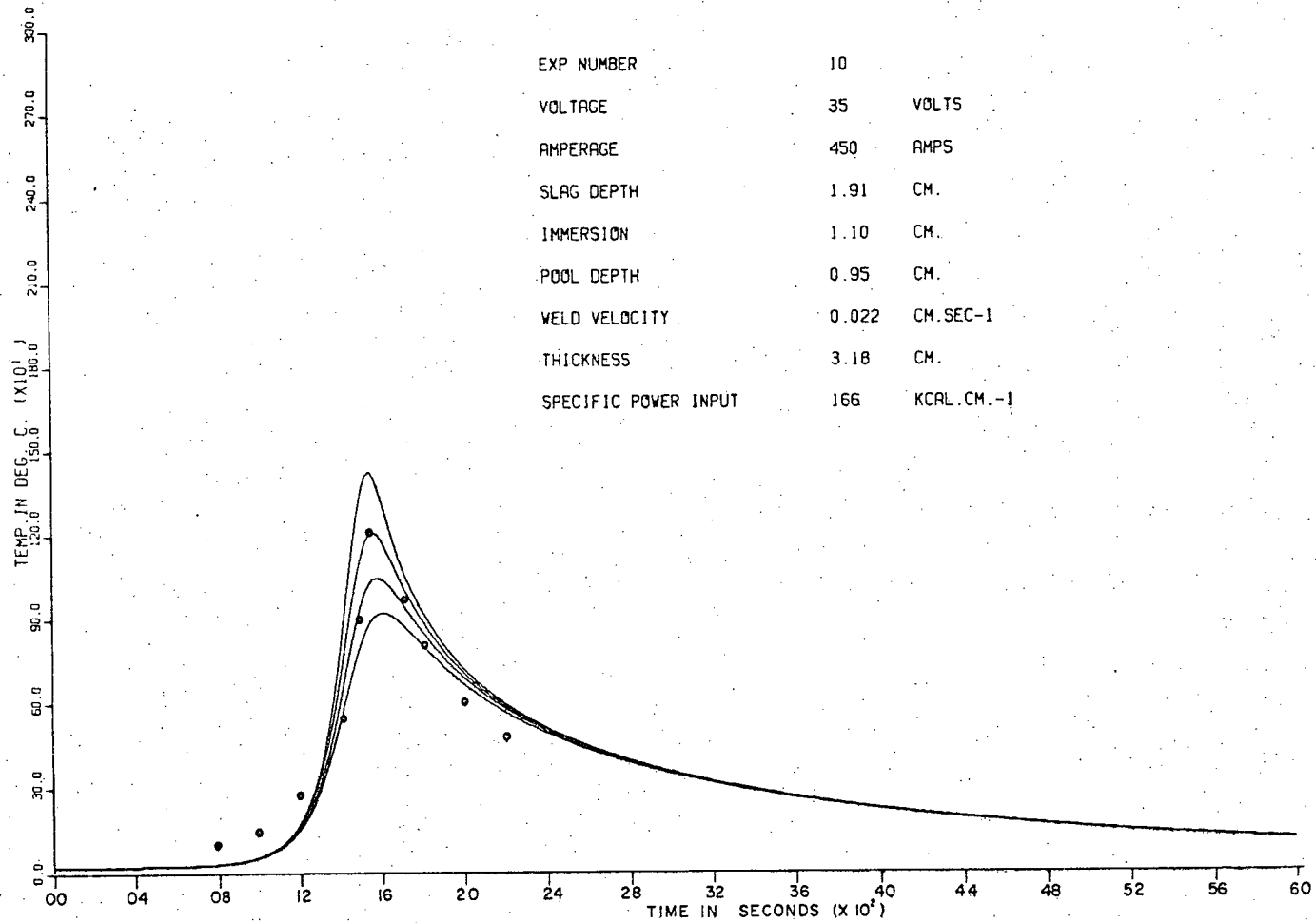


Figure 136 Model predicted thermal profile for P10.

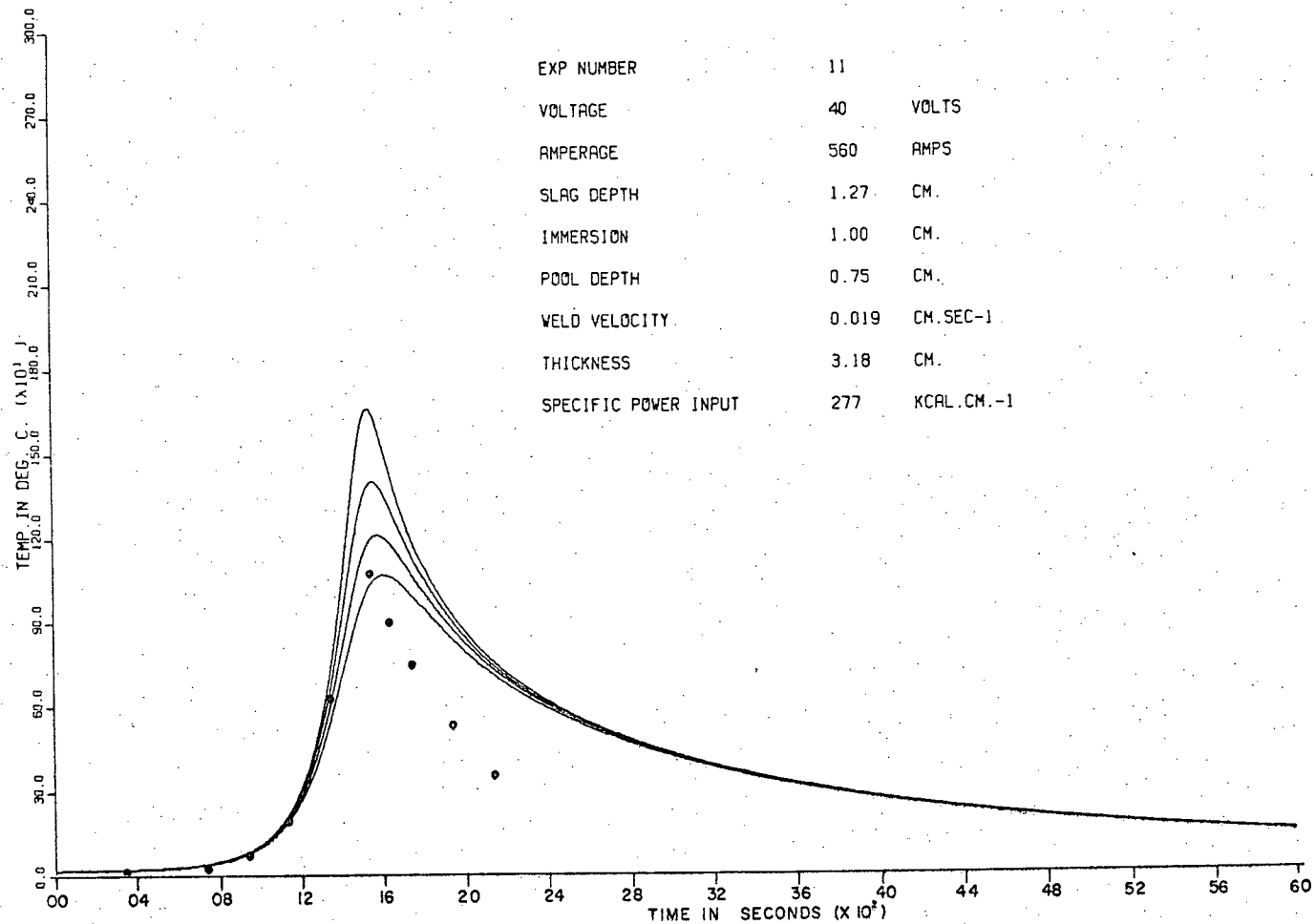


Figure 137 Model predicted thermal profile for P11.

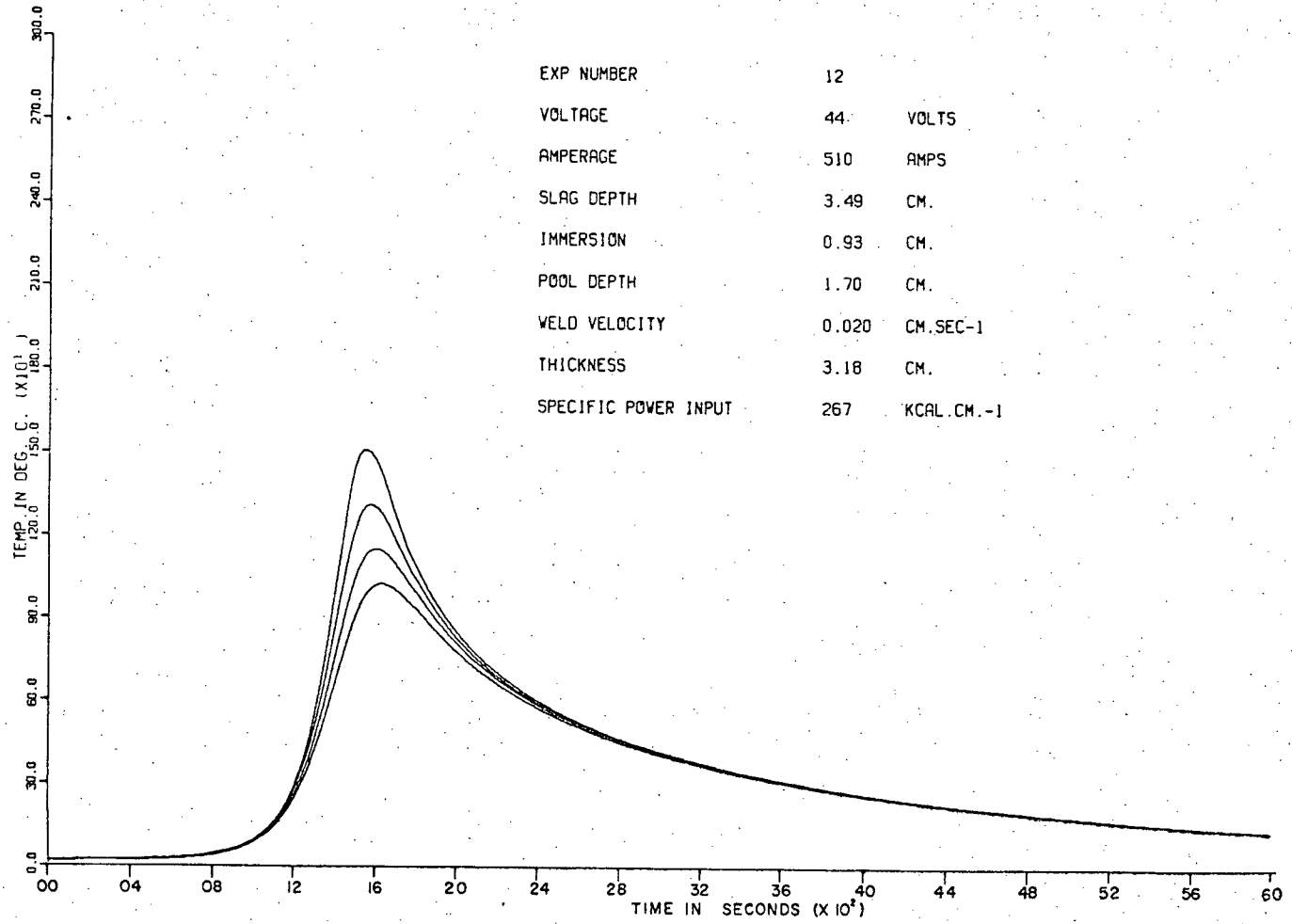


Figure 138 Model predicted thermal profile for P12.

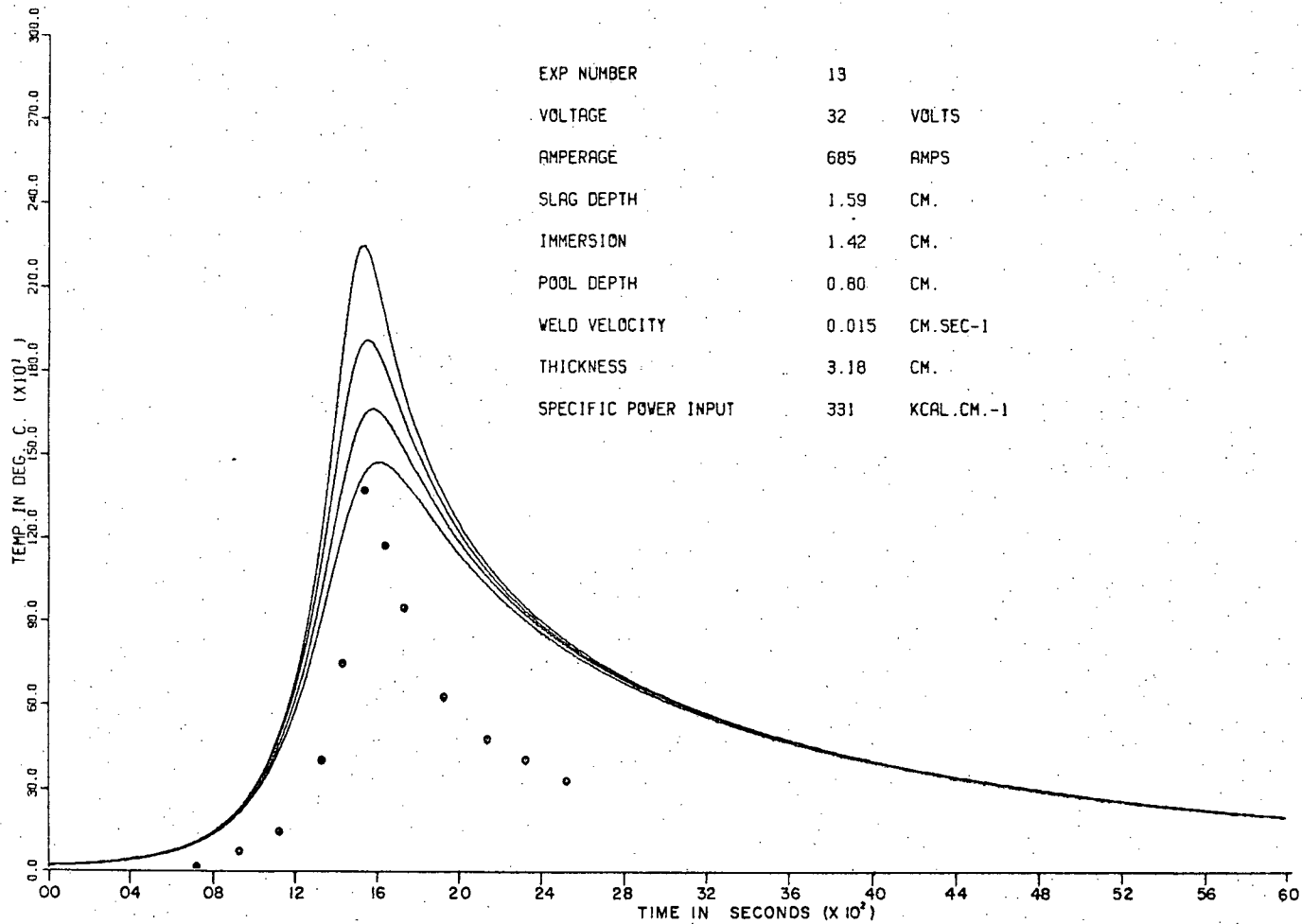


Figure 139 Model predicted thermal profile for P13.

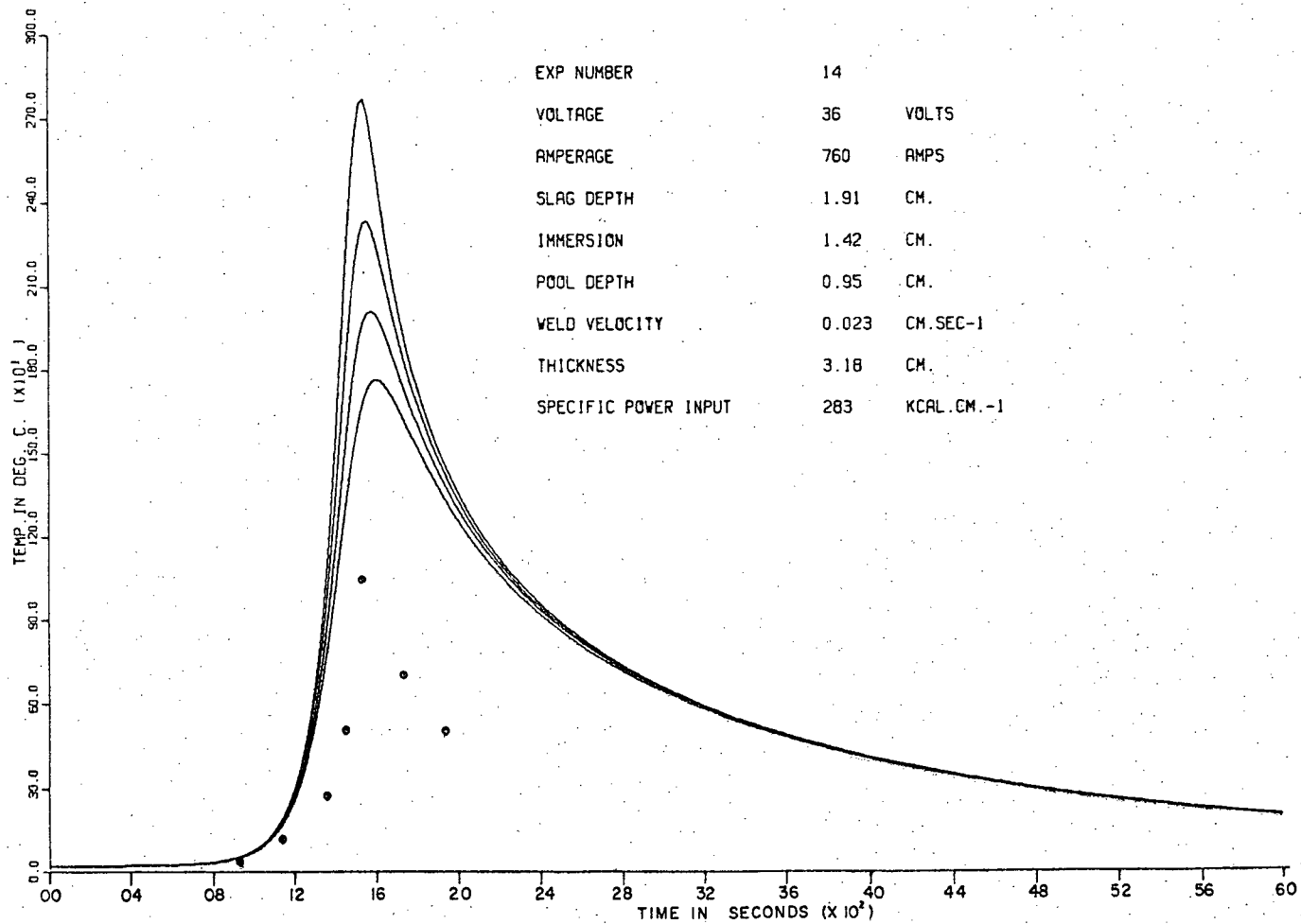
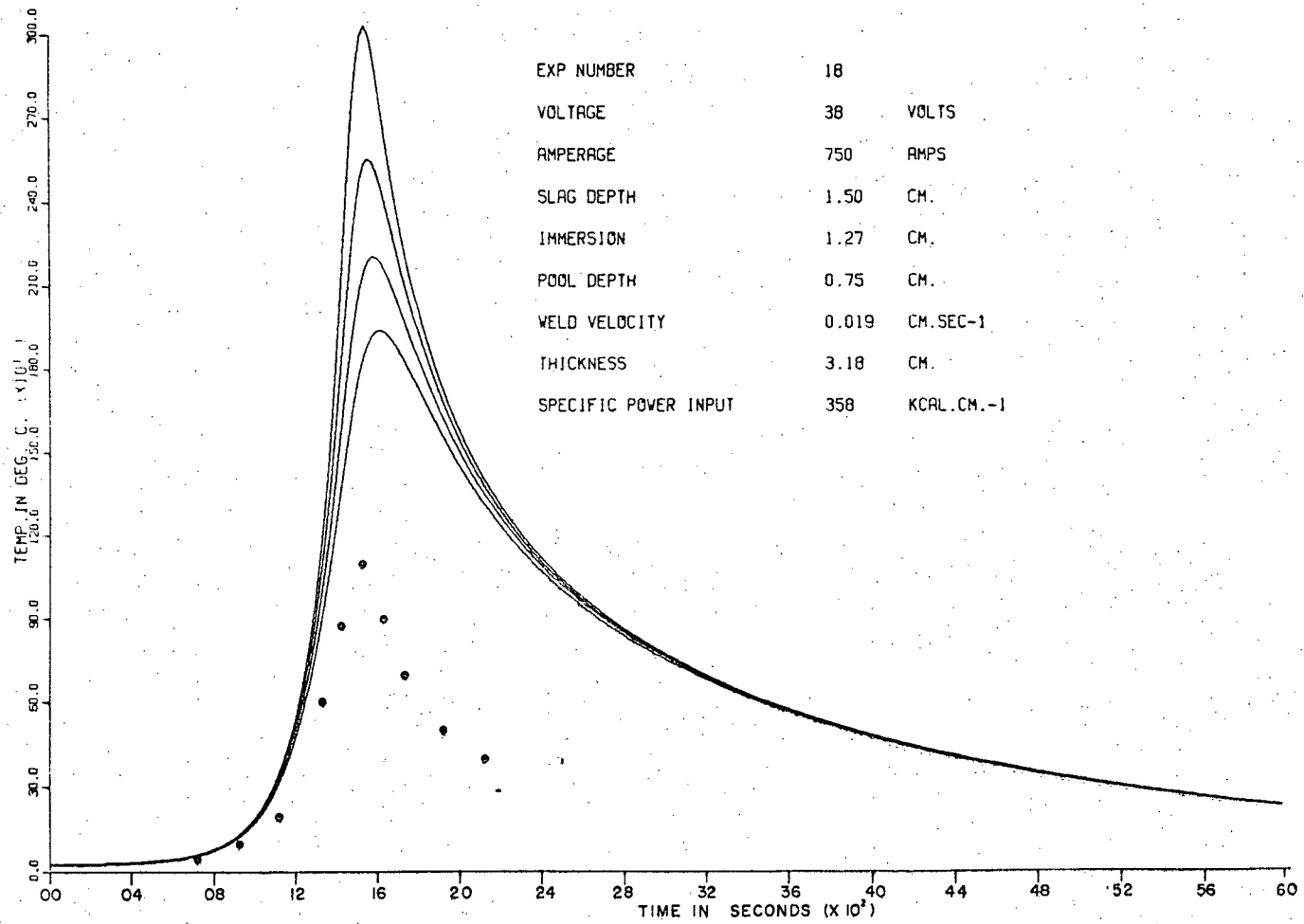
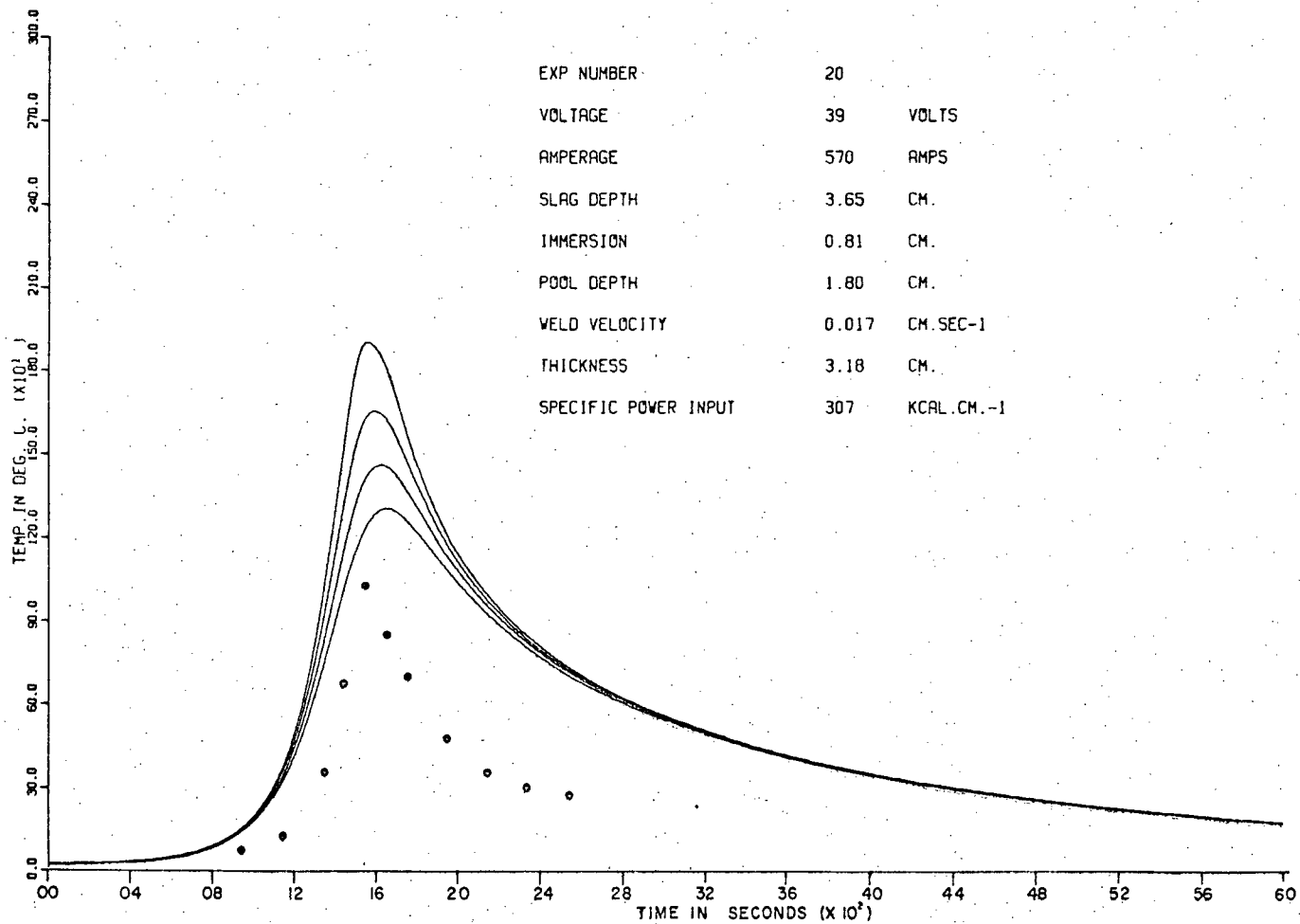


Figure 140 Model predicted thermal profile for P14.



EXP NUMBER 18
 VOLTAGE 38 VOLTS
 AMPERAGE 750 AMPS
 SLAG DEPTH 1.50 CM.
 IMMERSION 1.27 CM.
 POOL DEPTH 0.75 CM.
 WELD VELOCITY 0.019 CM.SEC-1
 THICKNESS 3.18 CM.
 SPECIFIC POWER INPUT 358 KCAL.CM.-1

Figure 141 Model predicted thermal profile for P18.



EXP NUMBER 20
 VOLTAGE 39 VOLTS
 AMPERAGE 570 AMPS
 SLAG DEPTH 3.65 CM.
 IMMERSION 0.81 CM.
 POOL DEPTH 1.80 CM.
 WELD VELOCITY 0.017 CM. SEC-1
 THICKNESS 3.18 CM.
 SPECIFIC POWER INPUT 307 KCAL. CM.-1

Figure 142 Model predicted thermal profile for P20.

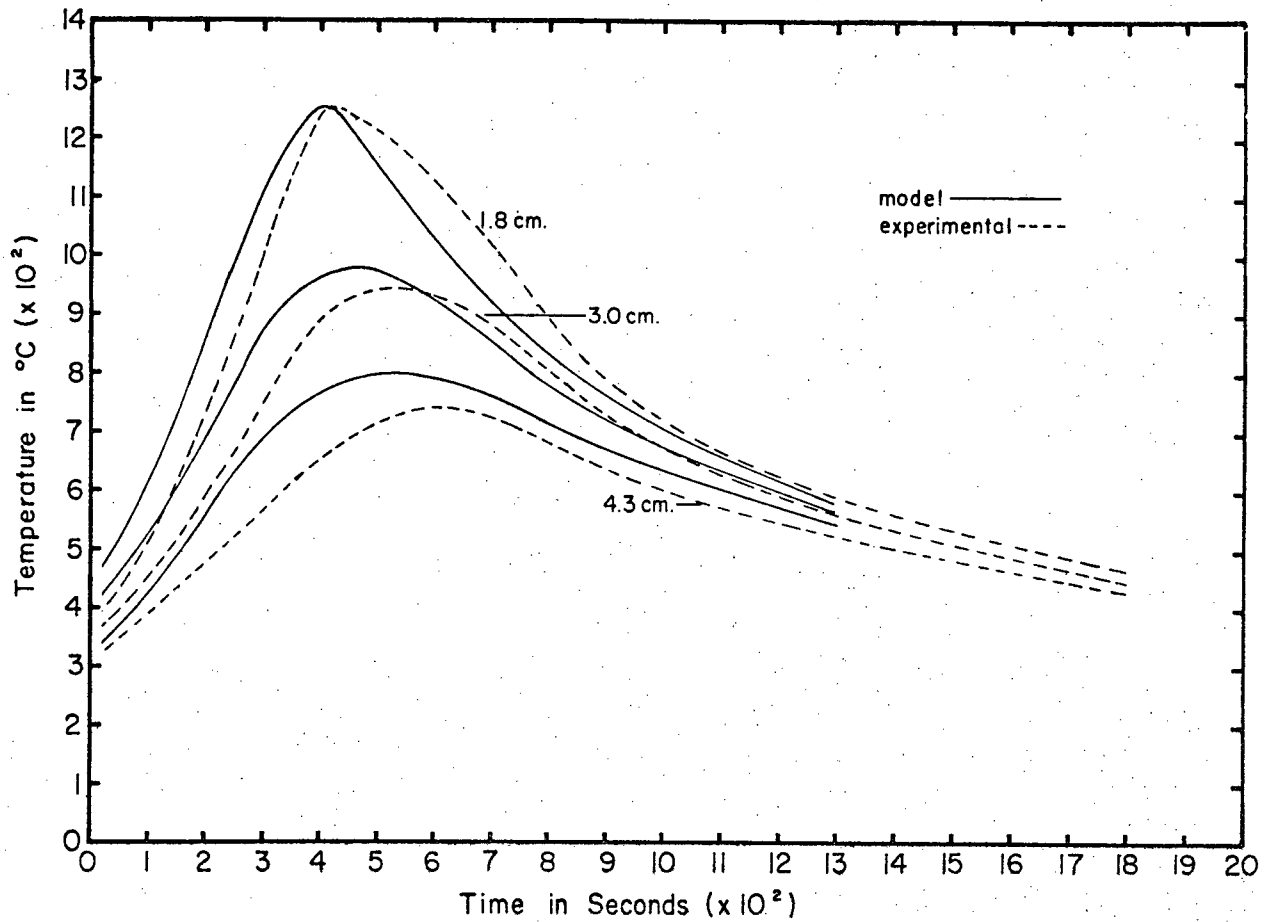


Figure 143 Predicted thermal profile for experiment 1(a), Pugin (16).

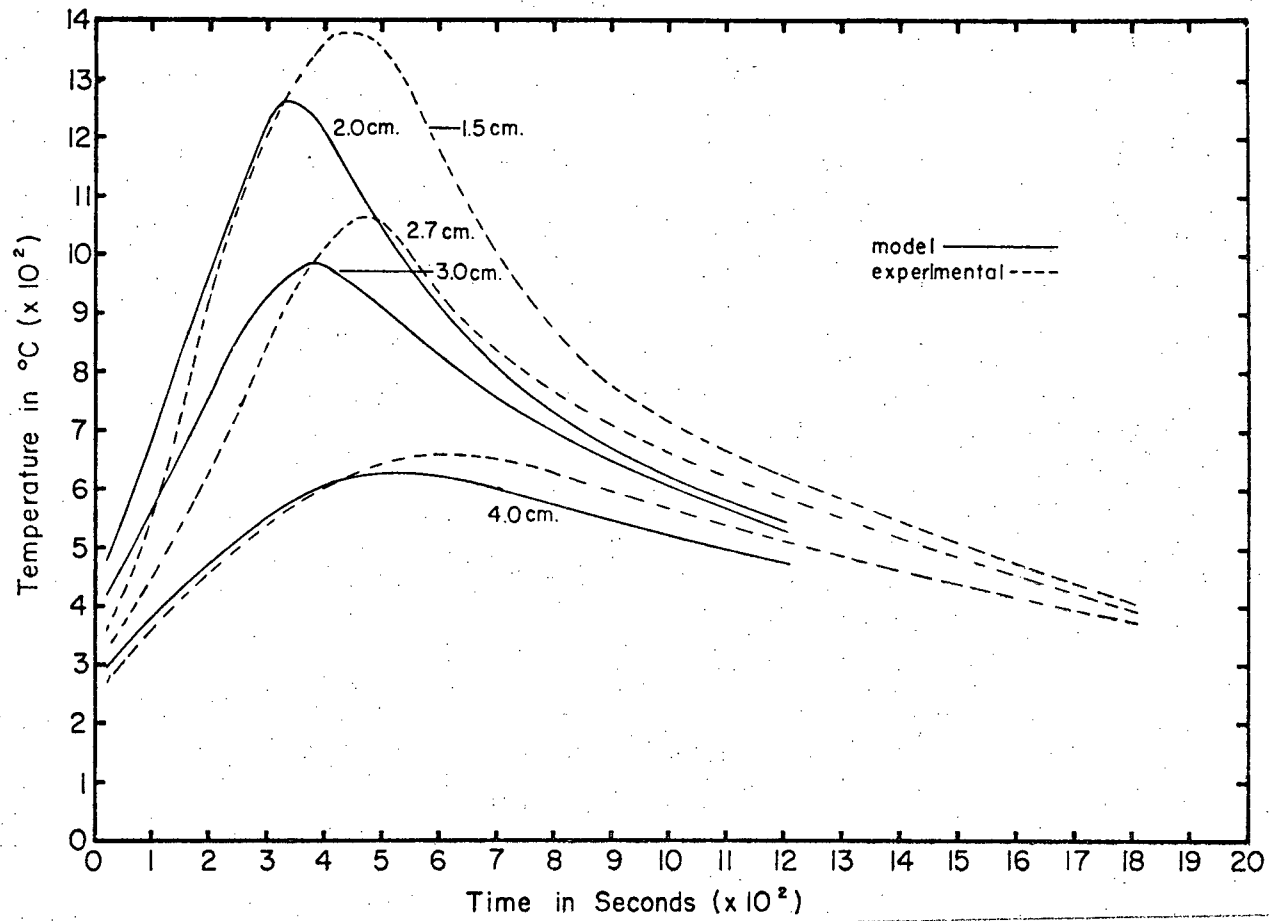


Figure 144 Predicted thermal profile for experiment 1(b), Pugin (16).

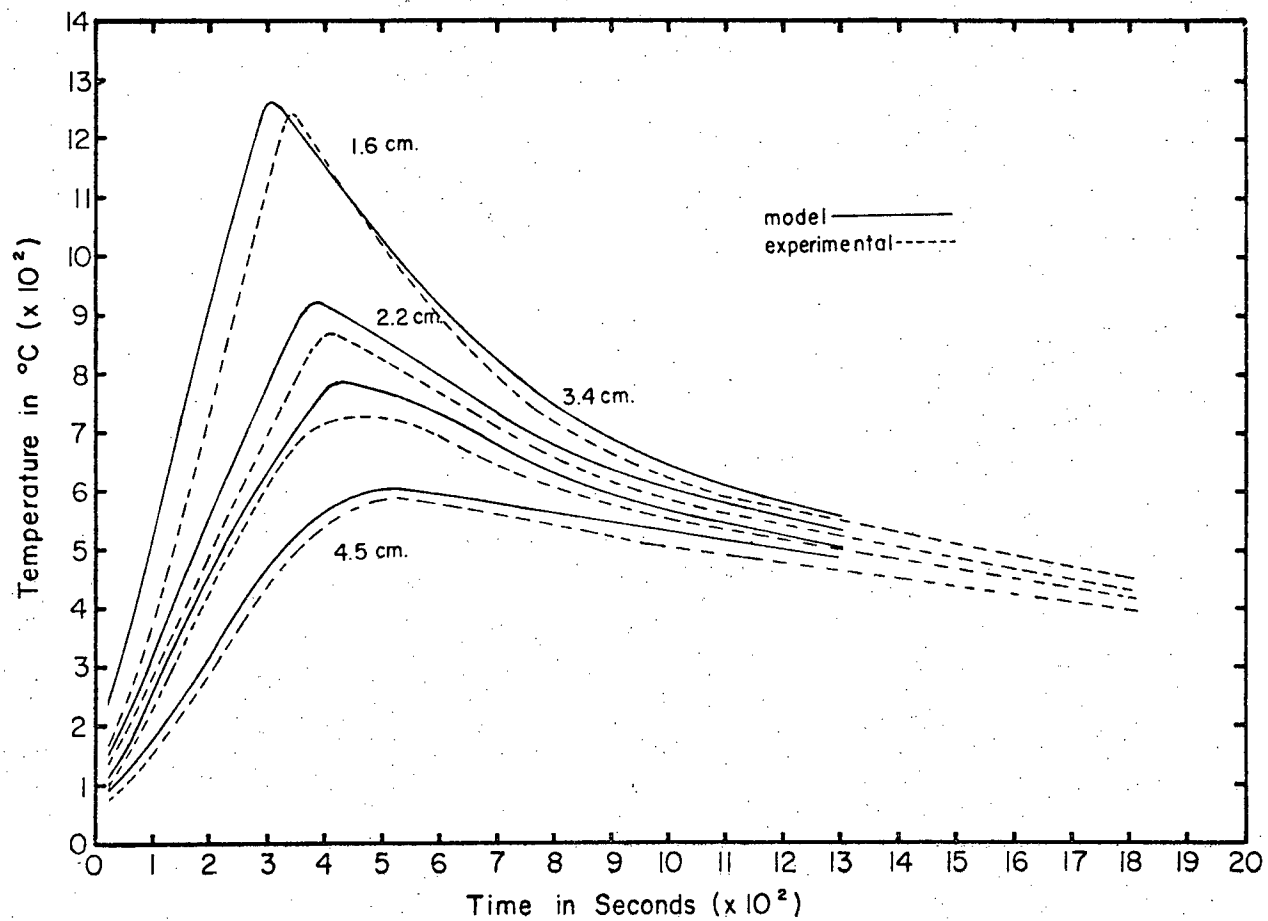


Figure 145 Predicted thermal profile for experiment 2, Pugin (16)

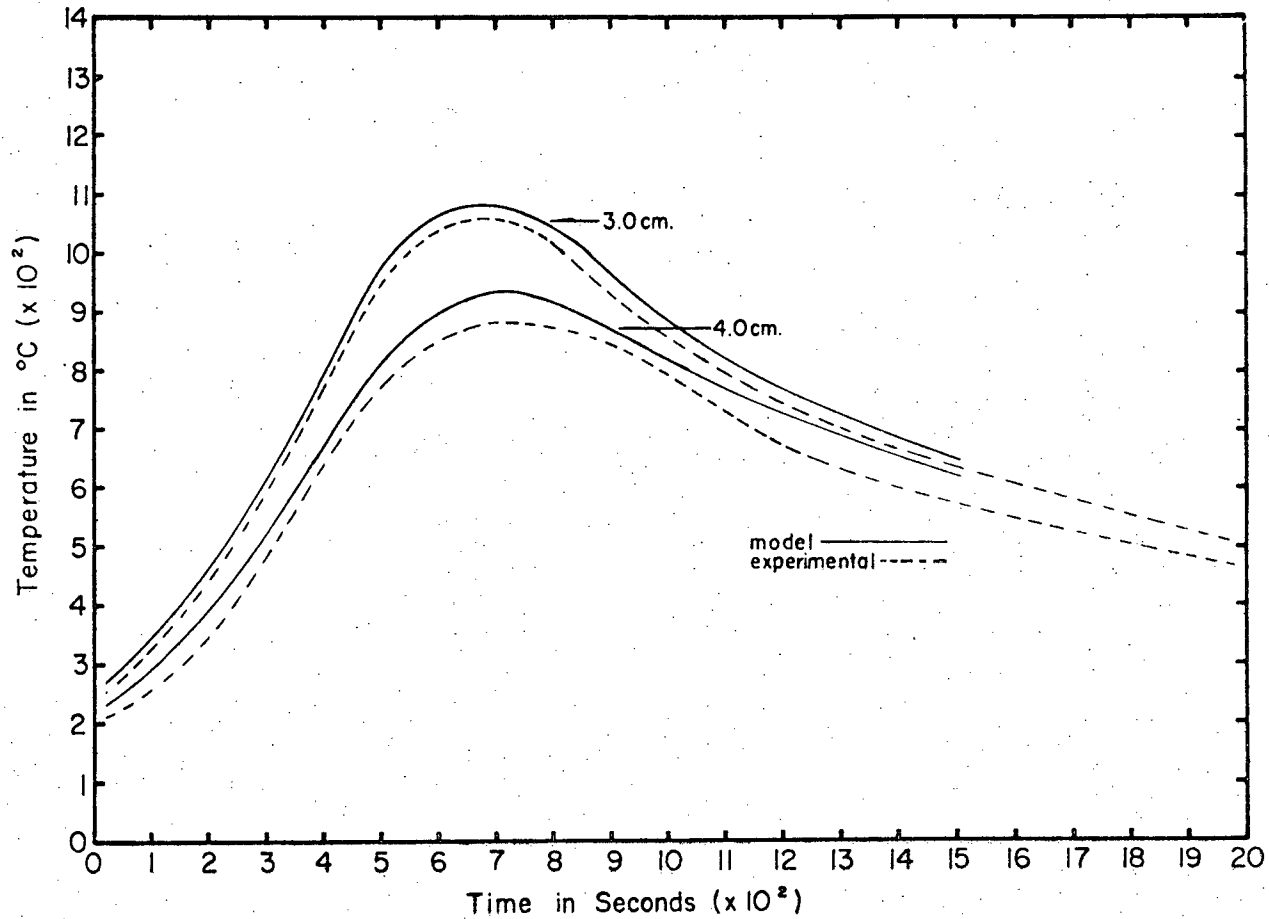


Figure 146 Predicted thermal profile for experiment 3, Pugin (16).

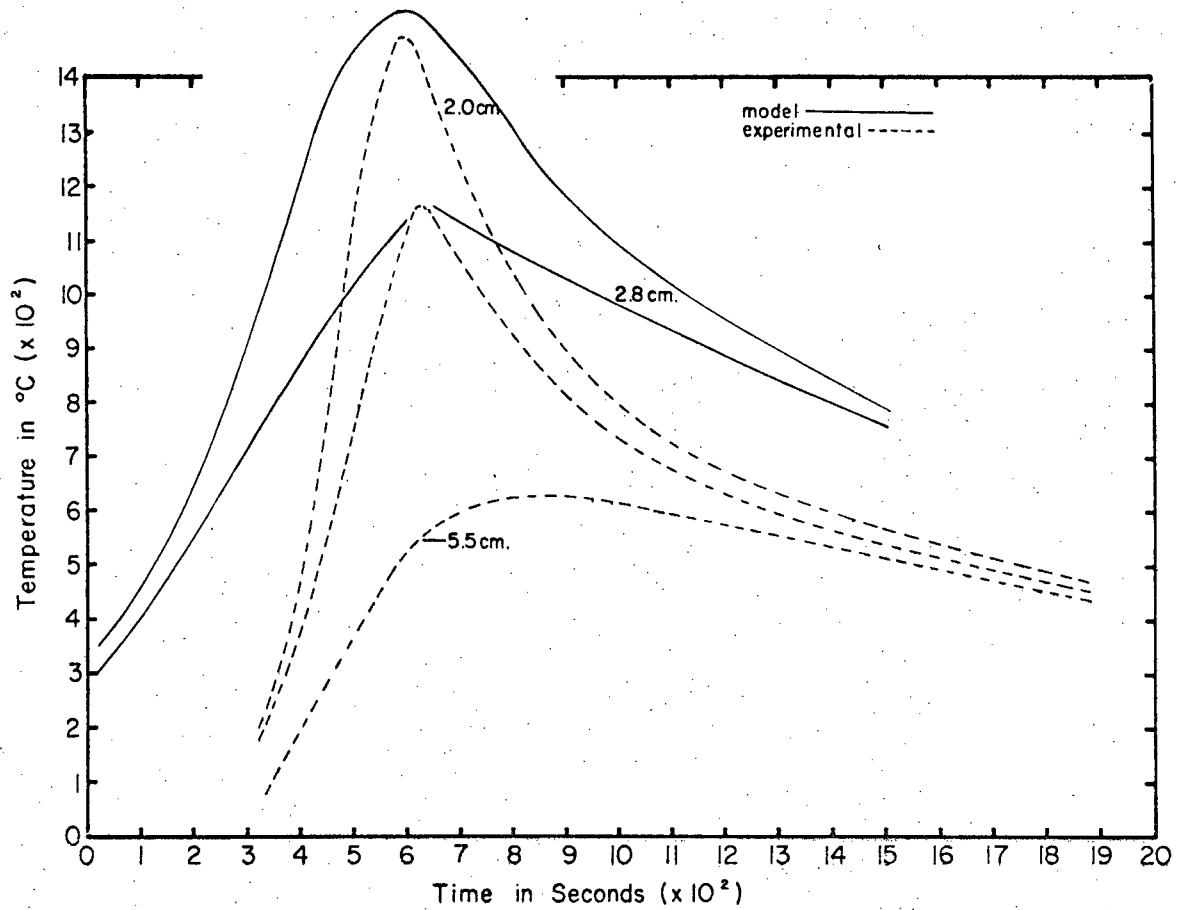


Figure 147 Predicted thermal profile for experiment 4, Pugin (16).

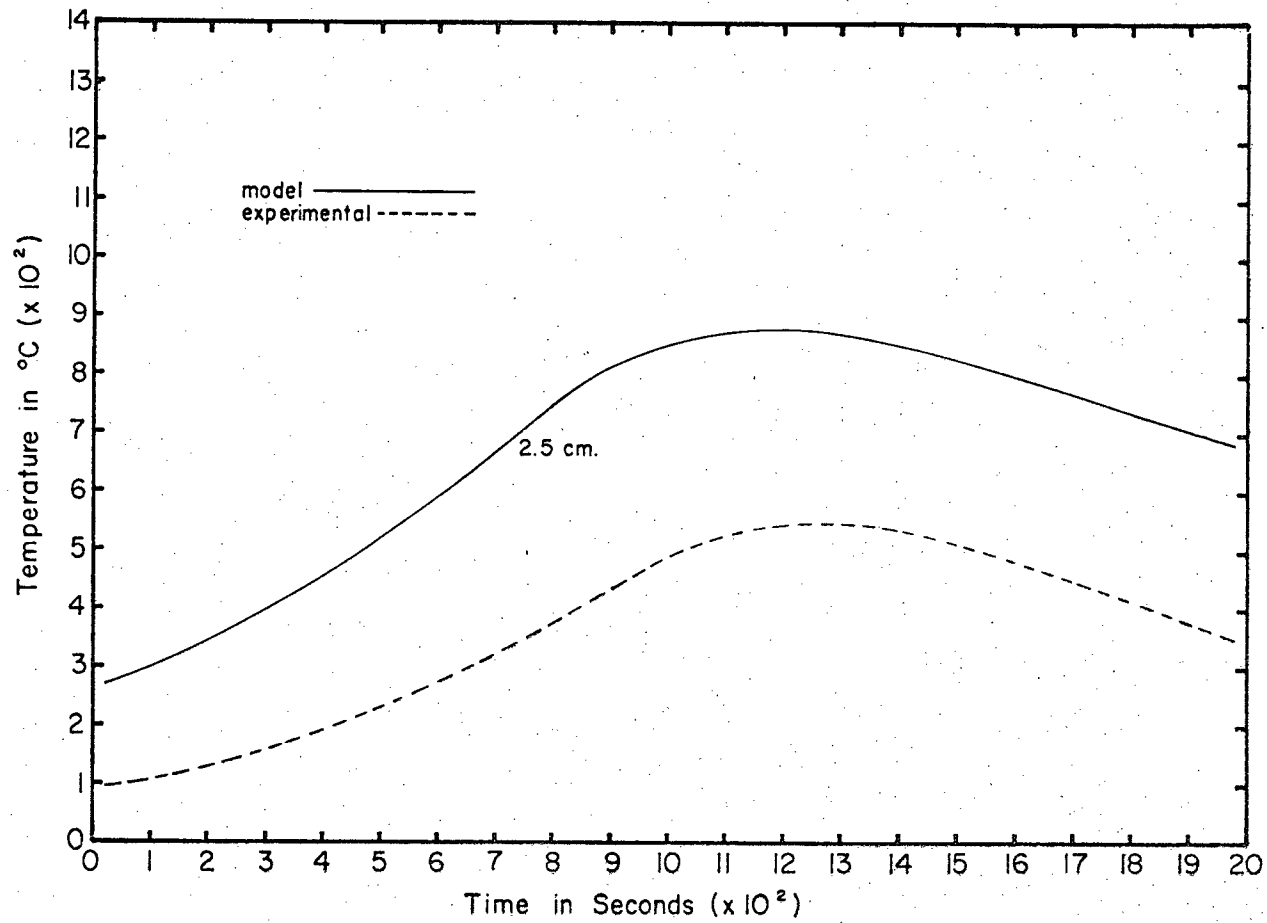


Figure 148. Predicted thermal profile for experiment 1, Sharapov (17).

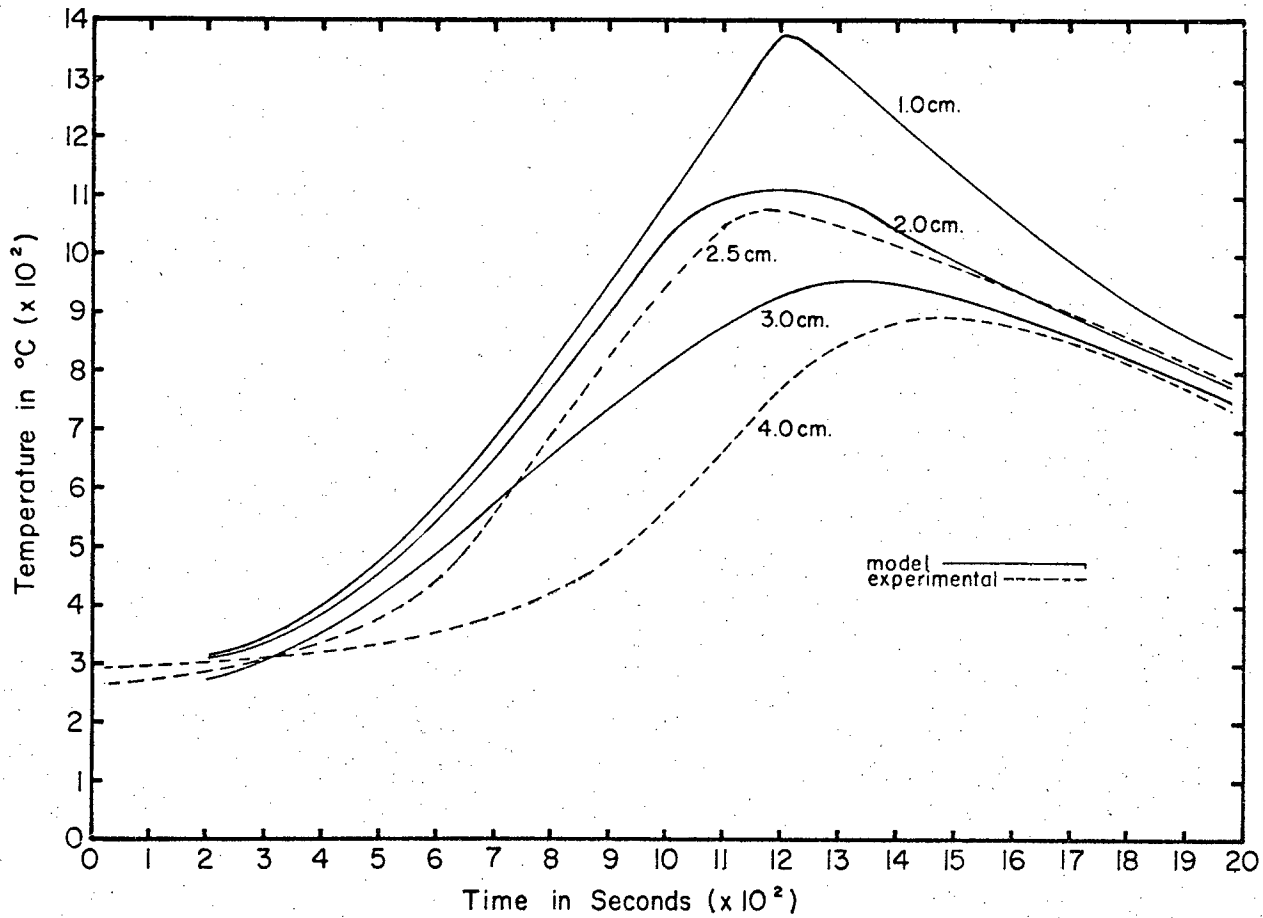


Figure 149 Predicted thermal profile for experiment b, Sharapov, (17).

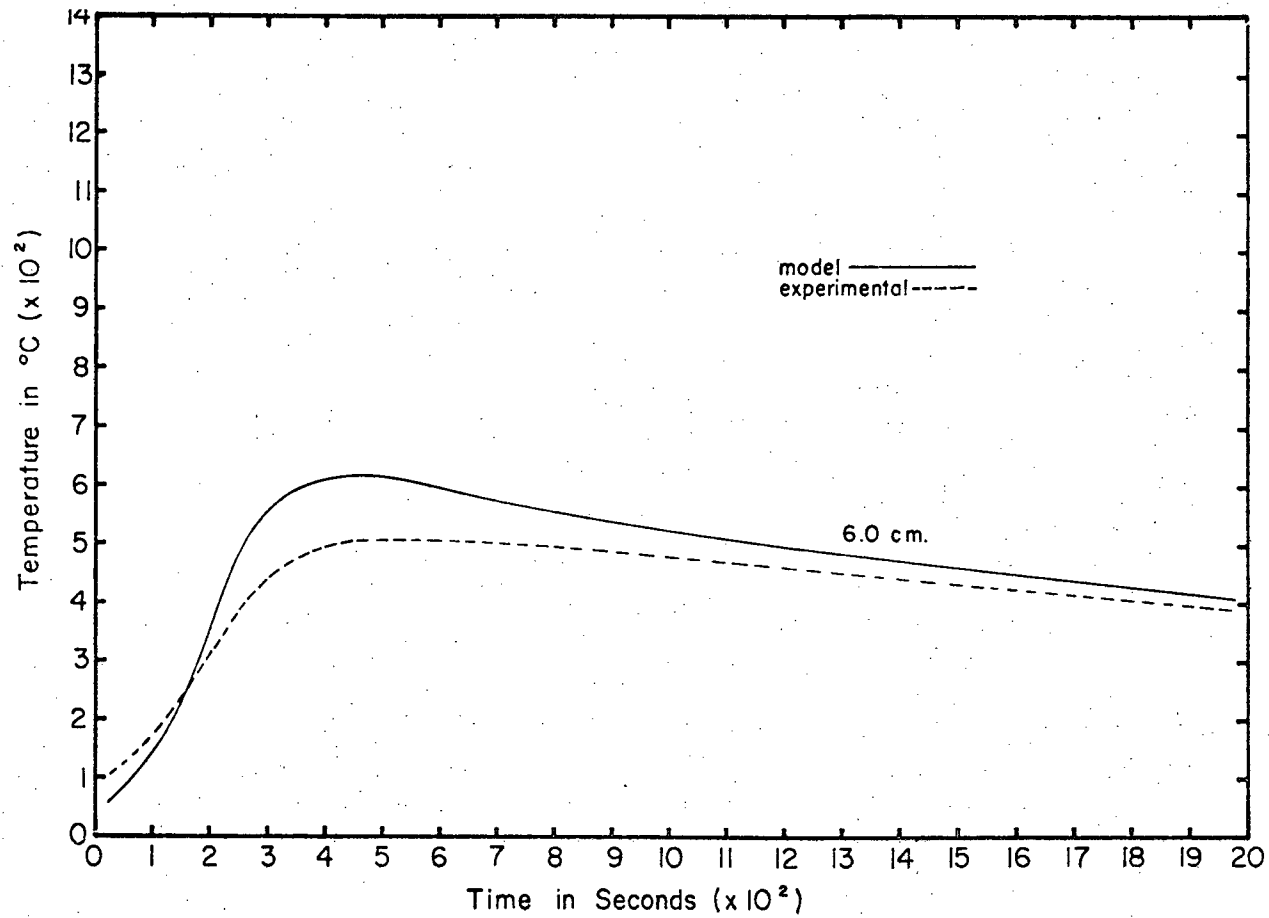


Figure 150 Predicted thermal profile for experiment 3, Sharapov (17).

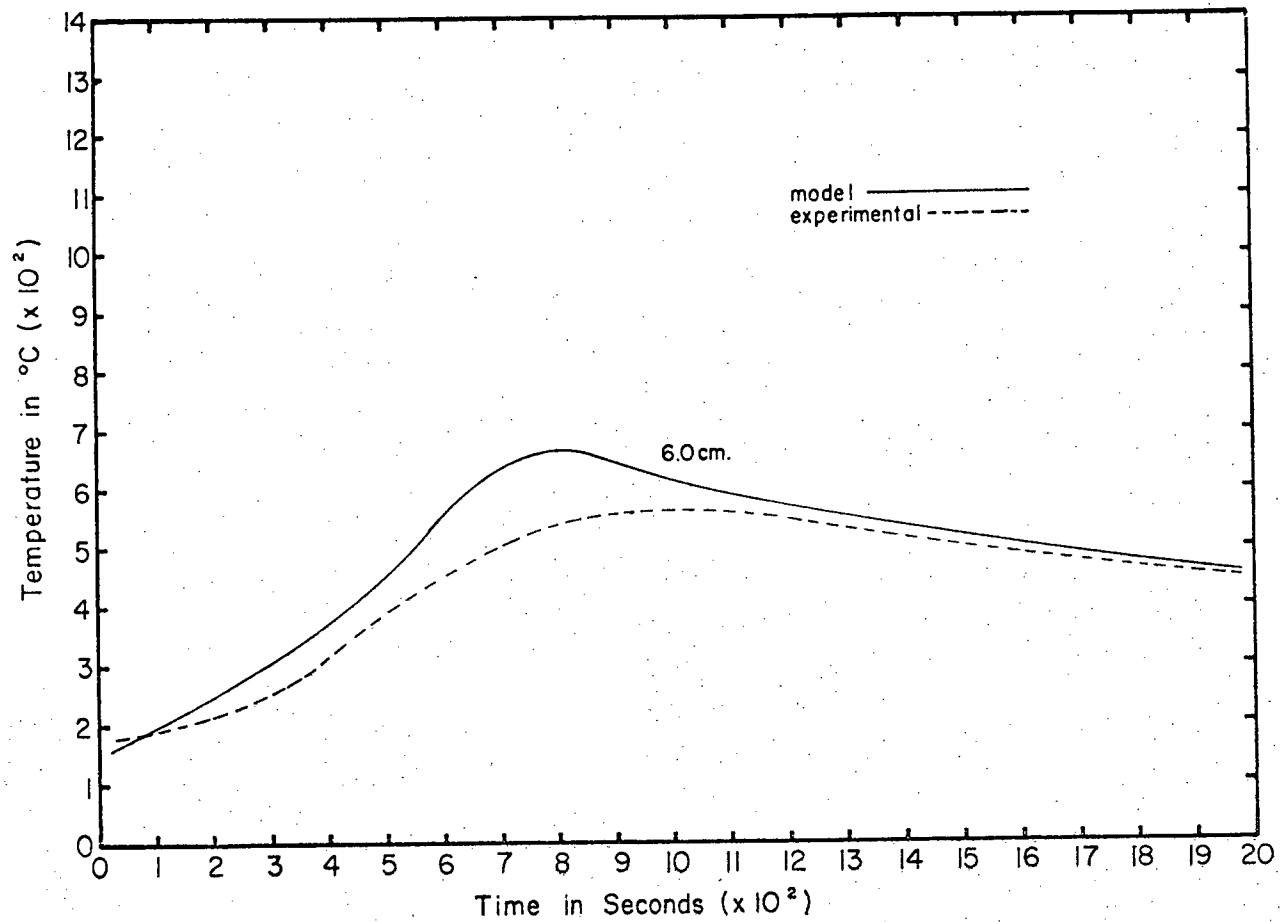


Figure 151 Predicted thermal profile for experiment 1, Sharapov (18).

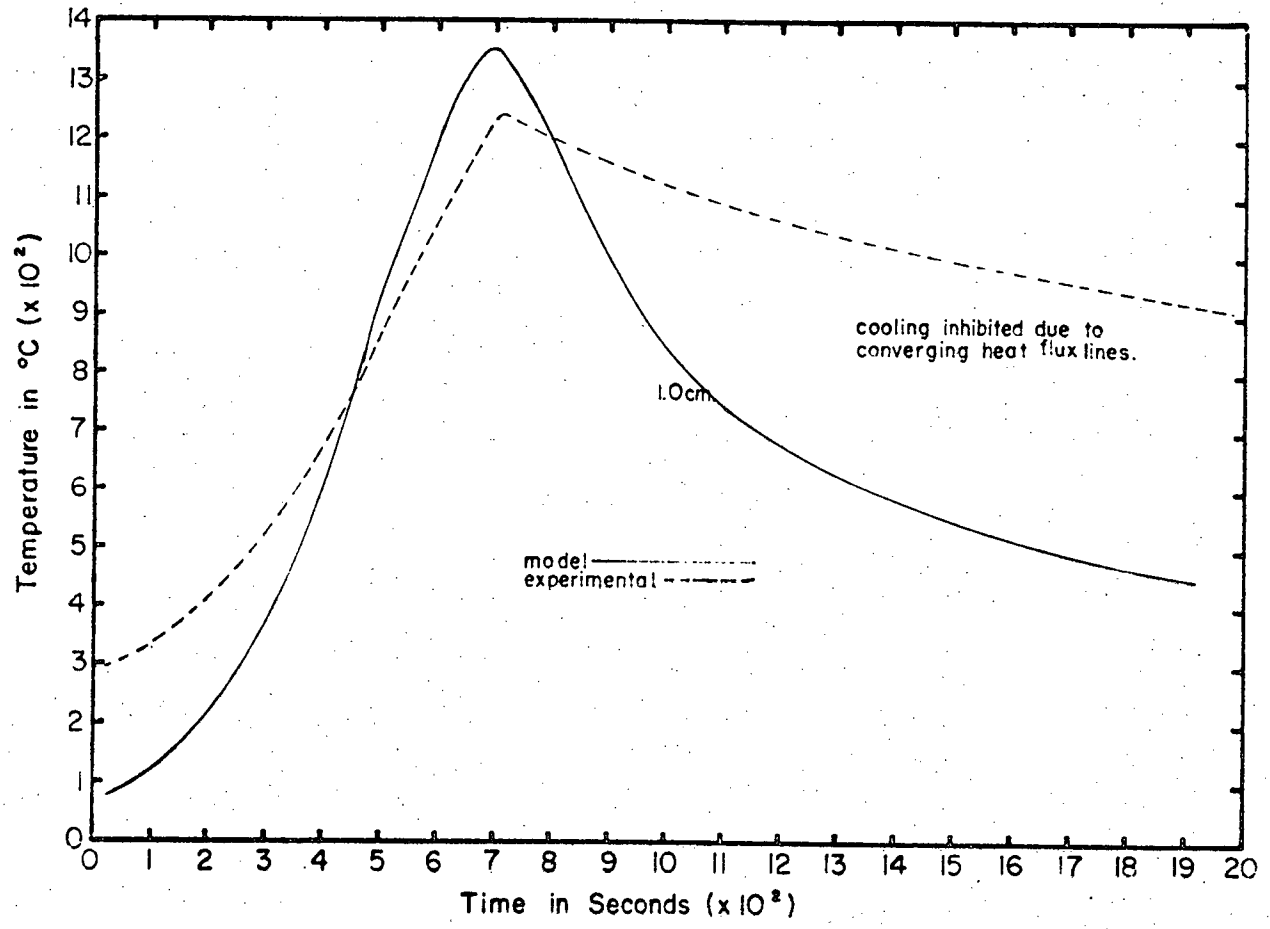


Figure 152 Predicted thermal profile for experiment 1, Trepov (19).

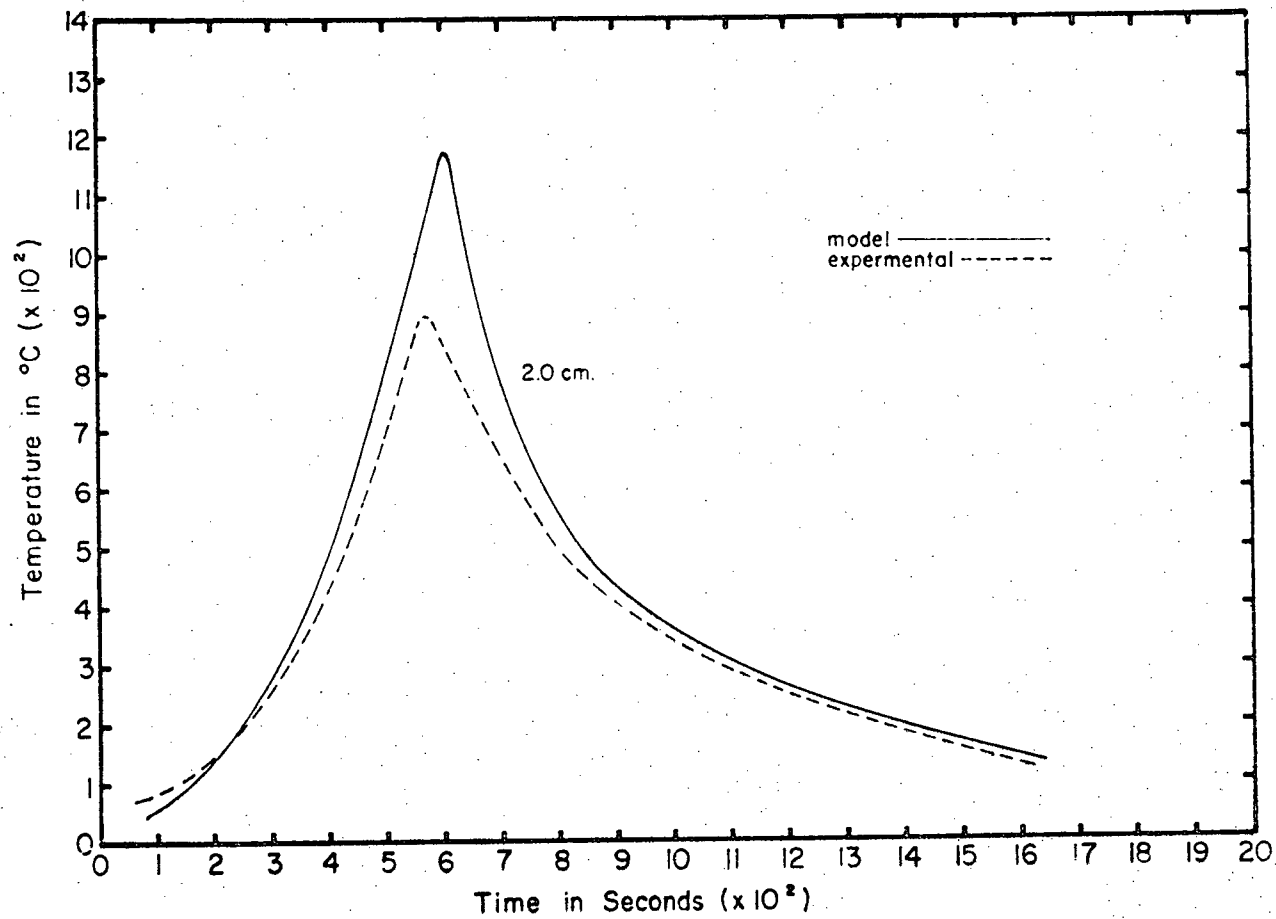


Figure 153 Predicted thermal profile for experiment. 2, Trepov (19).

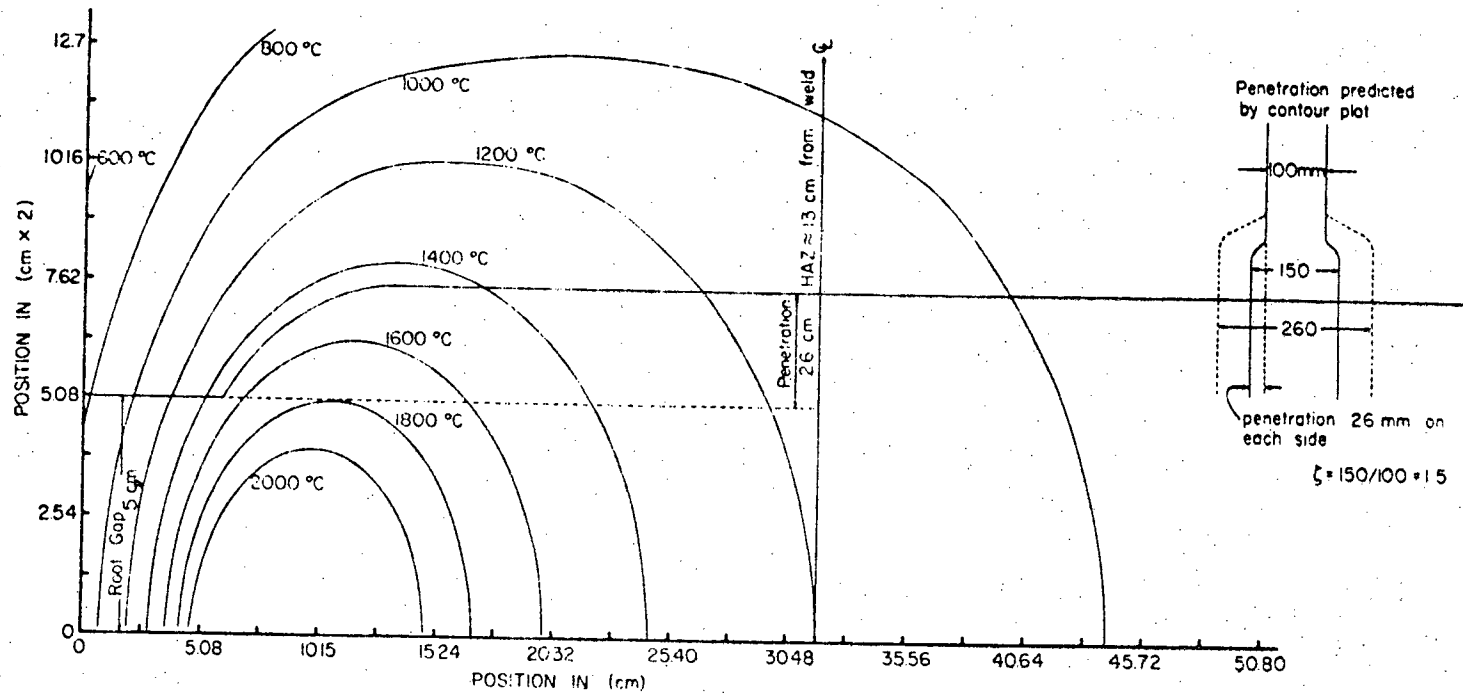


Figure 154 Predicted Isotherms in a large electroslog weld.